

Behavior of Reinforced Concrete Continuous Beams under Pure Torsion

Saad Khalaf Mohaisen

Assistant Professor

College of Engineering

Al-Mustansiriya University

eng_saad@uomustansiriyah.edu.iq

Ali Adel Abdulhameed

Assistant Lecturer

Department of Engineering Affairs

University of Baghdad

aliadel@uobaghdad.edu.iq

Majid Mohammad Kharnoob

Lecturer

Department of Engineering Affairs

University of Baghdad

dr.majidkharnoob@uobaghdad.edu.iq

ABSTRACT

Practically, torsion is normally combined with flexure and shear actions. Even though, the behavior of reinforced concrete continuous beams under pure torsion is investigated in this study. It was performed on four RC continuous beams under pure torsion. In order to produce torsional moment on the external supports, an eccentric load was applied at various distances from the longitudinal axis of the RC beams until failure.

Variables considered in this study are absolute vertical displacement of the external supports, torsional moment's capacity, angle of twist and first cracks occurrences. According to experimental results; when load eccentricity increased from 30cm to 60cm, the absolute vertical displacement increased about 46.92% and the angle of twist increased about 45.76% at failure. It has been also found that the ultimate failure loads decreased about 49.65% when the load eccentricity increased from 30cm to 60cm. Furthermore, the first crack was monitored and it was found that the first crack occurred at higher stages of loading with low loading eccentricity. The first crack records appeared at 75.86%, 70.80%, 63.16% and 54.79% of loading when the load eccentricities are 30, 40, 50 and 60cm, respectively.

Key words: angle of twist, continuous beam, eccentric loading, pure torsion, torsional moments.

سلوك العتبات الخرسانية المسلحة والمستمرة تحت تأثير عزوم اللي الصرفة

ماجد محمد خرنوب

مدرس

قسم الشؤون الهندسية

جامعة بغداد

علي عادل عبد الحميد

مدرس مساعد

قسم الشؤون الهندسية

جامعة بغداد

سعد خلف محيسن

أستاذ مساعد

كلية الهندسة

الجامعة المستنصرية

الخلاصة

عملياً عزوم اللي عادةً ما تشترك مع عزوم الأحناء وقوى القص. على الرغم من ذلك، تمت دراسة سلوك العتبات الخرسانية المسلحة والمستمرة تحت تأثير عزوم اللي الصرفة في هذا البحث حيث تمت دراسة تصرف أربعة عتبات مسلحة ومستمرة تحت تأثير عزوم اللي. ولغرض الحصول على عزوم اللي على المساند الخارجية، تم تسليط أحمال لامركزية وعلى مسافات مختلفة من المحور الطولي للعتبات الخرسانية المسلحة والمستمرة حتى فشل العتبة.

تتضمن المتغيرات التي تم دراستها في هذا البحث دراسة الهطول النسبي للمساند الخارجية، سعة العتبات المستمرة لتحمل عزوم اللي، زاوية اللي وحدوث التصدع الأولي. أظهرت النتائج عند زيادة بعد القوى المسلطة عن المحور الطولي للعتبة من 30سم الى 60سم أنتج زيادة الهطول النسبي للمساند الخارجية بنسبة 46.92% وزيادة زاوية اللي بنسبة 45.76% عند الفشل. بينت النتائج العملية نقصان في قوى التحمل القصوى للعتبات الخرسانية المسلحة بنسبة 49.65% عند زيادة بعد القوى المسلطة عن المحور الطولي للعتبة من 30سم الى 60سم. أيضاً تم مراقبة التصدع الأولي للعتبات حيث حدث التصدع الأولي عند تسليط أحمال بنسبة



المحور الطولي للعتبات المستمرة وعلى الترتيب. 75.86%، 70.8%، 63.16%، 54.79% من الحمل الأقصى وحالات التحميل اللامركزي لمسافات 30، 40، 50، 60 سم من

1. INTRODUCTION

Appreciable torsion does occur in many structures, such as in the main girders of bridges which are twisted by transverse beams or slabs. It occurs in buildings where the edge of a floor slab and its beams are supported by a spandrel beam running between the exterior columns. This situation is illustrated in **Fig.1**, where the floor beams tend to twist the spandrel beam laterally.

In complex structures such as helical stairways, curved beams, and eccentrically loaded box beams, the torsional effects dominate the structural behavior. Torsional moment tends to twist the structural member around its longitudinal axis, inducing shear stresses. However, structural members are rarely subjected to pure torsional moment. In most cases, torsional moments act concurrently with bending moment and shear forces, **Mahmoud, and Basile, 2007**.

Earthquakes can cause dangerous torsional forces in all buildings. This is particularly true in asymmetrical structures, where the centers of mass and rigidity do not coincide. Other cases where torsion may be significant are in curved bridge girders, spiral stairways, and balcony girders, and whenever large loads are applied to any beam "off center", **McCormac, and Brown, 2014**.

It is important for designers to distinguish between two types of torsions: equilibrium torsion and compatibility torsion. Equilibrium torsion occurs when the torsional resistance is required to maintain static equilibrium. For this case, if sufficient torsional resistance is not provided, the structure will become unstable and collapse. External loads have no alternative load path and must be resisted by torsion, **Kamara, and Rabbat, 2005**.

Compatibility torsion develops where redistribution of torsional moments to adjacent members can occur. The term compatibility refers to the compatibility of deformation between adjacent parts of a structure, **Fanella, and Rabbat, 1997**.

Depending upon the nature of applied loading, structural form and position of the member under consideration in the structural system, the twisting moments may be static or dynamic, transient or sustained and non-repetitive or cyclic. Static torsion occurs when the loads are applied gradually at a slow rate so that the twisting moment increases monotonically from zero to its full value. In this case the, internal resisting torque at any stage is in equilibrium with the external applied torque. Most of the torsion tests on concrete members and structural systems reported in the last decades deal with monotonically increasing static torsion. Transient or short-term twisting moments arise due to temporary live loads and environmental effects such as wind and seismic forces. On the other hand long time torsion is produced by dead loads and live loads, which are more or less permanent, **Kumar, et al., 2015**.

Reinforced concrete continuous beams under pure torsion were seldom studied, so the main objectives of this study were to investigate the torsional behaviors of reinforced concrete continuous beams under pure torsion condition.



2. EXPEREMENTAL WORK

2.1 Materials

All materials used in this experimental study have been tested according to international and Iraqi specifications and as follows:

2.1.1 Cement

Al-Mass ordinary Portland cement Type I cement was used. The cement was tested and checked according to **IQS no.5, 1984**. The chemical and physical properties of used cement are shown in **Tables 1 and 2**, respectively.

2.1.2 Fine aggregate

AL-Ukhaider natural sand of 4.75 mm maximum size was used throughout this work. **Table 3** shows the grading of fine aggregate. Results showed that the fine aggregate grading and sulfate content were within the requirements of the **IQSno.45, 1984**. The specific gravity, sulfate content and absorption of fine aggregate are shown in **Table4**.

2.1.3 Coarse aggregate

Crushed gravel with maximum size of 20 mm from Al-Niba'ee region was used. The grading of coarse aggregate is given in **Table 5** which confirms to the **IQS no.45, 1984**. The physical properties of coarse aggregate are given in **Table6**.

2.1.4 Reinforcing steel

Deformed steel reinforcement of 10 mm diameter was used for the main reinforcement and steel bars of diameter 8 mm are used for stirrups. Test results refer that the adopted steel bars conformed to **ASTM A615M-01** as shown in **Table 7**. The bars have been tested in the material laboratory of the Civil Engineering Department at Al-Mustansiriyah University, Baghdad, Iraq.

2.1.5 Water

Tap water was used for both mixing and curing of concrete.

2.2 Mix Design

Several trial mixes were made according to the recommendations of the **ACI 211.1-91**. Reference concrete mixture was designed to achieve cube strength of 31 MPa at 28 days. The mixture was (1 cement: 1.5sand: 3 gravel, by weight), and the slump was approximately 100 mm. Mixture details are given in **Table8**. It was found that the used mixture produces good workability and uniform mixing of concrete without segregation and the resulted compressive strength (avg. of 3 cubes at each age) was 23.5 MPa and 31.5 MPa at 7 and 28 days age, respectively.

2.3 Test Beams Details

To study the most influential variables on torsional behavior of reinforced concrete continuous two-equal spans beams under pure torsion, four reinforced concrete beams were reinforced and casted for this test and as shown in **Fig.2**.

Details of the reinforcement provided in the beam are explained herein. In order to avoid the failure of the beams at torsional cracking load, each beam was designed to have a steel

reinforcement of 1.5% for the flexural reinforcement and 1% for transverse (stirrups) to the volume of the concrete. The ratio of the steel longitudinal and transverse reinforcement along with the geometrical and mechanical properties of the RC members influence the angle of the diagonal cracking, **Chalioris, and Karayannis, 2013**.

The percentage of reinforcements provided in the beam was slightly higher than the minimum required maintaining the integrity of the beam beyond cracking. Also this will represent the case of a deficient beam in terms of reinforcement, **MacGregor, and Ghoneim, 1995**.

All of beams are typical in cross-sectional dimensions ($b=100$ mm, $h=200$ mm) and have the same reinforcement as shown in **Fig.3** and were reinforced with 4 no. 10 mm bars in the longitudinal direction, ($A_s = 283$ mm²) and reinforced with closed stirrups in the transverse direction with 8 mm bars spaced at 100 mm on center, in the test region.

In RC torsional members, diagonal cracks are formed due to the same mechanism that is responsible for the formation of shear cracks. The diagonal tension cracks are found to be common in both shear and torsion. The main difference between shear cracking and torsional cracking lies in the crack pattern. Spiral-like crack pattern are found in torsional members, **Mitchell, and Collins, 1974, Hsu, 1984**.

2.4 Test Setup

The hydraulic testing machine was used to test all beams. The normal load can be applied by this machine on the specimen at several points and the supports should be remaining fixed against rotating around the longitudinal axis, i.e. twisting. In this research the applied loads outside the bed of the hydraulic testing machine are needed in order to obtain torsional movement.

The experimental requirements need to transmit the load from the center of the hydraulic testing machine to external points that represent load eccentricity so as the moment arm. The special clamping loading frame on each end of the beam used in this research is shown in **Fig.4**. This frame consists of two large steel clamps which work as arms for applied loadings with separated faces to connect them over the sample by large bolts; four bolts are used for each arm. This frame was fabricated of a hot-rolled structural steel angles which have a cross-sectional dimensions of L 1½" x 1½" x ¼" and L 1¼" x 1¼" x 3/8" and attached by welding. This final shape is similar to a bracket around external support and extended on one side to a distance of 600 mm. These arms were capable of providing a maximum eccentricity of 600 mm with respect to the longitudinal axis of the beam. In order to get pure torsion, the center of external support should coincide with the center of the moment arm.

An additional clamping was made at the mid-span of the testing beams which is made from 10 mm thick steel rods and 50 mm wide which were connected to mid-support as an intermediate confinement (twisting restraint).

In order to obtain pure torsion, a wide-flange structural steel girder with a depth of 250 mm and 3 m length is used to transmit the loads of the hydraulic testing machine to varied eccentricities from external supports. This girder was clamped to the hydraulic testing machine as shown in **Fig.5** and **Fig.6**. Reinforced concrete beams were tested under monotonically increasing torque up to

failure, the load was applied gradually. At each load increment 5kN, readings were acquired manually. The torque increased gradually up to failure of the beam.

In order to measure the absolute vertical displacement or AVD in brief, two dial gauges were attached at the bottom fibers at both end of the beams at a point 40 mm from the center of the longitudinal axis of the beams to measure the downward and upward displacement readings as shown in **Fig.4**. Then AVD is calculated according to Eq. (1). Angles of twist and the torsional moments were calculated from Eq. (2) and Eq. (3), respectively.

$$\delta = |y_1| + |y_2| \quad (1)$$

$$\theta = \tan^{-1} \delta/a \quad (2)$$

$$M_T = P.x \quad (3)$$

where, (δ) is the absolute vertical displacement which is the summation of the readings of the absolute values two dial gauges multiplied by dial gauge factor which is 0.01, (y_1 and y_2) are the factored downward and upward displacement readings, respectively, (θ) is the angle of twist, (a) is the distance between dial gauges which have a fixed value of (80) mm, (M_T) is the torsional moments, (P) is the applied load and (x) is the eccentricity of loading.

3. TEST RESULTS AND DESCUSSION

Experimental test results for continuous beams B1, B2, B3 and B4 are shown in **Table9**. Variables considered in this experimental study were discussed herein.

3.1 Loading and Absolute Vertical Displacement

Fig.7 through **Fig.10** illustrate the relation between loadings and the absolute vertical displacement. Each figure has been gained from the average of the data of two beams which were tested under the same loading conditions. Four loading eccentricities were investigated with an increment of 10 cm in each stage. The loading eccentricities were 30, 40, 50 and 60 cm. The AVD was calculated by summing the absolute values of the adjacent gauges reading at each end multiplied by gauge reading factor.

The bar charts shown in **Fig.11** illustrate the recorded values of the 1st crack loading and failure loading for each case of load eccentricity. From the experimental test results and at failure loading stage; when the load eccentricity increased from 30cm to 60cm, the AVD increased by 11.27%, 32.1%, 46.92% for each 10 cm increment in eccentricity with reference to 30cm loading eccentricity, respectively. Also, it was found that each of the four beams behaved linearly under loading till first crack creation and then behaved non-linearly until failure. Also found from **Fig.11** that the load carrying capacity was decreased as the load eccentricity increased from 30cm to 60cm. The percentage of decrease in the load carrying capacity at failure stage were 22.07 %, 34.48 %, 49.65 % for each consecutive 10 cm increment in loading eccentricity with reference to 30cm loading eccentricity. This behavior obviously shows the major effect of load eccentricity so as the torsional moment on the beams.

3.2 Torsional Moments and Angle of Twist

The relation between torsional moments M_T and the angle of twist θ are shown in **Fig.12** through **Fig.15**. Each figure has been obtained from average of the data of two beams which were tested under the same loading conditions. For the four investigated loading eccentricity values, the torsional moments M_T and the angle of twist θ were calculated by Eq. (3) and (2), respectively. It was found that the torsional moments and at first cracking stage decreased as the load eccentricity increased from 30 cm to 60 cm. The percentages of decrease in the torsional moment values were 3.03 %, 9.09 %, 27.27 % for the each consecutive 10 cm increments in loading eccentricity with reference to 30cm loading eccentricity. This is demonstrated in the bar chart shown in **Fig. 16**.

At failure loading stage, the torsional moment of the beams undergoes increases in relatively high percentage and then under large eccentricity of loading values, the increasing rate was very slightly in comparison with low loading eccentricity value. The percentage of increasing in the torsional moments were 3.91%, 9.2%, 0.69% for each 10 cm increment in loading eccentricity with reference to 30cm loading eccentricity. This behavior is very clear as the relation between torsional moments M_T and loading eccentricities are directly proportional with reference to the decreasing of failure loading for each case as explained previously.

3.3 Continuous Reinforced Concrete Beams Behavior at First Cracking Stage

The behavior of the beams at first cracking stage under all loading eccentricities values is shown in the **Fig. 16**. It was found that at low load eccentricity value, beams were twisted much more than larger eccentricities values before the 1st cracking. So when the loading eccentricity values twice experimentally from 30 cm to 60 cm, the generated angle of twist under 30cm eccentricity was 158.41% times the generated angle of twist at 60 cm eccentricity. This behavior was due to the higher values of loading at low loading eccentricities which will induce greater values of AVD (before first cracking occur) as the angle of twist is directly proportional to AVD according to Eq. (2) as listed previously.

On the other hand, and at the failure stages; twisting of beams is seen to be increased as the load eccentricity values increased as shown in **Fig. 17**. The percentage of increasing in the angle of twist were 17.95%, 31.43%, 45.76% for each consecutive 10 cm increment in loading eccentricity with reference to 30cm loading eccentricity. The relation between the torsional moments M_T and the angle of twist θ still directly proportional but it changed to non-linear behavior.

4. CONCLUSIONS AND RECOMMENDATIONS

4.1. Conclusions

According to experimental results reported previously, the following conclusions are presented:

1. All of the tested RC beams cracked under pure torsion in a similar pattern.
2. The generated cracks in RC beams due to twisting were close especially near to external supports, i.e. near to points of eccentric applied loads.
3. The cracks in RC beams with large loading eccentricity values (50 cm and 60 cm) were limited to 2/3 of each span length (1m) as they start from each external support and vanish at the last 1/3 beams span.



4. The cracks in RC beams under low loading eccentricity values (30 cm and 40 cm) were extended to mid-support and met the cracks generated in the adjacent span forming a spiral cracks along beams.

4.2. Recommendations

The following research on RC continuous beams under pure torsions is recommended for future research work:

1. Investigating the torsional behaviour of different grades of concrete such as high strength and ultra high strength.
2. Retrofitting RC beams with carbon fibre reinforced polymers (CFRP) fabrics and laminates and retesting.
3. Investigating RC beams elongation under pure torsion.
4. Investigating the behaviour of RC beams under pure torsion by modelling of material properties in finite elements and nonlinear solution techniques.

REFERENCES

- American Concrete Institute ACI, 1997, *Standard Practice for Selecting Proportions for Normal, Heavy Weight and Mass Concrete*, ACI 211.1-91 (Re-approved 2002), ACI Manual of Concrete Practice.
- American Society for Testing Materials ASTM, 2002, *Standard Specification for Deformed and Plain Billet-Steel Bars for Concrete Reinforcement*, A 615/A 615M-01, Annual Book of ASTM.
- Central Organization of Standardizations and Quality Control, 1984, *Portland Cement*, Iraqi Standard No. 5.
- Central Organization of Standardizations and Quality Control, 1984, *Natural Aggregate used In Concrete and Construction*, Iraqi Standard No. 45.
- Chalioris, C. E., and Karayannis, C. G., 2013, *Experimental investigation of RC beams with rectangular spiral reinforcement in torsion*, Journal of Engineering Structures, Vol. 56, PP. 286-297.
- Fanella, D. A. and Rabbat, B.G., 1997, *Design of Concrete Beams for Torsion*, Engineering Bulletin EB106.02D, Portland Cement Association, Skokie, III.
- Hsu, T. T. C., 1968, *Torsion of Structural Concrete - Behaviour of Reinforced Concrete Rectangular Members*, Torsion of Structural Concrete, ACI Special Publication, SP-18, Vol. 11, No. 31, PP. 261-306.
- Hsu, T.T.C., 1984, *Torsion of Reinforced Concrete*, Van Nostrand Reinhold, Inc., New York, N.Y., 516 pages.



- Kamara, M. E. and Rabbat B. G., 2005, *Notes on ACI 318- 05 Building Code Requirements for Structural Concrete with Design Applications*, Portland Cement Association, EB705.
- Kamara, M. E. and Rabbat B. G., 2007, *Torsion Design of Structural Concrete Based on ACI 318-0*, Professional development series of Portland Cement Association PCA, Special Advertising Section.
- Kumar, C.A., Mohan, M., Rajesh, D. V. and Kulkarni, P., 2015, *Behavior of Fiber Reinforce Concrete Beam in Pure Torsion*, International Journal of Research in Engineering and Technology, Vol. 4, No. 5, PP. 551-556
- MacGregor, J. G. and Ghoneim, M. G., 1995, *Design for Torsion*, ACI Structural Journal, Vol. 92, No. 2, PP. 211-218.
- McCormac J. C. and Brown R. H., 2014, *Design of Reinforced Concrete*, John Wiley & Sons, Inc, Ninth edition.
- Mahmoud E. K., and Basile G. R., 2007, *Torsion Design of Structural Concrete Based on ACI 318-05*, Portland Cement Association, Professional Development Hours - Structural Engineer.
- Mitchell, D. and Collins, M.P., 1974, *Diagonal Compression Field Theory – A Rational Model for Structural Concrete in Pure Torsion*, Structural Journal of the American Concrete Institute, Vol. 71, No. 8, PP. 396-408.

NOMENCLATURE

a= distance between adjacent dial gage, mm.

M_T = torsional moments, kN.m.

P = applied load, kN.

x = eccentricity of loading, m.

y_1, y_2 = factored upward and downward displacement, mm.

δ = absolute vertical displacement, mm.

θ = angle of twist.

**Table 1.** Chemical properties of cement* used throughout this work.

Oxide Composition	Abbreviation	Percentage by Weight	Limit of Iraqi Specification NO.5/1984
Lime	CaO	63.23	–
Silica	SiO ₂	20.12	–
Alumina	Al ₂ O ₃	5.54	–
Iron Oxide	Fe ₂ O ₃	3.41	–
Sulphate	SO ₃	1.61	≤ 2.8 %
Magnesia	MgO	4.75	≤ 5.0 %
Potash	K ₂ O	0.36	–
Soda	Na ₂ O	0.2	–
Loss on ignition	L. O. I.	0.73	≤ 4.0 %
Insoluble residue	I. R.	1.24	≤ 1.5 %
Main Compounds (Bogue's Equations)			
Tricalcium Silicate	C ₃ S	57.74	–
Dicalcium Silicate	C ₂ S	14..21	–
Tricalcium Aluminate	C ₃ A	8.92	–
TetracalciumAlumino- Ferrite	C ₄ AF	10.34	–

*These chemical tests were carried out in the lab of Central Organization for Standardization and Quality Control.

Table2. Physical properties of cement* used throughout this work.

Physical Properties	Test Results	Limits of Iraqi Specification NO.5/1984
Specific surface area (Blaine method) (m ² /kg)	325	≥ 230
Soundness (Le-chatelier method) (mm)	0.66	<10
Setting time (Vicat's method)		
Initial setting (hrs:min.)	2:40	≥ 45 min.
Final setting (hrs:min.)	4:25	≤ 10 hrs
Compressive strength (MPa)		
3 days	18.90	≥ 15
7 days	28.70	≥ 23

*These physical tests were carried out in the lab of Central Organization for Standardization and Quality Control.

**Table 3.** Grading of fine aggregate

Sieve Size (mm)	Cumulative Passing (%)	Limits of the Iraqi Specification No.45/1984, Zone 3
10	100	100
4.75	92.6	90-100
2.36	87.3	85-100
1.18	77.9	75-100
0.60	63.1	60-79
0.30	28.5	12-40
0.15	7.4	0-10
Fineness modulus =2.43		

Table 4. Physical properties of fine aggregate

Physical Properties	Test Results	Limits of the Iraqi Specification No.45/1984
Specific gravity	2.65	-
Sulfate content %	0.2	≤ 0.5 %
Absorption %	0.70	-

Table 5. Grading of coarse aggregate

Sieve Size (mm)	Cumulative Passing (%)	Limitations of the Iraqi Specification No.45/1984
20.0	100	95-100
14.0	-	-
10.0	59	30-60
5.00	1	0-10
2.36	-	-

Table 6. Physical properties of coarse aggregate

Physical Properties	Test Result	Limit of Iraqi Specification No. 45/1984
Specific gravity	2.63	-
Sulfate content %	0.06	≤ 0.1 %
Absorption %	0.63	-

Table 7. Properties of steel reinforcement

Nominal Diameter (mm)	Measured Diameter (mm)	Modulus of Elasticity (Es) (GPa)	Yield Stress (fy) (MPa)	Ultimate Stress (fu) (MPa)
8	7.18	200	430	602
10	9.53	200	484	719

Table 8. Proportions of constituents of concrete mix

Parameter	Normal Strength Concrete Properties
Water/cement ratio	0.4
Water (kg/m ³)	156
Cement (kg/m ³)	390
Fine aggregate (kg/m ³)	585
Coarse aggregate (kg/m ³)	1170
Density (kg/m ³)	2577

Table 9. Experimental test results of test beams

Test Beams	Loading Eccentricity, m	Loading, kN		Torsional Moment capacity, kN.m	Absolute Vertical Displacement, mm		Angle of Twisting, degree	
		at First Cracking Stages	at Failure Stages		External Support 1	External Support 2	External Support 1	External Support 2
B1	0.3	55	72.5	21.75	11.5	11.71	8.18	8.33
B2	0.4	40	56.5	22.6	13.58	13.87	9.63	9.84
B3	0.5	30	47.5	23.75	15.26	15.4	10.82	10.89
B4	0.6	20	36.5	21.9	16.97	17.13	11.98	12.08

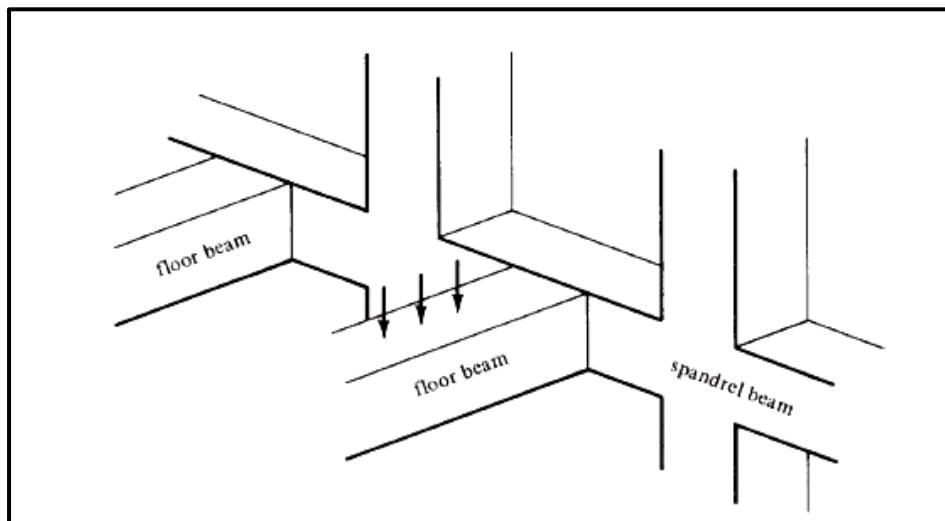


Figure 1. Torsion in spandrel beams.



Figure 2. Reinforced concrete test beams.

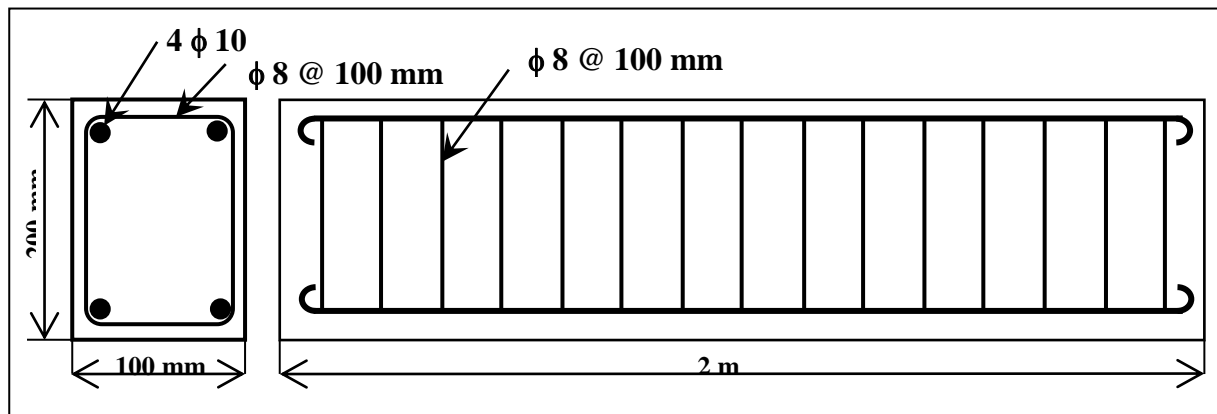


Figure 3. Reinforcement details for test beams.

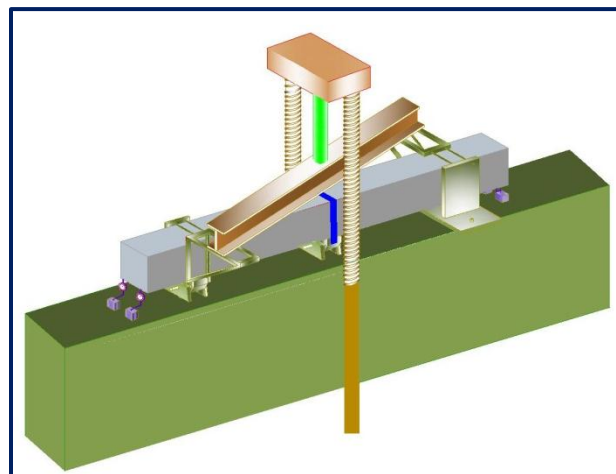


Figure 4. Test Setup.



Figure 5. Special clamping torsional frame



Figure 6. Steel girder fixed to testing machine

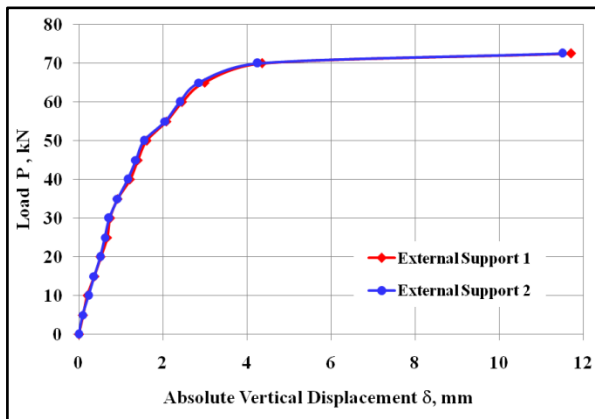


Figure 7. Variation of the 30-cm eccentricity load with the absolute vertical displacement

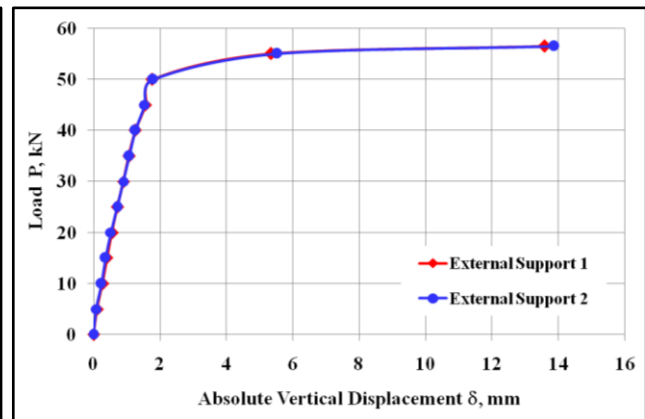


Figure 8. Variation of the 40-cm eccentricity load with the absolute vertical displacement

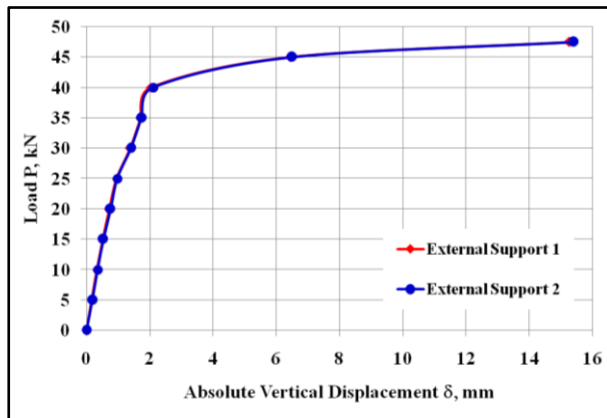


Figure 9. Variation of the 50-cm eccentricity load with the absolute vertical displacement

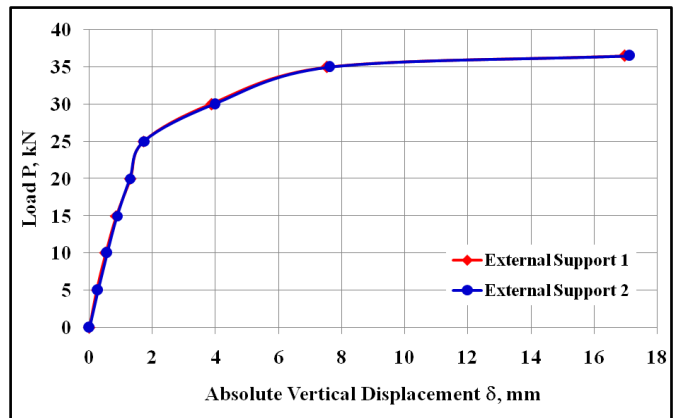


Figure 10. Variation of the 60-cm eccentricity load with the absolute vertical displacement

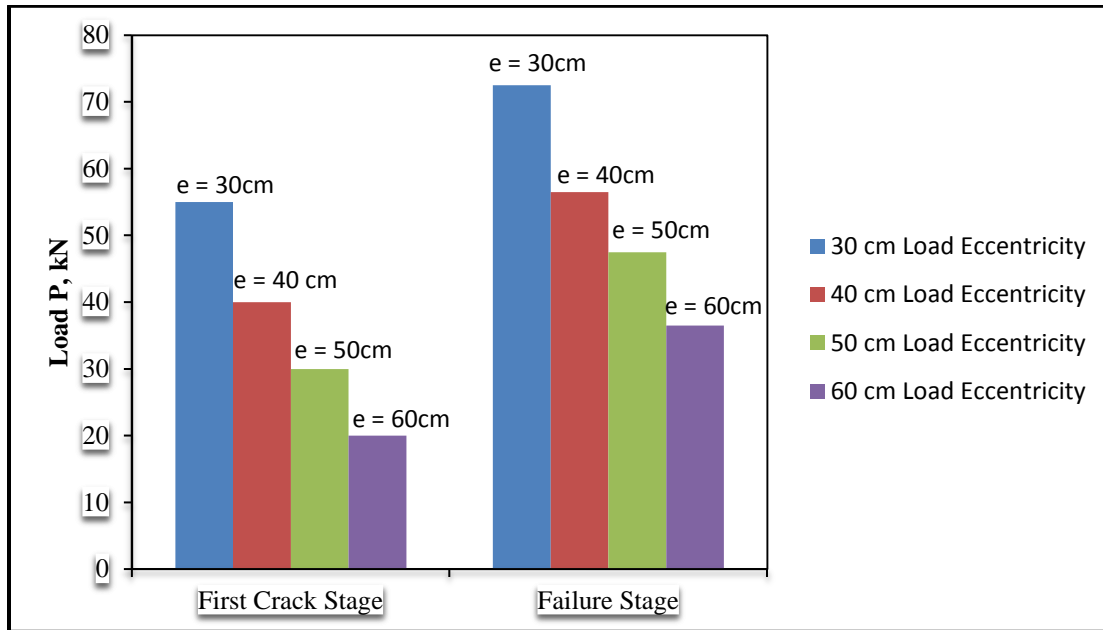


Figure 11. Loadcarrying capacity of beams at 1st cracking and failure stages

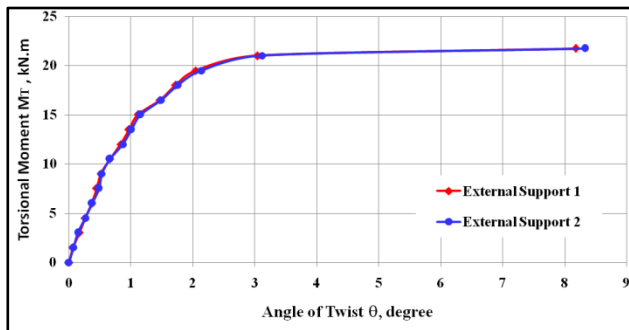


Figure 12. Variation of torsional moment vs. angle twist for 30 cm loading eccentricity

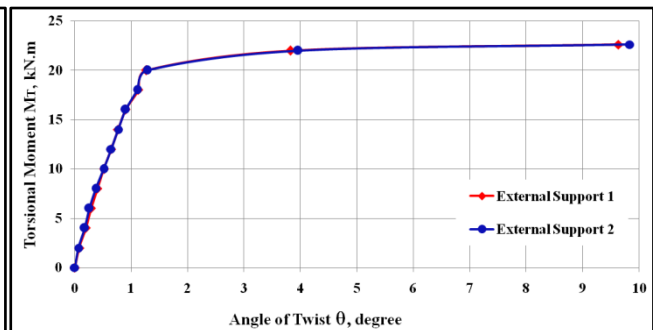


Figure 13. Variation of torsional moment vs. angle twist for 40 cm loading eccentricity

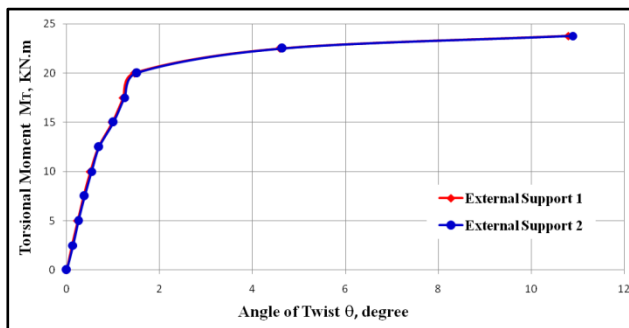


Figure 14. Variation of torsional moment vs. angle twist for 50 cm loading eccentricity

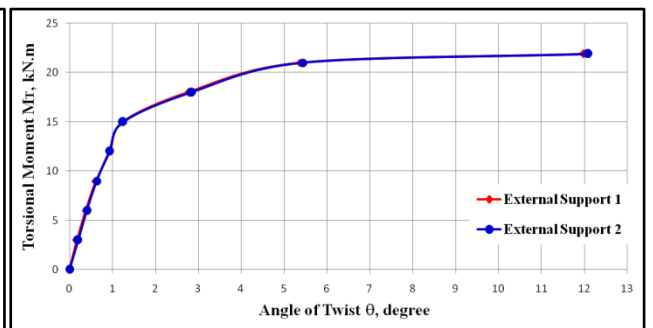


Figure 15. Variation of torsional moment vs. angle twist for 60 cm loading eccentricity

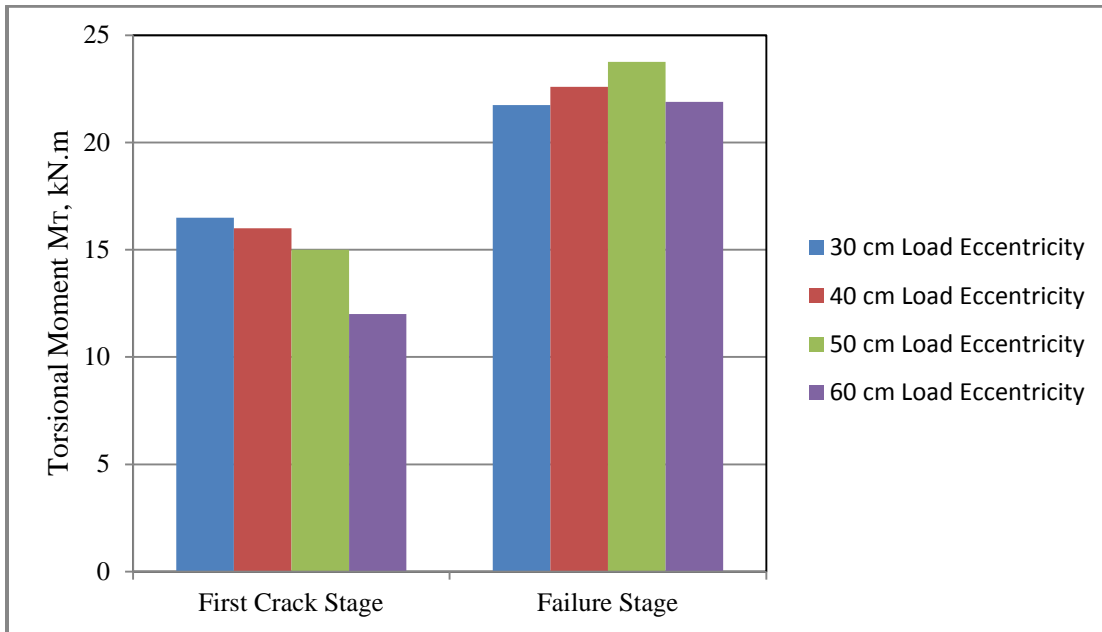


Figure 16. Torsional moment variation at 1st cracking and failure stages.

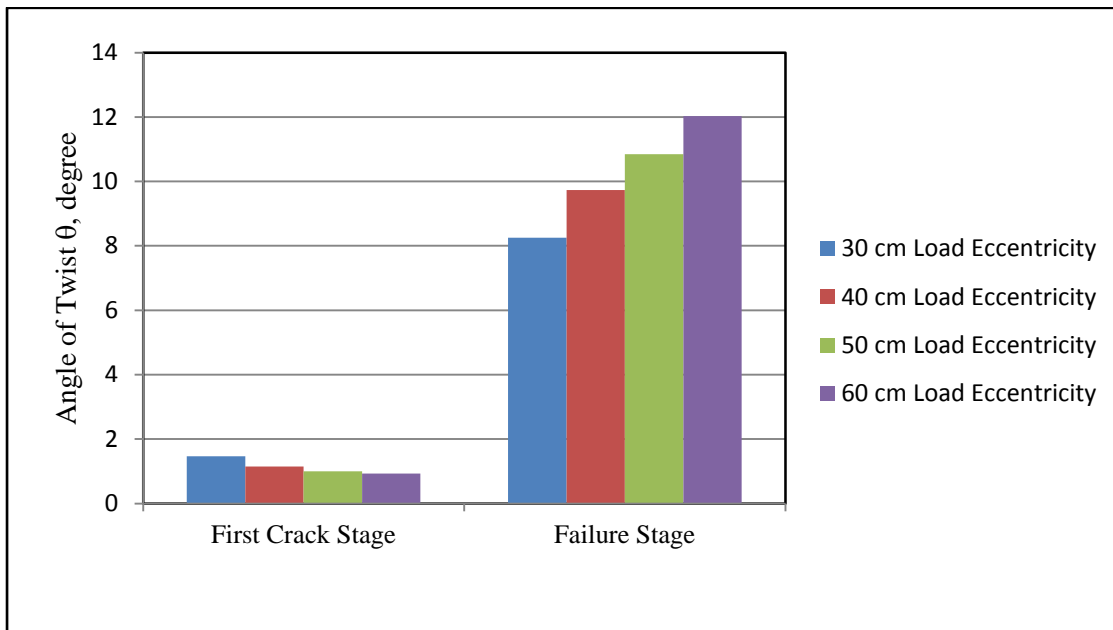


Figure 17. Angle of twisting variation at 1st cracking and failure stages

Improvement of Shear Strength of Sandy Soil by Cement Grout with Fly Ash

Haifaa Abdulrasool Ali (Ph.D.)

Lecturer

College of Engineering - University of Baghdad
haifaaali2013@yahoo.com

Yasir Muyuad Yousuf

Researcher

College of Engineering - University of Baghdad
yasir2010ci@yahoo.com

ABSTRACT

The effects of the permeation cement grout with fly ash on the sandy soil skeleton were studied in the present work in two phase; first phase the shear strength parameters, and the second phase effect of these grouted materials on volume grouted zone by injection (51) cm³ of slurry in sandy soil placed in steel cylinder model with dimension 15 cm in diameter and 30 cm in height. The soil sample was obtained from Karbala city and it is classified as poorly graded sand (SP) according to USCS. The soil samples were improved by cement grout with three percentages weight of water cement ratio (w:c); (0.1w:0.9c, 0.8w:0.2c, and 0.7w:0.3c), while the soil samples were dehydrated for one day curing time. Fly ash class (F) was used with cement grout as filler material; it was added to the mixture as a replacement material for cement in weight percentages; 10%, 25% and 40%. According to the results of tests, both shear strength and approximate volume of the effective grouted zone for treated samples soil with cement grout was increased when the water cement ratio decreased. Fly ash with cement grout needs to increase the water demand for the grout mixing to give best results in both shear strength and filling the soil voids.

Key words: Soil improvements, grouting with cement, filler materials, fly ash (F).

تحسين مقاومة القص للتربة الرملية باستخدام الحقن بالاسمنت و الغبار المتطاير

ياسر مؤيد يوسف

باحث

كلية الهندسة – جامعة بغداد

د.هيفاء عبد الرسول علي

مدرس

كلية الهندسة – جامعة بغداد

الخلاصة

ركزت الدراسة الحالية على تأثير الحقن باستخدام مادة الاسمنت مع الرماد المتطاير على مقاومة القص للتربة الرملية وكذلك تم دراسة تأثير المواد المستخدمة في عملية الحقن على حجم المنطقة المحقونة بواسطة حقن (51) سم³ في تربة رملية موضوعة في موديل حديدي اسطواني الشكل ذو قطر (15) سم وارتفاع (30) سم. عينات التربة الرملية تم جلبها من محافظة كربلاء وتم تصنيفها اعتماداً على التصنيف التربة الموحد و كانت ذات تدرج ضعيف (sp). التربة الرملية في البحث تم تحسينها بأسلوب الحقن بالاسمنت باستخدام ثلاث نسب وزنية من نسبة الماء الى الاسمنت وهي (0,9/0,1 ، 0,8/0,2 ، و 0,7/0,3) وتم ترك النماذج المعالجة بالحقن يوم واحد لغرض التصلب . الرماد المتطاير من صنف (F) تم استخدامه مع الاسمنت كمادة مألثة وتم اضافته للخليط كمادة بديلة عن الاسمنت وبثلاث نسب وزنية (10% ، 25% ، و 40%) . وقد لوحظ من نتائج الفحص ان مقدار مقاومة القص مع الحجم المتأثر بمنطقة الحقن تمت زيادتهما كلما قلت نسبة (الماء\الاسمنت). اما بالنسبة للغبار المتطاير فانه يحتاج الى زيادة في كمية الماء لخليط المستخدم في الحقن لاعطاء افضل لمقاومة القص و املاء اكثر لفجوات التربة.

الكلمات الرئيسية : تحسين تربة ، الحقن بالاسمنت ، مواد مألثة ، الغبار المتطاير صنف F.



1. INTRODUCTION

Grouting is the most common technical method used for soil improvement and strengthening. The principle of the grout is to introduce a substance into the rock fissure or into soil by pumping fluid or slurry down a small diameter tube to the required location, **Stadler, 2001**.

Grouting materials can be classified in two classes : (suspension type grouts and solution type grouts), the suspension type grout includes soil, cement, lime, asphalt, emulsion, etc., and the solution grout includes a wide variety of chemicals such as sodium silicates acrylamide, lignosulphonates, aminoplast, phenoplast, etc , **Shroff, A.V. , 2009**.

Permeation grouting is an effective method to send the grout materials into the ground without disturbing the soil structure, while increasing in cement content will increase load carrying capacity of the sandy soil, **P. Dayakar et al. 2012**.

Cement grout is most commonly used for sandy soil, it is a mixture of Portland cement, water, and, frequently, chemical and mineral additives. Cement grout can only travel in large voids. In the finer sized materials, the voids of the soils are too small to accept the cement grout. Fly ash is pozzolanic materials, which is fine gray powder resembling cement. It can be used in both concrete and grouting, it consists of impurities released by burning coal, which escapes and are carried away in exhaust gases of coal – burning furnace. Because there is considerable variety in the chemistry of different coals, the properties of the resulting by-product are likewise variable. Particles of fly ash are almost solid and hollow, and usually, contain varying amount of iron alumina and calcium as well as a very minor of other constituents. By itself, fly ash has little or no cementation properties but can react within the presence of moisture with the calcium hydroxide of lime or cement. The chemical reaction with Portland cement occurs when lime becomes free during cement hydration, this reaction forms addition cementation material, **Waner, 1989, 2004**. Fly ash may be used both as filler and an admixture with cement grout. It is used as filler for economic reason where substantial quantities of grout are required to fill large cavities in rock or in soil, trenches, and cavities, and to stem bore holes, shaft and tunnels, **U.S. Army Corps of Engineering, 1984**.

Fly ash is an important component in cement grout mix design because the particles are very small, which is helpful in increasing the density of the grout, and their spherical shape significantly reduces frictional losses during pumping, and decrease the cost of the grout when a large volume are wanted to gout, **Baker and Broadrick, 1997**.

Fly ash is primarily used to reduce cost, decrease shrinkage; increase flow ability, reduction of shrinkage upon drying, reduces heat generation during curing, and can give chemical stability **Vipulanandan et al, 2000** .

Polatty, (1982) pointed out that the water demand of cement fly ash in grout mix compared with using fine sand as filler material would be more so there is potentially more bleed with fly ash .

The objective of this research is to improve shear strength of sandy soil by cement grout with fly ash as filler material through laboratory testing for three (w:c) ratios with three percent of fly ash , and to show the effect of cement grout with fly ash in filling soil voids and how to influence on volume grouted zone.

2. MATERIALS USED

2.1 Sand soil

The sand is poorly graded clean sand obtained from Karbala city. Prior to testing, the sand is dried by the oven at (105 ° C) for (24 hrs.). Standard laboratory tests were used to obtain its physical properties. The tests are performed with loose sand corresponding to a dry unit weight of 15.5 kN/m³.

The test of grain size distribution curve that is shown in **Fig. 1** was done according to (ASTM D24884-2007) procedure. The sand is classified poorly graded sand, where the coefficient of uniformity (Cu) and coefficient of curvature (Cc) was (3.6) and (0.06) respectively. Other physical properties are shown in **Table 1**.

2.2 Cement Used

The cement used was sulphate resisting cement. The physical and chemical properties of cement were listed in **Table 2**. The tests were done in the National Center for Construction Laboratories and Research (NCCLR) - Ministry of Construction and Housing.

2.3 Fly ash used

The physical and chemical properties of fly ash class (F) were listed in **Table 3**. The tests were done in the National Center for Construction Laboratories and Research (NCCLR) - Ministry of Construction and Housing.

3. TESTING APPARATUS

In present work, cement grout with three weight percentages of water: cement ratio were used; (0.9w:0.1w, 0.8w:0.2c, 0.7w:0.3c). Fly ash was used as filler material with three percentages (10%, 25%, and 40%), and this material was added to the mixing as replacement material from cement. A rotary mixer with control speed was used for all mixes to have a homogeneous mixture.

3.1 Cylinder model Apparatus

The height of steel cylinder model that was used for the grouting process is (30) cm with diameter (15) cm. The cylinder was filled to (25) cm sand with dry unit weight 15.5 kN/m³. The slurry was injected under (1) kPa to depth (12.5 and 16.7) cm by using cylinder pipe for each (w:c). Slurry volume was used for this process is (51) cm³, this volume was chosen according to injected (1) cm³ (as grout material) in unconfined compressive strength model, so this rate has slight effect in soil structure.

After one day curing time by the humidity, the approximate dimensions were measured by vernier and then volumes of these grout zones were calculated.

3.2 Shear strength of the soil

Shear strength parameters of sandy soil before and after the grouting process was measured by direct shear test (for the sandy soil without any additive; the cohesion is equal zero). This test was carried out in accordance with the procedure given in ASTM D 3080-1998. A standard direct shear box of (60) mm square specimen was prepared in the steel box. After careful placing, an unconsolidated undrained direct shear test was conducted. The normal stresses applied were: 27.25, 54.5 and 109 kPa. The values of friction angle (Φ) and cohesion (C) were obtained according to Mohr-Coulomb failure criteria.

At a center of the direct shear box, $(1) \text{ cm}^3$ of the slurry was injected, as in **Fig. 1**, and after one day as curing time, the test was done.



Figure 1. The cylinder model

4. RESULTS AND DISCUSSION

4.1. Cylinder model test

According to the concept of the grout, the soil voids are filled, and to know correlation resulting between grout materials and soil voids and its impact on the volume of the grouted zone, approximate volume of the grouted zone is calculated as shown in **Figs. 2, 3** and **4**. A comparison of the percentage of the grouted volume zone with and without the fly ash is shown in **Table 4** and in **Figs. 5 to 7**.

From the result, approximate volume of the grouted zone was increased when the (w:c) decreased as a result of decreases of bonding material.

When using fly ash with cement grout as filler materials, and for (w:c) (0.9 w : 0.1 c) the approximate volume of the effective grouted zone was increased (when it was compared with approximate volume of the effective grouted volume zone for only cement grout) with three percent of fly ash (10%, 25%, and 40%). For the other (w:c) (0.8w : 0.2c) , the approximate volume of the effective grouted zone increase when using (10%) and (25%) of fly ash, while in (40%) of fly ash the approximate volume of the effective grouted zone decrease. The last (w:c) (0.7w:0.3c), the approximate volume of the effective grouted volume zone decreased with all the percentages of fly ash .

4.2. Shear strength of sand improvement by cementation gel grouted with fly ash additive

In this part, five groups of the sample with variable state sand were tested. The soil in the first group was natural loose sand with relative density (30%) and tested at its dry in-situ condition, while the second group for cement grouted sand with three (w:c) (0.9w:0.1) , (0.8w:0.2c) and (0.7w:0.3c). The third, fourth and fifth groups were with the same (w:c) but three percent of fly ash as filler material was used (10%, 25%,and 40%). The shear stresses versus horizontal displacement were plotted for selected tests. In addition, a relation between the maximum shear stress versus normal stress was drawn and the shear strength parameters, the angle of internal friction (ϕ) and cohesion (c) were measured.

In addition, the corresponding parameters are also presented in **Figs. 8 to 11**. The results have pointed out that the cohesion parameter is equal to zero for sandy

tested at natural dry state, whereas for soil grouted with cement and cement – fly ash, the cohesion had a value ranging between (2.1 to 8) kPa.

The result of the direct shear test for all cases and the rate of increase in angle of friction between treated soil by cement grout with and without fly ash and untreated are shown in **Table 5**. Then the rate of increase in angle of friction value ranged between (0%-15.6%) for treated with cement –fly ash and untreated soil. The shear stresses versus horizontal displacements and with normal stress were plotted for selected tests as shown in **Figs. 12 to 24**. The figures show that the displacement increases with the increase in shear stress to peak and then gradually decreases with less degree

The experimental work results show that angle of friction and cohesion increases when water cement ratio decreases without any additive as shown in **Figs. 25 and 26**, so the degree of the soil improvement and the shear strength of the soil increase in order to fill the soil voids and the bonding force that arise between the soil particles and the hydrated cement.

The relationship between the three (w:c) ratio used in present work (with all the percent of fly ash) and cohesion and angle of friction are shown in **Figs. 27 and 28**.

Using of fly ash in the present work, came for a reason which is the ability of fly ash to react chemically with Portland cement and produce cementations materials and for economic reason where the fly ash is available and environmentally friendly materials.

Shear strength for grouted gel at (w:c) (0.9w: 0.1c) increased (when it compared with grouted with only cement) when the rate of fly ash as filler materials increases in cement grout was limited. Cement grout with (40%) of fly ash as filler material decrease the shear strength for grouted gel at (w:c) (0.8w:0.2c) in order to decrease both the cohesion between the soil particles and angle of friction. The shear strength increased when (10%) of fly ash is used with cement grout as a filler material for (w: c) (0.7w: 0.3c). While shear strength for the same grouted gel at (w:c) with (25%) of fly ash is equal to shear strength for soil grouted with cement only, and the (40%) of fly ash with cement grout as a filler materials decrease the shear strength for grouted gel at (w:c) (0.7w:0.3c).

So, when the water cement ratio is decreased for cement grout with fly ash, both effective grouted volume zone and shear strength decreased in order to effect of fly ash on hydration water that wanted to continue the cement interactions between it and water to create harden material, so grout gel with cement and fly ash need to increase the water demand for the mixture.

5. CONCLUSIONS

The research work focuses on studying how to improve shear strength of sandy soil by using cement grout with fly ash as filler materials. The conclusions can be summarized as follows:

1. The water cement ratio for grouted sandy soil plays an important role by increasing the degree of the soil improvement and shear strength of soil, for bonding force that arises between the soil particles and the hydrated cement.
2. The shear strength parameters of the soil, the angle of internal friction (ϕ) and cohesion (c), increased together when the water cement ratio for the cement grout decreased.
3. Fly ash with cement grout can give a high degree of improvement by increasing both the shear strength of the soil and effective grouted volume zone but with limits.



4. Approximate volume of the grouted zone was increased when the (w:c) decreased as a result of decrease of bonding material.
5. When using fly ash with cement grout as filler materials and for (w:c) (0.9 w : 0.1 c) the approximate volume of the effective grouted zone was increased (when compared with approximate volume of the effective grouted volume zone for only cement grout) with three percent of fly ash (10%,25%,and40%). For the other (w:c) (0.8w : 0.2c) , the approximate volume of the effective grouted zone increased when using (10%) and (25%) of fly ash, while in (40%) of fly ash the approximate volume of the effective grouted zone decreased. The last (w:c) (0.7w:0.3c), the approximate volume of the effective grouted volume zone decreased with all the percent of fly ash.
- 6.The rate of increase in angle of internal friction (ϕ) between the treated soil by cement grout with fly ash as a filler materials and untreated soil value ranged between (0%-15.6%) for (w:c) (0.1w:0.9c, 0.8w:0.2c, and 0.7w:0.3c)with fly ash percentages as; (10%, 25% ,and 40%).
7. The cohesion for the treated soil by cement grout with fly ash as filler material has a value ranged between (2.5 to 8) kPa for (w:c) (0.1w:0.9c, 0.8w:0.2c, and 0.7w:0.3c) with fly ash with percentages as (10%, 25% ,and 40% .)
- 8 .Cement grout with the high percent of fly ash can effect on required hydration water for cement and cause the decrease in both of effective grouted volume zone and shear strength, so the grout gel with cement and fly ash needs to increase the water demand for the mixture.
9. Fly ash with cement grout needs to increase the water demand for the grout mixing to give best results , so cement grout with fly ash can be used in sites when high water table or to reduce the permeability of the soil.

REFERENCE

- ASTM D 3080-1998, Standard Test Method for Direct Shear Test of Soils Unconsolidated Undrained Conditions.
- ASTM D 4253-2000, Standard Test Method for Maximum Index Density and Unit Weight of Soils Using a Vibratory Table.
- ASTM D 4254-2000, Standard Test Method for Minimum Index Density and Unit Weight of Soils and Calculation of Relative Density.
- ASTM D 854-2000, Standard Test Method for Specific Gravity of Soil Solids by Pycnometer.
- ASTM D24884-2007, Standard Test Method for Classification of Soils for Engineering Purposes (Unified Soil Classification System)
- Baker, A. C., and Broadrick, R. L. 1997, Compaction Grouting, Proc., 1997 ASCE Florida Annual Meeting.
- Das, B. M. 2007, Principles of Foundation Engineering, Sixth Edition Adapted.
- J, Warner, 1989, Construction and Design of Cement Grout, New York.
- J, Warner, 2004, Practical Handbook of Grouting in Soil, Rock and structures, New York.
- P. Dayakar, K. Venkat Raman, Dr. K.V.B. Raju, 2012, Study on Permeation Grouting Using Cement Grout In Sandy Soils, IOSR Journal of Mechanical and Civil Engineering (IOSR-JMCE) ISSN: 2278-1684, Volume 4, Issue 4 (Nov-Dec. 2012), PP 05-10.



- Polatty , J,M (1982) , Discussion of Conference on Grouting in Geotechnical Engineering , Vol. 2,ASCE,New Orleans,3.
- Shroff,A.V. (2009), Development in design and executive in grouting practice, 31st IGS annual lecture at IGC-2009, Guntur.
- Stadler, G., 2001, Permeation Grouting, ASCE Seminar Publications, New York.
- U.S. Army Corps of Engineers 1984, Grouting technology - Engineer Manual ,1110-2-3506 ,EM 1110-2- 350620 January 1984.
- Vipulanandan, C. and Kumar, M. (2000) “Properties of Fly Ash-Cement Cellular Grouts for Sliplining and Backfill Applications.” Advances in Grouting and Ground Modification: pp. 200-214.

NOMENCLATURE

ASTM	American society for testing and materials
H	Height of the injected from the surface of the cylinder
C_u	Coefficient of uniformity
C_c	Coefficient of curvature
D_{10}, D_{30}, D_{60}	Particle sizes corresponding to 10%, 30%, and 60%
D_r	Relative density
G_s	Specific gravity
ϕ	Angle of internal friction
γ_{max}	Maximum dry density
γ_{min}	Minimum dry density
σ	Normal stress
C	Cohesion of soil
w:c	water cement ratio
w	water
c	cement

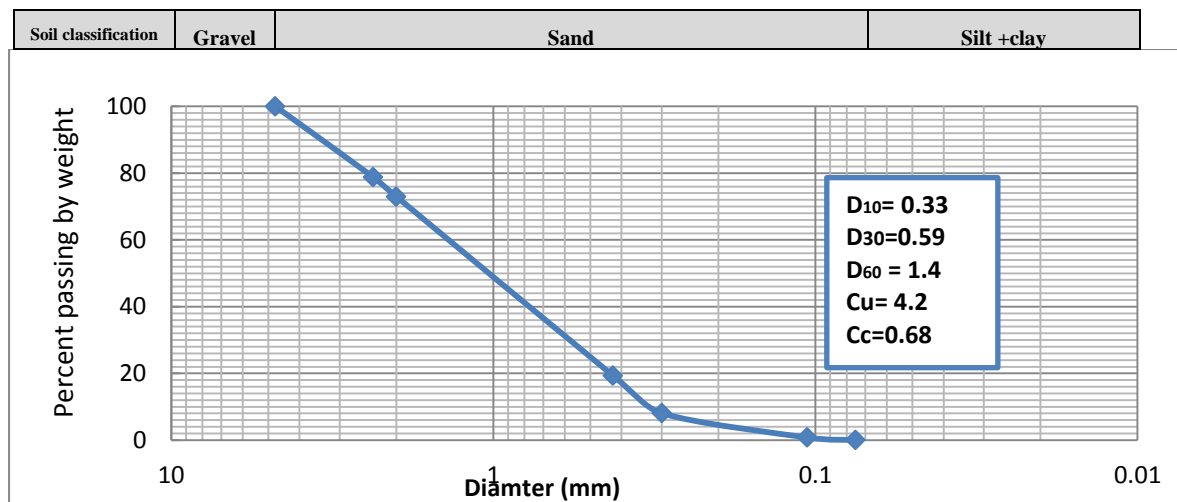


Figure 1. Grain size distribution of the soil.

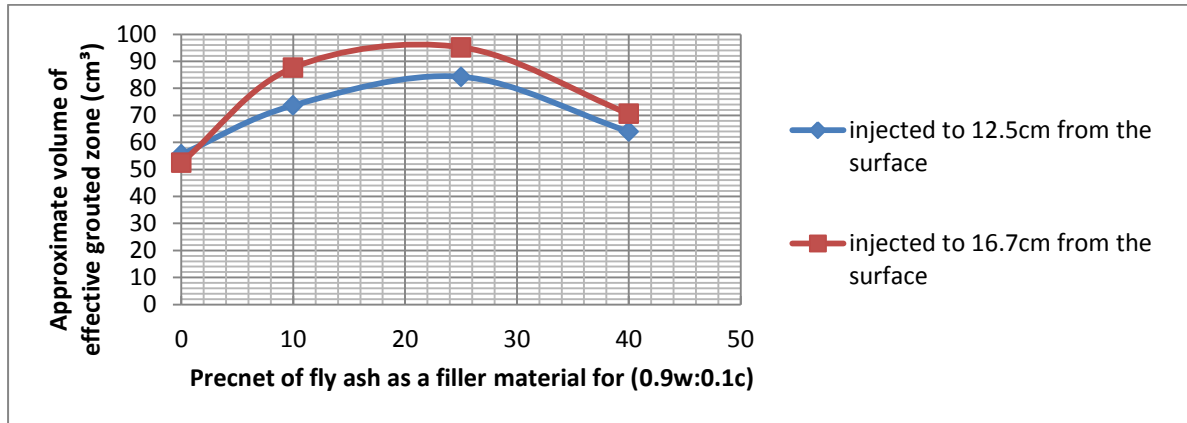


Figure 2. Approximate volume of the effective grouted volume zone after one day curing time when using cement as (0.9w : 0.1 c) with fly ash.

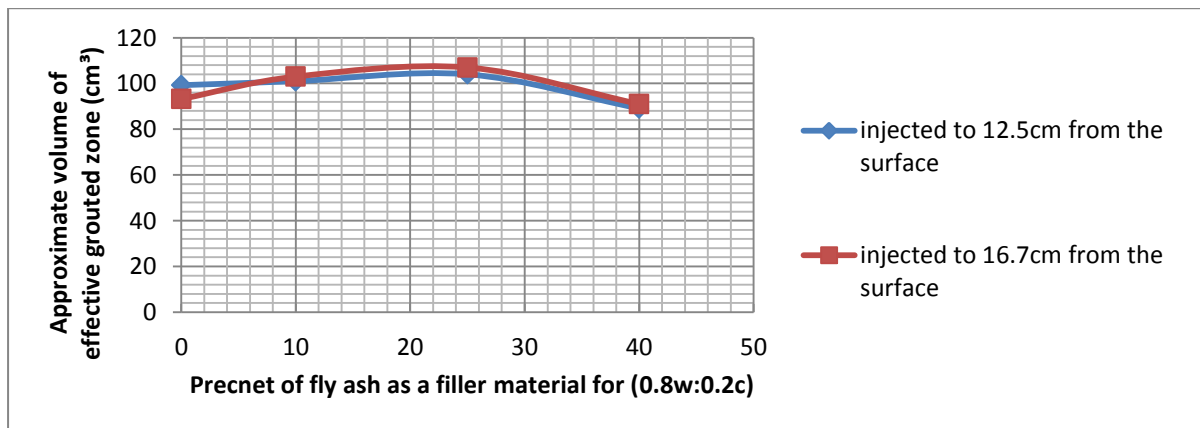


Figure 3. Approximate volume of the effective grouted volume zone after one day curing time when using cement as (0.8w : 0.2c) with Fly ash.

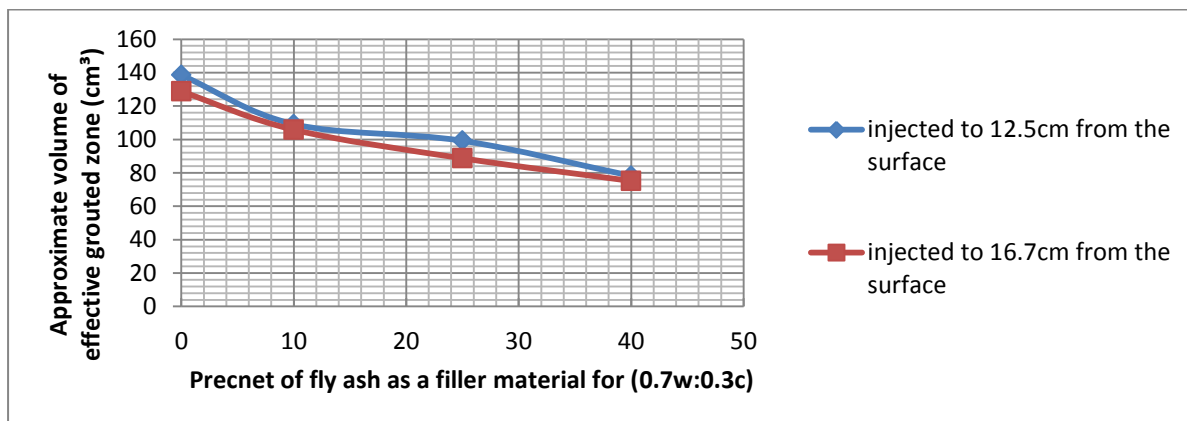


Figure 4. Approximate volume of the effective grouted volume zone after one day curing time when using cement as (0.7 w : 0.3 c) with fly ash.

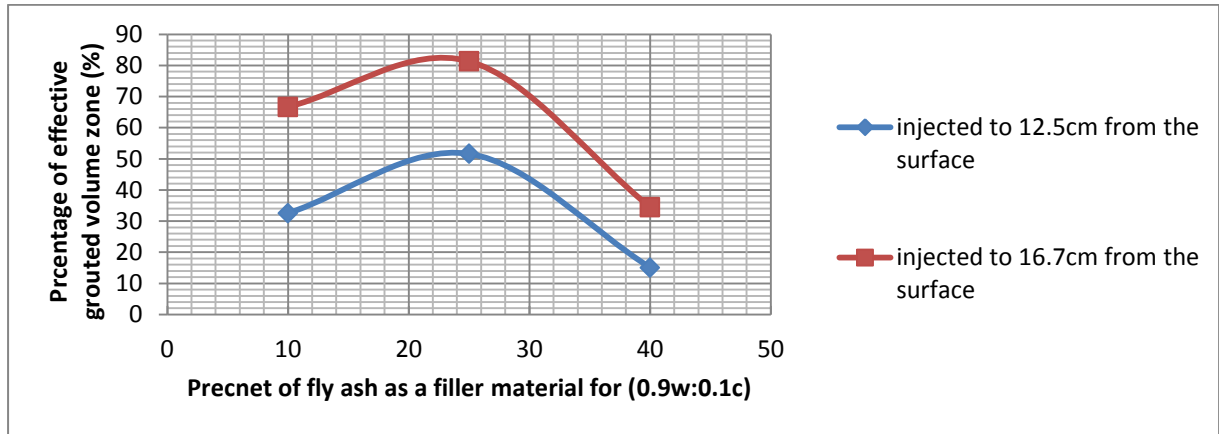


Figure 5. The comparison between the percentage of grouted zone effective volume with and without the fly ash for (w:c) (0.9 w : 0.1c).

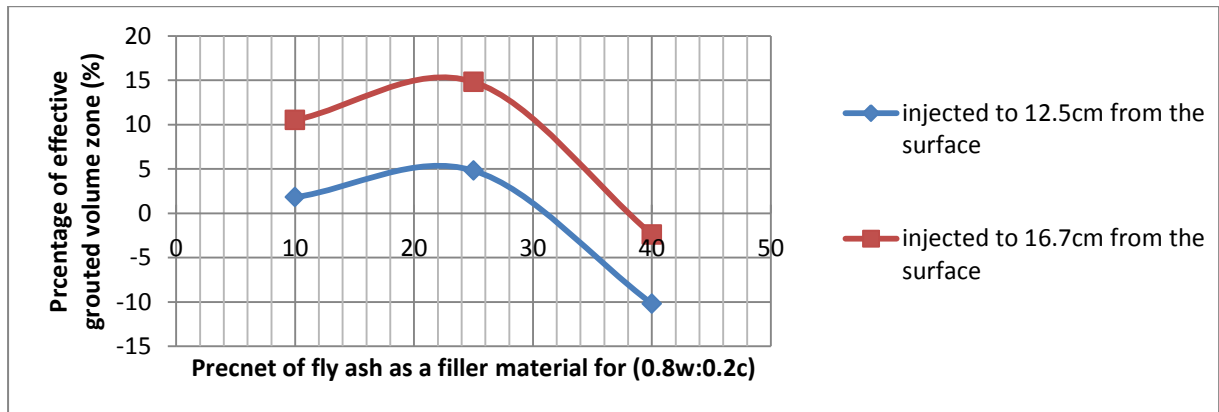


Figure 6. The comparison between the percentage of grouted zone effective volume with and without the fly ash for (w:c) (0.8 w : 0.2c).

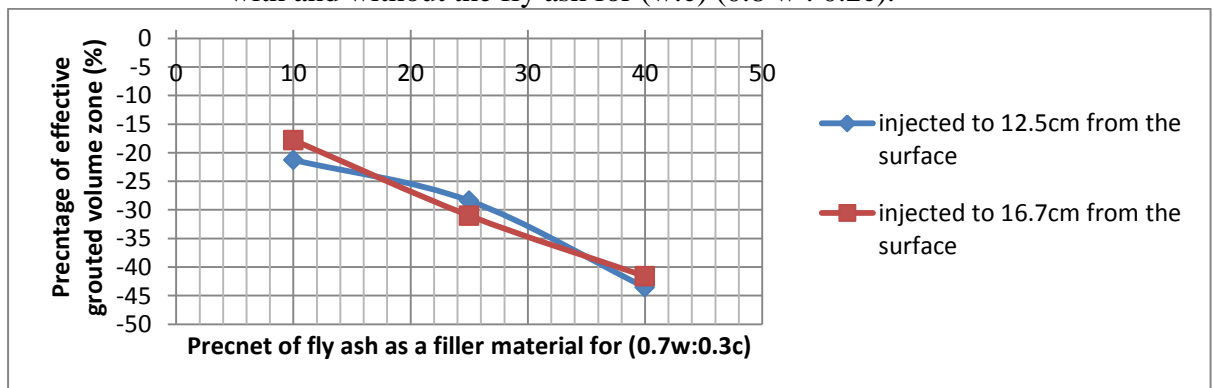


Figure 7. The comparison between the percentage of grouted zone effective volume with and without the fly ash for (w:c) (0.7 w : 0.3c).

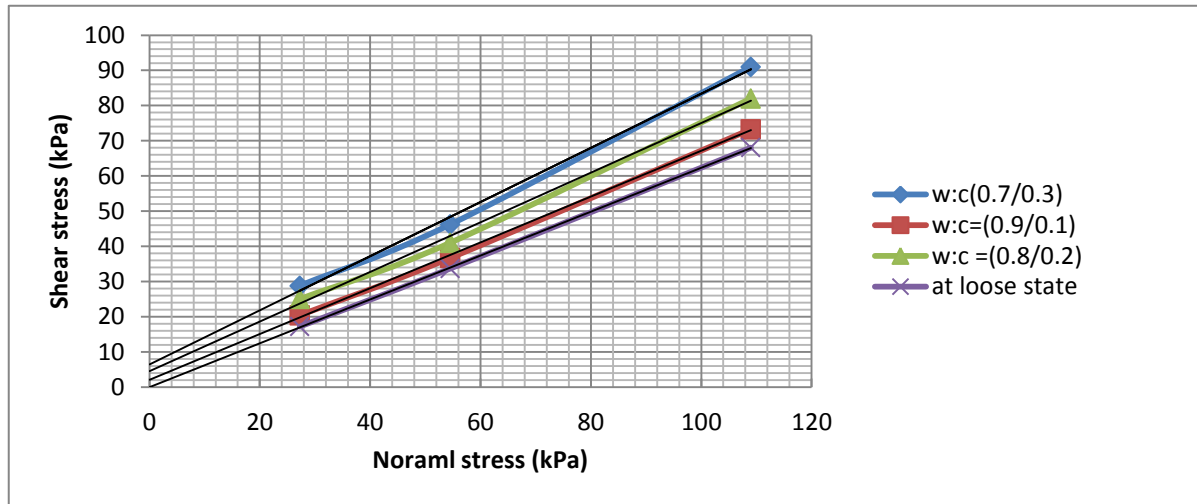


Figure 8 . Shear stress verses normal stress for soil sample with and without cement grout by direct shear .

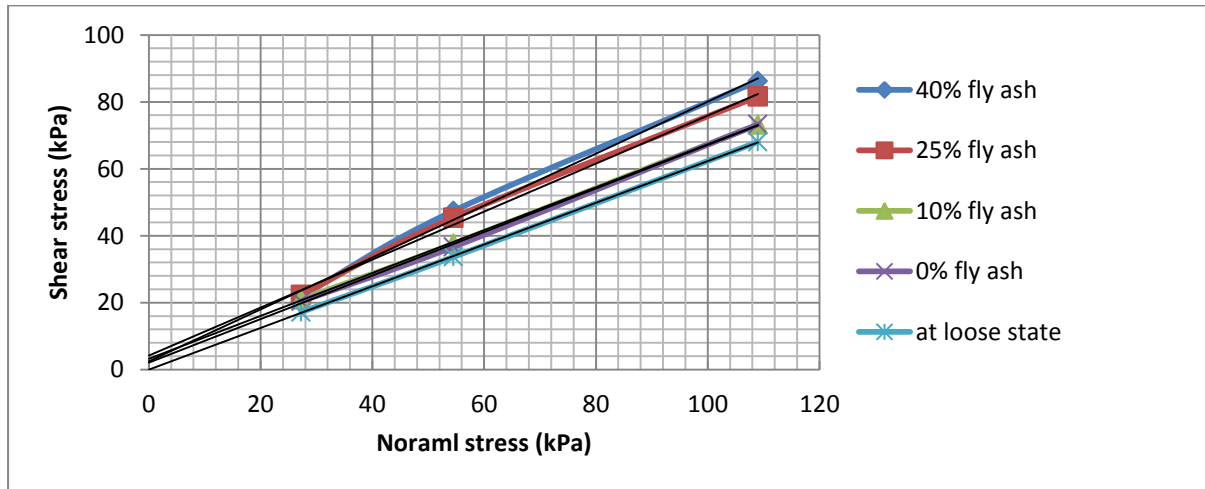


Figure 9. Shear stress verses normal stress for soil sample with and without cement grout with fly ash for grout gel at (w:c) (0.9w: 0.1c) by direct shear.

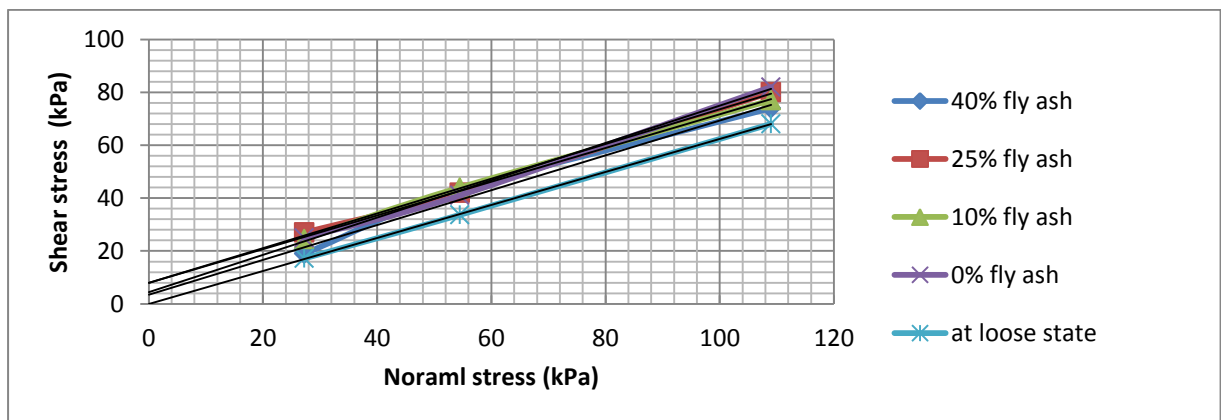


Figure 10. Shear stress verses normal stress for soil sample with and without cement grout with fly ash for grout gel at (w:c) (0.8w: 0.2w) .

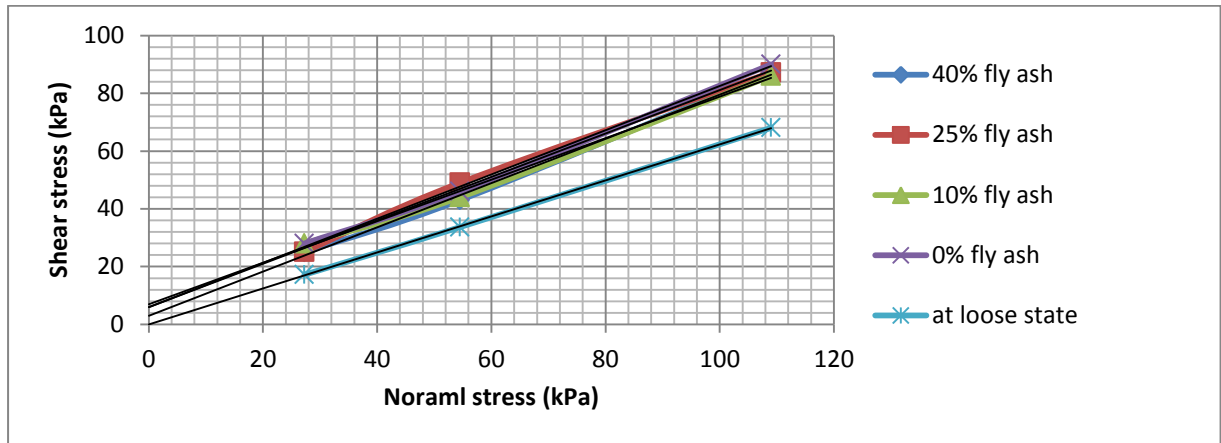


Figure 11. Shear stress versus normal stress for soil sample with and without cement grout with fly ash for grout gel at (0.7w: 0.3c) .

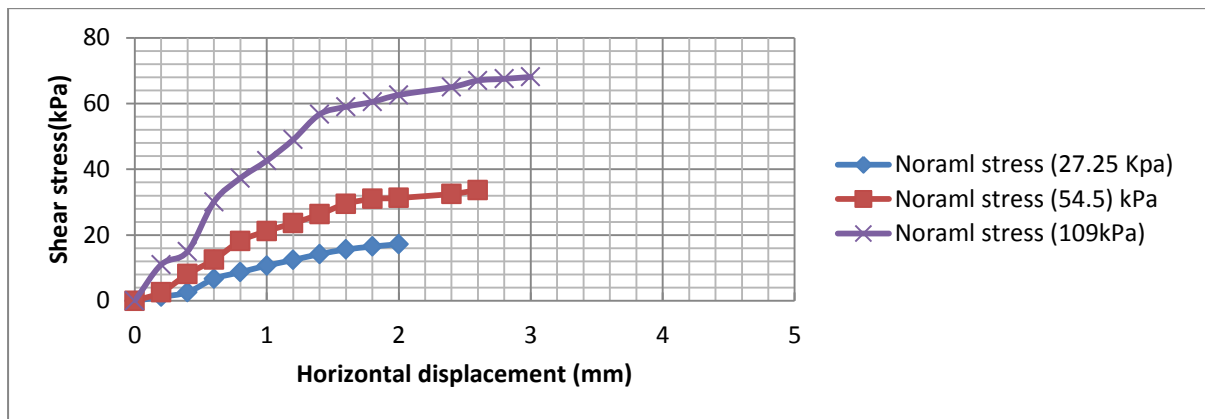


Figure 12 .Shear stress–horizontal displacement relationships at loose state.

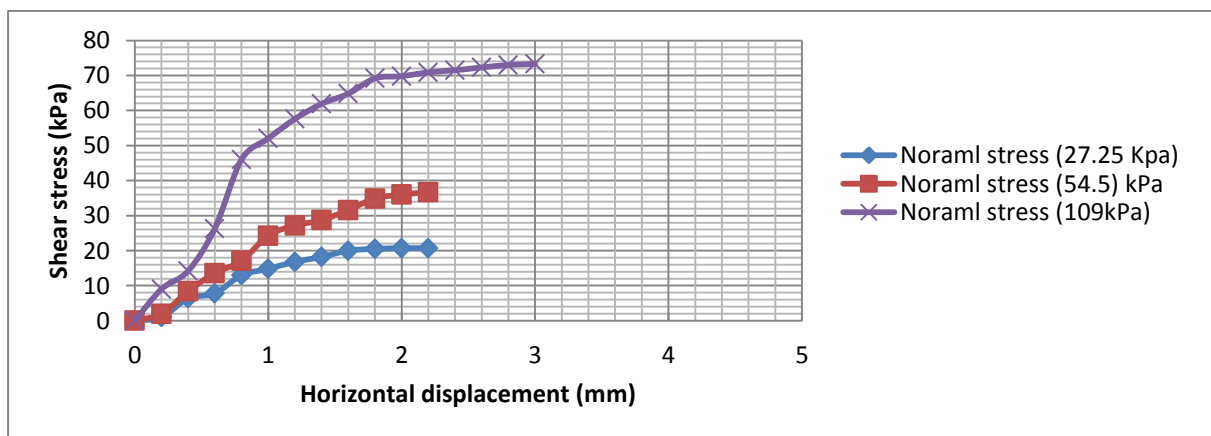


Figure 13 .Shear stress–horizontal displacement relationship for grout gel at (w:c) (0.9w:0.1c).

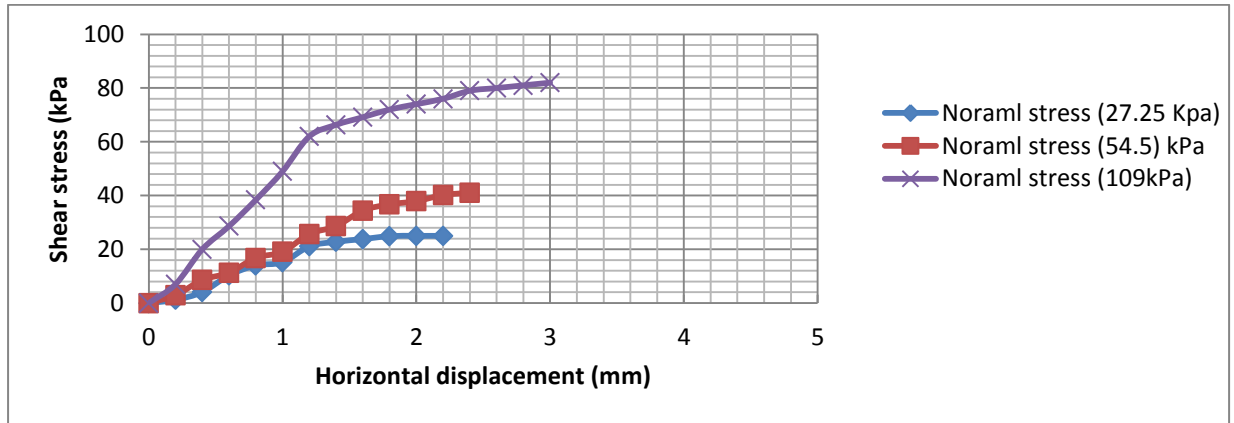


Figure 14 .Shear stress–horizontal displacement relationship for grout gel at (w:c) (0.8w:0.2c).

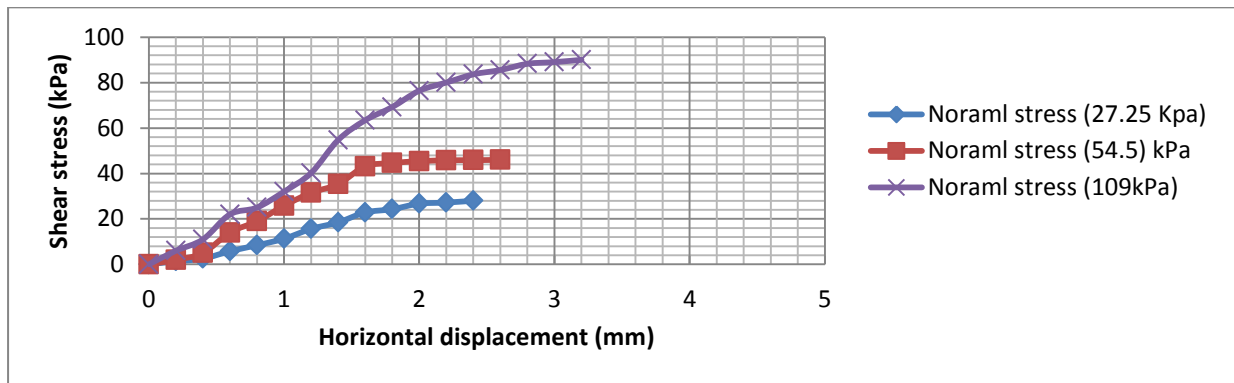


Figure 15 .Shear stress–horizontal displacement relationship for grout gel at (w:c) (0.7w:0.3c).

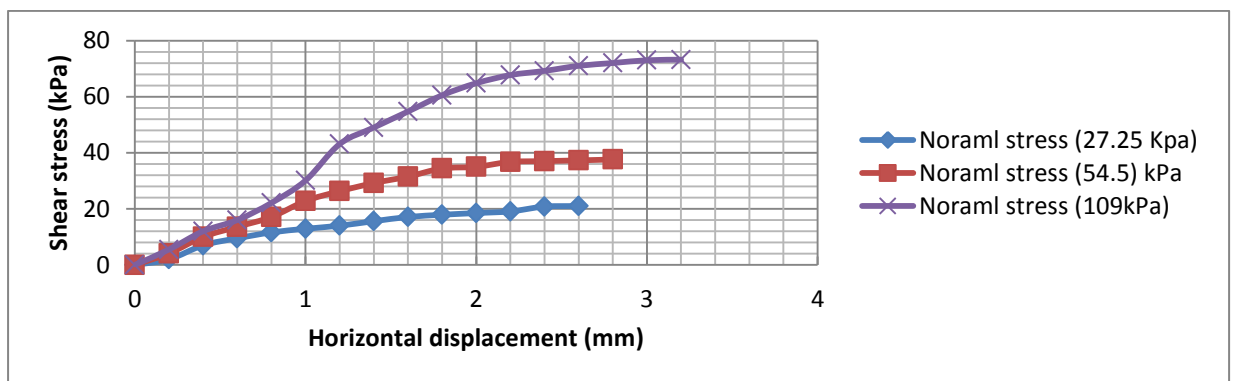


Figure 16 .Shear stress–horizontal displacement relationship for grout gel at (w:c) (0.9w:0.1c) with 10% fly ash .

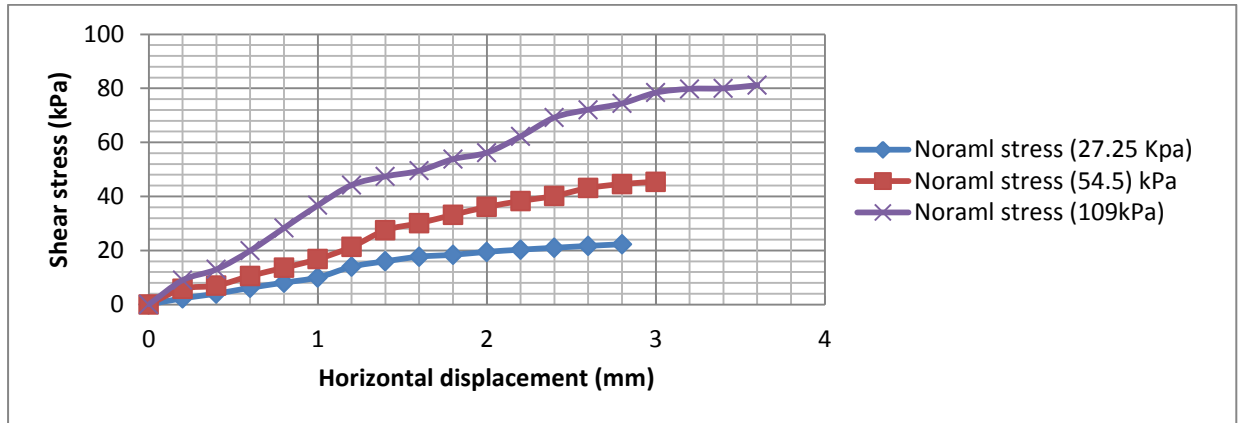


Figure 17 .Shear stress–horizontal displacement relationship for grout gel at (w:c) (0.9w:0.1c) with 25% fly ash

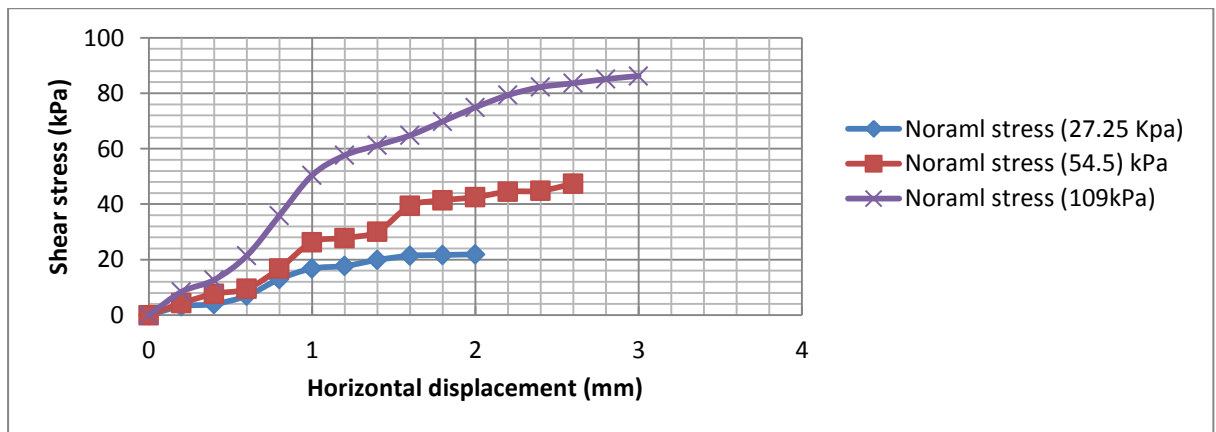


Figure 18 .Shear stress–horizontal displacement relationship for grout gel at (w:c) (0.9w:0.1c) with 40% fly ash.

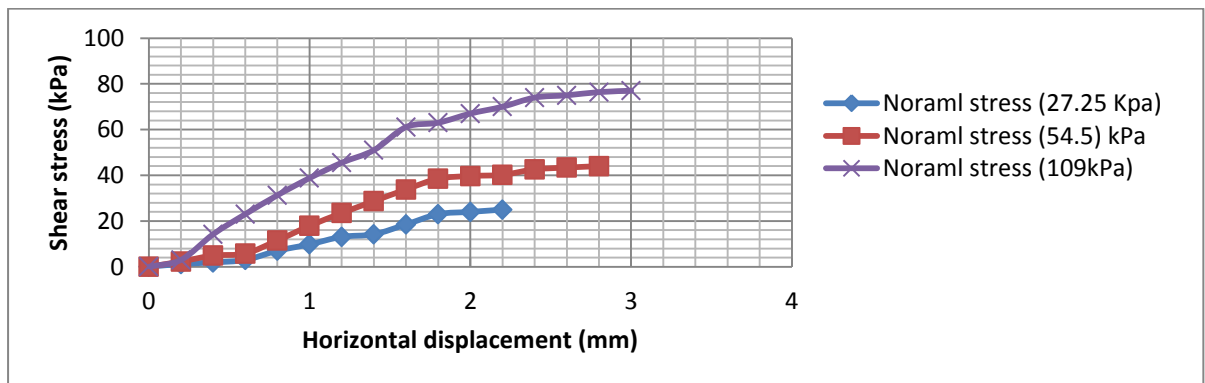


Figure 19 .Shear stress–horizontal displacement relationship for grout gel at (w:c) (0.8w:0.2c) with 10% fly ash.

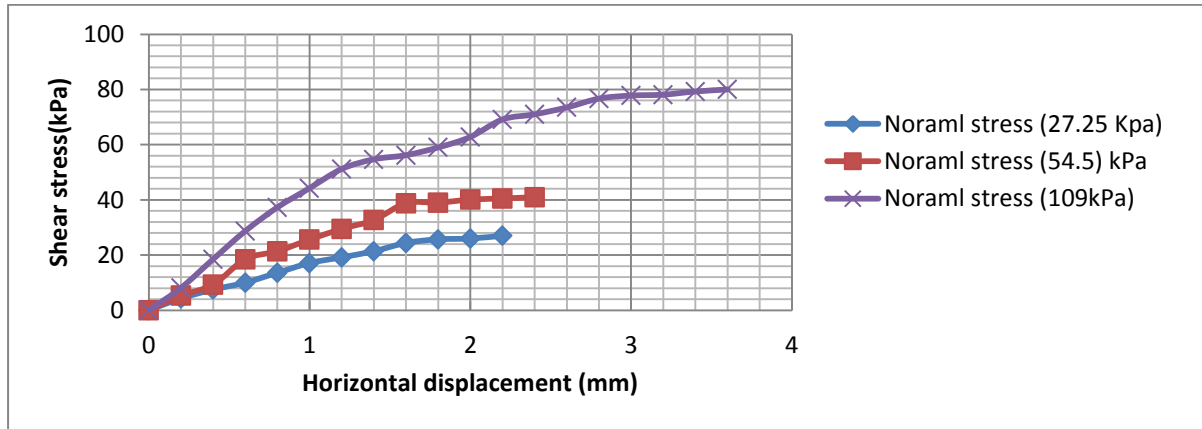


Figure 20 .Shear stress–horizontal displacement relationship for grout gel at (w:c) (0.8w:0.2c) with 25% fly ash .

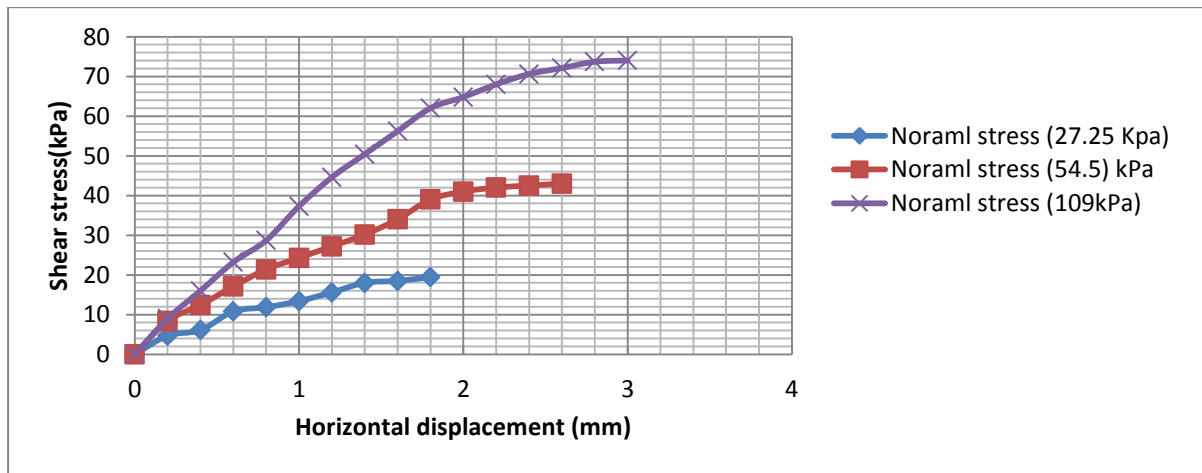


Figure 21 .Shear stress–horizontal displacement relationship for grout gel at (w:c) (0.8w:0.2c) with 40% fly ash.

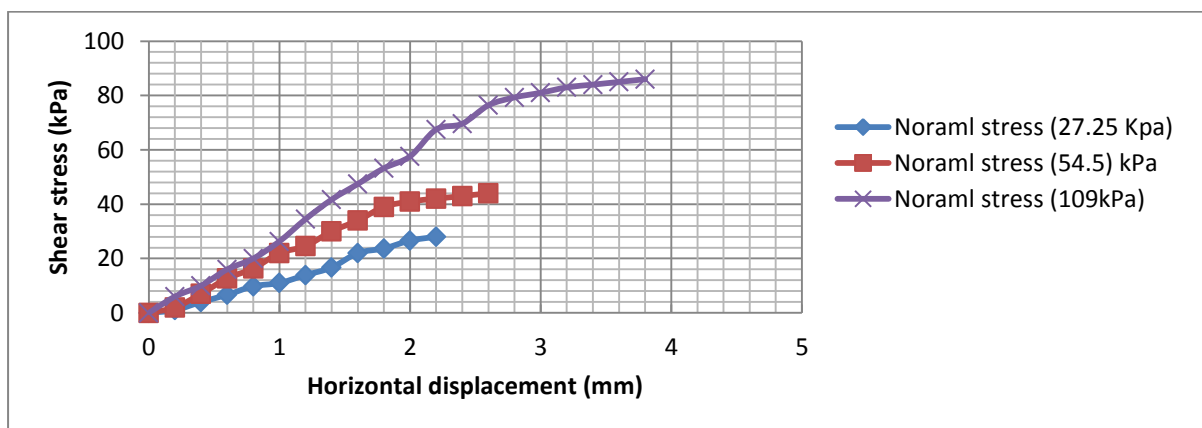


Figure 22 .Shear stress–horizontal displacement relationship for grout gel at (w:c) (0.7w:0.3c) with 10% fly ash.

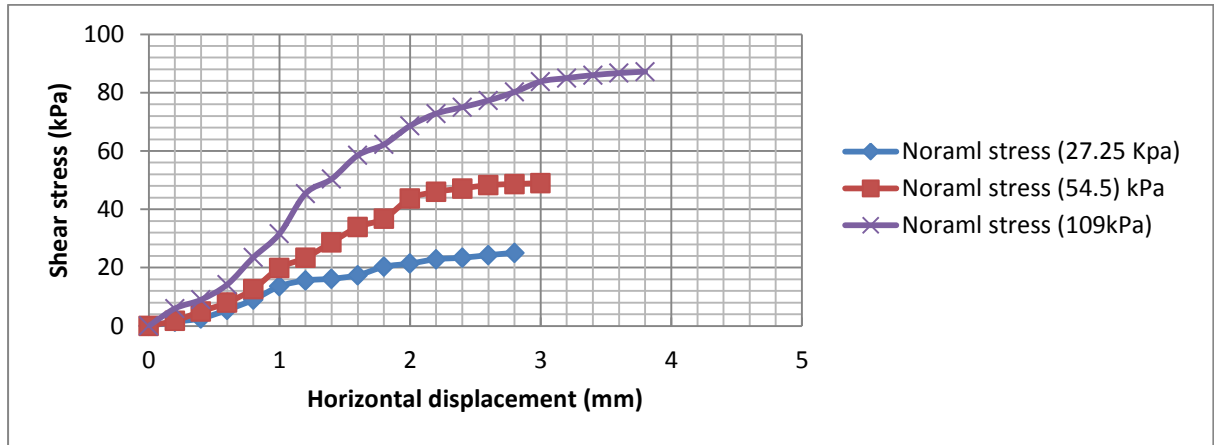


Figure 23 .shear stress–horizontal displacement relationship for grout gel at (w:c) (0.7w:0.3c) with 25% fly ash.

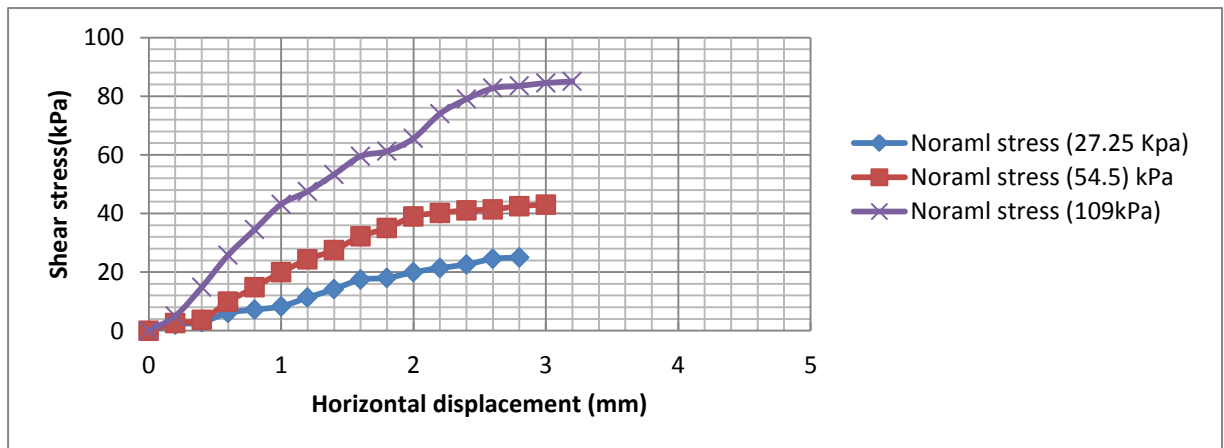


Figure 24 .Shear stress–horizontal displacement relationship for grout gel at (w:c) (0.7w:0.3c) with 40% fly ash.

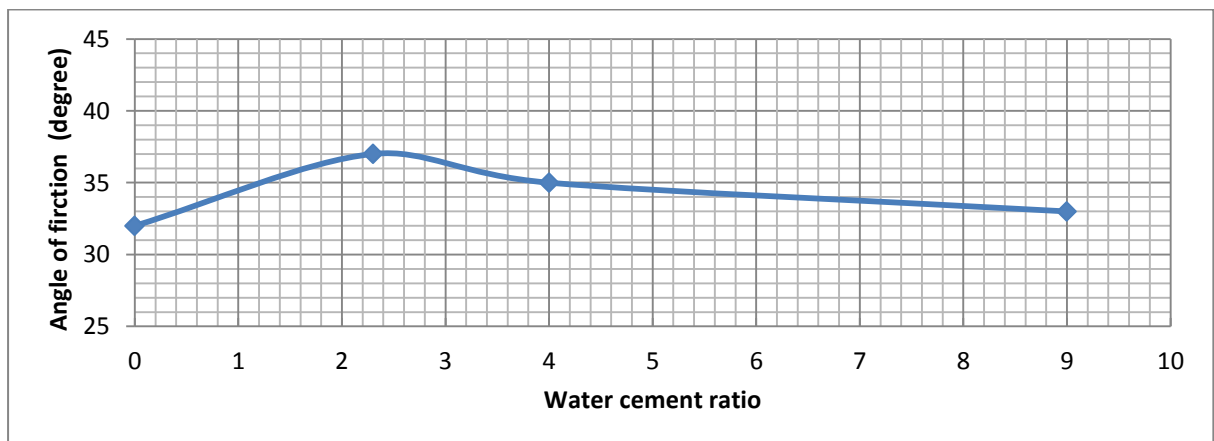


Figure 25. The Relationship between the (w:c) ratio for only cement grout and angle of friction.

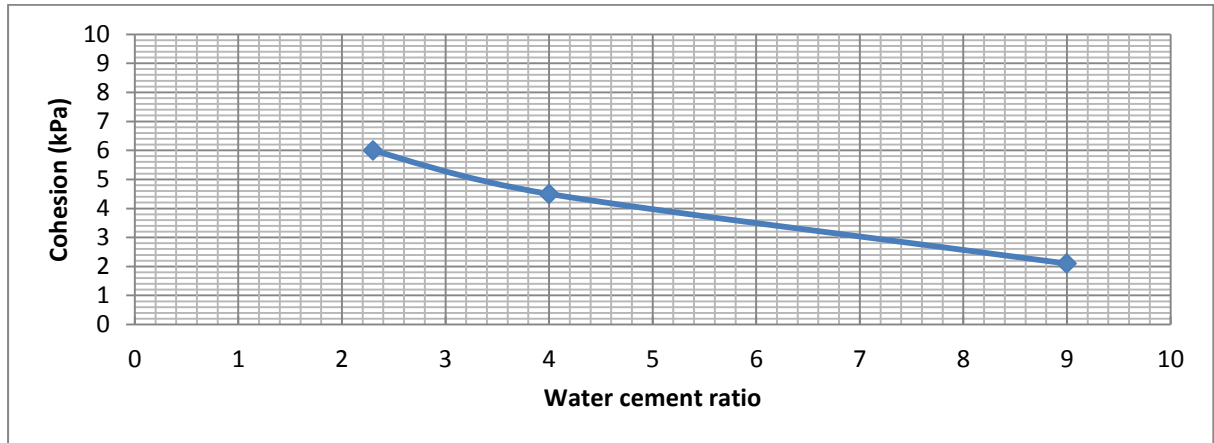


Figure 26. The relationship between the (w:c) ratio for only cement grout and cohesion.

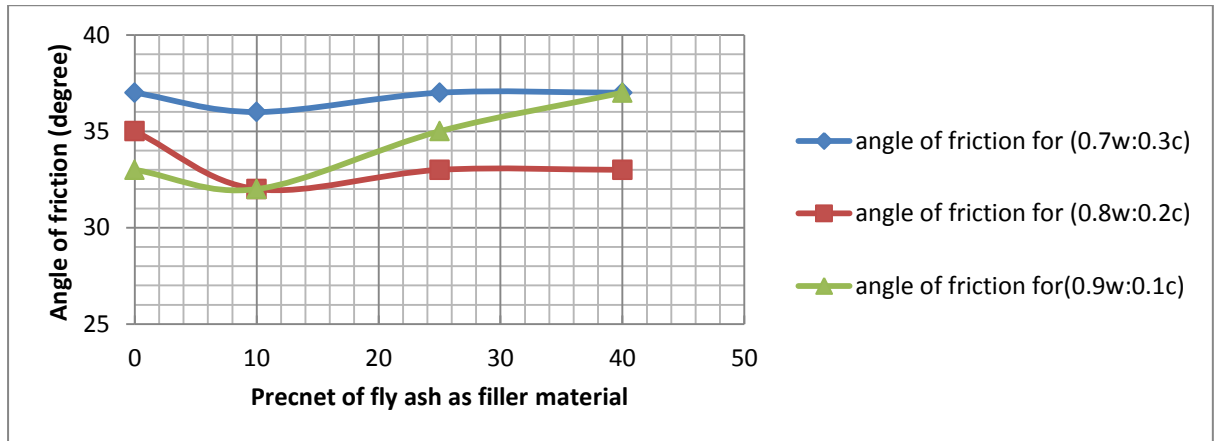


Figure 27. The relationship between the (w:c) ratio for cement grout with fly ash and angle of friction.

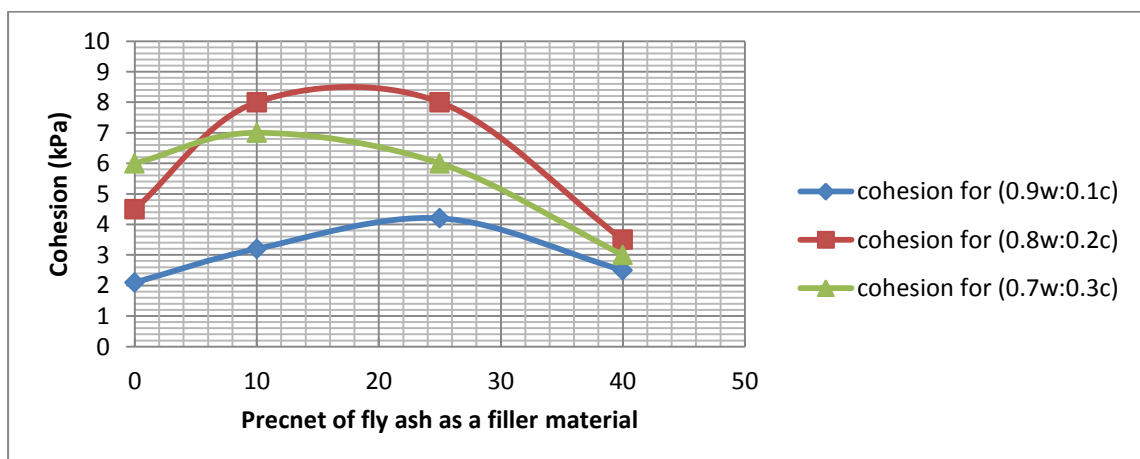


Figure 28. The relationship between the (w:c) ratio for cement grout with fly ash and cohesion.

**Table 1.** The physical Properties of sand soil.

Specific Gravity (G_s)	2.67	ASTM D854–2005
Maximum unit weight (γ_{max})	17.34 KN/m ³	ASTM D4253- 2000
Minimum unit weight (γ_{min})	14.79 KN/m ³	ASTM D4254–2000
Relative Density (D_r)	30%	-----
D_{10} , mm	0.33	-----
D_{30} , mm	0.59	-----
D_{60} , mm	1.4	-----
C_u	4.2	-----
C_c	0.68	-----

Table 2. Physical and chemical properties of cement.

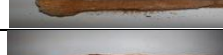
Index property	Index value
Compressive strength after 3 days (MPa)	27
Compressive strength after 7 days (MPa)	32.5
Time of initial setting (hour)	2.167
Time of final setting (hour)	4.167
SiO ₂ (%)	19.37
CaO (%)	64.36
Al ₂ O ₃ (%)	4.12
Fe ₂ O ₃ (%)	4.99
MgO (%)	2.41
SO ₃ (%)	2.44
C ₃ A (%)	2.47
LOI (%)	1.00
Salts insoluble (%)	1.24
Losses in heating (%)	3.25
Fineness of Cement (Blaine s Sp. Surface) (m ² /kg)	370

Table 3. Physical and chemical properties of fly ash.

Index property	Index value
SiO ₂ (%)	83.717
K ₂ O(%)	10.401
Al ₂ O ₃ (%)	2.314
Fe ₂ O ₃ (%)	2.213
CaO (%)	0.908
Sc ₂ O ₃ (%)	0.046
ZnO (%)	0.138
MnO (%)	0.179
PbO (%)	0.023
CuO (%)	0.009
Ir ₂ O ₃ (%)	0.007
Rb ₂ O (%)	0.004
Y ₂ O ₃ (%)	0.003
SrO (%)	0.010
TiO ₃	0.016
ZrO ₂	0.013
Fineness (Blaine s Sp. Surface) (m ² /kg)	295

Table 4. The comparison percentage of the grouted zone effective volume with and without the fly ash



For (0.9w:0.1c) + 5% Fly ash				
Injected depth	Grouted volume zone by cement only (cm ³)	Grouted volume zone by cement + fly ash (cm ³)	Increase or decrease in grouted volume zone	Picture for the sample after one day curing
h= 12.5 cm	55.6	73.69	32.53%	
h= 16.7 cm	52.5	87.65	66.76%	
For (0.9w:0.1c) + 25% fly ash				
h= 12.5 cm	55.6	84.3	51.61%	
h= 16.7 cm	52.5	95.2	81.33 %	
For (0.9w:0.1c) + 40% fly ash				
h= 12.5 cm	55.6	64	15.1 %	
h= 16.7 cm	52.5	70.6	34.48 %	
For (0.8w:0.2c) + 10% fly ash				
h= 12.5 cm	99.25	101	1.8%	
h= 16.7 cm	93.21	103	10.5%	
For (0.8w:0.2c) + 25% fly ash				
h= 12.5 cm	99.25	104 c.m3	4.8 %	
h= 16.7 cm	93.21	107 c.m3	14.8%	
For (0.8w:0.2c) + 40% fly ash				
h= 12.5 cm	99.25	89.1	-10.2 %	
h= 16.7 cm	93.21	91 c.m3	-2.4 %	
For (0.7w:0.3c) + 10% fly ash				
h= 12.5 cm	138.5	109.1	-21.227 %	
h= 16.7 cm	128.7	105.8	-17.793 %	
For (0.7w:0.3c) + 25% fly ash				
h= 12.5 cm	138.5	99.2	-28.4 %	
h= 16.7 cm	128.7	88.7	-31 %	
For (0.7w:0.3c) + 40% fly ash				
h= 12.5 cm	138.5	78.2	-43.537%	
h= 16.7 cm	128.7	75.15	-41.60 %	

- The negative sign refers to decrease in volume.



Table 5. Results of direct shear test for soil treated by grouting method with different (w:c) with and without fly ash

(w:c) with percent of filler materials		Result of direct shear test		Increasing in ϕ (%) for treated soil
(w:c)	percentage of Fly ash	ϕ degree	C kPa	
0	0	32	0	-
(0.9w:0.1c)	0	33	2.1	3%
	10%	32	3.2	0%
	25%	35	4.2	9.4%
	40%	37	2.5	15.6%
(0.8w:0.2c)	0	35	4.5	9.4%
	10%	32	8	0%
	25%	33	8	3%
	40%	33	3.5	3%
(0.7w:0.3c)	0	37	6	15.6%
	10%	36	7	12.5%
	25%	37	6	15.6%
	40%	37	3	15.6%

Numerical and Experimental Investigations of the Effect of PVD and Vacuum Pressure on the Degree of Saturation

Dr. Ala Nasir Aljorany
Professor
College of Engineering
University of Baghdad
E-mail:alaAljorany@gmail.com

Fatema Safaa Noori
PhD student
College of Engineering
University of Baghdad
E-mail:fatemasafaa@yahoo.com

ABSTRACT

Soft clays are generally characterized by low shear strength, low permeability and high compressibility. An effective method to accelerate consolidation of such soils is to use vertical drains along with vacuum preloading to encourage radial flow of water. In this research numerical modeling of prefabricated vertical drains with vacuum pressure was done to investigate the effect of using vertical drains together with vacuum pressure on the degree of saturation of fully and saturated-unsaturated soft soils. Laboratory experiments were conducted by using a specially-designed large consolidometer cell where a central drain was installed and vacuum pressure was applied. All tests were conducted with a vacuum pressure of 40 kPa applied for a period of 30 days where a degree of soil consolidation of 90% was attained. At the end of the test period fifteen samples were taken from different locations distributed along the depth and radially to measure the water content. Consolidation settlements were recorded with time for all tests. The results showed that using vacuum pressure with vertical drains is a very effective method to accelerate consolidation of soils. As the thickness of unsaturated top layer increases, the settlement of soil surface decreases. The water content decreased after 30 days of application of the vacuum pressure.

Key words: degree of saturation, PVD, vacuum, and degree of consolidation.

تحليل نظري وعملي لتأثير أعمدة الصرف الطولية وضغط التفريغ على درجة التشبع

فاطمة صفاء نوري
طالبة دكتوراه
كلية الهندسة- جامعة بغداد

د. علاء ناصر حريب
استاذ
كلية الهندسة- جامعة بغداد

الخلاصة

تتكون الترب الرخوة في مناطق ترسيب الأنهار أو البحار أو البحيرات. تتكون هذه الترب على شكل طبقات تتداخل مع طبقات من الرمل والغرين التي تعرضت الى حالات الجفاف والترطيب بصورة دورية قرب السطح. ولغرض دراسة سلوك التربة الرخوة باستخدام أعمدة التصريف الطولية والمفرغ تم تصميم وإنشاء خلية إنضمام خصيصا لهذه الدراسة. تم إجراء فحوصات مخبرية بتسليط ضغط سالب مقداره 40 kPa لمدة لاتقل عن ثلاثين يوم. بالإضافة الى الدراسة العملية أجريت دراسة نظرية بالإعتماد على طريقة العناصر المحددة باستخدام برنامج ABAQUS بإصداره 6.13 لدراسة تأثير أعمدة الصرف الطولية والمفرغ على درجة تشبع الترب المشبعة وغير المشبعة حيث أظهرت النتائج كفاءة هذه الطريقة في تحسين التربة وتقليل الزمن اللازم للوصول الى إنضمام عالي داخل التربة. وأظهرت النتائج تقارب كبير بين الفحوص العملية والتحليل النظري .
الكلمات الرئيسية: درجة التشبع، وأعمدة الصرف الطولية، والمفرغ، و درجة الإنضمام.



1. INTRODUCTION

Large areas covered with thick deposits of soft clay layers which are not suitable for construction of many infra structures. The growing need for infrastructures in urban and the lack of sites suitable for development increased land prices dramatically. Accordingly, lands having poor geotechnical properties (low shear strength and high compressibility) were utilized as construction sites. Prefabricated Vertical Drains, PVDs, together with vacuum pressure have been widely used to accelerate the consolidation of soft soils **Indraratna, and Rujikiatkamjorn, 2004, and AL-Shammarie, 2013**. This technique shortened the horizontal drainage path to half of the drain spacing. Moreover, propagation of vacuum pressure along the PVD increases the hydraulic gradient and creates an additional surcharge load. The concept of drainage through vertical drains was initially developed in the 1920s. The property of sand being more permeable than clay silty soil was utilized by creating sand columns in lesser permeable soils and these sand columns functioned as drains. The first prefabricated vertical drain was developed by **Kjellman, 1940** (as cited by Indraratna, et al, 2005). Several other types of PVDs have been developed since then such as Geodrain, Alidrain, and Mebradrain. PVDs consisted of few channels imprinted into a stiff card board core **Indraratna, et al., 2003**.

The basic idea of the PVD depends upon the radial consolidation of soils since the PVD provides a lateral path and facilitates dissipation of pore-water pressure during the loading process, thus, accelerating the consolidation process. **Barron, 1948** analytically solved radial consolidation for free- and equal-strain conditions. **Indraratna, et al., 2005** developed a radial consolidation formula that involves compression indices. Their derivation was based upon several assumptions among them is that the relationships void ratio-effective stress and void ratio-horizontal coefficient of permeability can be found from:

$$e = e_o - c_c \log \frac{\sigma'}{\sigma_i} \quad (1)$$

and

$$e = e_o + c_k \log \frac{k_{hp}}{k_{hi}} \quad (2)$$



where c_c , compression index, c_k , permeability index, e , void ratio, e_o , average void ratio corresponding to the initial in-situ effective stress, k_{hi} , initial coefficient of horizontal permeability of undisturbed soil, σ' , vertical effective stress, and σ'_i , initial effective vertical stress.

Average degree of consolidation can be expressed in terms of excess pore-water pressure or strain as follows:

$$U_p = 1 - R_u \quad (3)$$

or

$$U_s = \frac{\rho}{\rho_\infty} \quad (4)$$

where U_p , average degree of consolidation calculated from pore-water pressure, R_u , average excess pore water pressure ratio, U_s , average degree of consolidation calculated from strain, ρ , settlement at any time, and ρ_∞ settlement at effective stress equal to initial effective stress plus the additional load.

2. THEORETICAL ANALYSIS

The effect of using PVD and vacuum pressure on the degree of saturation of fully saturated and saturated-unsaturated soils was investigated by using ABAQUS software version 6.13. Five different cases were investigated including fully saturated, and partially saturated (50% degree of saturation) with different depths of unsaturated layer namely $1/8 L$, $1/4 L$, $3/8 L$, and $1/2 L$ thick lay on a fully saturated layer, where L is the total depth of the soil sample. A half-unit cell 0.35 m in diameter and 0.8 m deep was analyzed by using ABAQUS software. **Fig. 1** shows the geometry of the five different cases together with the mesh. In the analysis it was assumed that the soil element is eight noded and axi-symmetric, quadrilateral, biquadratic displacement, bilinear pore-water pressure, and reduced integration were adopted, abbreviated as CAE8RP. The soft soil was analyzed as elasto-plastic material obeying Modified Cam-Clay Model, MCC. The input data to the MCC were: slope of normal consolidation line, λ , 0.18; slope of the critical-state line, M , 1.2; initial yield surface, a_o , wet surface size, ζ , and flow stress ratio, k , both assumed to be 1. The input data to the porous elastic model included: slope of over consolidation line, κ , 0.08, and Poisson's ratio, ν , 0.3. The unit weight and permeability of the soil were 18 kN/m^3

and 2.11×10^{-8} m/sec, respectively. The PVD was assumed to behave as an elastic material with Young's modulus, E , equal to 1800 kPa and Poisson's ratio equal to 0.4. In order to define the unsaturated element in ABAQUS, the sorption effect should be included since ABAQUS depends upon soil-water characteristic curve to define the degree of saturation of soil. **Fig. 2** shows the soil-water characteristic curve, SWCC, based upon results obtained from the plate-pressure method.

3. APPARATUS of EXPERIMENTAL WORK

In this research, a cylindrical steel container (consolidometer cell) was specially designed and manufactured to be used for the investigation of the improvement of the behavior of soft soils by using PVD. The cell was designed to be air and water tight with removable top and bottom flanges. The cell contained seven openings to insert the wires; four of them were used to insert the piezometers and the remaining three to insert the pressure cells. **Fig. 3** is a schematic representation of the consolidometer used in this research and shows the distribution of the openings along the wall of the cell. The cap of the model contained an opening to connect the vacuum pump; an opening to insert a point gauge; and a circular glass window for inspection. The base of the model contained a drainage hole; 5 mm in diameter and provided with a valve.

4. TEST PROCEDURE

Five separate series of tests were conducted, the first series involved applying a vacuum pressure of 40 kPa at the top of a fully saturated soft-soil while the other series of tests involved applying a vacuum pressure of 40 kPa at the top of an unsaturated soil with different depths (1/8L, 1/4 L, 3/8 L, and 1/2 L thick, and 50% degree of saturation) laid on a fully saturated soft-soil layer, where L is the total depth of the soil placed in the cell. The testing procedure involved three main steps namely preparation of reconstituted clay, installation of the drain, and collection of oedometer samples.

The preparation of reconstituted clay was done according to the procedure suggested by **Burland, 1990** (as cited by Indraratna, et al, 2005), where the clay specimen was mixed thoroughly with distilled water at water content slightly greater than the liquid limit. The clay was placed and tamped in layers in the consolidometer



cell; the unsaturated layer was then placed on the top of the saturated soft soil with a thickness equal to $1/8$, $1/4$, $3/8$, and $1/2$ the total depth of the soil sample. Then a $25 \text{ mm} \times 3 \text{ mm}$ band drain was inserted through the total depth of the soil by using a steel mandrel. During the placement of the soil in the cell four piezometers were placed at 19, 35, 50 and 80 cm from the top of the soil. A vacuum pressure of 40 kPa was applied for 30 days and the corresponding settlement and pore-water pressure were measured. **Table 1** shows the physical and chemical properties of the natural soft-soils brought from AL-Basrah city south of Iraq. At the end of the test period for fully and saturated-unsaturated soft soil, fifteen samples were taken from different locations distributed along the depth and radially to measure the water content.

5. RESULTS AND DISCUSSION

A comparison between the settlement of a fully saturated soft soil and that of a saturated soil overlaid by a layer of unsaturated soil whose thickness is $1/8$, $1/4$, $3/8$, and $1/2$ of the total soil depth is shown in **Fig. 4**. Settlement of soil was measured by using a point gauge. It is obvious that the presence of an unsaturated layer reduces soil settlement. The degree of consolidation based upon soil settlement was found to be more than 90 % after 30 days of vacuum application (for two-way drainage conditions) while applying a surcharge with same magnitude without a PVD requires more than 93 days to reach 90 % degree of consolidation.

Figs. 5 through 9 show the variation of measured water content with the depth and radial distance as compared with the results obtained from numerical analysis. From these figures, it is obvious that the water content for fully saturated soils decreased after 30 days of application of vacuum pressure. During the experimental test, water started to flow out from the soil after some time and was collected in the vacuum container. Water content at the face of the drain decreased more rapidly than that at the boundary. Due to the insertion of mandrel a disturbed zone near the PVD is formed causing the horizontal permeability to be less than that in the undisturbed zone. Accordingly, the water content would be less at the interface of the PVD than at the boundary of the soil sample. The water content for the unsaturated soil layer increases with time due to the high matric suction in the unsaturated layer. Application of vacuum pressure also accelerates the transmission of water from the saturated layer to the unsaturated layer. Also as the depth of the



unsaturated layer increases the time required for water to appear on the soil surface increases. A good agreement was found between the numerical and the experimental work.

6. CONCLUSIONS

The results show that a system of prefabricated vertical drains accompanied with the application of vacuum pressure is an effective method to accelerate the consolidation of soft soils where the degree of consolidation was found to reach more than 90% in 30 days instead of 93 days for two-way drainage conditions. Presence of unsaturated soil reduces soil settlement. The degree of saturation of the fully saturated and saturated-unsaturated soft soil changes by 30 % depending upon the initial moisture content of the soil. A good agreement was found between experimental work and numerical analysis.

REFERENCES

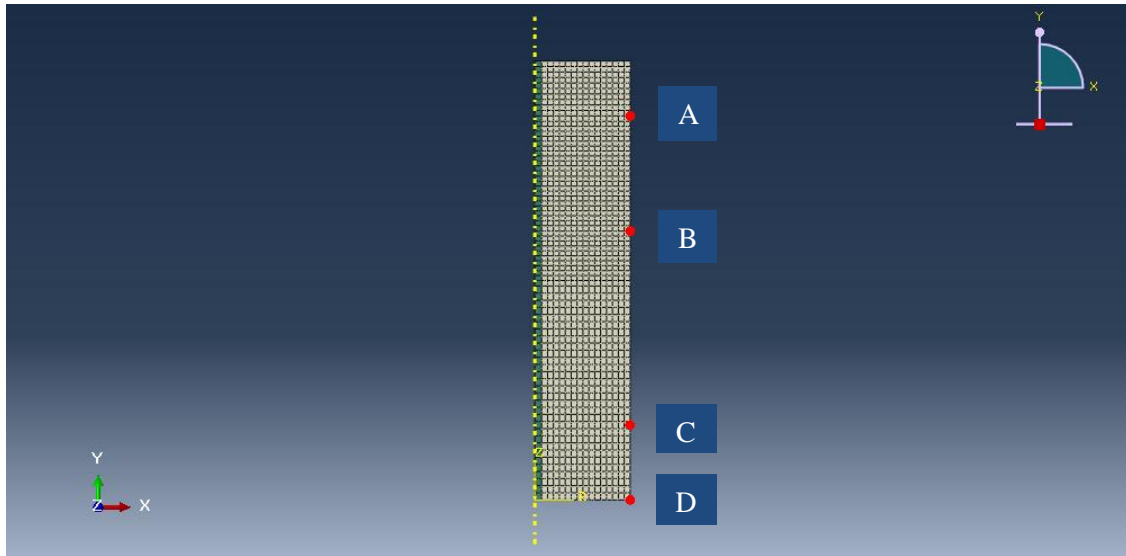
- AL-Shammarie H., 2013, *An Experimental and Theoretical Study on Ordinary and Encased Stone Column underneath Embankment*, Ph D Thesis, University of Baghdad.
- Barron R., 1984, *Consolidation of Fine-Grained soils By Drains Wells*, ASCE, vol. 113, No. 1, January, pp. 718-742.
- Das M., B, 2007, *Principles of Geotechnical Engineering*, Thomson, Canada.
- Indraratna B., and Rujikiatkamjorn C., 2004, *Laboratory Determination of Efficiency of Prefabricated Vertical Drains*, 15th Southeast Asian Geotechnical Conference, Pathumthani, Thailand, SEAGS, pp 453-456.
- Indraratna B., Bamunawita C., Redana I., and Mcintosh G., 2003, *Modelling of Prefabricated Vertical Drains in Soft Clay Evaluation of Their Effectiveness in Practice*, 4th International Conference on Ground Improvement Techniques, vol. 7, No 3, Kuala Lumpur, pp 127 – 137.
- Indraratna B., Rujikiatkamjorn C., and Sathananthan I., 2005b, *Radial Consolidation of Clay Using Compressibility Indices and Varying Horizontal Permeability*, Canadian Geotechnical Journal, vol. 42, No 5, October, pp 1330 – 1341.



- Mohamedlhasan E., and Shang J. Q., 2002, *Vacuum and Surcharge Combined One-Dimensional Consolidation of Clay Soils*, Canadian Geotechnical Journal, vol. 39, September, pp 1126 – 1138.
- Terzaghi K., 1943, *Theoretical Soil Mechanics*, John Wily and Sons, New York.

LIST OF SYMBOLS

c_c	=	compression index, dimensionless
c_k	=	permeability index, dimensionless
e	=	void ratio, dimensionless
e_o	=	average void ratio at the initial in-situ effective stress, dimensionless
k_{hi}	=	initial coefficient of horizontal permeability of undisturbed soil, m/sec,
R_u	=	average excess pore water pressure ratio, dimensionless
U_p	=	average degree of consolidation based upon pore-water pressure, dimensionless
ρ	=	settlement at any time, m
ρ_∞	=	settlement at effective stress equal to initial effective stress plus the additional load, m
σ'	=	vertical effective stress, kPa, and
σ'_i	=	initial effective vertical stress, kPa.



Geometry of the fully-saturated soil and nodal number

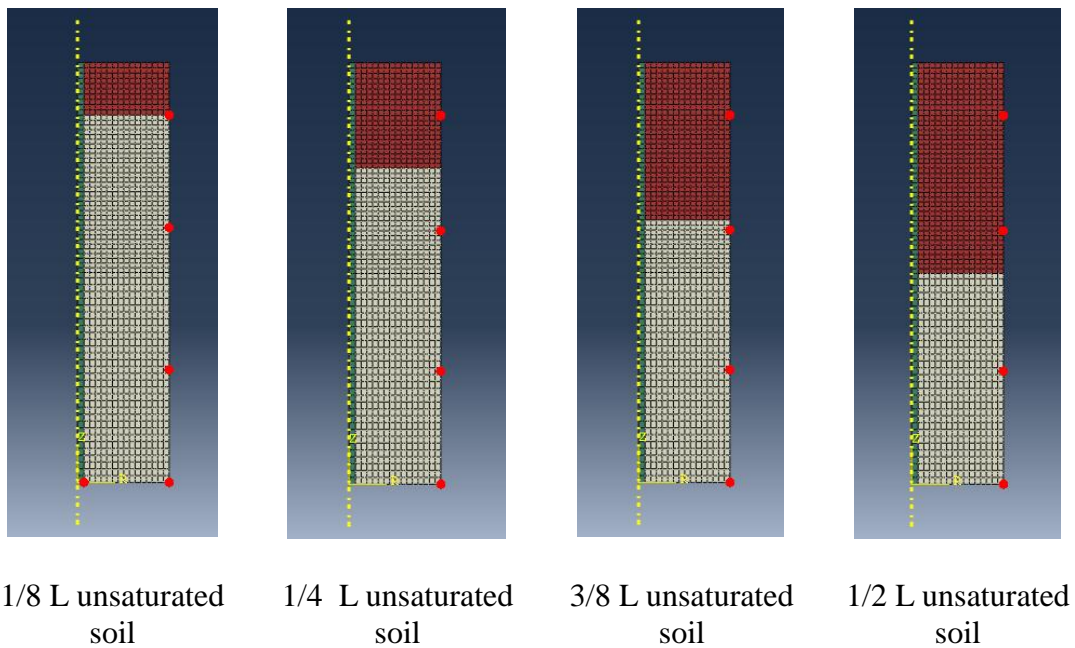


Figure 1. Geometry of half unit, mesh, and nodal positions and numbers.

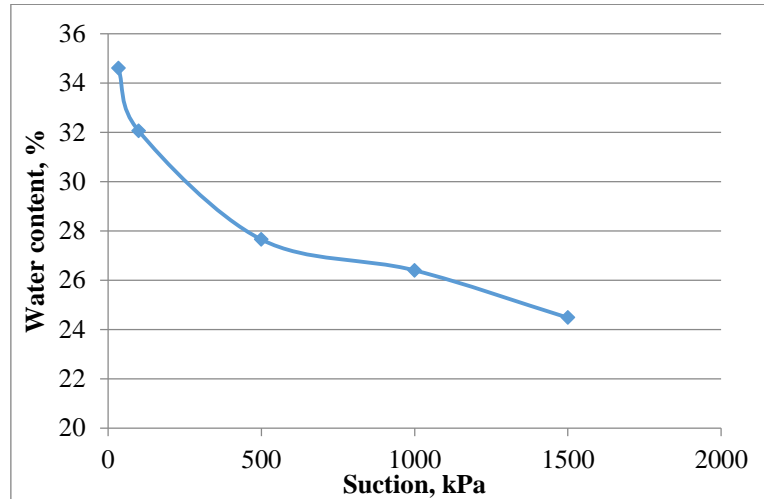
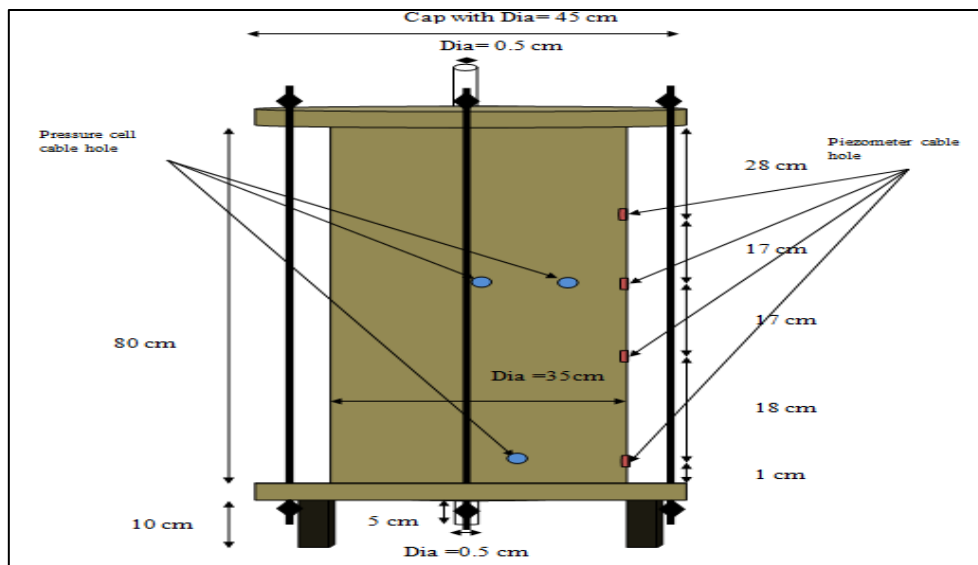


Figure 2. Soil-water characteristic curve, SWCC, based upon results obtained from the plate-pressure method.



(a)

Figure 3. Schematic diagram of the designed consolidometer cell.



(b)

Figure. 3 Cont.

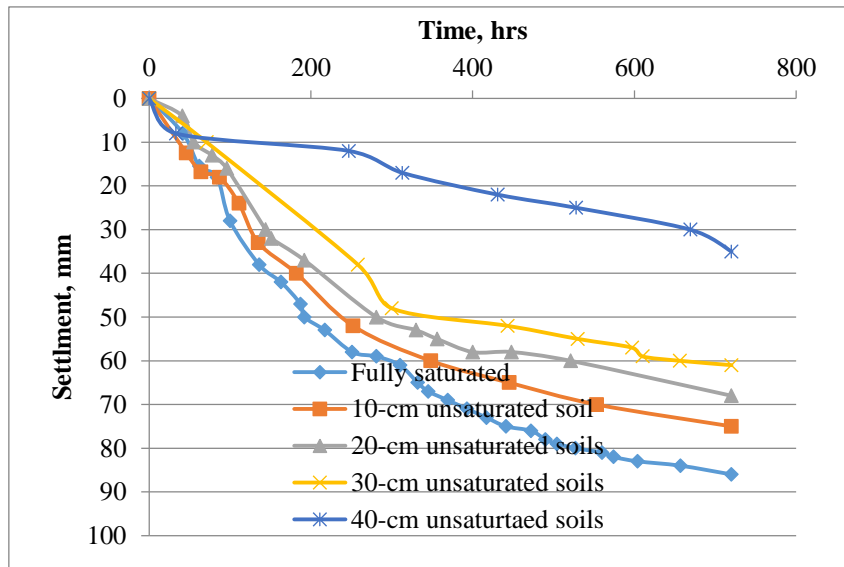
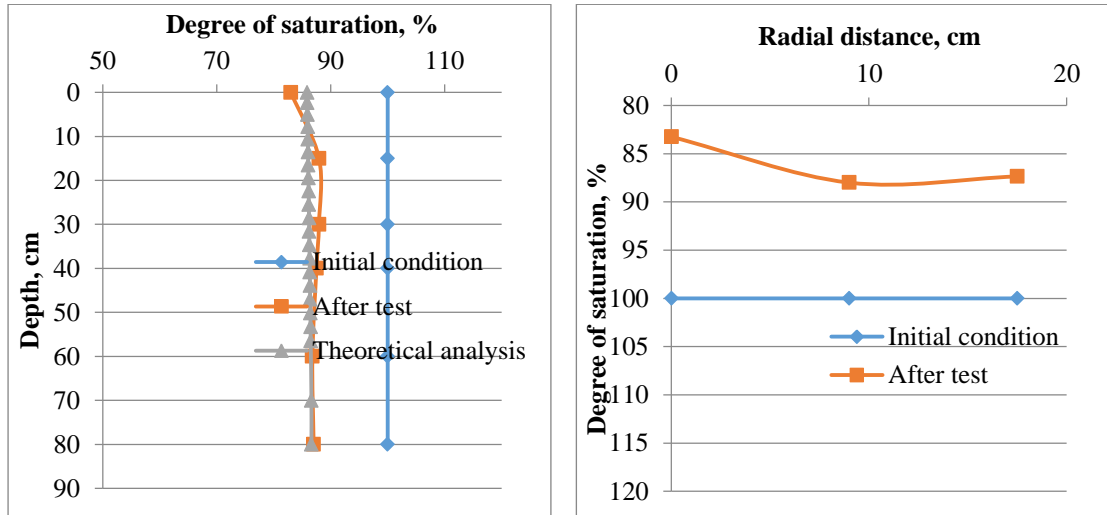
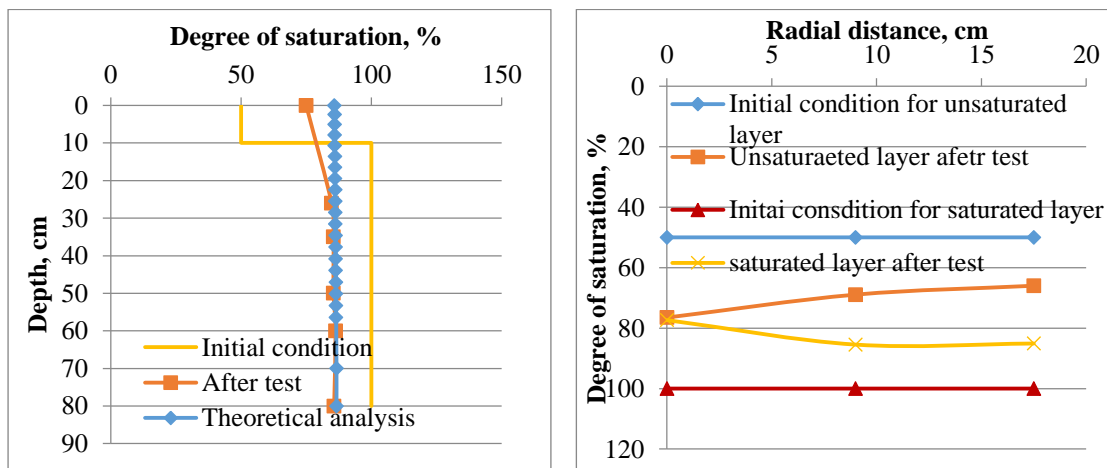


Figure 4. Variation of soil settlement with time.



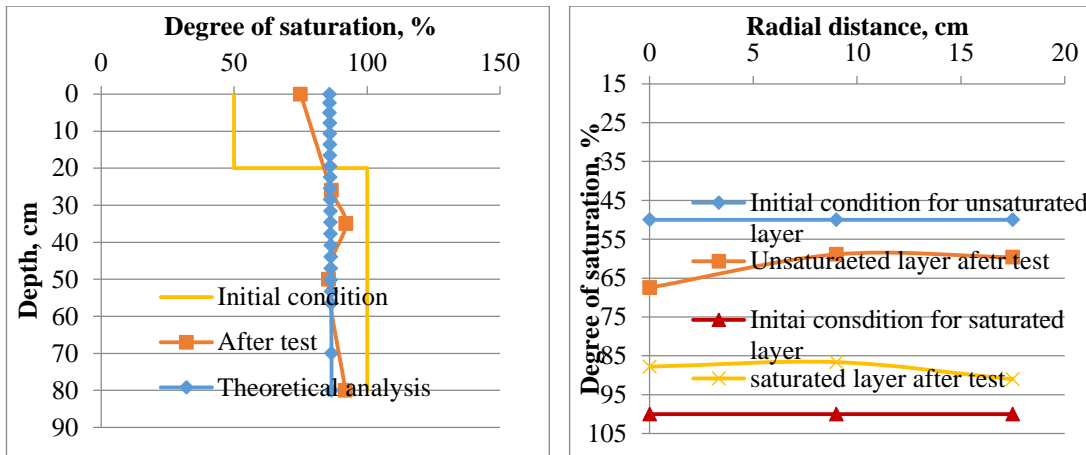
(a) Variation of water content with depth (b) Radial variation of water content

Figure 5. Variation of water content after 30 days of applying vacuum pressure on a fully saturated soft soil.



(a) Variation of water content with depth (b) Radial variation of water content

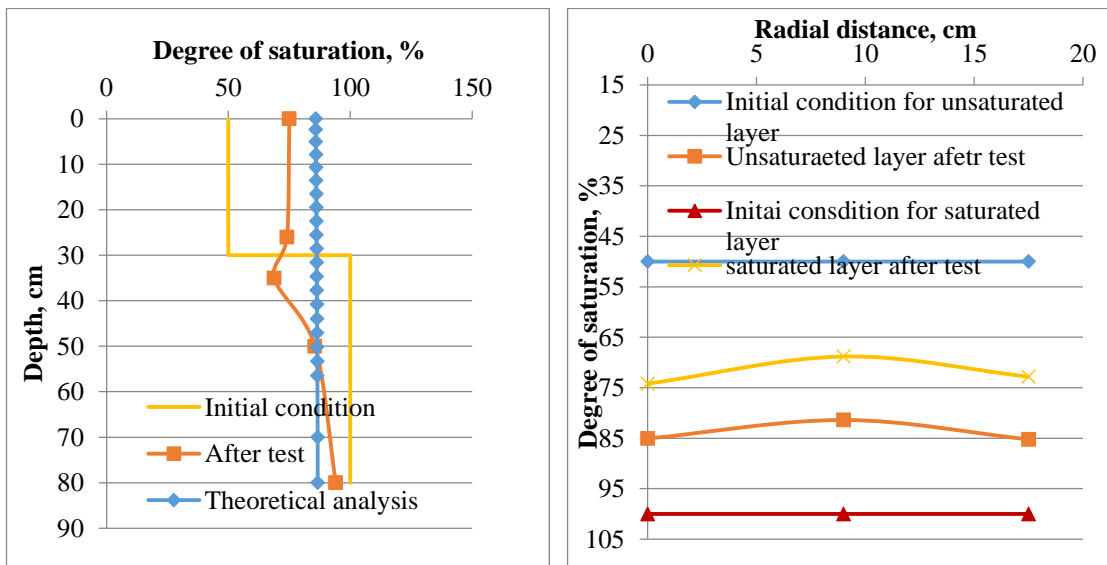
Figure 6. Variation of water content after 30 days of applying vacuum pressure on 1/8 L unsaturated soils.



(a) Variation of water content variation with depth

(b) Radial variation of water content

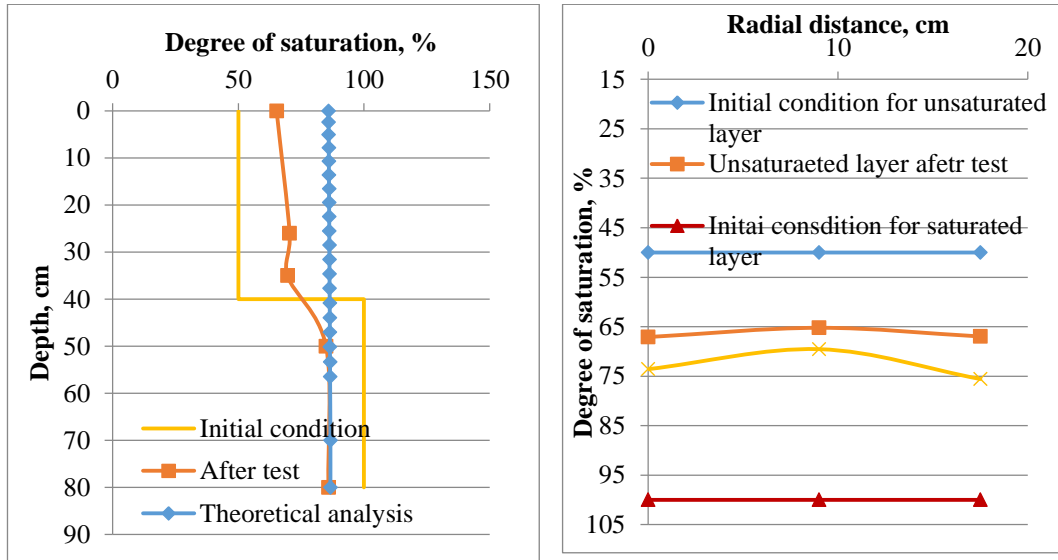
Figure 7. Variation of water content variation after 30 days of applying vacuum pressure on a 1/4 L unsaturated soils.



(a) Variation of water content variation with depth

(b) Radial variation of water content variation

Figure 8. Variation of water content after 30 days of applying vacuum pressure on a 3/8 L unsaturated soils.



(a) Variation of water content with depth

(b) Radial variation of water content

Figure 9. Variation of water content after 30 days of applying vacuum pressure on a 1/2 L unsaturated soils.

Table 1. Physical and chemical properties of the natural soil used in the experiments.

Property	Value
Liquid limit, LL	36%
Plastic limit, PL	18%
Liquidity index, LI	0.61
Specific gravity, G _s	2.73
Clay content < 0.005 mm	45.3 %
Silt content 0.005 to 0.074 mm	49.21 %
Sand content > 0.074 mm	5.49 %
Maximum dry unit weight, kN/m ³	17.06
Optimum moisture content,	19%
Soil symbol according to USCS	CL
Organic material	2.1 %
SO ₃	3.20 %
Total soluble salts	10 %
pH	8.1
Gypsum content	7.224 %
Radiation	Negative
Initial void ratio, e ₀	1.092
Compression index, c _c	0.4
Coefficient of vertical consolidation, c _v , m ² /day	1.46*10 ⁻³
Swelling index, c _r	0.03



A Laboratory Study Attempt of Flow and Energy Dissipation in Stepped Spillways

Thulfikar Razzak Abdul-Mehdi

Lecturer Ph.D

College of Engineering - University of AL-Qadisiyah

Thulfikar.AbdulMehdi@qu.edu

Haider Ali Al- Mussawy

Lecturer Ph.D

College of Engineering -Al-Mustansiriyah University

E-mail:h_a_m_s76@yahoo.com

Abdul- Sahib Tafteeq Al-Madhhachi

Lecturer Ph.D

College of Engineering -Al-Mustansiriyah University

E-mail:abdu@okstate.edu

ABSTRACT

A new laboratory study conducted on stepped spillways in order to investigate their efficiency of dissipating flow energy. All previous study on stepped spillway indicated that the flow energy dissipation decreased as increasing in discharge. Increasing in the step numbers and the spillway slope led to energy dissipation decrease. In this study, an experimental attempt to increase energy dissipation at variable discharges was performed on stepped spillway and that leads to decreasing the cost of initiating the stilling basin or may be ignoring it. Five spillways were constructed from concrete and tested to investigate and compare among them. Three were roughed by gravel with different size for each one, one of them was stepped without any addition, and the last one was stepped with cavitation. The height of stepped spillways was 18 cm with unique numbers of steps ($n = 3$), and unique downstream slope of stepped face ($\theta = 30^0$) were utilized. The percentage of relative energy dissipation (R.E.D) was increased using rough surface with coarse gravel. When the size of gravel increased, the R.E.D was increased and when using the ratio between heights of gravel to steps of 0.5, the R.E.D was increased to about triple compared with traditional spillways. The R.E.D was decreased when the cavitation on the stepped surface was utilized compared to the stepped spillway without any addition for large discharges and that was inverse for small discharges. Comparing to steps without any addition, the rouged steps with the larger size of gravel maximized the energy dissipation for both small and large discharges. The relative energy dissipation was 26.73 % compared with traditional spillway and 16.73 % compared with stepped spillway without any addition, since the stepped spillways more effective than traditional spillways by 10 %. In general, the R.E.D was decreased when increasing the discharge.

Key words: Flow energy dissipation, stepped spillways, flow types, gravel roughed surface, cavitation.

محاولة دراسة مختبرية للجريان و الطاقة المتشعبة في المطامح المدرجة

حيدر علي مهدي الموسوي
مدرس دكتور
كلية الهندسة - الجامعة المستنصرية

ذو الفقار رزاق عبدالمهدي
مدرس دكتور
كلية الهندسة-جامعة القادسية

عبدالصاحب توفيق عبدالصاحب المنحجي
مدرس دكتور
كلية الهندسة-الجامعة المستنصرية

الخلاصة

تم تقديم دراسة مختبرية جديدة على المطامح المدرجة لغرض التحري عن كفاءتها في تشتيت طاقة الجريان. ان كل الدراسات السابقة عن المطامح المدرجة بينت ان نسبة تشتت طاقة الجريان تقل عند زيادة التصريف. وان زيادة عدد مدرجات المطامح وزاوية ميلانه يؤدي الى تقليل تشتيت الطاقة. في هذه الدراسة تم اجراء محاولة عملية لزيادة تشتيت الطاقة على المطامح المدرجة عند عدة التصريف. وذلك لان زيادة تشتيت الطاقة عند تلك المطامح يؤدي الى تقليل او الاستغناء عن احواض تشتيت الطاقة وبالتالي التقليل من مخاطر القفزة الهيدروليكية. تم انشاء خمس نماذج خرسانية من المطامح المدرجة لغرض اجراء تلك الدراسة والمقارنة بينها. تم تخشين سطح ثلاث من تلك النماذج باستخدام حصي ذات اقطار مختلفة لكل واحد منها وواحد بدون أي إضافة والأخير تم تخشين سطحه باستخدام التجوفات. تم استخدام ارتفاع موحد قدره 18 سم وعدد مدرجات موحدة وهي 3. كذلك تم استخدام زاوية ميلان واحدة لجميع تلك النماذج وهي 30 درجة. تم زيادة تشتيت نسبة طاقة الجريان (R.E.D) باستخدام الحصى وكلما زاد قطر الحصى زاد تشتيت الطاقة وخصوصا عند معدل نسبة ارتفاع قطر تلك الحصى الى ارتفاع المدرجة وقيمته 0.5 وهذا أدى الى زيادة تشتيت طاقة الجريان الى تقريبا ثلاث اضعاف مقارنة بالمطامح التقليدية غير المدرجة. ان نسبة تشتيت الطاقة تقل عند استخدام التجوفات عند التصريف العالية وتزداد عند التصريف القليلة مقارنة بالمطامح المدرجة التي لا تحوي أي إضافة. اما فيما لو استخدم الحصى فان ذلك يؤدي الى زيادة تشتيت الطاقة عند التصريف العالية والقليلة. ان الزيادة في نسبة تشتيت طاقة الجريان كانت 26.73% مقارنة بالمطامح التقليدية و16.73% مقارنة بالمطامح المدرجة التي لا تحوي أي إضافة. لان المطامح المدرجة التي لا تحوي أي إضافة تكون اكثر كفاءة في تشتيت طاقة الجريان بنسبة 10% مقارنة بالمطامح التقليدية غير المدرجة. وبصورة عامة فان نسبة تشتيت طاقة الجريان تقل بزيادة التصريف.

الكلمات الرئيسية: تشتيت الطاقة ، المطامح المدرجة، انواع الجريان ،خشونة سطح الحصى ،تجوف.

1. INTRODUCTION

Usually the flood flow is released through the dam by spillway. A major part of the dams construction cost was due to design and contraction of spillways. A 20% and 80 % of total dam construction costs were for small and large dams, respectively ,**Yousefian, 1996**. The design and construction of spillways are very complicated and usually faced with difficulties such as cavitation and high flow kinetic energy due to the high flow discharge over the spillways , **Novak et al., 1990**. It becomes usual to protect the spillway surface from cavitation erosion by introducing air next to the spillway surface using aeration devices located on the spillway bottom and sometimes on the sidewalls ,**Chanson, 1997**. Stepped spillways allow continuously dissipating a considerable amount of the flow kinetic energy. For instant, the downstream stilling basin of the residual energy was dissipated by hydraulic jump. This could be largely reduced in dimensions of spillway. In addition, the cavitation risk along the spillway decreases significantly due to smaller flow velocities and the large air entertainment rate ,**Rajaratnam, 1990**.

Al-Talib, 2007 found that stepped weirs were more efficient than flat sloped weirs and the maximum energy dissipation ratio in stepped weirs was approximately 10 % higher than in flat sloped weirs. **Chamani and Rajaratnam, 1999** showed that in a stepped spillway, jet flow occurred at relatively smaller discharges and skimming flow occurred at larger discharges. **Alghazali and Jasim, 2014** performed 12 stepped spillway models to investigate flow regime limits. They performed three downstream slope angles (25, 35, and 45°), and four numbers of steps (5, 10, 15, and 20). **Alghazali and Jasim, 2014** tested five configurations of steps (conventional flat, pooled, porous end sills, pooled with gabions, and porous end sills with gabions). Their results showed that the end sills highly affect flow regime type for the lower limits of skimming flow. **Alghazali and Jasim, 2014** found that gabions reduced the effects of end sills on the lower limit of skimming flow regime to near the limit of flat steps. They suggested new empirical equations based on the experimental results.

Barani, et al., 2005 investigated the energy dissipation of the flow over stepped spillways of different step shapes; a physical wooden model has been built. Experiments have been carried out for different types of step shapes (plain steps, end sill steps with thickness of 1, 2, 3, and 4 cm and steps with bottom adverse slope of 15°, 26°, 36°, and 45°). Overall, the hydraulic parameters of flow over the model were measured, and the energy dissipation of flow was calculated. The results showed that the energy dissipation of the flow over the end sill and inclined stepped spillways were more than the plain one. The energy dissipation was increased by increasing the thickness of end sill or the adverse slope size.

El-Jumaily and Al-Lami, 2009 studied the flow characteristics and energy dissipation over traditional and stepped spillway with semicircular crest. Their experimental results showed that when increasing the ratio between upstream water depth to the water depth at crest and Froude number at spillway toe led to increase energy dissipation on traditional and stepped spillway. **El-Jumaily and Al-Lami, 2009** suggested a design of Bastora stepped spillway as a prototype to build a physical wooden model with scale of 1:20 (length of model to length of prototype). Experiments have been carried out on the model with slope of upward inclined steps of 420, 280, 140 and 100. For every slope of the steps, experiments were conducted in three flow regimes, nappe, transition, and skimming. Results showed that the energy dissipation decreases with increasing the discharge, and the energy dissipation of flow on stepped spillways with upward inclined steps is more than on the horizontal stepped spillways, it increases with increasing the adverse slope of steps. **Chen, et al., 2002** examined the flow of the stepped spillway by applying the finite volume method and utilized the kinetic energy model for the determination of the flow turbulence. They found that the turbulence numerical simulation is an efficient and useful method for the complex stepped spillway overflow.

Recent studies (**Wuthrich and Chanson, 2015; Zhang and Chanson, 2016; Sabbagh-Yazdia and Misaghiana, 2016**) were investigated and performed gabion stepped spillway to study flow characteristics, interactions between free-surface, cavity, and seepage flows. No study till now investigated the influence of roughed steps spillway by gravel on energy dissipation. The aim of this study is to investigate the flow characteristics and the energy dissipation on roughed stepped spillway using different sizes of gravel and on cavitation stepped spillway.

2. GENERAL THEORETICAL IN STEPPED SPILLWAY

The following general relationships for the flow energy dissipation were applied at upstream and downstream of each stepped spillway (**Chen, et al., 2002**):

$$E_0 = y_0 + \frac{\alpha v_0^2}{2g} \quad (1)$$

$$E_1 = y_1 + \frac{\alpha v_1^2}{2g} \quad (2)$$

$$\frac{\Delta E}{E_0} = \frac{(E_0 - E_1)}{E_0} \quad (3)$$

where y_0 is depth of water at upstream, cm, y_1 is depth of water at toe of spillway, cm, v_0 is velocity at upstream, m/sec, v_1 is velocity at downstream at toe of spillway, m/sec, α is kinetic correction coefficient for turbulent flow and it is generally equal to 1.1 according to (**Chen, et al., 2002**), g is acceleration due to gravity, m/s^2 , E_0 is upstream energy, m, E_1 is downstream energy, m, and $\frac{\Delta E}{E_0}$ is relative energy dissipation (R.E.D) between upstream and downstream of stepped and flat sloped spillway, %.

3. MATERIALS AND METHODS

3.1. Laboratory Flume and Stepped Spillway Models

The experimental work was performed using a flume at the hydraulic laboratory, college of Engineering, Al- Mustansiriyah University. The flume is a rectangular with a length of 5 m, width of 30 cm, and depth of 30 cm as shown in **Fig.1**. A sharp crested weir with a height of 2.5 cm was installed at the end of flume to obtain required flow condition. Discharges were measured by a calibrated flow meter installed at the channel outlet and the maximum discharge of the flume was $0.05m^3/sec$. The upstream flow heads were initiated to measure at a location more than $(9 y_c)$ upstream of the spillway model, where y_c is the depth of water over the spillway crest. Using an accurate point gauge reading to 0.1 mm, the water surface levels were measured at different locations. A large sump tank was constructed beside the flume and above the laboratory floor. Water was stored in this tank and pumped to the flume through a 10cm pipe. A manually operated valve, installed on the circulation system pipe, was utilized to control the flow discharge.

Chow, 1959 and **Henderson, 1966** presented the crest length and radius of curvature of upstream face as:

$$\frac{L_{crest}}{H_T - h_c} > 1.5 - 3 \quad (4)$$

$$R = 0.2(H_r - h_e) \quad (5)$$

where L_{crest} is the broad crested weir length, cm, H_r is upstream total head above the channel bed, cm, h_e is the weir height above the channel bed, cm, and R is the radius of curvature of upstream face.

In this study, the height of all models used was constant and equal to 60 % of the flume height (i.e. 18 cm). All spillways were installed at distance of 0.75 m from the flume entrance to eliminate turbulence flow. One angle ($\theta = 30^\circ$) of the spillway faces were used for each model. These angles are equal or greater than the critical value as defined by **Chanson, 1994** of $\theta = 27^\circ$. The installation allows mainly observing the different flow regimes. The maximum upstream head above bed channel was 26 cm, and the height of spillways that was considered in this work was 18 cm. Therefore, the length of crest was about 15 cm from using equation 4 and the upstream edge radius of all spillways was 2 cm using equation 5 to prevent separation of stream flow from the crest. Five models were constructed from concrete and utilized in this study as shown in **Fig.2** and **Table 1**.

For each model ten runs were utilized to measure the following parameters: the discharge (Q), upstream flow depth (y_0), critical flow depth over spillway (y_c), and the downstream flow depth (y_1) for each run. Overall, 50 experiments were done, the hydraulic parameters of flow over the models were measured and the energy dissipation of flow were calculated.

3.2. Flow type limits

Normally, there are three types of flow in stepped spillway: nappe, transition, and skimming flows. The experimental results showed that the nappe flow was less than $8 \text{ m}^3/\text{h}$, while the skimming flow was larger than $24 \text{ m}^3/\text{h}$, **Table 2**. Both shape characteristic and the step surface quality were affecting the flow regime variation. **Fig.3** shows the three types of flow which was established in this study. From **Tables 1** and **2** the range of flow types for nappe flow was increasing when using rough surface with size (20-25) mm and cavitation at small discharges. Therefore, the efficiency of energy dissipation using these two cases was increased at small discharges.

3.3. The limits of transition flow

The limits of transition flow in this experimental application were observed. To govern these limits, the depth of water at spillway crest (y_c), and the spillway shape (which is the non-dimensional ratio, y_c / h , where h is the height of step) were considered in this study. **Table 3** represents the values of y_c / h for all models. **Table 4** indicated several authors who have taken this proposition into account in their researches. The maximum value of the ratio (y_1/y_c) which corresponds to the structures of this experiment is equal to 20.84. This value is remarkably less than the limit value of ($y_1/y_c < 35$) according to **Chafi, et al., 2010**.

4. RESULTS AND DISCUSSION

4.1. Energy dissipation analysis

The energy dissipation for the stepped spillway without any addition was analyzed according to experimental data. The relationship between discharge and relative energy dissipation (R.E.D) was shown in **Fig.4**. It could be observed that the R.E.D decreased when the discharge increased with a good fit of $R^2=0.97$ and inverse relation of $(R.E.D = 99.21e^{-0.03Q})$.

4.2. Roughed step with gravels

The main aim of this research was to increase the energy dissipation on stepped spillway with different roughed gravel sizes. Therefore, three cases were used which were the stepped roughed with gravel size (10-14) mm, roughed steps with size (14-20) mm, and roughed stepped with size (20-25) mm. In order to increase energy dissipation on stepped spillway, the steps of spillway was roughed with gravel size of (10 -14) mm having porosity of 41 % within the recommended range (38-41) % according to **Alghazali and Jasim, 2014**. **Figs. 5a** and **6a** showed the application of roughed steps and the relationship between discharges and relative energy dissipation with fit of goodness of $R^2=0.93$ and inverse relation of $(R.E.D = 105.80e^{-0.023Q})$, respectively.

The steps of spillway was also roughed with gravel size of (14 -20) mm having porosity of 40.5 % within the recommended range also in order to increase energy dissipation on stepped spillway. **Figs. 5b** and **6b** showed the application of roughed steps and the relationship between discharge and relative energy dissipation with fit of goodness of $R^2=0.95$ and inverse relation of $(R.E.D = 100.20e^{-0.017Q})$, respectively. The steps of spillway were roughed using gravel with size (20 -25) mm having porosity of 39.4 % within the recommended range. **Figs. 5c** and **6c** presented the application of roughed steps and the relationship between discharge and relative energy dissipation with fit of goodness of $R^2=0.97$ and inverse relation of $(R.E.D = 98.12e^{-0.015Q})$, respectively. In this study, the average ratio between gravel height and step height was 0.5.

4.3. Roughed steps with cavitation

As a novel of this study, the steps of spillway were cavedated using cavitation holes to increase the energy dissipation on stepped spillway. The average ratio between volume of cavitation and volume of each step was 0.12. **Figs. 7** and **8** presented the application of cavitation on steps and the relationship between discharge and relative energy dissipation with a good fit of $R^2=0.88$ and inverse relation of $(R.E.D = 126.44e^{-0.041Q})$, respectively.

4.4. Results analysis

As expected, the relative energy dissipation (R.E.D) was decreased when the discharge increased for all cases utilized in this study. **Fig.9** shows that the roughed steps with gravel (20- 25) mm have the maximum relative energy dissipation (R.M.S.E = 16.73) compared to other cases. **Al-Talib, 2007** found that stepped weirs were more efficient than flat sloped weirs and the maximum



energy dissipation ratio in stepped weirs was approximately 10 % higher than in flat sloped weirs due to roughed surface by stepped sloped in stepped spillway compared to flat one of flat sloped. Therefore, in this study the stepped spillways were more efficient by 26.73% than the flat sloped spillway of pervious researches. The results of this study lead to understand that when the size of gravel increased the relative energy dissipation was increased. The steps with cavitation have large efficiency of energy dissipation for small discharges but have the lowest efficiency for large discharges compared with all cases of steps including steps without any addition.

Mann-Whitney rank sum tests (**Mann and Whitney, 1947, Al-Madhhachi, et al., 2014**) were performed to determine statistical differences of relative energy dissipation (R.E.D) among all five models. The mean values, median values, standard deviation, standard error, and the difference between the 25th and 75th percentiles were informed for R.E.D of all five models as shown in **Table 5**. The results confirmed that the roughed steps with maximum gravel size of (20- 25) mm have the maximum relative energy dissipation compared to other models and there was significant statically differences among all models with P-value of less than 0.001 regarding to R.E.D values.

4. CONCLUSIONS

In this experimental study, an attempt to increase the relative energy dissipation over stepped spillway compared with flat sloped spillways using roughed steps with gravels have three different sizes and steps with cavitation. By a comparison with steps without any addition, the maximum energy dissipation occurred with larger gravel size for small and large discharges, and that led to increase relative energy dissipation by 26.73 % compared with flat sloped spillway and 16.73 % compared with stepped spillway without any addition. Using the ratio between heights of gravel to steps of 0.5, the R.E.D was increased to about triple compared with traditional spillways. On the other hand, the results showed that the cavitation has large energy dissipation for small discharges but have smaller energy dissipation for large discharges.

REFERENCES

- Alghazali, N.S., and Jasim S.M., 2014, *Experimental study on the limits of flow regimes for different configurations of stepped spillway*, Civil and Environment Research, Vol. 6 (6), pp (30-40).
- Al-Madhhachi, A.T., Fox G. A., Hanson G. J., Tyagi A. K., and Bulut R., 2014, *Detachment rate model for the erodibility of cohesive soils due to fluvial and seepage forces*, J. Hydraulic Eng., ASCE, Vol. 140 (5), 10.1061/(ASCE)HY.1943-7900.0000836, 04014010.
- Al-Talib, A. J., 2007, *Laboratory study of flow energy dissipation using stepped weirs*, MSc., Engineering College, Mosul University, Iraq.
- Barani, G.A., Rahnama M.B., and Sohrabipoor N., 2005, *Investigation of flow energy dissipation over different stepped spillways*, AM J APPL SCI, Vol. 2 (6), pp (1101-1105).



- Chafi, C., Hazzab A., and Seddini A., 2010, *Study of flow and energy dissipation in stepped spillway*, Jordan Journal of civil engineering, Vol. 4 (1), pp (1-11).
- Chamani M.R., and Rajaratnam N., 1999, *Characteristic of skimming flow over stepped spillways*, Hydraulic Eng., ASCE, Vol.125, pp (361-367).
- Chanson, H., 1997, *Air bubble entrainment in free surface turbulent shears flows*, Academic Press, London, UK.
- Chanson H., 1994, *Comparison of energy dissipation Nappe and skimming flow regime on stepped chutes*, Journal of hydraulic research I.A.H.R., Vol. 32 (2), pp (213-218).
- Chen Q., Dai G., and Liu H., 2002, *Volume of fluid model for turbulent numerical simulation of stepped spillway over flow*, Journal of Hydraulic Engineering, ASCE, Vol. 128 (7), pp (683-688).
- Chow, V. T., 1959, *Open-Channel Hydraulics*, McGraw- Hill Book Company.
- Degoutte, G., Peyras L., and Royet P., 1992, *Skimming flow in stepped spillways: Discussion*, Journal of Hydraulic Engineering, ASCE, Vol. 118 (1), pp (111-114).
- El-Jumaily K., and Al-Lami M.H., 2009, *Study of convenience of using stepped spillway in roller compacted dams (RCCD)*, Eng. And Tech. Journal, Vol.27 (16), pp (415-426).
- Essery, I.S., and Horner M.W., 1978, *The hydraulic design of stepped spillways*, CIRIA report, 3rd edition, London, UK.
- Henderson, F.M, 1966, *Open channel flow*, MACMILAN PUBLISHING CO. IN., NewYork.
- Kells, J.A, 1995, *Comparison of energy dissipation between nappe and skimming flow regimes on stepped chutes*, Journal of hydraulic research, I.A.H.R., Vol. 33 (1), pp. (128-134).
- Mann, H. B., and Whitney D. R., 1947, *On a test of whether one of two random variables is stochastically larger than the other*, Annals of Mathematical Statistics, Vol.(18), pp. (50-60).
- Matos, G., and Quintela A., 1995, *Flow resistance and energy dissipation in skimming flow over stepped spillways*, Journal of hydraulic research, I.A.H.R., Vol. 33(1), pp (135-139).
- Novak, P., Maffat A.I., and Narayanan R., 1990, *Hydraulic structures*, The academic division of uniwin, Ltd.



- Rajaratnam, N., 1990, *Skimming flow in stepped spillways*, Journal of Hydraulic Engineering, ASCE, Vol. 16(4), pp. (587-591).
- Sabbagh-Yazdia, S., and Misaghiana M., 2016, *Effect of water infiltration through concrete block spillways on the slope stability of earth overflow dams*, European Journal of Environmental and Civil Engineering, DOI:10.1080/19648189.2016.1150898.
- Wuthrich, D., and Chanson H., 2015, *Aeration performances of a gabion stepped weir with and without capping*, Environmental Fluid Mechanics, Vol. 15(4), pp. (711-730).
- Yousefian, H., 1996, *Hydraulic design of Labyrinth spillways based on the physical model*, M.Sc. Thesis, Isfahan University of Technology, Iran.
- Zhang, G., and Chanson H., 2016, *Gabion Stepped Spillway: Interactions between Free-Surface, Cavity, and Seepage Flows*, J. Hydraul. Eng., ASCE, Vol. 142(5), 10.1061.

Table 1. Characteristics of the five step spillway models.

Step spillway cases	without addition	gravel (10-14) mm	gravel (14-20) mm	gravel (20-25) mm	cavitation
Model No.	1	2	3	4	5

Table 2. Flow type limits.

Step cases	Limit of flow
Stepped without addition	- Nappe ≤ 8.3 m ³ /h - transition ($8.4 \leq Q \leq 18$) m ³ /h - skimming ($Q \geq 18.1$) m ³ /h
Roughed with gravel size (10-14) mm	- Nappe ≤ 8.2 m ³ /h - transition ($8.3 \leq Q \leq 18$) m ³ /h - skimming ($Q \geq 18.1$) m ³ /h
Roughed with gravel size (14-20) mm	- Nappe ≤ 8.0 m ³ /h - transition ($8.1 \leq Q \leq 18$) m ³ /h - skimming ($Q \geq 18.1$) m ³ /h



Roughed with gravel size (20-25) mm	- Nappe ≤ 10 m ³ /h - transition ($10.1 \leq Q \leq 18$) m ³ /h - skimming ($Q \geq 18.1$) m ³ /h
Stepped with cavitation on surface	- Nappe ≤ 10 m ³ /h - transition ($10.1 \leq Q \leq 18$) m ³ /h - skimming ($Q \geq 18.1$) m ³ /h

Table 3. Values of ratio (y_c / h) in this study.

Step case	values of y_c / h
Stepped without addition	0.5-0.73
Roughed with gravel size (10-14) mm	0.5-0.73
Roughed with gravel size (14-20) mm	0.5-0.71
Roughed with gravel size (20-25) mm	0.5- 0.69
Stepped with cavitation on surface	0.53-0.71

Table 4. Values of ratio (y_c / h) as recommended in pervious researches.

Authors	Essery et.al. (1978)	Rajaratnam (1990)	Degoutte (1992)	Chanson (1994)	Kells (1995)	Matos et. al. (1995)	Chafi (2010)
y_c / h	0.81	0.80	0.69	0.80	0.50	0.83	0.67

Table 5. Results from Mann-Whitney Rank Sum tests for differences among five models of R.E.D values. All tests were performed with $n = 10$.

Model type	Mean	Median	Standard Deviation	Standard Error	25% Percentiles	75% Percentiles	P-value
Without gravel	58.41	51.97	19.77	6.25	38.6	80.07	<0.001
Gravel (10-14) mm	67.38	69.34	18.05	5.71	49.04	85.48	<0.001
Gravel (14-20) mm	71.51	73.96	14.31	4.53	57.86	85.71	<0.001
Gravel (20-25) mm	73.18	75.07	12.78	4.04	60.05	85.89	<0.001
Cavitation	59.41	59.79	25.53	8.07	39.58	85.46	<0.001



Figure 1. Indoor flume with stepped spillway at Al- Mustansiriyah University Hydraulics Laboratory used for testing.

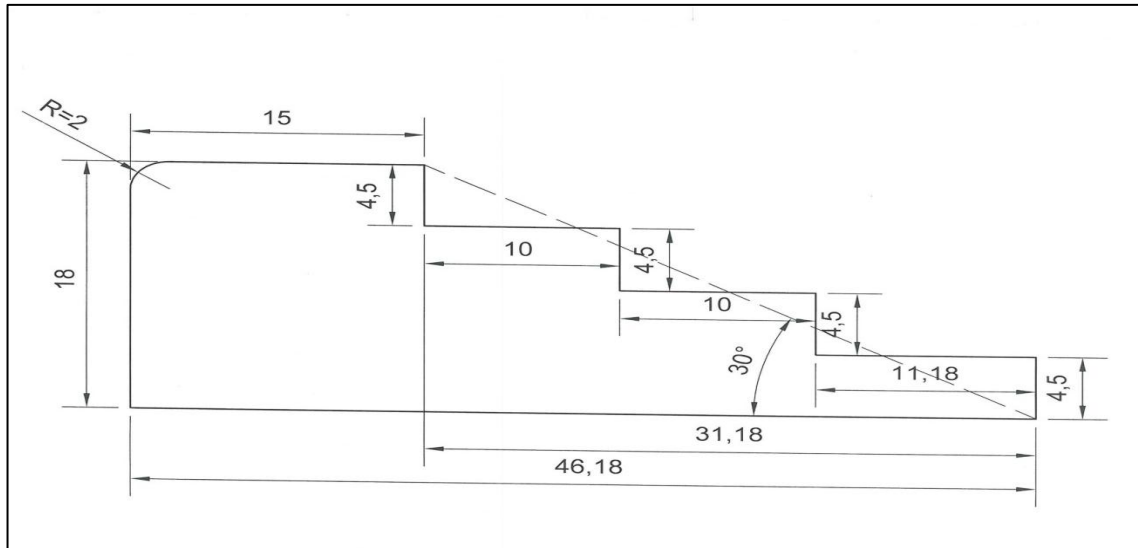
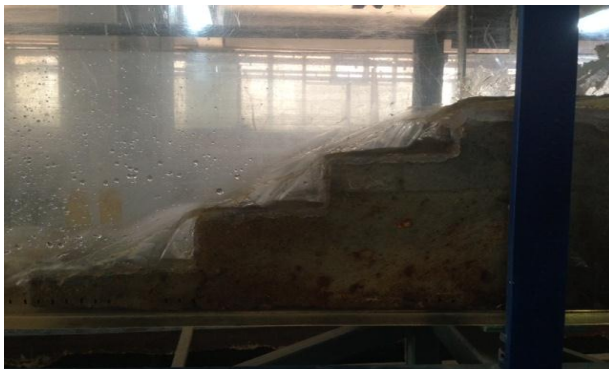


Figure 2. Dimension designs of five step spillway models.

a) Nappe flow

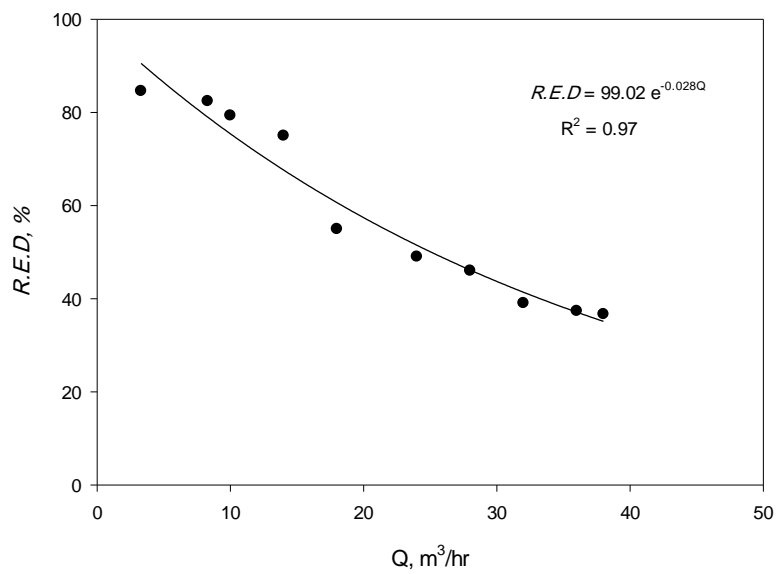


b) Transition flow





c) Skimming flow

Figure 3. Image of flow regimes: a) nappe flow, b) transition flow, and c) skimming flow.**Figure 4.** The R.E.D relationship of stepped spillway without addition.

a) Gravel size (10-14)mm

b) Gravel size (14-20)mm



c) Gravel size (20-25)mm



Figure 5. Stepped spillway provided with different gravel sizes: a) (10-14) mm, b) (14 -20) mm, and c) (20-25) mm.

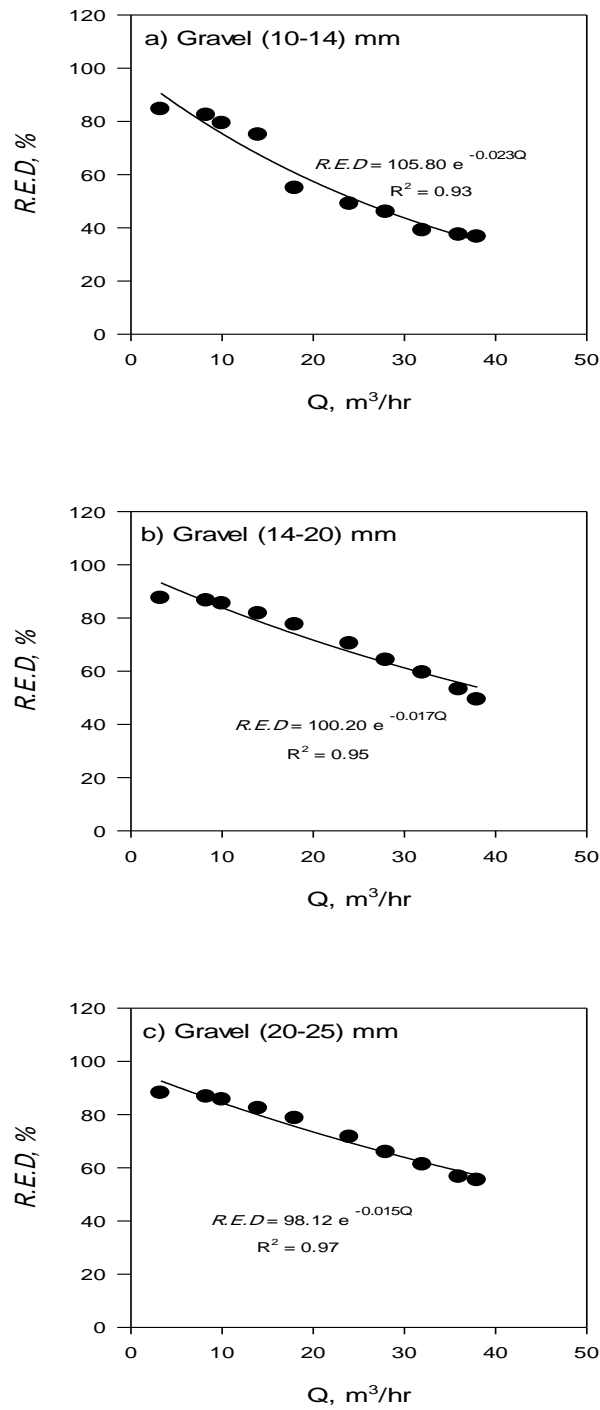


Figure 6. Relation between relative energy dissipation and discharges for Stepped spillway with different gravel sizes: a) (10-14) mm, b) (14 -20) mm, and c) (20-25) mm.



Figure 7. Stepped spillway provided with cavitation.

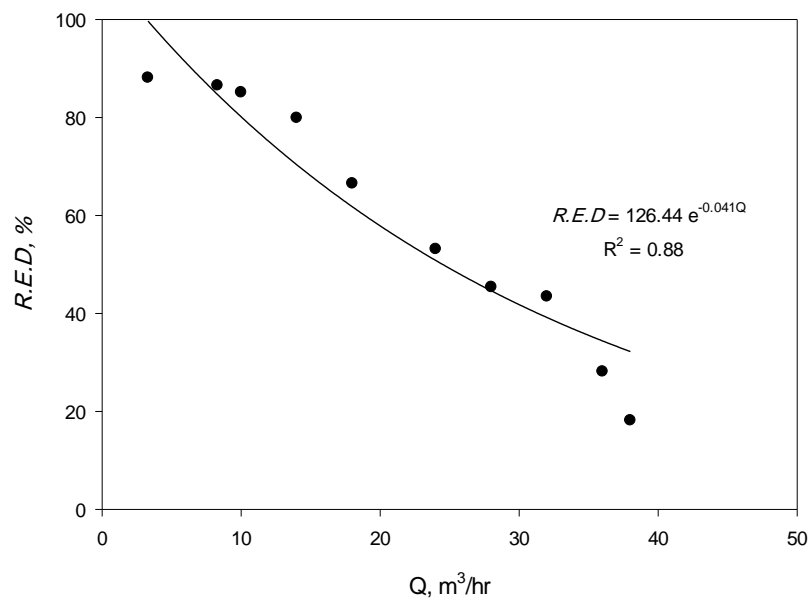


Figure 8. Relation between relative energy dissipation and discharges for stepped spillway with cavitation.

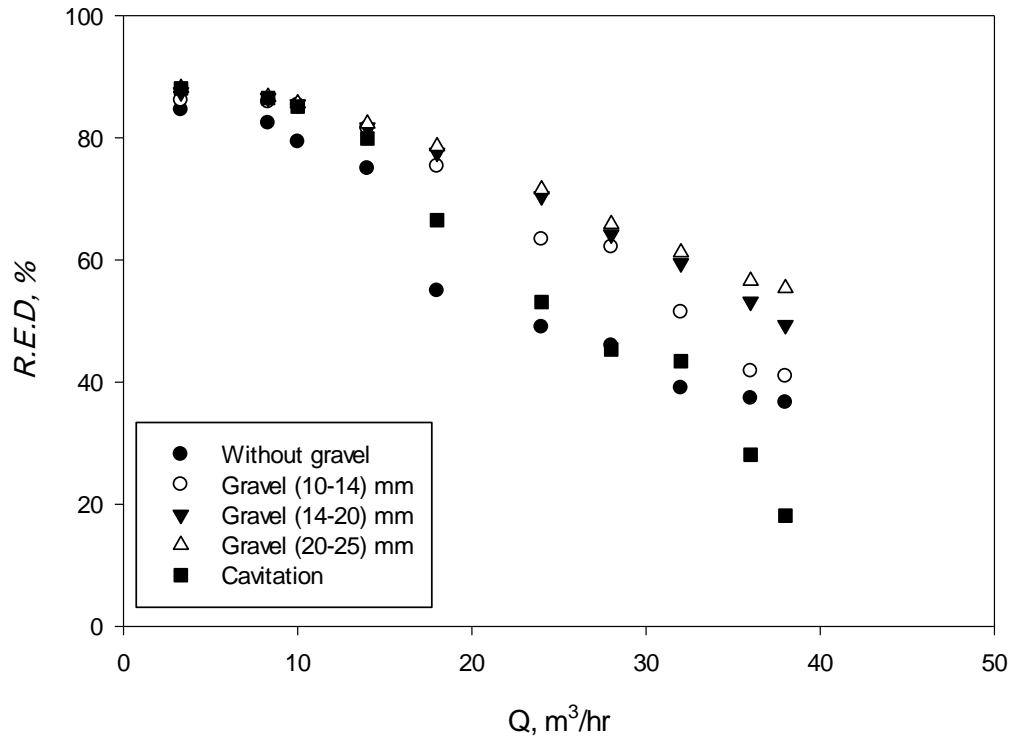


Figure 9. Relation between relative energy dissipation and discharges for five models.

A Hybrid Coefficient Decimation- Interpolation Based Reconfigurable Low Complexity Filter Bank for Cognitive Radio

Ibtihaj H. Qadoori

University of Baghdad/College of Engineering

Lectural Dr. Mahmood A.K. Abdulsattar

University of Baghdad/College of Engineering

ABSTRACT

Non uniform channelization is a crucial task in cognitive radio receivers for obtaining separate channels from the digitized wideband input signal at different intervals of time. The two main requirements in the channelizer are reconfigurability and low complexity. In this paper, a reconfigurable architecture based on a combination of Improved Coefficient Decimation Method (ICDM) and Coefficient Interpolation Method (CIM) is proposed. The proposed Hybrid Coefficient Decimation-Interpolation Method (HCDIM) based filter bank (FB) is able to realize the same number of channels realized using (ICDM) but with a maximum decimation factor divided by the interpolation factor (L), which leads to less deterioration in stop band attenuation (SA). The proposed architecture is able to realize a greater number of sub-bands locations. The proposed (HCDIM) based (FB) shows an inherent low complexity offered by the (CIM) technique when compared with the alternative FBs. The reduction in the number of multiplications is by 50.77% compared with ICDM in non-uniform channelization, while the reduction in the number of multiplications is about 59.64% over the discrete Fourier transform (DFTFB) and 31.19% over ICDM based FB in uniform channelization.

Key words: filter bank (FB), hybrid coefficient decimation-interpolation method (HCDIM), coefficient interpolation method (CIM), low complexity.

مجموعة مرشحات قائمة على هجين من معامل الهلاك ومعامل الاستيفاء المعاد تشكيلها والمنخفضة التعقيد

المدرس د. محمود عبد القادر عبد الستار
كلية الهندسة/جامعة بغداد

ابتهاج حميد قدوري
كلية الهندسة/جامعة بغداد

الخلاصة

تشاطر القنوات الغير منتظم مهمة حرجة في اجهزة الاستلام الراديوية المعرفية للحصول على قنوات منفصلة من اشارة ادخال رقمية الاتساع في فترات مختلفة من الزمن. المتطلبين الرئيسيين في شاطر القنوات هي اعادة التشكيل وانخفاض التعقيد. هذا البحث يقترح بنية قابلة لاعادة الهيكلية فيها الجمع بين طريقة معامل الهلاك المتطورة وطريقة معامل الاستيفاء. هذه الطريقة المختلطة المقترحة قادرة على تحقيق نفس العدد من القنوات التي تتحقق باستخدام طريقة معامل الهلاك المتطورة ولكن باستخدام معامل هلاك مقسوما على معامل الاستيفاء، الامر الذي يؤدي الى تدهور اقل في توهين حزمة التوقف. الهيكل المقترح قادر على تحقيق عدد اكبر من الحزم الفرعية. مجموعة المرشحات القائمة على اساس الهيكل المقترح تظهر تعقيد اقل وانخفاض في عدد عمليات الضرب نتيجة لاستخدام طريقة معامل الاستيفاء فيه مقارنة بباقي المرشحات.

Cognitive Radio (CR) can offer competent utilization of the radio, electromagnetic spectrum. The Simple principle of CR is detecting the spectral occupancy over a wide frequency range permitting unlicensed users (called secondary users) to have adaptable access of the available frequency bands prearranged to licensed users (called primary users), **Ambede, et al., 2012**. The role of CR is to use those unused spectrum allocations when the primary (i.e., licensed) users are not present without additional license, by approving a concept of dynamic spectrum resource managing, **Powell, et al., 2003**. The ability of CR to precisely detect the spectrum usage status over a wide frequency range attending various wireless communication standards ensures its successful use **Park, et al., 2009**. In a usual CR, the non-uniform channels of various wireless standards simultaneously coincide in the input signal. The spectrum sensing block need to be used to observe these channels accurately and the distinct channels must to be extracted using the channelizer, so demanding the capability of implementing multi-standard channelization. Digital FBs show a significant role in channelization and spectrum sensing in the CRs. The frequency range of wideband input is divided into non-uniform or uniform sub-bands using FBs in FB-based spectrum sensing, and the existence of signals is then sensed using other techniques for example energy detection **Ambede, et al., 2015**. A low complexity reconfigurable Finite Impulse Response (FIR) filters were proposed in, **Vinod, and Mahesh, 2008**, using coefficient decimation method (CDM). Variable frequency responses can be generated using CDM by working upon stable filter coefficients using two coefficient decimation operations, one to change the pass-band width of the modal filter (named CDM-II) and another to produce multi-band frequency responses (named CDM-I). A real valued design algorithm for oversampled FIR FB of five channels even order filter banks is proposed in, **Chougule, and Patil, 2011**. The frequency bands and order of filter are selected which cause noise removal and reduction in amplitude distortion and in-band aliasing. This system is suitable for any image format. A Modified Coefficient Decimation Method (MCDM) was proposed in, **Vinod, et al., 2012**, to obtain reconfigurable FIR filters with improved frequency response flexibility and twice the center frequency resolution when related to the conventional CDM. A higher degree of reconfigurability can be provided using MCDM and the FIR filters obtained show less stop-band attenuation deterioration when compared with those obtained using conventional CDM, and have a lower complexity due to lower order modal filter in the MCDM. The modified CDM (MCDM-II) was combined with the conventional (CDM-II) in, **Ambede, et al., 2012**, to design a new channel filter, the new method termed as improved coefficient decimation method II (ICDM-II), in which the channel filter has a considerably lower complexity when compared to other channel filters based on CDM, **Mahesh, and Vinod, 2011**. A combination of MCDM-I and the conventional CDM-I is presented in, **Ambede, et al., 2014**, to employ uniform FB which is termed as the Improved coefficient decimation method I (ICDM-I). After performing ICDM-I operations on the modal filter, the desired sub-bands can be extracted from the multi-band frequency responses obtained, using low order wide transition bandwidth (TBW) frequency response masking (FRM) filters. The ICDM-I, ICDM-II and (FRM) technique are combined in, **Ambede, et al., 2014**, and named as an improved coefficient decimation method (ICDM). The ICDM eliminates the least common divisor LCM constraint in, **Ambede, et al., 2012**, as the compensation in group delay is not required because the filters resulting after performing ICDM-I operations have the similar filter order. But the transition bandwidth (TBW) is the minimum standard TBW divided by the decimation factor corresponds to that standard, which leads to a narrow TBW and higher order modal filter with increasing value of decimation factor. In this paper, a hybrid combination of ICDM and the CIM digital FB is proposed to serve uniform and non-uniform channelization. Using the proposed architecture (named HCDIM); the desired sub-bands extracted using Frequency Response asking (FRM) technique can be obtained. The

procedure starts by inserting zero coefficients between every two coefficients of the modal filter and then applying the CDM on the resulting filter. In the proposed HCDIM-based FB, the overall sharp transition-band filter can be composed using wider transition-band modal filter by using the CIM technique. Hence, it offers inherent low complexity features. The number of the resulting sub-bands represents the product of the interpolation factor and the decimation factor; i.e. a particular sub-band can be obtained using smaller decimation factor than that used in ICDM method. The deterioration in the stop-band attenuation increases with increasing the decimation factor. As the decimation factor is reduced in the proposed approach, the stop-band deterioration is reduced too, i.e. less filter order. The HCDIM-based FB also has a higher flexibility of $\pi/(M \times L)$ in terms of the possible number and locations of its sub-bands when compared with the other FBs in the literature.

Outline of the Paper: In Section 2, a revision of coefficient decimation, the improved coefficient decimation method and an explanation for the coefficient interpolation method is presented. In Section 3, the proposed HCDIM-based FB is presented with the design steps of the proposed FB for various channelization scenario situations. The design examples are involved in section 4 as well as the complexity comparison of the HCDIM-based FBs designed using our method with that of the ICDM-FB designed for the same required conditions. A performance comparison in terms of pass-band ripple and stop-band attenuation of final filter and the flexibility of the proposed FB is presented in the same section. The conclusion is given in Section 5.

2 COEFFICIENT DECIMATION, IMPROVED COEFFICIENT DECIMATION METHOD AND COEFFICIENT INTERPOLATION METHOD

In the conventional CDM, **Vinod, and Mahesh, 2008**, if the coefficients of a low pass modal filter are decimated by a decimation factor M , i.e., reserving every M th coefficient and substituting the others by zeros, the resulting FIR filter will be a multi-band uniform sub-band bandwidth (BW) frequency response. The resultant center frequency locations of the sub-bands are given by $2\pi k/M$, where k is an integer ranging from 0 to $(M - 1)$. If $H(e^{j\omega})$ represents the Fourier transform of the modal filter coefficients, then the Fourier transform of the resulting filter coefficients is given by:

$$H(e^{j\omega}) = \frac{1}{M} \sum_{k=0}^{M-1} H(e^{j(\omega - \frac{2\pi k}{M})}) \quad (1)$$

This process is called CDM-I. After performing CDM-I by decimation factor M , if all the reserved coefficients in the resulting filter are collected together by removing the intermittent zeros, a low pass frequency response is obtained with its pass band and transition band widths M times that of the modal filter. This operation is called CDM-II.

When the coefficients of the modal filter are decimated by M , every M th coefficient is reserved and the sign of every alternative reserved coefficient is reversed. All the other filter coefficients are substituted by zeros. This operation is called the modified coefficient decimation method I (MCDM-I), **Ambede, et al., 2012**, and gives an FIR filter with a multiband frequency response with center frequencies of the sub-bands given by $(2k+1)\pi/M$. The Fourier transform of the resulting filter coefficients is represented by:

$$H(e^{j\omega}) = \frac{1}{M} \sum_{k=0}^{M-1} H(e^{j(\omega - \frac{\pi(2k+1)}{M})}) \tag{2}$$

A high pass frequency response of a pass band and TBWs M times that of the modal filter can be obtained after grouping all the reserved coefficients in the MCDM-I together and removing the intermittent zeros. This operation is termed as MCDM-II.

It can be noted from Eq. (1) that the center frequency locations of the achievable sub-bands after performing CDM-I operations are even multiples of π/M , while the center frequency locations from Eq. (2) are odd multiples of π/M using MCDM-I operations. The ICDM-I is a combination of CDM-I and MCDM-I, and the ICDM-II is a combination of CDM-II and MCDM-II. A combination of ICDM-I and ICDM-II is performed in ICDM, **Ambede, et al., 2014**. In all ICDM operations, the order of the desired modal FIR filter (N) can be obtained using, **Bellanger, 1982**:

$$N = -\frac{4 \log_{10}(10 * \delta p * \delta s)}{3(f_s - f_p)} - 1 \tag{3}$$

where f_p is the desired pass band frequency and f_s is the desired stop band frequency (normalized in the range 0–1, with 1 corresponding to the Nyquist frequency) and δp is the desired pass band peak ripple and δs is the desired stop band peak ripple.

It can be noted that the increase in the value of M causes a deterioration in stop band attenuation (SA) of the resulting filters, **Vinod, and Mahesh, 2008**, and its mathematical expression is:

$$\delta_{s(mod)} = \frac{\delta_{s(final)}}{M} \tag{4}$$

where $\delta_{s(mod)}$ is the SA of the modal filter, and $\delta_{s(final)}$ is the SA of the resulting filter after performing a CDM and MCDM operations by M . The deterioration in SA can be overcome by overdesigning the modal filter. If a CDM is performed by a factor of M to a filter, the SA of the resulting filter can be kept within desired value δs from Eq. (3) and Eq. (4), and the minimum order of the overdesigned modal filter can be calculated using:

$$N = \left[-\frac{4 \log_{10}(10 * \delta p * \delta s)}{3(f_s - f_p)} - 1 \right] + \frac{4 \log_{10} M}{3(f_s - f_p)} \tag{5}$$

The second term in Eq. (5) represents the rise in order of the overdesigned modal filter essential to compensate the SA deterioration happened after performing coefficient decimation method by M .

On the other hand, the Coefficient Interpolation Method (CIM) is an efficient technique to synthesize FIR filters with sharp transition bands, using wide transition-band filter with low complexity since the resulting filter will have many sparse coefficients, **Mahesh, and Vinod, 2007**. Suppose a low-pass modal filter $H_a(z)$ of order N , its frequency response can be shown in **Fig. 1 (a)**. If $(L - 1)$ zeros are added between every two coefficients of $H_a(z)$, which is equivalent

to replacing each delay element of $H_a(z)$ by L delays, then the resulting L subbands of $H_a(z^L)$ are factor of L narrower than that of $H_a(z)$ as shown in Fig 1.b, where L is the interpolation factor. The resulting L multiband will lie on $(2\pi k)$ where $(k = 0, 1, \dots, L-1)$. If the pass band edge and the stop band edge of the modal filter is f_p and f_s respectively as can be shown in Fig. 1 (a), then the pass band edge, and the stop band edge of the resulting sub-band after performing (CIM) is $\frac{f_p}{L}$, $\frac{f_s}{L}$ respectively as shown in Fig. 1 (b).

3 PROPOSED FILTER BANK

In this paper, a method to realize reconfigurable, low complexity filter bank based on combined decimation, interpolation and frequency response masking is proposed. The proposed architecture consists of three stages. The first stage is the design of modal filter. The second stage is interpolation by the L factor. The third stage is decimation by the M factor, resulting in an $(M \times L)$ sub-bands. The desired channels are extracted by using suitable masking filters to mask the unwanted channels. The complexities of the masking filters are low, as they have large TBWs. The principle of (FRM) was originally introduced in, **Lim, 1986**. The (HCDIM) proposed in this paper offers two grades of freedom, M and L . Therefore, this method pointedly improves the filter architecture flexibility and reduces the coefficient decimation factor M that used to extract the same channels number that extracted in ICDM. The number of extracted channels in the proposed method is $(M \times L)$.

The HCDIM operations are further clarified with the help of a descriptive example. Consider the modal filter in Fig. 2 (a) that has a pass band frequency of 0.12, and a stop band frequency of 0.132. The peak pass band ripple is selected as 0.1 dB, whereas, the stop band attenuation of the filter is selected as -50dB. Fig. 2 (b) represents the modal filter frequency response after interpolation by a factor of $(L=3)$ i.e. by inserting $(L-1=2)$ zeros between modal filter coefficients. It can be noted from Fig. 2 (b) that the resulting filter has a transition band width narrower by a factor of 3 than that of modal filter. Figures 2 (c) to 2 (g) show a few of the frequency bands that can be achieved after performing CDM on the interpolated modal filter. Figure 2 (c) represents the frequency response achieved after performing MCDM-II on the frequency response of Fig. 2 (b), using $M=4$. Fig. 2 (d) represents the frequency response achieved when performing CDM-I on a modal filter interpolated by $L=2$, using $M=3$. Fig. 2 (e) represents the frequency response resulted after performing both MCDM-I and CDM-I on the frequency response of Fig. 2 (b), using $M=2$. Fig. 2 (f) represents the frequency response achieved after performing both MCDM-I and CDM-I on the frequency response of Fig. 2 (b) using $M=3$. Fig. 2 (g) represents the frequency response achieved after performing both MCDM-I and CDM-I on the frequency response of Fig. 2 (b) using $M=4$. It can be noted that the number of resulting sub-bands in Figure 2 (d) to 2 (g) are 6, 6, 9, 12 respectively, which represent the product of the decimation factor and the interpolation factor. It can be observed that the number of distinct sub-bands is increased and the flexibility of the location of center frequency is enhanced. As can be seen in Fig. 2 (e), (f) and (g), the frequency responses obtained for CDM and MCDM are mirror images of each other. The modal filter used in this example has a normalized stop band frequency $f_s = 0.132$. Therefore, M values greater than $\lceil 1/0.132 \rceil = 7$ will

cause aliasing and cannot be used in the coefficient decimation operations. The maximum decimation factor allowed in coefficient decimation operations after performing CIM ($L = 3$) in HCDIM approach is $\lceil 1/0.044 \rceil = 22$. According to formula advanced by Bellanger Eq. (3), the order of the modal filter is (457) and the over designed filter order is (524). The resulting filter after interpolation has specifications of ($f_p = 0.04$ and $f_s = 0.044$) as shown in **Fig. 2** (b). A filter of order (1374) should be used to obtain such sharp TBW, and the over designed filter order is (1441). Thus, this type of filter bank offers an inherent reduction in the complexity as can be further explained in multiplication complexity comparison in the design example.

To achieve the proposed FB for different applications, the design steps which are similar to that described in, **Ambede, et al., 2014** are used with some modifications in steps three, four and six concerned with the use of CIM in the proposed FB. Let the different communication standards be sampled at sampling frequency f_{sam} . Their bandwidths are BW_1, BW_2, \dots, BW_m , where m represents the number of standards. The TBW specifications are $TBW_1, TBW_2, \dots, TBW_m$. The desired passband peak ripple specifications and stopband attenuation specifications for the channels of m standards are $\delta_{p1}, \delta_{p2}, \dots, \delta_{pm}$ and $\delta_{s1}, \delta_{s2}, \dots, \delta_{sm}$, respectively. The steps for extracting m different communication standards simultaneously using the proposed HCDIM-based FB are as follows:

Step one: All channel BW and TBW specifications should be normalized to $f_{sam}/2$.

Step two: Divide the pass-BW of each standard by 2.

Step three: Recognize the interpolation factor L required to perform CIM on the modal filter for obtaining suitable sharp transition bandwidth.

Step four: Calculate the modal filter's pass band width (BW_{mod}) as the greatest common divisor (GCD) of the pass band widths obtained in step two multiplied by L .

$$BW_{mod} = \text{GCD} \left\{ \frac{BW_1}{2}, \frac{BW_2}{2}, \dots, \frac{BW_m}{2} \right\} * L \tag{6}$$

Step five: Specify the decimation factors required for performing ICDM-II operations on the modal filter or the interpolated modal filter to get low and high pass frequency responses corresponding to the channel bandwidths of the m standards. These values is identified as D_1, D_2, \dots, D_m .

Step six: Calculate the new TBW of each standard by dividing the TBW of each standard by its corresponding D . The TBW of the modal filter (TBW_{mod}) is the minimum of the computed values multiplied by L .

$$TBW_{mod} = \min \left\{ \frac{TBW_1 * L}{D_1}, \frac{TBW_2 * L}{D_2}, \dots, \frac{TBW_m * L}{D_m} \right\} * L \tag{7}$$

Step seven: The set of decimation factor value used in HCDIM-I operations should be identified to obtain frequency responses which are used to extract the wanted channels in the filter bank. The value of maximum decimation factor is indicated as M_{max} .

Step eight: The stop band attenuation of the modal filter δ_{smod} is the minimum of the new SA for each standard:

$$\delta_{smod} = \min \left\{ \frac{\delta_{s1}}{D_1 * M_{1max}}, \frac{\delta_{s2}}{D_2 * M_{2max}}, \dots, \frac{\delta_{sm}}{D_m * M_{mmax}} \right\} \tag{8}$$

The peak pass band ripple of the modal filter (δ_p) is the minimum of the m standards.

Step nine: The modal filter order corresponding to the obtained specifications is calculated using Eq. (3). The HCDIM processes are performed on the modal filter with the specified values of interpolation and decimation factor to obtain the corresponding frequency responses. The design examples in the next section will make the above steps applicable.

4 DESIGN EXAMPLES

Two design examples are presented here to compare the proposed methodology with the previously used approaches. The modal filter and the masking filters in both design examples are designed using equiripple (Parks-McClellan algorithm) transposed direct-form FIR filter technique. The maximum error between desired frequency response and actual frequency response is minimized in equiripple technique by spreading the approximation error uniformly over each band, **Kumer, et al., 2015**. The transposed direct-form FIR filter structure is that exploits the property of filter coefficients symmetry. This type of implementation is preferred because extra shift register for input signal is not needed and extra pipeline stage for the adder of the products to achieve high throughput is not needed.

4.1 Fixed Channel Stacking Channelization

The proposed HCDIM-based FB is used in this section, to extract uniform sub-bands using a design example to compare with other FBs used which is the same design example used in the ICDM and DFTFB-FB that consists of 8-channel whose output frequency response is as shown in **Fig. 3**. The prototype filter has a frequency edges similar to those of sub-band one (sb1). The pass band frequency is $f_p = 0.1125$, and the normalized stop band frequency is $f_s = 0.1375$. The desired pass band peak ripple is 0.1 and the desired stop band peak ripple is -40 dB. The order of the prototype filter is 160 according to Eq. (3). To obtain the desired 8-point DFTFB, the prototype filter has to be followed by an eight-point IDFT process. In the proposed HCDIM based FB, the pass band and the stop band frequencies of the modal filter are different from those of the prototype filter used in DFTFB and the modal filters used in ICDM designs. As the CIM is used in the proposed approach so the pass band and stop band edges of the modal filter are of factor L wider than that of the prototype filter and the modal filters used in the former methods designs. In order to extract the five sub-bands in **Fig. 3**, the modal filter pass band and stop band frequencies should be multiplied by L .

Let the interpolation factor L be 2, the corresponding pass band and stop band frequencies are ($f_p = 0.1125 \times 2 = 0.225$) and ($f_s = 0.1375 \times 2 = 0.275$) respectively. Using the same peak pass band ripple and stop band ripple used in DFTFB, CDM and ICDM of 0.1dB and -40 dB, respectively. The order of the new modal filter is (80) using Eq. (3). The maximum decimation factor elaborated in the HCDIM design is 4 and the equivalent overdesigned order of the modal filter using (5) is 97. Different stages of the HCDIM-FB are shown in **Fig. 4** and the associated frequency responses of the output. **Fig. 4** (a) represents the frequency response of the modal filter. **Fig. 4** (b) represents the frequency response of the modal filter after performing CIM on the modal filter by a factor of $L = 2$. Sb1 can be extracted after masking the frequency response of **Fig. 4** (b) by a wide transition band width low order ($N=4$) low pass masking filter 1 (MF1) ($f_p = 0.1125$, $f_s = 0.8625$). Sb5 can be obtained by masking the same frequency response by a wide transition band width low order ($N=4$) high pass masking filter (MF5) ($f_p = 0.8875$, $f_s = 0.1375$). **Fig. 4** (c) represents the frequency response resulted when MCDM-I is performed on the interpolated modal filter with $M = 2$, which gives the desired band sb3. Sb2 and sb4 are obtained from **Fig. 4** (d), which represents the frequency response after performing MCDM-I

using $M = 4$ on the response of **Fig. 4** (b). Sb2 and sb4 can be extracted by using wide TBW low order ($N=18$) masking filter 2 (MF2) ($f_p = 0.3875, f_s = 0.6125$) and masking filter 4 (MF4) ($f_p = 0.6125, f_s = 0.3825$). Thus, the five desired sub-bands can be obtained using the proposed HCDIM-FB. The maximum decimation factor elaborated in the design of the proposed HCDIM-FB is 4. Sb2 and sb4 can be separated by the same masking filters used in CDFB and ICDM designs should be used for reasonable comparison. The masking filters used to extract sb1 and sb2 are particular in the proposed FB only. In this design example, the order of the modal filter can be further reduced if a higher L is used. For example, let $L = 4$, the frequency specification of the modal filter will be ($f_p = 0.1125 \times 4 = 0.45$) and ($f_s = 0.1375 \times 4 = 0.55$). The frequency response of such filter is shown in **Fig. 5** (a). **Fig. 5** (b) represents the frequency response of the modal filter after performing CIM, using $L = 4$, which is similar to the frequency response obtained after performing CDM-I on the interpolated modal filter using $M=4$. The three low-order masking filters (as shown in **Fig. 5** (b)) are employed to extract the three sub-bands, MF1 ($f_p = 0.1375, f_s = 0.625$), MF3 ($f_{p1} = 0.3625, f_{s1} = 0.0.1375, f_{p2} = 0.6375$ and $f_{s2} = 0.8625$) and MF5 ($f_p = 0.8625, f_s = 0.6375$). **Fig. 5** (c) represents the frequency response obtained after performing MCDM-I, using $M=4$ on the interpolated modal filter which represents sb2 and sb4. Two masking filters (as shown in **Fig. 5** (c)) similar to those used in the previous example are required to extract sb2 and sb4. It can be noted that sb1, sb3 and sb5 can be extracted using appropriate masking filters after performing CIM, using $L = 4$ without using the decimation method. But this means that upsampling operation is not followed by downsampling operation which leads to increasing sampling frequency. The modal filter order used in this example is 39 according to Eq. (3). The maximum decimation factor elaborated in the HCDIM design in this example is 4 and the equivalent overdesigned order of the modal filter using Eq. (5) is 41. In contrast to just 1 maximum decimation factor involved in modal filter of **Fig. 5** (a), the involved maximum decimation factor is 7, using the HCDIM design technique. It can be noted that using a higher value of L ($L = 4$), additional masking filter to extract sb3 (MF3), and higher order masking filters to extract sb1 and sb5 are required. Thus, using larger values of L , narrower TBWs masking filters need to be designed, which may increase the complexity and lead to inefficient implementation.

The complexity of the proposed FB (which depends on the number of multiplication operations involved) and various FBs designed to serve uniform channelization, is summarized in Tab. 1. The length of N order FIR filter (represented as l) can be calculated as $l = N + 1$, **Proakis, and Manolakis, 2007**. The total multiplications number in the DFTFB is the sum of the prototype filter length (l_p), and the multiplications number needed for an 8-point fast Fourier transform (FFT) computation ($S \log_2 S$ multiplications for S -point FFT, **Proakis, and Manolakis, 2007**, used in S -channel DFTFB, **Vaidyanathan, 1990**). The modal filter and masking filters used in both these FBs are implemented with the transposed direct-form FIR filter structure, exploiting the coefficients symmetry property. Let the modal filter and masking filter lengths, be denoted as l_{Mod} and l_{Mas} , respectively. Using the transposed direct-form FIR filter structure, the number of multiplications required to modal filter and masking filter implementation are $(l_{Mod}/2)$ and $(l_{Mas}/2)$, respectively, **Vaidyanathan, 1990**. The complexities of multiplication ICDM and HCDIM-based FB are lower than that of the DFTFB because of using transposed direct-form FIR filter structure for implementation of the modal filter. It can be noted from the design example described in this section that as the proposed FB employs both CDM and CIM operations, the modal filter essential in the proposed HCDIM-based FB has a lower order than the modal filter essential in the ICDM-based FB. From **Tab. 1**, it can be noted that the proposed HCDIM based FB, using $L = 2$, offers a reduction in multiplication

complexity of 59.46% over DFTFB, and 31.19% over ICDM based FB, while the reduction in complexity using $L = 4$ is about 63.24% over DFTFB and 37.61% over ICDM based FB. It can be observed that in, **Ambede, et al., 2015**, the maximum value of the decimation factor involved is less than that used in the proposed HCDIM-FB due to the use of complementary delays approach to perform sb2 and sb4. If this approach is applied in our proposed design method, the corresponding over designed modal filter order will be reduced and the percentage reduction in multiplication will be enhanced. Thus, for the same modal filter specifications, the worst SA value observed in the ICDM based design is half of that detected in the HCDIM based approach having the same TBW.

4.2 Multi-Standard Channelization

In this section, the capability of the proposed HCDIM-based FB to perform multi-standard channelization is confirmed and demonstrated. The frequency response of an input spectrum is shown in **Fig. 6**. In this figure, four Bluetooth (BT) channels, one Zigbee channel, and one wideband code division multiple access (WCDMA) channel are simultaneously existing at different locations in the wideband frequency range.

The channel bandwidths of BT, Zigbee and WCDMA standards are 1, 4, and 5 MHz, respectively, and their corresponding transition bandwidth specifications are chosen as 50, 200, and 500 KHz, respectively. The sampling frequency is chosen as 40 MHz. The desired pass band and stop band peak ripple specifications for Zigbee and WCDMA channels are 0.1 and -40 dB, and for BT channels 0.1 and -55 dB, respectively. According to design steps described in section 5, an HCDIM-based FB can be used to obtain the different channels shown in **Fig 6**. According to step one, the normalized channel BWs of BT, Zigbee, and WCDMA are computed to be 0.05, 0.2, and 0.25, respectively. Let the interpolation factor (L) be 2. The GCD of $\{0.05, 0.2, 0.25\}$ is obtained as 0.05 which represents the pass-BW of the modal filter according to Eq. (6) in step four. The decimation factor values required to achieve the low pass and high pass frequency responses with their pass bandwidths corresponding to the channel BWs of the three standards are $D1 = 1$, $D2 = 2$, and $D3 = 5$, according to step 5. The TBW of modal filter is then calculated to be 0.005 using Eq. (7) in step six. The pass band and stop band edge frequency specifications of the modal filter are chosen as $f_p = 0.045$ and $f_s = 0.05$, respectively. The three sets of decimation factor value to be used in HCDIM operations to obtain the sub-bands corresponding to the three standards are $\{5\}$, $\{2\}$, and $\{1\}$, respectively, according to step seven. The pass band and stop band attenuation specifications are obtained according to step eight as 0.1 dB and -60 dB, respectively. The modal filter is designed with the calculated specifications values and the equivalent filter order is 1396 using Eq. (3). Suitable HCDIM operations are performed on the designed modal filter using the recognized values of decimation factor. The frequency responses of each stage in the HCDIM-based FB is shown in **Fig. 7**. **Fig. 7 (a)** represents the frequency response of the modal filter after performing CIM, using $L = 2$. Then CDM-I is performed on the interpolated modal filter using $M = 5$ to obtain the frequency sub-band corresponding to the BT2 as shown in **Fig. 7 (b)**. To extract channel BT2 from the multiband frequency response obtained, a masking filter (MF2) of order 39, designed according to Eq. (3). To extract BT1, BT3, and BT4 channels, perform MCDM-I using $M = 5$ on the modal filter, as shown in **Fig. 7 (c)**. Three masking filters of the low order 39 (MF1, MF3 and MF4) are used to extract the three channels. The WCDMA channel is extracted using the frequency response obtained after performing MCDM-II on the modal filter using $M = 5$ as shown in **Fig. 7 (d)**. To obtain Zigbee sub-band channel, perform CDM-II on the modal filter using $M = 2$ as shown in **Fig. 7 (e)**, then

perform MCDM-I using $M = 2$ on the resulting filter to get Zigbee sub-band as shown in **Fig. 7** (f). Hence, all the BT, Zigbee and WCDMA standards channels which are simultaneously existing in the input signal can be extracted using the proposed FB. A block diagram that summarizes various stages in HCDIM-based FB is shown in **Fig. 8**.

Since the bandwidths of Zigbee and WCDMA standards are not integer multiples of each other, the multiple FBs need to be designed in both the MPRB and the CMFB approaches to extract the different frequency channels in **Fig. 6**, **Ambede, et al., 2014**.

It can be noted that if ICDM-FB is used to extract the different frequency channels in **Fig. 6**, the channel BT2 can be obtained after performing CDM-I using $M = 10$. The rest BT channels can be obtained after performing MCDM-I using $M = 10$. All BT channels can be extracted by means of the proposed HCDIM-based FB using CDM-I and MCDM-I at $M = 5$, which is half the M value required in the ICDM-FB case. In this design example, the order of the modal filter can be further reduced if a higher L is used. For example, let $L = 5$, the frequency specification of the modal filter will be ($f_p = 0.0225 \times 5 = 0.1125$) and ($f_s = 0.025 \times 5 = 0.125$). The frequency response of such filter is shown in **Fig. 9** (a). **Fig. 9** (b) represents the frequency response of the modal filter after performing CIM, using $L = 5$. To extract BT channels, perform CDM-I, using $M=2$ to obtain a frequency response similar to that of **Fig. 7** (b), then perform MCDM-I, using $M=2$, to obtain a frequency response similar to that of **Fig. 7** (c). To extract the Zigbee channel, an MCDM-I on the modal filter, using $M=2$, is performed. Perform CIM on the modal filter, using $L = 2$ and then perform CDM-II, using $M=5$ to extract WCDMA channel. According to design steps in Section 5, the stop band attenuation is -60, and the corresponding modal filter order is 531.

It can be noted that while the order of a modal filter is 1396, 531, using $L = 2$ and 5 respectively, in the proposed HCDIM-based FB (where the maximum necessary value of $M = 5$ using $L = 2, 5$ respectively, and TBW of modal filter is wider by a factor of L). The modal filter order required in the ICDM-based FB is 2928 (wherein the maximum required value of $M = 10$). A summary of the number of multiplications required to implement the HCDIM-FB and ICDM that are designed for obtaining the different standards of **Fig. 7**, is presented in Tab. 2. It can be noted that proposed HCDIM-based FB offers a multiplication complexity reduction (using $L = 2$) of 44.40% over ICDM. The multiplication complexity reduction (using $L = 5$) is about 77.61% over ICDM. The proposed HCDIM-based FB achieves a lower complexity than the ICDM because of using both coefficient interpolation and decimation methods and the masking filters involved, that result in modal filter of lower order.

It can be noted from the frequency responses obtained using HCDIM technique, that the increase in the value of M deteriorates the stop band attenuation (SA) of the filters obtained after performing coefficient decimation method. This is an intrinsic disadvantage of CDM and is existing in HCDIM too. The mathematical expression of the deterioration in SA can be given by Eq. (4). The SA deterioration problem is overcome by overdesigning the modal filter given in Eq. (5). The design steps described in section 5 have taken into account the SA deterioration problem too. This problem occurs when CDM is used only, so the use of CIM in the proposed FB has no action on the SA deterioration. The maximum required value of M is 10 using ICDM to extract channels of **Fig. 7** and the corresponding SA is -65dB. Using the proposed HCDIM approach to extract channels of **Fig. 6**, a maximum required value of M is 5, and the corresponding value of SA is -60dB according to Eq. (8). It is clear that the deterioration in SA means the larger filter order and the decreasing of this deterioration is an advantage. It can be noted in **Fig. 7** (f) that there seems to be a deterioration in the pass band magnitude in sb3 since the resulting response obtained after performing CDM-II, using $M=2$ is scaled by 2, then scaled

by 2 after performing MCDM-I, using $M=2$. The resulting response needs to be scaled by 2 again to have a 0 dB magnitude. Hence, in all HCDIM operations as well as ICDM operations, the pass band ripple does not alter and remains constant (0.1dB) after scaling the resulting response by the appropriate M .

It can be noted that the resolution of center frequency in the resultant multiband frequency responses in ICDM operations, is π/M . While possible center frequency sub-bands locations of $2\pi/M$ are achievable in the M -channel DFTFB. Using HCDIM based FB, the resolution of center frequency in the resultant multiband frequency responses is $\pi/(M \times L)$. Reconfigurable CD and FRM methods offer only one degree of freedom (M and L , respectively) to change the location of center frequency and BWs of channels, whereas the HCDIM based FB offers two degrees of freedom, M and L , which can be changed individually. Hence, the proposed method considerably improves the flexibility of the filter architecture to adapt to the channel spacing of different communication standards.

5 CONCLUSIONS

Reconfigurable filter bank architecture for dynamic channel adaptation for a CR terminal, based on decimation, interpolation and frequency response masking is proposed in this paper, and termed as HCDIM based FB and used for non-uniform and uniform channelization. The proposed architecture is a flexible alternative to other kinds of FBs since the resulting filter is an $(M \times L)$ sub-bands and has a center frequency resolution of $\pi/(M \times L)$ in the resultant multiband frequency responses. Also, if the same modal filter is used to obtain ICDM based channel filter, the worst case transition bandwidth and stop band attenuation values detected in the HCDIM based design are enhanced. Complexity analysis regarding the design examples shown clearly specify that the proposed architecture offers a better filter length saving compared to that of the other methods. The reduction in the number of multiplications is about 31.19% over ICDM based FB in uniform channelization and 50.77% in non-uniform channelization. The complexity of the modal filter can be further reduced if a higher interpolation factor is used. Thus, the proposed HCDIM-based FB is highly appropriate for use in applications of resource constrained such as portable CR handsets because of its significant advantages in terms of flexibility, complexity, and resource utilization over the other FBs.

REFERENCES

- Ambede, A., Smitha, K. G., and Vinod, A. P., 2012, *An Improved Coefficient Decimation based Reconfigurable Low Complexity FIR Channel Filter for Cognitive Radios*, In Proc. ISCIT, Gold Coast, Australia, Oct. pp. 22–27.
- Ambede, A., Smitha, K. G., and Vinod, A. P., 2012, *A Modified Coefficient Decimation Method to Realize Low Complexity FIR Filters With Enhanced Frequency Response Flexibility and Passband Resolution*, In Proc. 35th Int. Conf. TSP, Prague, Czech Republic, pp. 658–661.
- Ambede, A., Smitha, K. G., Vinod, A. P., 2013, *A New Low Complexity Uniform Filter Bank Based on the Improved Coefficient Decimation Method*, School of Computer Engineering, Nanyang Technological University, Nanyang Avenue, Singapore 639798.



- Ambede, A., Smitha, K. G., and Vinod, A. P., 2015, *Flexible Low Complexity Uniform and Nonuniform Digital Filter Banks with High Frequency Resolution for Multistandard Radios*, IEEE Transactions on Very Large Scale Integration (VLSI) Systems, vol. 23, no. 4, pp. 631-641.
- Bellanger, M., 1982, *On Computational Complexity in Digital Transmultiplexer Filters*, IEEE Trans. Commun., vol. 30, no. 7, pp. 1461–1465, Jul. 1982.
- Cruz-Roldan, F., et al., 2009, *A Fast Windowing-Based Technique Exploiting Spline Functions for Designing Modulated Filter Banks*, IEEE Transactions on Circuits and Systems -I: regular papers, vol. 56, no. 1.
- Chougule, S., Rekha, P., Patil, 2011, *Oversampled Perfect Reconstruction FIR Filter Bank Implementation by Removal of Noise and Reducing Redundancy*, UCMA 2011, Part I, CCIS 150, pp. 76-90, Springer.
- Farhang-Boroujeny, B., 2008, *Filter Bank Spectrum Sensing for Cognitive Radios*, IEEE Trans. Signal Process., vol. 56, no. 5, pp. 1801–1811.
- Fahmy, S., Doyle, a., Linda, 2010, *Reconfigurable polyphase filter bank architecture for spectrum sensing*, P. Sirisuk et al. (Eds.): ARC 2010, LNCS 5992, pp. 343–350. Springer-Verlag Berlin Heidelberg.
- Kumar, A., Singh, G.K., Anurag, S., 2015, *An Optimized Cosine-Modulated Nonuniform Filter Bank Design for Subband Coding of ECG Signal*, Journal of King Saud University - Engineering Sciences, Volume 27, Issue 2, Pages 158–169.
- Lim, Y. C., 1986, *Frequency-response masking approach for the synthesis of sharp linear phase digital filters*, IEEE Transactions on Circuits and Systems, vol. 33, no. 4, p. 357- 364.
- Mahesh, R., Vinod, A. P., 2007, *Frequency Response Masking based Reconfigurable Channel Filters for Software Radio Receivers*, IEEE International Symposium on Circuits and Systems, pp. 2518-2521.
- Mahesh, R., and Vinod, A. P., 2008, *Reconfigurable Frequency Response Masking Filters for Software Radio Channelization*, IEEE Transaction on Circuits and Systems-II: Express Briefs, vol. 55, no. 3.
- Mahesh, R., Vinod, A. P., 2008, *Coefficient decimation approach for realizing reconfigurable finite impulse response filters*, IEEE International Symposium on Circuits and Systems, ISCAS 2008, pp. 81-84, Seattle, Washington, USA, 18-21.
- Mahesh, R., Vinod, A. P., 2011, *A low-complexity flexible spectrum-sensing scheme for mobile cognitive radio terminals*, IEEE Transactions on Circuits and Systems II, vol.58, no.6, pp.371-375.

- Mahesh, R., and Vinod, A. P., 2011, *Low complexity flexible filter banks for uniform and non-uniform channelisation in software radios using coefficient decimation*, IET Circuits, Devices Syst., vol. 5, no. 3, pp. 232–242.
- Park, J., et.al, 2009, *A Fully Integrated UHF-Band CMOS Receiver With Multi-Resolution Spectrum Sensing (MRSS) Functionality for IEEE 802.22 Cognitive Radio Applications*, IEEE J. Solid-State Circuits, vol. 44, No. 1.
- Powell, C., et.al, 2003, Notice of Proposed Rule Making and Order (NPRM 03-322), *Facilitating Opportunities for Flexible, efficient, and Reliable Spectrum Use Employing Cognitive Radio Technologies*, Federal Communications Commission, ET Docket No.03-108.
- Proakis, J. G., and Manolakis, D. G., 2007, *Digital Signal Processing: Principles, Algorithms, and Applications*, 4th edition.
- Smitha, K.G., Mahesh, R., and Vinod, A. P., 2008, *A Reconfigurable Multi-stage Frequency Response Masking Filter Bank Architecture for Software Defined Radio Receivers*, 978-1-4244-1684-4/08/\$25.00 © IEEE.
- Vaidyanathan, P. P., 1990, *Multirate digital filters, filter banks, polyphase networks, and applications: a tutorial*, Proceedings of the IEEE, vol. 78, no. 1, p. 56-93.

ω Frequency, rad/sec..

δ_p Passband ripple, dB.

δ_s Stopband attenuation, dB.

f_p Normalized passband frequency.

f_s Normalized stopband frequency.

Table 1. Comparison of multiplication complexity: design example of uniform channelization

	DFTFB	ICDM	Proposed HCDIM based FB	
			$L = 2$	$L = 4$
Prototype/modal filter length (l_p/l_{Mod})	$l_p=161$	$l_{Mod}=177$	$l_{Mod}=97$	$l_{Mod}=42$
Masking filter length (l_{Mas})	–	$19*2=38$	$19*2+5*2=48$	$19*2+17*2+17=89$
No. of multiplications = ($\lceil l_{Mod}/2 \rceil + \lceil l_{Mas}/2 \rceil$)	161	$\{\lceil 177/2 \rceil + (2 * \lceil 19/2 \rceil)\} = 109$	$\{\lceil 97/2 \rceil + (2 * \lceil 19/2 \rceil + 2 * \lceil 5/2 \rceil)\} = 75$	$\{\lceil 42/2 \rceil + (2 * \lceil \frac{19}{2} \rceil + 3 * \lceil \frac{17}{2} \rceil)\} = 68$

No. of multiplications for S-point DFT (S=8)	$S \log_2 S = 8 \log_2 8 = 24$	-	-	-
Total no. of multiplications	185	109	75	68

Table 2. Multiplication complexity comparison: non-uniform channelization design example

	ICDM	Proposed HCDIM based FB	
		$L = 2$	$L = 5$
Modal filter length (l_{Mod})	2929	1397	532
Masking filter length (l_{Mas})	$40 * 4 = 160$	$40 * 4 = 160$	$40 * 4 = 160$
No. of multiplications $= (\lceil l_{Mod}/2 \rceil + \lceil l_{Mas}/2 \rceil)$	$\{ \lceil 2929/2 \rceil + (4 * \lceil 40/2 \rceil) \}$ =1545	$\{ \lceil 1397/2 \rceil + (4 * \lceil 40/2 \rceil) \}$ =859	$\{ \lceil 532/2 \rceil + (4 * \lceil 40/2 \rceil) \}$ =346
Total no. of multiplications	1545	859	346

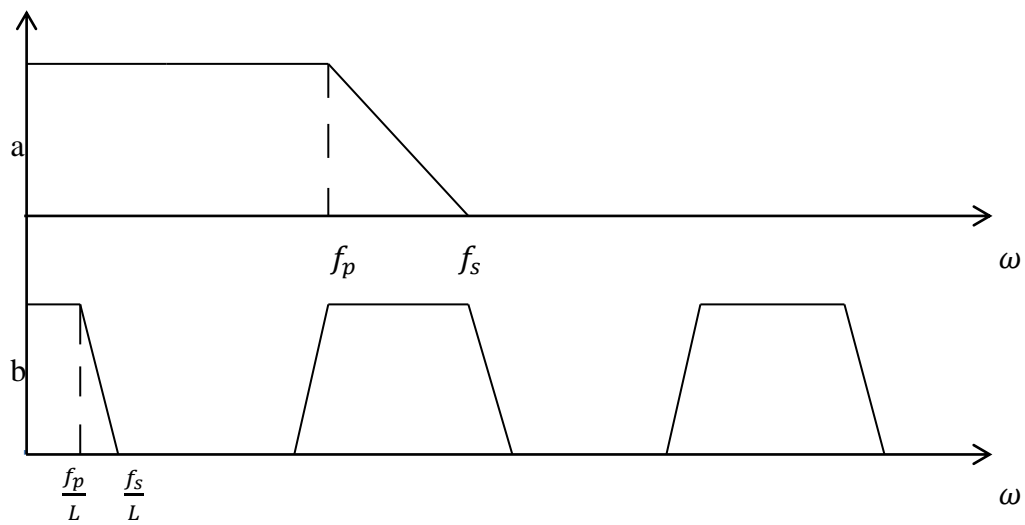


Figure 1 Coefficient interpolation method by a factor of L .

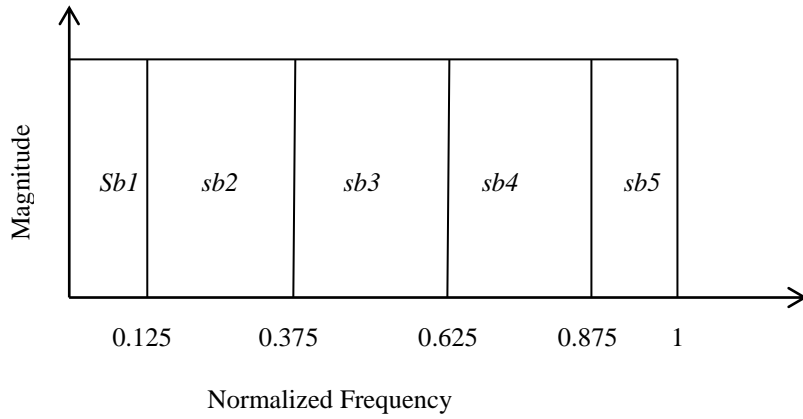
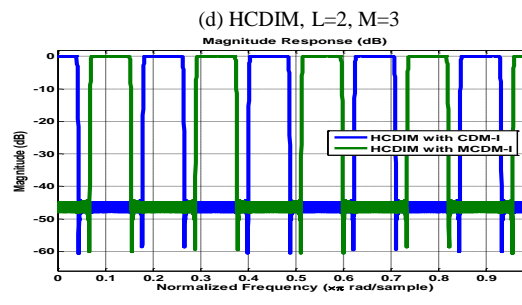
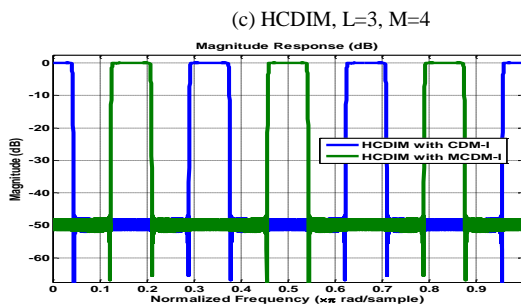
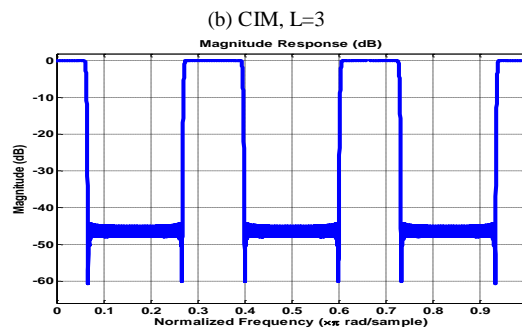
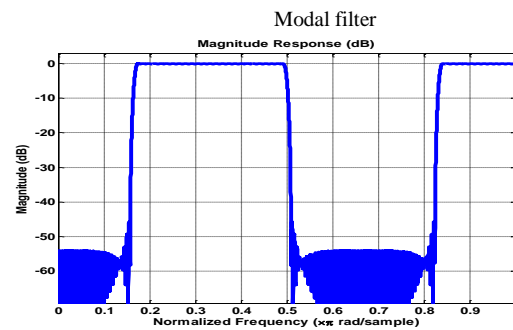
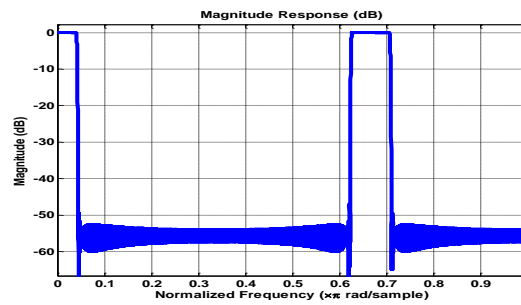
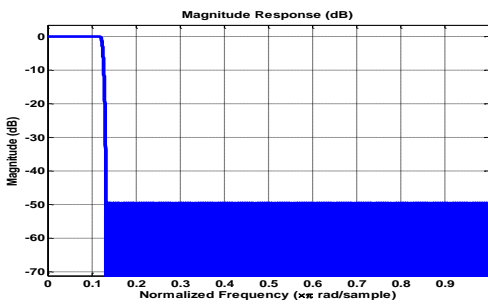


Figure 3 Frequency response of uniform design example



(e)HCDIM, L=3, M=2.

(f) HCDIM, L=3, M=3

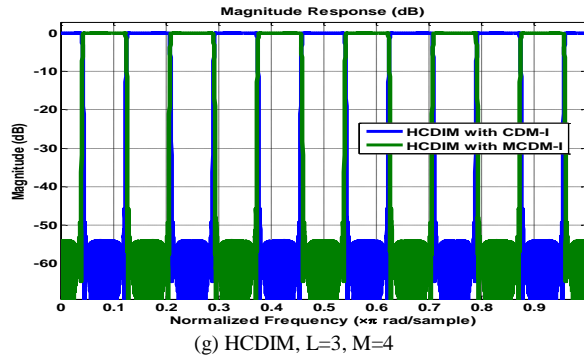


Figure 2 HCDIM operations on modal filter having $f_p = 0.12$ and $f_s = 0.132$

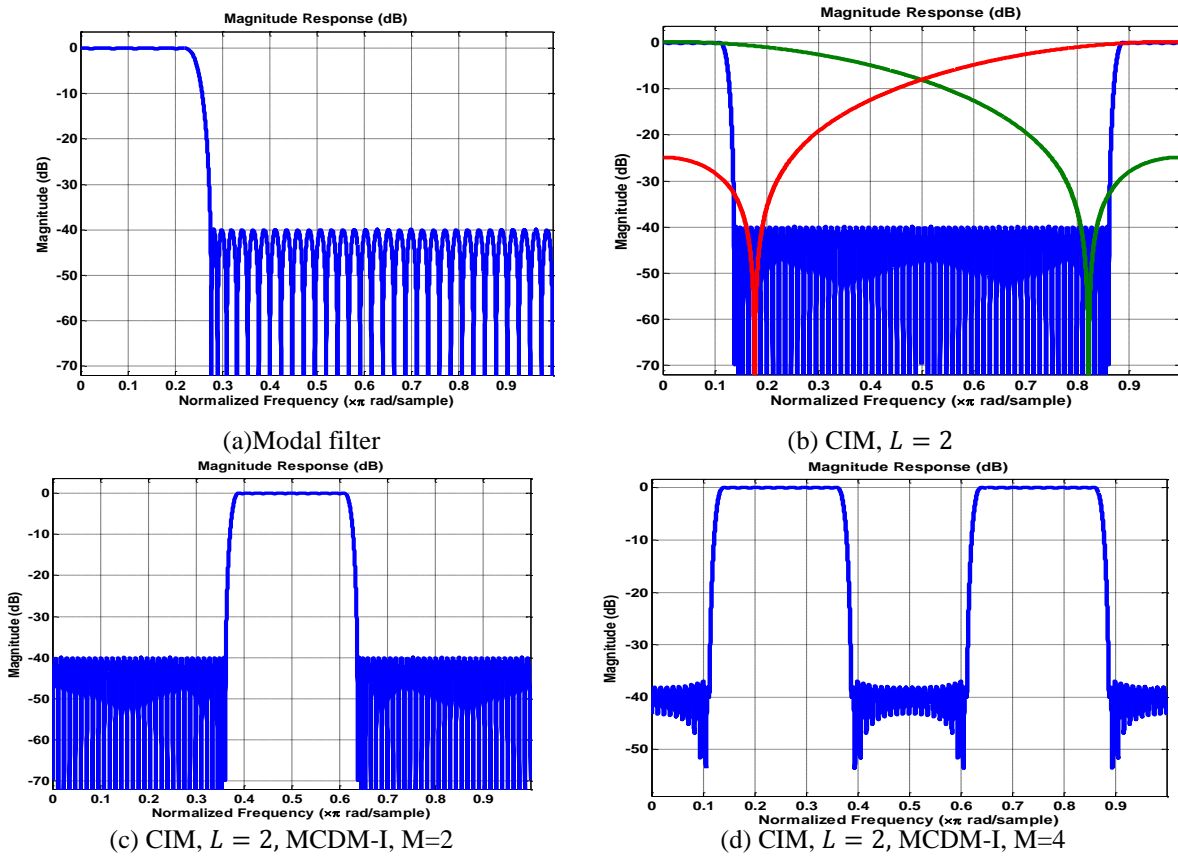


Figure 4 HCDIM-based FB for uniform channelization

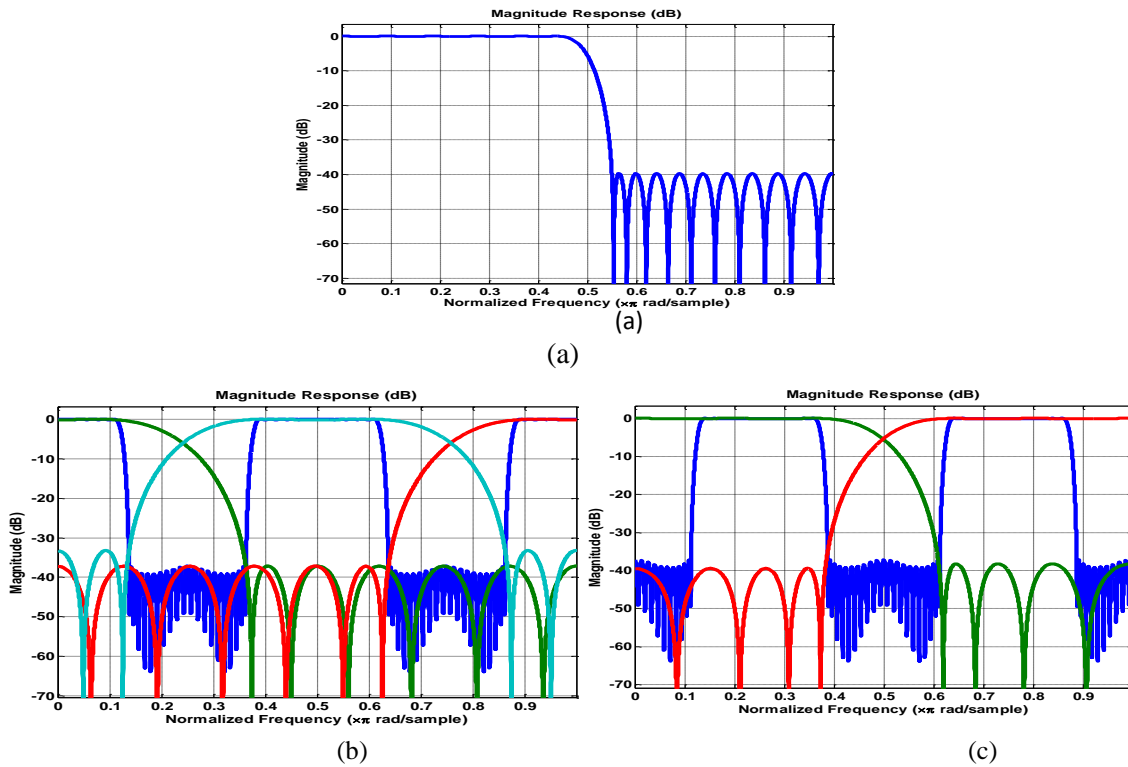


Figure 5 (a) Frequency response of modal filter (b) Frequency response of modal filter after performing CIM, using $L=4$ and CDM-I, using $M=4$ and appropriate masking filters (c) Frequency response of modal filter after performing CIM, using $L=4$ and MCDM-I, using $M=4$ and appropriate masking filters .

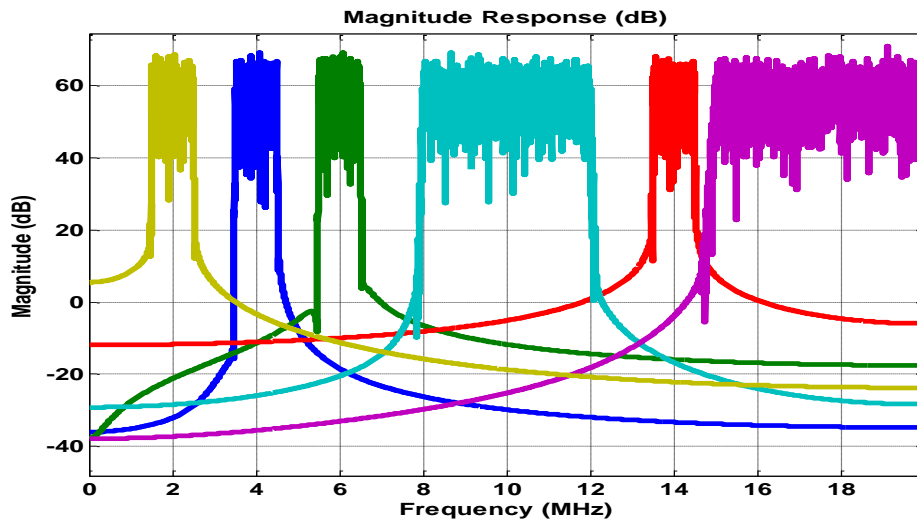
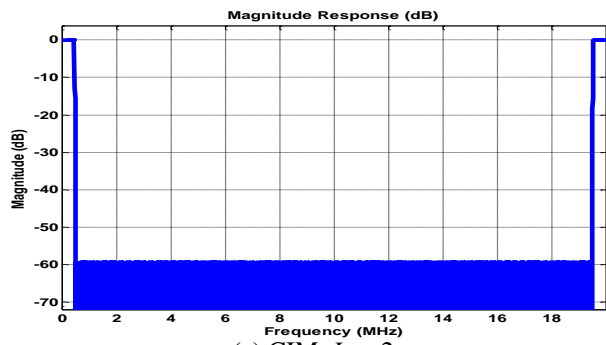
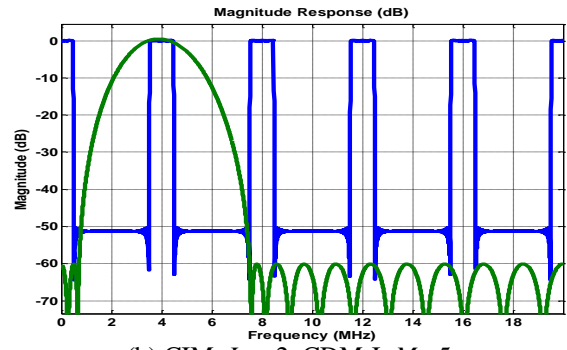


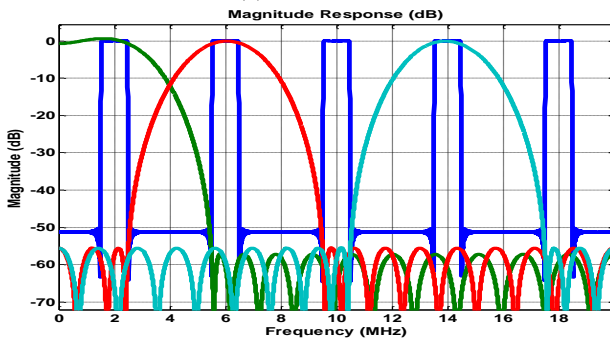
Figure 6 Design example of multi-standard channelization



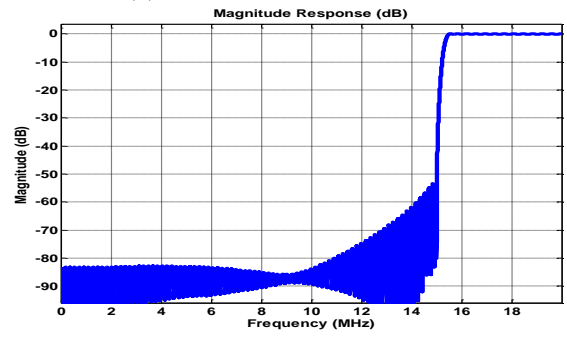
(a) CIM, $L = 2$



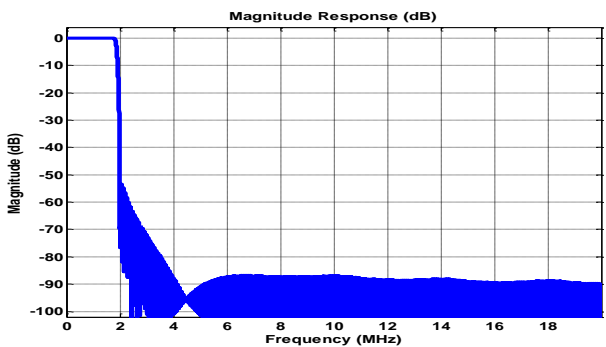
(b) CIM, $L = 2$, CDM-I, $M = 5$



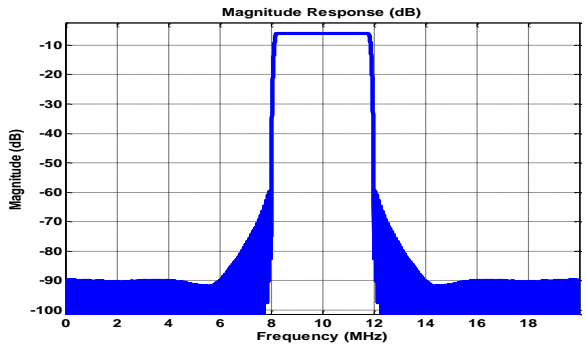
(c) CIM, $L = 2$, MCDM-I, $M = 5$



(d) MCDM-II, $M = 5$



(e) CDM-II, $M = 2$



(f) CDM-II, $M = 2$, MCDM-I, $M = 2$

Figure 7 HCDIM based FB for non-uniform channelization using $L = 2$

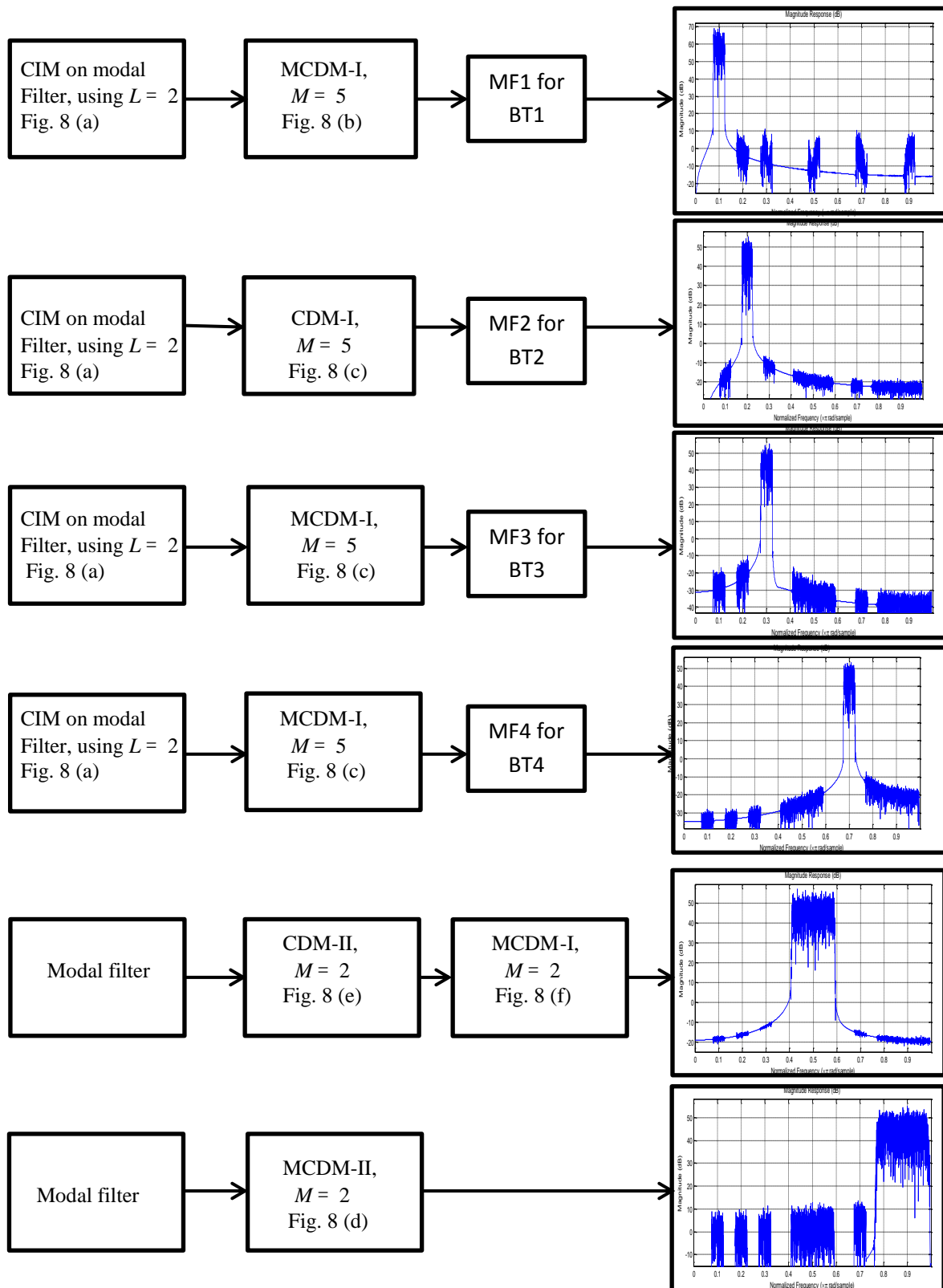
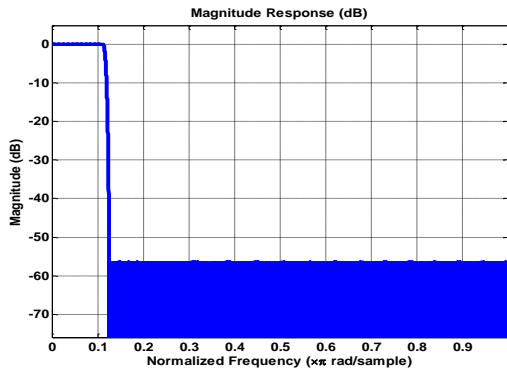
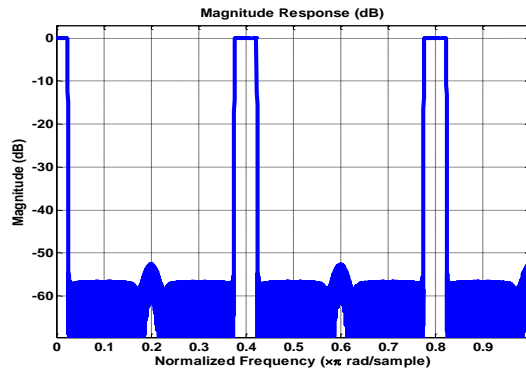


Figure 8 Block diagram of HCDIM: non-uniform channelization (using $L = 2$)



(a)



(b)

Figure. 9 (a) Frequency response of modal filter (b) Frequency response of modal filter after performing CIM, using $L = 5$



Evaluating the Recharge of Ground Water within Al-Wand River Basin.

Amer Hassan Al-Haddad

Assistant Professor

College of Engineering-University of Baghdad
email: Ameralhaddad1950@yahoo.com

Zainab Kadhim Jabal

Instructor

College of Engineering-University of Baghdad
email: zainabkadham@yahoo.com

ABSTRACT

The estimation of recharge to ground water is the important basics to improve the use of ground water with other available resources, and to save ground water resource from depletion, especially when using large quantity of ground water during a long time such as for agricultural purposes. Al-Wand River Basin in Iraq suffers from water shortage of its requirement of Blajo–Al-Wand Project, and to cover this shortage, the ground water plays a good role to overcome this problem. In this study, three methods were used to estimate the recharge and ground water storage for Al-Wand Basin, these methods are: Water Table Fluctuation (WTF), Water Balance of Climatic for Basin, and Water Table Balance for Basin. The results showed differences between the methods used to estimate recharging and ground storage for this basin. The approximated values between drawl water from production wells and water balance of climate for basin method make it better the other methods, which the difference percentage was large with drawls water. Also, classifying the methods by assumptions found make (WTF) better method, because it contains less assumptions compared to the other methods.

Key words: ground water, recharge of ground water, WTF method, water balance of climate basin method, water balance of basin.

تقييم تغذية المياه الجوفية لحوض نهر الوند

زينب كاظم جبل
الباحث
جامعة بغداد/كلية الهندسة

عامر حسن الحداد
استاذ مساعد
جامعة بغداد/كلية الهندسة

الخلاصة

تعد عملية تقدير تغذية المياه الجوفية من الاساسيات المهمة لتحسين استخدام الماء الجوفي مع المصادر المائية الاخرى ولحفظ مصادر المياه الجوفية من الاستنزاف ، خصوصاً عند استخدام مياهها بكميات كبيرة ولوقت طويل مثل استخدامها للاغراض الزراعية. ان حوض نهر الوند يعاني من انخفاض في كميات المياه التي تمر به لذا تستعمل المياه الجوفية لغرض سد هذا النقص. تم استخدام ثلاث طرق في هذه الدراسة لتخمين تغذية المياه الجوفية والخزين الجوفي لهذا الحوض وهذه الطرق هي : تذبذب مناسيب المياه الجوفية ، الموازنة المائية المناخية للحوض والموازنة المائية للحوض. اظهرت النتائج اختلاف كبير في قيم تغذية المياه الجوفية لهذا الحوض. التقارب بين قيم الماء المسحوب من الابار المنتجة بطريقة الموازنة المناخية للحوض يجعلها افضل من الطرق الاخرى التي تكون نسبة الفرق واضحة فيها مع الماء المسحوب من الابار، كذلك تصنيف الطرق حسب الافتراضات المستخدمة في الطرق يجعل طريقة تذبذب مناسيب افضل من الطرق الاخرى، لانها تحتوي على اقل عدد من الافتراضات.

الكلمات الرئيسية : المياه الجوفية ، تغذية المياه الجوفية ، نظرية تذبذب مناسيب المياه الجوفية ، نظرية الموازنة المناخية للحوض ، نظرية الموازنة المائية للحوض .



1. INTRODUCTION

The important factors when using ground water are the limited recharge and the strategy of drawls the water from aquifer. This is especially when there is a high need for ground water due to water increase for agricultural purpose, and when there is a shortage in the surface water recourse. The method to define the recharge resources is the main objective for Al-Wand Basin. This basin is located in Iraq and Iran. Most part of the basin lies within the Iranian borders. So, the estimation of recharging and ground storage is for Iraqi part, because the information of the Iranian part is limited for the same basin.

1.1 Recharging Ground Water

The fundamental components of the water balance of any basin is the recharge of water to ground water reservoir, many methods are used to estimate the recharge of ground water, one of these methods is direct measurement, which is widely used with complexity and costly, **Risser, 2005**. The rate of recharge and volume of recharge are connected with rainfall quantity, the conditions of geology in the ground water basin such as surface and subsurface condition affect the availability and distribution from supply surface water to the ground water basin, all these points are very important to indicate the aquifer recharge, **Dudley, and Fulton, 2005**. There are many methods of recharging water to ground. Selecting the proper method depends on the type of aquifer and if the surface water in basin is available. These methods as presented by **Dedley, and fulton, 2005** are:

- 1- Natural recharge: This is considered as simple methods of replenish ground water reservoir in almost all basins by percolating the water to aquifer from available surface water sources as a stream, lakes, rivers and applied irrigation water in fields. Natural recharge does not need to infrastructure or surface water supply because the water already exists through the aquifer in natural conduction, because that this method consider slowest of replenishing the water to aquifer system, and relatively unmanaged from human.
- 2- In-lieu recharge: This method can be applied when using the ground water in any basin and this basin does not include as a natural surface water resources, so it is recommend providing the aquifer with water from application of surface irrigation water and seepage water due to low of conveyance facilities. The advantages of this method are leaving more ground water in aquifer storage for later use, reducing the demands on aquifer system from ground water extraction, and can be implemented under virtually any soil and geologic conditions, but the disadvantages are when using recharge by this method because it is very complex and expensive to implement especially when the area of basin need to construct a special irrigation networking system to recharge water for aquifer basin.
- 3- Aquifer injection: The recharge of ground water by using method of injection water to aquifer system by operating wells in backwards. The use of this method is limited because of geological condition, and when the other methods of recharge are not suitable for the aquifer. At large scale area this method is very expensive, and includes the costs of well construction, pump operation, cost necessary to treat the water prior to injection, and mechanical maintenance existing with aquifer injection. In artificial recharge method such aquifer injection must be available with good quality and when supplied to aquifer with free of turbidity, bacteria, bio-matter, and viruses.

Limiting of the methods that are used to estimate the recharge of ground water reservoir is difficult to apply since it must be available in the primary measurement for evaporation and deep percolation or other parameter input that affect balance of hydrologic cycle, and these methods are:

1. Physical or natural method: this method can be applied by considering the properties of soil and the measurements of the water quantity which inflows under root zone.
2. Chemical method: Can be used by following the relative presence of solution tendency material in water such as chloride and matches through the soil during deep percolation.

The methods that are used to estimate the recharge of ground water in Al-Wand Basin (the part of Iraq) in this research are:

1.1.1 Water table fluctuations

Water table fluctuation method may be the most widely used as a technique for estimating the recharge, the specific yield and change in water level must be available during a period of time as a requirements of this only. There are many methods that use water level to estimate the recharge of ground water, but these methods are based on Darcy equation, instead of that (WTF) method depends on knowing the specific yield that can be determined, in addition to that the water levels change method will give the accuracy than the other method. The simple and insensitivity of mechanics in (WTF) method makes it useful especially when water moves through the unsaturated zone, **Healy, and Cook, 2002**.

Ramadhan, et al., 2013, presented the evaluation of ground water recharge for arid and semiarid regions by using four methods (fluctuating water table, water balance of the basin, numerical modeling and balance of chloride ion mass in unsaturated zone). The result of these methods showed the there is a difference in value of recharge, but it was closer to real result when comparing with volume of water in inventories renewed when using chloride ion method in unsaturated zone.

The (WTF) is based on the rises of ground water levels in unconfined aquifer, and the recharge of water that will arrive to the water table is calculated as:

$$R = Sy \Delta h / \Delta t \quad (1)$$

where:

Sy = specific yield,

Δh = difference of water table, m , and

Δt = the time of recharge calculating.

And the ground storage of ground water is given as:

$$\Delta S = R * A_t * C \quad (2)$$

where:

ΔS = ground storage, m^3 ,

A_t = total area of basin, ha , and

C = conversation unit.

1.1.2 Recharge from water balance of climate for basin method

The recharges from water balance of climate for basin method is a widely used in world to evaluate the recharge of ground water for any basin. The main parameters of this method depend on the theoretical balance basin parameters which the other methods depend on too, especially the data of surface water and ground water system at unsaturated and saturated zone, **Ibrahim, et al., 2011**. The water balance for hydrologic system must be equal to input and output parameter which is contained in this system, otherwise the change of ground storage will appear if these parameter increase or decrease one to other, the water balance is as follows:

$$\text{Input} - \text{output} = \text{change in storage} \quad (3)$$

The rainfalls or snow are the only input in water balance budge, and the output parameters which can be limited are:

- Evapotranspiration: the evaporation process is the loss of water from water surface or the soil, while the transpiration is the process of loss water from the plants, and the two processes are called evapotranspiration. Many methods are used to estimate evapotranspiration for any study area especially the cultivated area.
- Soil moisture content: is the second parameter of the balance climate for basin method and depends on the type, texture and depth of soil. The soil moisture content (SMC) affects the amount runoff and recharge of ground water and this cannot be satisfactory except when soil reaches the saturated state, or the average of soil filtration of water reaches low level, and when the capacity of filtration at high level, **Famiglitti, et al., 1998**. Run off of water occurs when the average of filtration decreases and rainfall intensity is higher than average of filtration rate and before the soil reaches to saturation level, **Domenico, and Schwartz, 1998**.

The water surplus is a result of the difference between the rainfall and evapotranspiration average which is formulated as:

$$WS = P - Et \quad (4)$$

where:

WS = monthly water surplus, mm ,

P = monthly average rainfall, mm , and

Et = monthly potential evapotranspiration, mm .

The recharge of ground water is not considered the only affecting factor in water surplus (WS), but the surface runoff and soil moisture content are main factors affecting water surplus which is equal to:

$$WS = Gr + SR + SM \quad (5)$$

where:

Gr = recharge of ground water, (mm),

SR = surface runoff, (mm), and

SM = soil moisture content.

The surface runoff equation can be used in the upper soils of Adhime basin to estimate the annual runoff of Al-Wand basin, **SOGREA, 1983**.

$$SR = 0.168 (P - 180) \quad (6)$$

where:

P = annual rainfall in, mm .

The water balance of climate to estimate the ground storage can be formulated as:

$$P - (Et + SM + SR) = \pm \Delta S \quad (7)$$

where:

ΔS = change of ground storage in month, (mm).

Ibrahiem, et al., 2012 used the climatic water balance for evaluating the recharge of ground water for Tikrit sub basin. In his study, he depends on the climate parameters such as rainfall, temperature and evapotranspiration which are estimated using, **Thornthwait formula, 1948**. He also used other parameters for the balance which are surface runoff, soil moisture content as a recharge for ground water. The climate balance illustrated the increasing of average evapotranspiration on the average of rainfall which causes the decreasing in water surplus that affect the recharge of ground water.

1.1.3 Water balance for basin method

Water balance method illustrated the natural parameters which are used as input in water balance of basin method to evaluate the recharge of ground water, which is recharged from rainfall, base flow from rivers, seepage from surface, and from irrigation water application. The discharge parameters from water balance system can be indicated by drag wells which are draw water out for any purpose, and evapotranspiration from ground water.

Sethi, et al., 2002 used the ground water balance model as a way to connect it with conjunctive use for agricultural purposes in a Coastal river basin. The linear program of optimization is applied with ground water balance to maximize the economic returns for optimal cropping pattern.

The conceptual for this method can be formulated as the recharge of ground water, discharge of ground water, and the change of ground storage which are effected by recharge and discharge, of all these parameter that will illustrated below:-

- Recharge of ground water

This parameter is input parameter which plays a role in recharge of ground water and it changes according to the nature of study area and properties such as type of soil, cropping pattern, and the networking of irrigation system and the last one can be indicated by estimated conveyance and irrigation efficiency, all these parameter are illustrated below:

$$GR = R_r + RC + RBF + RSF \quad (8)$$

where:

GR = ground water recharge, m^3 ,

R_r = recharge from rainfall, m^3 ,

RC = recharge from irrigation area and conveyance system,

RBF = recharge from base flow, m^3 , and

RSF = recharge from seepage from drain, m^3 .



1- Recharge from rainfall (R_r)

Chandra, and Saxena, 1975 presented an equation to calculate the recharge from rainfall, depended on the average annual of rainfall, and is illustrated below:

$$R_{r1} = 3.984 (R_{av} - 40.64)^{0.5} \quad (9)$$

where:

R_{r1} = recharge from rainfall as, *cm*, and

R_{av} = average annual rainfall, *cm*.

Then the volume of recharge measured as (m^3):

$$R_r = R_{r1} * A_t * C \quad (10)$$

where:

R_r = volume of rainfall recharge, (m^3).

2- Recharge from irrigation area

Recharge from irrigated area depends on the irrigation efficiency, which is estimated amount from, **Ground Estimaation Committee, 1984**.

3- Recharge from base flow

Recharge from base flow as rivers, lakes or any resources of surface water. Many methods are used to estimate the percolation from rivers as annual average to ground water which flows with gradient from both sides of rivers, and from cross-sectional area such as in the application of Darcy law. Also, the direct measurement methodology is used to estimate the base flow by using the available information for hydraulic conductivity of river beds soil when it is estimated by using Falling Head parameter method in the laboratory, the curve tangent method, the chemical, isotope and the basin area method, all these methods are used to determine the recharge from base flow of rivers, **Delleur, 1998**.

4- Recharge from seepage flow of drains

The amount of seepage from open drains is affected by the dimensions of wetted perimeter, and length of drains. Many researchers assumed a percentage of runoff as a recharge to ground water and this percentage equals 40% rainfall from total run off goes to drains, **Sarma, et al., 1983**, and 8% of total run off goes directly to drains, **Chandra, and Saxena, 1975**.

- Discharge from ground water

The discharge from ground water can be defined as the quantity of water draft from ground water, which includes the discharge from wells, evapotranspiration from ground water, and discharge out way to another aquifer. The total discharge for this method is as below:

$$GD = GDW + GDE \quad (11)$$

where:

GD = ground water discharge, m^3 ,

GDW = ground water discharge from wells, m^3 , and



GDE = ground water evapotranspiration discharge, m^3 .

1. Discharge from draft well

The discharge production from the wells depends on the number of draft wells that draws water from the aquifer, and the time of wells operation during the year. The other important factor that effects on the well yield is depth of these wells.

2. Discharge due to evapotranspiration

When the aquifer is unconfined, and the water table is close to ground surfaces the water table level may be changed due to the evaporation and transpiration. The two processes play a role as discharge from ground water due to temperature atmosphere, and this phenomenon can occur in the region that has a high temperature, **Todd, 2005**.

Evaporation from ground water is influenced also by soil structure and texture which control the capillary tension above the water table. Field measurements to determine the evaporation can be done by using Lysimeters. The evaporation is largely controlled by atmospheric condition and the evaporation value rate decrease with water table depth. Transpiration from ground water can be estimated when water table approaches to ground surface and the region cultivated with vegetation, and when crops roots depths reach the saturated stratum, **Todd, 2005**.

- Ground-reservoir storage

The storage of ground water is the volume of water existing in the effective voids of geological layers in unconfined aquifer, and the storage in confined aquifer is the volume of water stored in pores under the artesian layers. In the type of two aquifers, the storage of ground water differs from aquifer to another due to quantity and percentage of their volumes. There are two types of storage one called Renewed Storage and the other is Fixed Storage. Renewed storage has a dynamic objective and a function of time, and affected by natural and boundaries of layers. Fixed storage has volumetric satirical quantity and a function of properties of geological layers dimensions (pressure and pores), **Al-Jawid, 1999**.

To avoid the overdraft which is defined as a condition of ground water basin which is the amount of water drawn by pumping that exceeds the amount of water that is recharged to the basin during a period of years. So that was important condition on using conjunctive use management as located in California State – USA, the storage ground water to prevent the overdraft case that might be happen, and to be at safe side, **California water plane, 2009**.

2. STUDY AREA PROPERTIES

This research have been carried out in Al-Wand Basin and the following paragraph describes the properties of this study area which includes, the geography, climates, investigation of soil, and the geology.

2.1 Geography

The Iraqi part of Al-Wand River Basin is located in the eastern part of Iraq, in Diyala Governorate. It is located in middle of Iraq with border crossings with Iran (Monthiriah and Mandali). It lies near the Iranian border and north–west of town Khanaqin. Specifically, the

project study is located between (34° 18'), (34° 30') north latitude, and (45° 12'), (45° 24') east longitude **Fig. 1**.

Al-Wand River passes through the study area, and it is one of the most important rivers shared between Iraq and Iran. It is also one of the most important tributaries of Diyala River in the southern part. It flows from the mountains of Iran and joins with the Diyala River in Iraq. The length of river from its source to its mouth in Jalula is about (152km) of which (63km) is inside the Iraq land. The area of basin which is feeding Al- Wand river is about (3340 km²), in Iran the basin area is about (2780km²), and about (560km²) inside Iraq.

2.2 Climates

The main climatic features of the region of the project is long and hot summer (from May to October), and the precipitations of annual average is of 282mm, falling only during the winter (from December to February). The climatic features of the Al-Wand region irrigation project are assessed on the basis of the climatic data recorded in Khanaqin Meteorological Station, which is located quite near to the irrigated area on (34° 18') latitude and (45° 26') longitude. The parameters of climate can be illustrated as annual average for 20 years. The annual rainfall average during this period is (282.16mm) only, and the humidity is equal to (48.52%) as an average for the period (1981-2000), and the averages of temperature in winter is (12C°), and (33C°) in summer and during the same interval. The average wind speed is (2.18 m/s), and the annual average of evaporation for interval (1988-2008) is (260mm), **National Center of Water Resource, 2014**.

2.3 Soils

According to the soil survey which was conducted in 1978 by an Iraqi team of experts from (State Organization of Soils and Land Reclamation) the soils in the project area are divided in three groups of soil depending on their permeability properties, **Alamdar, et al., 1978**.

- a) First group – one layer soil.
- b) Second group – two – layers soil with permeability decreasing in depth.
- c) Third group – two – layers soil with permeability increasing in depth.

The main properties of these soils are:

- Alluvial soil, suitable for irrigation and cultivation with good depth.
- Texture is fine – moderate (permeability with average (0.5 m/d)).
- Gravel deposits in the depths of 200 cm in some areas.
- No salinity and gypsum problems.
- Infiltration rate ranging between (3.7 - 6) cm/hr.
- Low percentage of organic matter ranging between (0.2 - 2%).
- Soil pH ranging between (7.1 – 8.4).
- Land capability (USDA System): class II and class III are the dominate in the area which means that the area classified as productive land.

2.4 Geology

Al-Wand River valley basin is created due to the erosion, it consists of deposits of Quaternary Age almosin which is a type of (almarl) and sandstones, most of the rock layers

tend towards the North and North-East of angle (10 - 20) degree. Most of these rocks are covered by alluvial deposits. The most tracts Al -Wand river basin is an alluvial deposits, ranging from depths of (1.5 – 10m) which resulted from the historical phases of the age of the river and the transmission of these materials through runoff and floods on the river. Gypsum is found in almarl stones and sandy stones at ground bases in the form of small isolated pools and tests have shown that these stones were not self-executing and zaoian for gypsum or access filter. Due to the investigation of ground water from the wells which are excavated in area, the aquifer is unconfined aquifer.

3. RESULTS AND DISCUSSION

The properties of study area of Al-Wand River Basin were clarified as the input data which have been applied and which is available at many information offices. These data were applied in the recharge equation and the estimation of ground water storage. The results of recharge for three methods are illustrated below:

3.1 Water Table Fluctuation Method

Three observation wells are disturbed in study area to record the variation of water table of ground water due to draft and recharge process, the geographical locations with details for Binmel well, Mekhis well and Ahmed Taher well listed in **Table. 1**. The monthly variation of water levels during the period (2010-2013) for these wells are listed in, **Table. 2, Table. 3** and **Table. 4**. The monthly average for each observation well was shown in **Fig. 2, 3 and 4**. From these figures the maximum level due to recharge and minimum level due to draws from well were noticed, which is increasing to cover the agricultural needed. The difference between April and October for Binmel well, Mekhis and Ahmed Taher are (0.81, -0.876 and 0.105 m) respectively, **General Commission of Ground Water, 2014**, which make the average difference of water table (fluctuation Δh_{av}) was used in **Eq.1**

The data for specific yield in study area are not available due to the data form pumping test were not practiced when excavated the production wells. So, the specific yield was assumed by depending on the last studies for the same basins as equal to (0.05). **Table. 5** presents the values of recharge to ground water and the amount of ground storage (ΔS_{ava}) for each well, and by knowing the total area of the project which is about 10181ha, the recharge to the ground water 28.85mm and the grand average of ground storage is about 3039028.5m³.

3.2 Recharge from Water Balance of Climate for Basin Method

- Rainfall is the important input data to estimate the recharge of Al-Wand River Basin. **Table. 6** showed value of rainfall with average during (1988-2008). The annual rainfall average during this period is 282.16 mm.
- **Table. 7** shows monthly the evapotranspiration with other parameters of this method, **National Center of Water Resource, 2014**.
- The value of soil moisture content can be measured by many methods such as experimental measurements by calculating the saturation percentage of soil, field measurements by using the Lysimeters in study area and based on the last studies for same soil properties especially for the same Iraqi soil in (Adhime, Diayla and Lower Zap) basins as estimation for the saturation quantity, **Al-Furat Center for Designs of Irrigation project, 2000**. Because there is no available data for soil moisture content and there is no accuracy data for soil depth layers in soil properties report of this basin, it is assume that there is no



possibility that the soil moisture content will recharge to ground water. **Table. 7** shows the monthly water surplus, and annual water surplus is 31.45mm . Annual surface Runoff calculated using **Eq. 6** is 17.16mm so the annual recharge of ground water (Gr) is 14.29mm . By applying **Eq. 7** the change of ground storage is $+14.29\text{mm}$ and volume of ground storage is 1454864.9m^3 .

3.3 Water Balance for Basin Method

The recharging of ground water by using this method can be obtained by calculating each parameter used in **Eq. 8** of recharge and it can estimate the discharge of ground water to evaluate the ground storage of Al-Wand Basin.

- Recharge from rainfall is calculated by applying **Eq. 8** as an annual average recharge of ground water. (R_{r1}) is 61.91mm depth, and for annual average volume recharge of ground water (R_r) is 6303195.56m^3 .
- The recharge from irrigation depends on the irrigation efficiency and conveyance efficiency and which were unknown in the project, in addition to that the depth of water table is deep from ground surface which make the recharge from irrigation fields neglected.
- The recharge from base flow which depends on the type of source of surface water as Al-Wand River which suffers from shortage of water and sometime has no flow during some months making this value negligible.
- The recharge from seepage of open drains depends on the network of drains and its dimension to estimate the recharge from it. But this network of drainage system was complete as a design and implement in Blajo-Al-Wand Project, so the recharge from seepage drains is also neglected.
- The discharge from ground water has been showed as a discharge from well, which is used for agricultural purposes, all details of these are well listed in **Table. 8**. The other source of discharge from ground water is the evapotranspiration, which depends on depth of reservoir from ground surface, if this depth is shallow the reservoir will be affected by the temperature atmospheric condition Blajo -Al-Wand Project which have ground water reservoir very deep .So, the effect of this parameter on the discharge phenomena can be neglected. If the operation of production wells was assumed by (12hr/day) in year, and as the average discharge for each well is $(0.003\text{m}^3/\text{s})$, the estimated discharge well (GDW) is 1418342.4m^3 .

The ground storage for Al-Wand basin was calculated using **Eq. 11** is 4884853.16m^3 . **Table. 9** shows the results of the three methods to estimate the recharge and ground storage of Al-Wand Basin.

4. CONCLUSIONS

Table. 9 represent the results of final calculation of recharging and the effects on ground water storage. The results showed difference between the three methods. To select the best method which is used to estimate recharging and ground storage by comparing with volume of water which draws from production wells (it is explained by water balance for basin method as a volume 1418342.4m^3). The Percentage value between draws volume and WTF method is 47%, percentage between draws volume and water balance of climate for basin method is 97%, and last percentage between draws volume and water balance for basin method is 29%. So, water balance of climate basin is better than method due to nearest with



water drawls from production wells. Also, depending on assumptions in the methods make the estimated recharging not accuracy. WTF method less used the assumption than the other methods, which used many assumptions due to data of study area are not available.

REFERENCES

- Alamdar, H., Majeed, A. S., and Alwan, H., 1978, *Soil Survey and Land Classification of Al-Wand Irrigation Project*, State Organization for Soil and Reclamation Iraq.
- Al-Jawaid, S. B., 1999, *Development the Advantage of Ground Water in Iraq*, Not Emittted Research, (Language Arabic).
- California Department of Water Resources., 2009, *Conjunctive Management and Ground Water*, Volume 2 Resources Management strategies, California water plan update 2009.
- Chandra, S., and Saxena, R. S., 1975, *Water Balance Study for Estimation of Ground Water Resources*, Irrigation and Power Journal, CBIP, New Delhi, vol. 32, No. 4, pp 443-449.
- Delleur, J. W., *The Hand Book of Ground Water Engineering*, CRC press and springer – Verlag, 1998, pp I 34 – 35.
- Domenico, P. A., and Schwartz, F. W., 1998, *Physical and Chemical Hydrogeology*, John wiley and sons Inc., New Yourk, 506 p.
- Dudley, T., and Fulton, A., 2005, *Conjunctive Use Water Management: What is it? Why Consider it? What are the Challenges?*, Agriculture and Natural Resources, University of Collfornia, 1111 Franklin, 6th Floor, Oakland, CA 94607-5200, Phone (510) 987-0096.
- Famiglietti, J. S., Rudnicki, J. W., and Rodell, M., 1998, *Variability in Surface Moisture Content Along a Hill Slop Transect*, Journal of Hydrogeology, Rattlesnake Hill, Texas, No, 210 p. 81 – 259.
- General Commission for Ground water, Ministry of Water Resources. Unpublished data, 2014.
- Ground Water Estimation Committee., 1984, *Norms for Ground Water Assessment*, National Bank of Agriculture and Rural Development, Bombay, Indi.
- Healy, R. W., and Cook, P. G., 2002, *Using Ground Levels to Estimate Recharge*, Hydrogeology Journal. DOI 10. 1007/s10040 – 001 – 0178 – 0, p. 91 – 109.
- Ibrahim, O. S., Salih, S. A., and Ali, N. H., 2012, *Using of Climatic Water Balance to Assess the Reality of Ground Water Recharge in Baiji – Tikrit Sub Basin North West of Iraq*, Karkok Journal university, vol. 7, No. 1, p. 79 – 107. (In Arabic Language).
- National Center for Water Resources Management, Ministry of Water Resources. Unpublished data 2014.
- Ramadhan, A. A., Ali, M. H., and Al-Kubaisy, R. K., 2013, *Evaluation of Ground Water Recharge in Arid and Semi-Arid Regions Case Study of Dibdiba Formation in Karballa – Najaf Plateau*, Iraqi Journal of Science – University of Baghdad, vol. 54, No. 4, p. 902 – 910.
- Risser, D. W., Gburek, W. J., and Folmar, G. J., 2005, *Comparison of Methods for Estimating Ground Water Recharge and Base Flow at as Small Watershed Underlain by Fractured Bedrock in the Eastern United States*, U. S. Geological Survey Scientific Investigations Report, vol. 5038, 30 p.
- Sarma, P. S., Sodhi, S. K., and Rao, N. H., 1983, *Ground Water Management and Development in MRBC Area*, Resources Analysis and Plan for Efficient Water



Management, A case study of Mahi Right Bank Command Area, Gujarat, W.T.C., IARI, New Delhi.

- Seith, L. N., Kumar, D. N., Panda, S. N., and MAL, B. C., 2002, *Optimal Crop Planning and Conjunctive Use of Water Resources in a Coastat River Basin*, Water Resources Management: Kluwer Academic publishers. Printed in the Netherlands. vol. 16, p. 145 – 169.
- SOGREAH., 1983, *Upper Adhime Dams Project, Appendix (I)*, Republic of Iraq, Ministry of Irrigation – State Organization for Dams.
- Thornthwait, C. W., 1948, *An Approach Toward a Relation Classification of Climate*, Geographical Review 38: 55-94.
- Todd, D. K., *Ground Water Hydrology*, third Edition. John Wiley and Sons., Inc.2005.613p.

NOMENCLATURE

A_t	= total area, <i>ha</i> .
C	= conversation unit, dimensionless.
E_t	= potential evapotranspiration, <i>mm</i> .
GD	= discharge of ground water, m^3 .
GDE	= discharge from ground water, m^3 .
GDW	= discharge of ground water, m^3 .
GR	= recharge of ground water B, m^3 .
G_r	= recharge of ground water, <i>mm</i> .
P	= average of rainfall, <i>mm</i> .
R	= recharge of ground water for (WTF), <i>mm</i> .
R_{av}	= annual average rainfall, <i>mm</i> .
RBF	= recharge from base flow, m^3 .
RC	= recharge from irrigation fields, m^3 .
R_r	= recharge from rainfall, m^3 .
R_{r1}	= recharge from rainfall, <i>mm</i> .
RSF	= recharge from seepage flow of drains, m^3 .
SM	= soil moisture content, <i>mm</i> .
SR	= surface runoff, <i>mm</i> .
S_y	= specific yield.
WS	= water surplus, <i>mm</i> .
Δh_{ava}	= average of water Fluctuation (WTF). <i>m</i> .
ΔS	= change of ground storage, m^3 .
Δt	= period of recharge estimation, year.

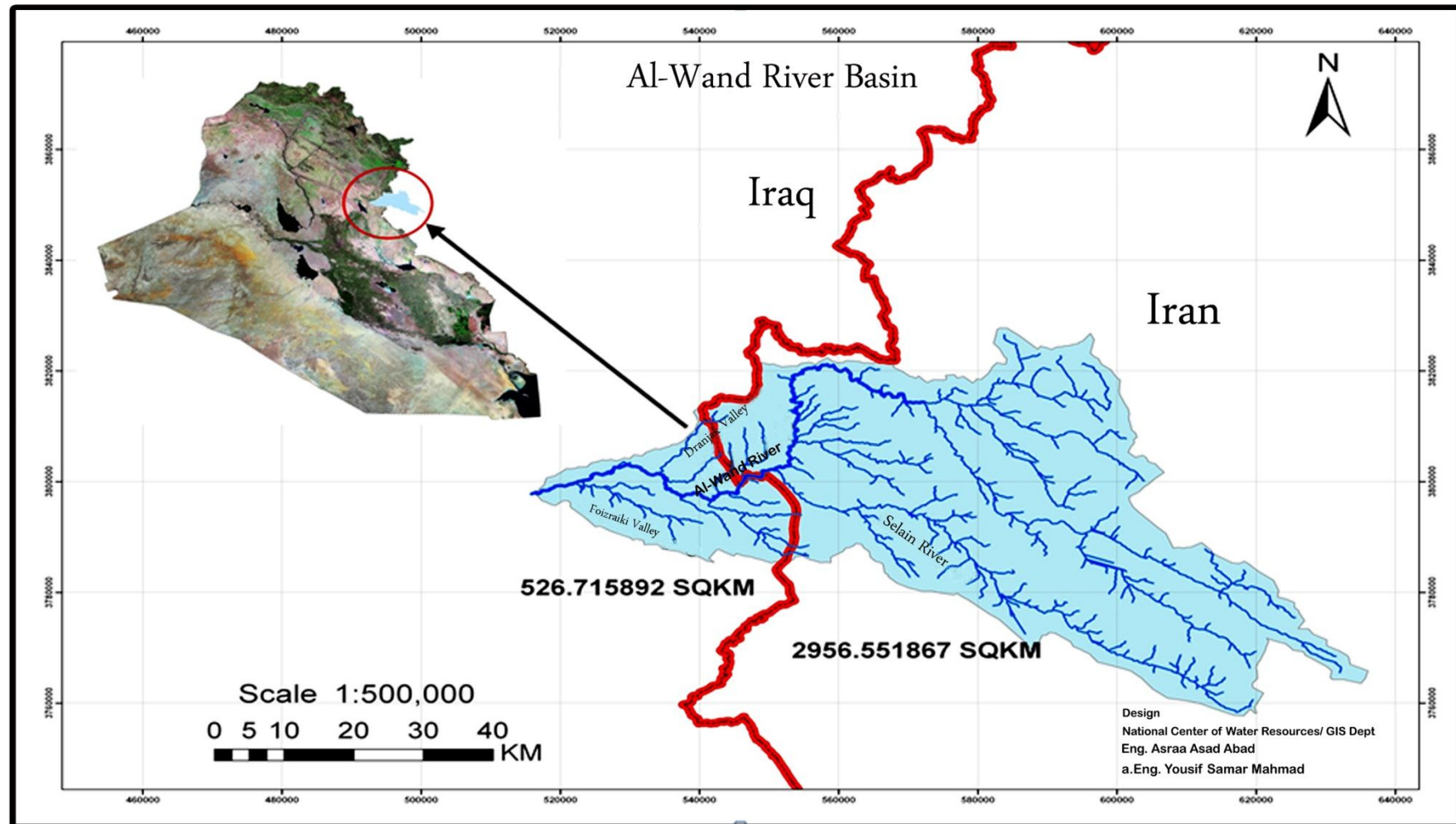


Figure 1. The geographic and basin of Al-Wand River, National Center of Water Resource.

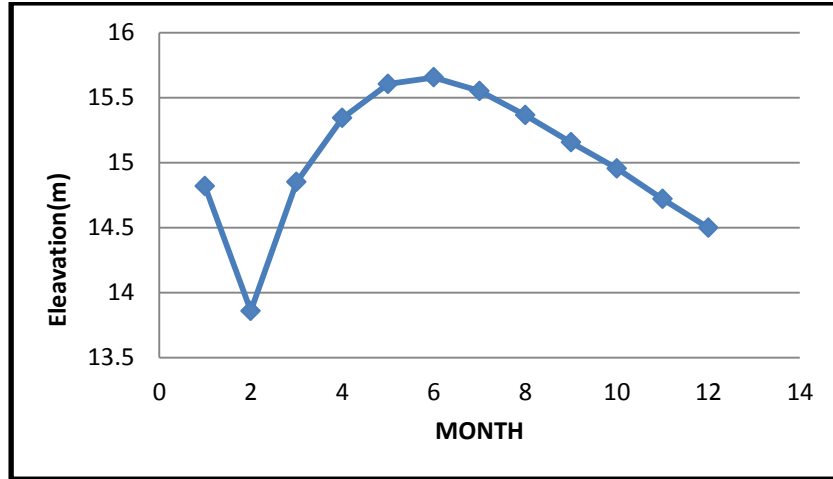


Figure 2. Average fluctuation of Bimmel observation well.

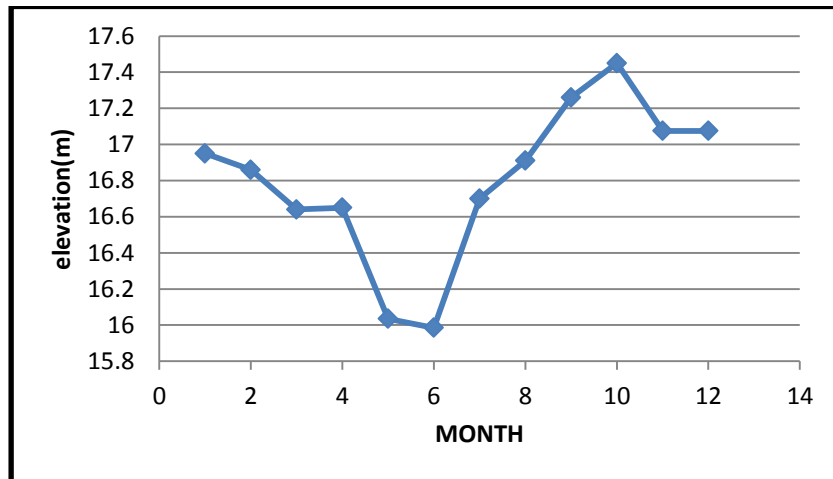


Figure 3. Average fluctuation of Mekhis observation well.

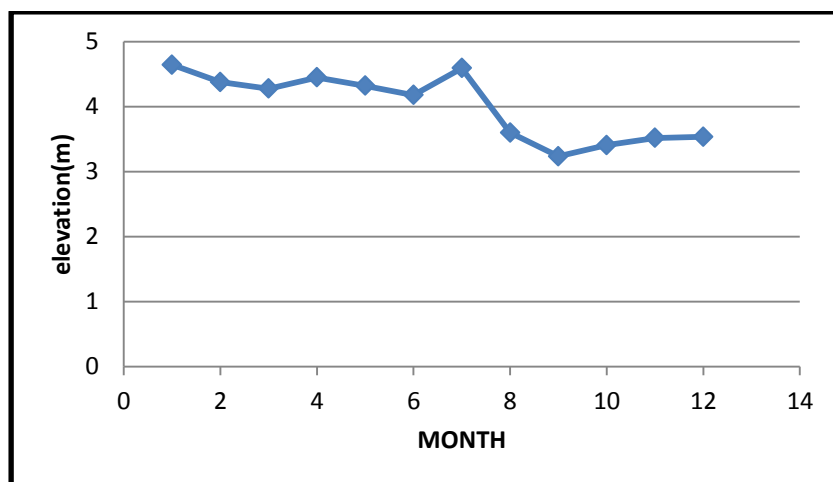


Figure 4. Average fluctuation of Ahmed Taher observation well.



Table 1. Observation wells details for Al-Wand River Basin.

No	well	Longitude	Latitude	Bed level (m). a.m. s.l	Depth (m)
1.	Binmel	45° 24' 19'	34° 18' 88'	190	60
2.	Mekhis	45° 21' 79'	34° 23' 23"	179	60
3.	Ahmed Tahar	45° 19' 13.1"	34° 19' 9.2"	171	60

Table 2. The elevations water of Binmel well (m), General Commission of Ground Water, 2014.

Month	1	2	3	4	5	6	7	8	9	10	11	12
2010	15	15	14.5	15	15.2	15.5	15.7	15.8	15.45	15.15	14.27	13.94
2011	14.5	13.07	14.07	14.57	14.97	15.03	15.04	15.06	14.63	14.33	13.91	13.01
2012	14.07	13	15.85	16	16.28	16.2	16.46	16.34	16.34	16.12	16.4	16.65
2013	15.7	14.37	14.98	15.8	15.97	15.89	15	14.26	14.2	14.22	14.3	14.4
average	14.817	13.86	14.85	15.342	15.605	15.655	15.55	15.365	15.155	14.955	14.72	14.5

Table 3. The elevations water of Mekhis well (m), General Commission of Ground Water, 2014.

Month	1	2	3	4	5	6	7	8	9	10	11	12
2010	17	17	16.5	16.5	16.25	16.15	16.2	16.3	16.7	17	17.08	17.06
2011	16.9	16.72	16.78	16.8	15.82	15.82	17.2	17.52	17.82	17.9	17.07	17.09
2012	-	-	-	-	-	-	-	-	-	-	-	-
2013	-	-	-	-	-	-	-	-	-	-	-	-
average	16.95	16.86	16.64	16.65	16.035	15.985	16.7	16.91	17.26	17.45	17.075	17.075

Table 4. The elevations water of Ahmed Taher well (m), General Commission of Ground Water, 2014.

Month	1	2	3	4	5	6	7	8	9	10	11	12
2010	4.5	4.5	4	4.4	4.35	4.3	4.38	3.75	3.7	4.26	4.31	4.32
2011	4.82	5.24	5.48	5.8	5.56	5.56	4.93	4.12	4.26	4.3	4.59	4.62
2012	4.65	4.18	4.28	4.36	4.25	3.87	5.8	4.1	2.95	2.94	2.93	2.95
2013	4.6	3.58	3.34	3.23	3.12	2.98	3.25	2.42	2.03	2.13	2.24	2.25
average	4.642	4.375	4.275	4.447	4.32	4.177	4.59	3.597	3.235	3.407	3.517	3.535



Table 5. The recharge and ground storage are for observation wells for (WTF) method.

No	well	Recharge(mm)	$\Delta S(m^3)$
1.	Binmel	40.5	4123305
2.	Mekhis	43.8	4459278
3.	Ahmed Tahar	5.25	534502.5

Table 6. Mean monthly rainfall (mm) for period (1988-2008), National Center of Water Resource.

Years	Jan.	Feb.	Mar.	Apr.	May.	Jun.	Jul.	Aug.	Sep	Oct.	Nov.	Dec.
1988.00	68.00	62.30	51.80	39.90	0.00	0.00	0.00	0.00	0.00	9.90	6.70	57.20
1989.00	13.90	63.20	16.40	0.00	0.10	0.00	0.00	0.00	0.00	0.00	49.60	31.40
1990.00	33.70	109.10	90.30	26.30	0.00	0.00	0.00	0.00	0.00	0.40	12.50	15.10
1991.00	43.30	95.50	65.50	8.60	8.00	0.00	0.00	0.00	0.00	10.40	12.20	117.30
1992.00	62.20	69.20	11.20	81.60	81.60	0.00	0.00	0.00	0.00	0.00	18.00	55.90
1993.00	71.10	46.70	47.50	22.20	5.30	0.00	0.00	0.00	0.00	31.90	54.20	42.40
1994.00	71.30	13.80	64.40	78.20	78.20	0.80	0.00	0.00	0.00	52.00	132.30	50.80
1995.00	6.40	67.00	86.90	31.80	31.80	0.20	0.00	0.00	0.00	0.00	24.20	32.30
1996.00	103.80	11.90	94.70	34.80	4.90	0.00	0.00	0.00	0.00	1.90	0.50	38.80
1997.00	60.50	16.10	102.70	8.60	0.00	0.00	0.00	0.00	0.00	14.00	112.10	70.70
1998.00	118.30	10.50	0.50	5.50	0.00	0.00	0.00	0.00	0.00	0.00	28.80	0.00
1999.00	90.50	43.70	29.00	3.20	0.00	0.00	0.00	0.00	0.00	11.00	0.00	19.50
2000.00	38.70	2.70	59.70	7.70	1.70	0.00	0.00	0.00	0.00	1.40	59.30	154.40
2001.00	31.90	44.20	55.30	61.50	0.00	0.00	0.00	0.00	0.00	1.20	18.60	58.10
2002.00	105.80	41.60	24.60	24.60	0.00	0.00	0.00	0.00	0.00	7.60	39.50	55.30
2004.00	89.90	21.00	4.40	9.00	20.10	0.00	0.00	0.00	0.00	0.00	59.10	65.60
2005.00	57.40	34.00	0.80	19.90	0.80	0.00	0.00	0.00	0.00	0.80	73.70	21.70
2006.00	57.40	65.40	8.00	35.80	0.00	0.00	0.00	0.00	0.00	0.00	7.40	16.80
2007.00	89.40	57.30	10.80	59.10	4.00	0.00	0.00	0.00	0.00	16.90	17.70	4.00
2008.00	52.00	16.80	8.30	0.00	0.00	0.00	0.00	0.00	0.00	0.00	0.00	12.60
Average	62.45	44.60	41.64	27.92	11.83	0.00	0.00	0.00	0.00	11.33	36.39	46.00

Table 7. The monthly water surplus for Water Balance of Climate to Basin method.

No	Average rainfall(mm)	ET(mm)	WS
Jan.	62.45	38	24.45
Feb.	44.6	52	0
Mar.	41.64	89	0
Apr.	27.92	135	0
May	11.83	199	0
Jun.	0	237	0
Jul.	0	254	0
Aug.	0	236	0
Sep	0	178	0
Oct.	11.33	135	0
Nov.	36.39	69	0
Dec.	46	39	7

Table 8. The details of the productivity wells that situated in Al-Wand Basin, **General Commission of Ground Water, 2014.**

No	X	Y	Well depth (m)	Dynamic water depth* (m)	Static water depth* (m)	Discharge (L/S)
1.	45 23 18.6	34 18 15.8	54	22.5	25	3
2.	45 23 33.5	34 18 22.0	52	24	25.6	2
3.	45 21 08.1	34 21 04.2	42	18.29	21	5
4.	45 21 32.9	34 20 39.0	65	20.6	28.46	6
5.	45 21 31.2	34 20 24.1	60	19.32	23.67	2
6.	45 21 31.3	34 20 28.0	54	14	18.2	2
7.	45 15 25.0	34 23 15.9	17	5.5	7.5	2
8.	45 13 05.2	34 21 59.7	50	5	7.2	9
9.	45 21 16.7	34 23 52.9	9	4.15	5.5	3
10.	45 20 51.4	34 24 00.0	14	7	8.75	4
11.	45 21 05.2	34 24 00.2	12	3	4.5	2
12.	45 21 14.4	34 23 50.5	14	3.7	5.3	3
13.	45 21 06.3	34 23 40.7	12	3.65	5.4	3
14.	45 23 34.1	34 22 51.4	9	3.24	5	3
15.	45 23 34.4	34 22 47.7	72	4.5	25.25	5
16.	45 23 27.7	34 22 45.0	52	4.75	9	3
17.	45 23 31.6	34 22 53.7	54	5.5	13	3
18.	45 22 27.4	34 21 43.2	8	6.59	7.5	2
19.	45 23 07.6	34 22 34.5	45	20	35	3
20.	45 23 36.3	34 22 33.4	42	13.12	17.2	3



Table 8. continued

21.	45 23 20.2	34 22 40.5	52	15	45	2
22.	45 23 10.8	34 22 41.7	44	16	40	1
23.	45 22 38.9	34 21 49.1	30	9.65	12.5	4
24.	45 22 37.8	34 21 47.3	13	9.15	10.35	3
25.	45 22 00.3	34 21 29.4	12	7.3	9.2	3
26.	45 22 02.2	34 21 27.6	12	7.33	9.35	3
27.	45 22 05.9	34 21 29.8	12	7.71	9.75	3
28.	45 22 04.3	34 21 30.8	12	7.36	9.13	3
29.	45 22 08.1	34 21 30.6	16	7.37	9.47	3
30.	45 22 14.8	34 21 36.6	13	7.5	9.5	3
31.	45 22 16.8	34 21 39.3	30	7.3	8.95	4
32.	45 22 06.1	34 21 34.7	13	7.51	8.9	3
33.	45 22 04.5	34 21 36.0	12	7.25	8.85	3
34.	45 22 02.3	34 21 33.3	12	7.17	8.44	3
35.	45 20 59.9	34 21 40.0	12	6.5	9	3
36.	45 20 56.4	34 21 44.4	8	6.1	7.35	3
37.	45 20 53.1	34 21 45.7	7	7	8.9	3
38.	45 20 57.8	34 21 43.0	14	6.15	7.9	4

* The datum from ground surface.

Table 9. The recharge and ground storage for suggested methods.

No	Method	Recharge(mm)	$\Delta S(m^3)$
1.	Water Table Fluctuation	28.85	3039028.5
2.	Water Balance of Climates	14.29	1454864.9
3.	Water Balance of basin	61.91	4884853.16

Experimental Investigation of Natural Convection into a Horizontal Annular Tube with Porous Medium Effects

Saad Najeeb Shehab

Lecturer

Engineering College- Al-Mustansiriyah University

E-mail: saad_najeeb16@yahoo.com

ABSTRACT

In this work, an experimental investigation has been done for heat transfer by natural-convection through a horizontal concentric annulus with porous media effects. The porous structure in gap spacing consists of a glass balls and replaced by plastic (PVC) balls with different sizes. The outer surface of outer tube is isothermally cooled while the outer surface of inner tube is heated with constant heat flux condition. The inner tube is heated with different supplied electrical power levels. Four different radius ratios of annulus are used. The effects of porous media material, particles size and annulus radius ratio on heat dissipation in terms of average Nusselt number have been analyzed. The experimental results show that the average Nusselt number increases with increasing annulus radius ratio and particle diameter for same porous media material. Furthermore, two empirical correlations of average Nusselt number with average Rayleigh number for glass and PVC particles are developed. The present experimental results are compared with previously works and good correspondence is showed.

Key words: annular tube, porous medium, horizontal, balls, natural-convection.

تقصي عملي للحمل الطبيعي داخل أنبوب حلقي أفقي مع تأثير الوسط المسامي

سعد نجيب شهاب

مدرس

كلية الهندسة - الجامعة المستنصرية

الخلاصة

في هذا البحث أجري تقصي عملي لانتقال الحرارة بالحمل الطبيعي خلال تجويف حلقي أفقي متحد المركز مع تأثير الوسط المسامي. يتكون الوسط المسامي في الفراغ البيني للتجويف الحلقي من كرات زجاجية وأستبدلت بكرات بلاستيكية وبأحجام مختلفة. تم تبريد السطح الخارجي للأنبوب الخارجي بثبوت درجة الحرارة بينما تم تسخين السطح الخارجي للأنبوب الداخلي بثبوت الفيض الحراري. تم تسخين الأنبوب الداخلي بعدة مستويات للقدرة الكهربائية المجهزة. أستخدمت أربع نسب مختلفة لنصف قطر التجويف الحلقي. تم تحليل تأثير مادة الوسط المسامي المستخدم وحجم (قطر) الكريات ونسبة نصف القطر للتجويف الحلقي على التبريد الحراري بدلالة معدل رقم نسلت. بينت النتائج العملية أن معدل رقم نسلت يزداد مع زيادة نسبة نصف القطر للأنبوب الحلقي وقطر الكريات لنفس مادة الوسط المسامي. إضافة إلى أستنباط علاقتين ارتباطيتين عمليتين تحكم معدل رقم نسلت مع معدل رقم ريليه للكريات الزجاجية والبلاستيكية. تم مقارنة النتائج العملية للبحث الحالي مع بحوث سابقة وأظهرت توافقاً جيداً.

الكلمات الرئيسية: أنبوب حلقي ، وسط مسامي ، أفقي ، كريات ، الحمل الطبيعي .



1. INTRODUCTION

The porous media is used generally to improve the heat transfer rate in thermal systems which work by heat convection. The convective heat transfer through a porous media has many thermal engineering and industrial applications including the systems of nuclear reactor cooling, nuclear waste disposal, engineering of thermal insulation, grain storage and drying, ground water flows and filtration processing, systems of water purification (RO), solar collectors, heat exchangers, electrochemical processes, oil recovery processes, extraction of the geothermal energy, thermal storage systems, regenerators systems, furnaces and ceramic processes, ... etc.

Prasad, and Kulacki, 1985 studied numerically and experimentally the natural-convection through short concentric vertical cylinders filled with porous media for wide range of radius ratio and height to gap width ratio. They used glass beads and water as porous media. They obtained a good agreement between measured temperatures at different locations with predicted temperatures from numerical solution. **Atwan, et al., 2000** investigated experimentally the heat transfer and flow by forced-convection through a horizontal annulus filled with porous medium. They found that the larger values of convection heat transfer coefficient are obtained with packing particles of higher thermal conductivity and the Nusselt number increases with the ratio of inner to outer cylinders radii increasing. **Khanafar, and Chamkha, 2003** presented a numerical study for mixed-convective heat transfer inside a horizontal annulus filled with a fluid saturated porous media by heating the inner cylinder and cooling the outer cylinder. They used the finite element method to solve the governing equations of problem. They discussed the influence of Darcy number on the isotherms, streamlines and heat transfer rate as well as the average Nusselt number at different annulus gap. They compared the numerical data with a previous works and the results show excellent agreement. **Shi, et al., 2006** presented a numerical solution using finite difference method (FDM) based lattice Boltzmann model to simulate the fluid flows and isotherms of free-convection heat transfer in a horizontally concentric annulus for wide range of Prandtl and Rayleigh numbers. They showed good stability of the numerical model and well agreement of presented results compared with the previous studies. **Al-Joboury, et al., 2009** studied theoretically and experimentally free heat convective between two concentric horizontal pipes filled with two types of materials, iron and glass beads as a porous medium under conditions of constant heat flux on the inner pipe surface and constant temperature on the outer pipe surface. They showed that the using of iron spheres porous media as high conductivity material canceled the heat transfer by convective through the gap of annulus. Also they found that the heat dissipation ability from the surface of inner pipe is a function of Rayleigh number. **Hussein, et al., 2009** investigated theoretically and experimentally natural-convection heat transfer through the annulus of two concentric vertical cylinders filled with gravel porous media under constant heat flux condition of inner cylinder. They solved that the governing equations by Fluent package and plotted the temperature profiles for three different radius ratio and different heat fluxes. They developed the empirical correlations between Nusselt number with Rayleigh number and Nusselt number with radius ratio of concentric cylinders. **Mahdi, et al., 2013** presented a review investigation for improvement of natural convective heat transfer using porous medium and nano-fluids. They showed that the convection heat transfer in terms of heat transfer coefficient increased with porous medium because the best thermal conductivity and thermal dissipation area of beads. **Ahamad, et al., 2014** presented a numerical study of natural heat convection inside vertical annular cylinders with porous medium effects. They visualized the fluid flow and convection heat transfer as streamlines and isotherms with influence of radius ratio and aspect ratio using finite element technique.

The purpose of the present work is to present an experimental study for natural convective heat transfer through a horizontal concentric annular tube filled with a porous media. It is focused on the influence of several parameters like packing material, particle (ball) diameter, radius ratio of the annular tube and wall heat flux on the characteristics of natural-convective such as average convection heat transfer coefficient, average Nusselt number and average Rayleigh number. The present work is carried out for two packing materials namely, glass and plastic (PVC) balls with air as a fluid working for different particle sizes and wide range of the annulus radius ratios.

2. EXPERIMENTAL WORK

2.1 Experimental Test Rig

The experimental test rig shown in **Fig. 1** is especially designed and manufactured for covering experiments of the present work. It consists of test-section, two V-wooden blocks, water inlet and outlet, voltage regulator with digital display, digital multi-meter, data logger thermometer, thermocouples and planar table.

The test section involves a horizontal annulus from two concentric tubes as shown in **Fig. 2**, the outer tube made of polished steel has fixed inner radius (r_o) of 38 mm and wall thickness of 2 mm while the inner tube made of polished aluminum has four different outer radius (r_i) of 6, 8, 10 and 12.5 mm to obtain a wide range of the annulus radius ratio (R) and wall thickness of 1 mm. Each tube has constant length (L) of 400 mm. The annulus gap is carefully filled with glass solid balls (thermal conductivity of 1.1 W/m.K) with diameter (d_p) of 12.5 mm and replaced by plastic PVC (polyvinyl-chloride) solid balls (thermal conductivity up to 0.16 W/m.K) with two particle diameters (d_p) namely, 6.25 and 12.5 mm. The inner tube of annulus is heated electrically from inside with different heat input levels using heating element with power up to 600 W and kept along the center of inner tube. The small gap between the heating element and inner surface of inner tube is filled by the sand to ensure natural-convection in the electrical heater. The voltage regulator with digital display type SAKO-TDGC₂ is used to govern the supplied voltage input to the electrical heater. Also a digital multi-meter type VICTOR-VC890C⁺ is used to measure voltage and alternating current (AC) passing through the heater.

The ends of the concentric annulus are closed by two Teflon (polytetrafluoroethylene) covers (thermal conductivity up to 0.25 W/m.K) with large thickness up to 25 mm to minimize heat lost from annulus ends and to fix the two tubes of concentric annulus. One of these covers is drilled with small drill to pass the thermocouples wires and electrical heater cable and then sealed by thermal epoxy. The outer tube of annulus is isothermally cooled by circulation water system through a coiled copper pipe around the outer surface of outer tube and then the whole test-section is covered and insulated by thick layer about 50 mm of glass wool to minimize the heat dissipating to surrounding. The test-section assembly is horizontally put on two V-wooden blocks and planar table.

The outer surface temperature of inner tube and inner surface temperature of outer tube are measured using twelve type-K calibrated thermocouples; six to every tube are inserted longitudinally with angular displacement of 180° between them at suitable locations. The thermocouples are joined with twelve-channels of data logger thermometer type BTM-4208SD. Another two same K-type calibrated thermocouples are oppositely inserted in the middle of outer surface for the outer tube to record the temperatures by digital multi-meter. Additional two same type-K calibrated thermocouples are used to read the temperatures difference through Teflon covers to estimate the thermal dissipation lost by conduction as illustrated in **Fig. 2**.

2.2 Experimental Procedure and Calculations

Twenty four cases are tested and studied according to the flow chart in **Fig. 3**. The cases includes two different wall heat fluxes ($q= 800$ and 1750 W/m^2), glass and plastic (PVC) porous media, one particle (ball) diameter ($d_p= 12.5 \text{ mm}$) for glass porous media and two particle diameters ($d_p= 6.25$ and 12.5 mm) for plastic porous media and four radii ratios of annular tube ($R= r_i / r_o$) namely, 0.16 , 0.21 , 0.26 and 0.33 . The readings of thermocouples have been recorded after (90-120) minutes and when the difference between two temperature readings within was $0.5 \text{ }^\circ\text{C}$ under steady-state condition, the supplied voltage and current to the heating element are recorded.

The electrical power input (Q_{in}) to the heating element inside inner tube of the annulus is:

$$Q_{in} = I V \quad (1)$$

It is transformed to thermal energy and transferred through the annulus gap by natural heat convection (Q_c), heat radiation (Q_r) in addition to heat conduction (Q_{cd}) from ends of horizontal annular tube. Hence,

$$Q_{in} = Q_c + Q_r + Q_{cd} \quad (2)$$

The radiation heat lost (Q_r) between outer surface of inner tube and inner surface of outer tube of the annulus is computed as **Lienhard, 2008** and **Long, and Sayma, 2009**:

$$Q_r = \frac{\sigma A_i (T_i^4 - T_o^4)}{\frac{1}{\varepsilon_i} + \frac{A_i}{A_o} \left(\frac{1}{\varepsilon_o} - 1 \right)} \quad (3)$$

It is found that (Q_r) is small about 4% to 7% of electrical heat input (Q_{in}) for all cases because of inner and outer tubes are made from low emissivity materials namely polished aluminum ($\varepsilon_i= 0.05$) and polished steel ($\varepsilon_o= 0.1$) respectively.

The thermal lost by conduction (Q_{cd}) is defined as thermal potential difference to thermal resistance. It is found very small (less than 2%) of heat input (Q_{in}) across ends of annular tube because it's well insulated using Teflon covers and can be neglected, then equation (2) can be written as follows:

$$Q_c = I V - Q_r \quad (4)$$

Also the heat transfer rate by free-convection (Q_c) to porous medium is calculated by Newton's equation of cooling, **Favre-Marient, and Tardu, 2009**:

$$Q_c = h_{av} A_i (T_{iav} - T_{oav}) \quad (5)$$

Hence, the average convection heat transfer coefficient (h_{av}) is evaluated as:

$$h_{av} = \frac{I V - Q_r}{A_i (T_{iav} - T_{oav})} \quad (6)$$

where, T_{iav} and T_{oav} are the average surface temperatures of inner and outer tubes respectively, measured as:



$$T_{iav} = \sum_{i=1}^n \frac{T_i}{n} \quad (7)$$

and;

$$T_{oav} = \sum_{i=1}^n \frac{T_o}{n} \quad (8)$$

A_i and A_o are the outer surface area of inner tube and the inner surface area of outer tube respectively, they are computed as follows:

$$A_i = 2 \pi r_i L \quad (9)$$

$$A_o = 2 \pi r_o L \quad (10)$$

The average Nusselt number (Nu_{av}), based on the annulus gap (δ) as characteristics length of geometry can be simply computed as, **Vafai, 2005** and **Nield, and Bejan, 2013**:

$$Nu_{av} = \frac{h_{av} \delta}{k_e} \quad (11)$$

where,

$$\delta = 2(r_o - r_i) \quad (12)$$

k_e is the effective (overall) thermal conductivity of the porous media and defined as a weighted arithmetic mean of thermal conductivities of fluid (air) and solid (balls) as **Vafai, 2005** and **Nield, and Bejan, 2013**:

$$k_e = \phi k_f + (1 - \phi) k_s \quad (13)$$

ϕ is the porosity of porous media and defined as ratio between volume of the void space (ϑ_v) to bulk volume (ϑ_b) then **Vafai, 2005** and **Nield, and Bejan, 2013**:

$$\phi = \frac{\vartheta_v}{\vartheta_b} = \frac{\vartheta_b - \vartheta_p}{\vartheta_b} \quad (14)$$

The bulk volume (ϑ_b) is calculated as, **Vafai, 2005** and **Nield, and Bejan, 2013**:

$$\vartheta_b = \pi L (r_o^2 - r_i^2) \quad (15)$$

and the particles volume (ϑ_p) is the product of particles (balls) number (N) by volume of one ball as:

$$\vartheta_p = N \left[\frac{4}{3} \pi \left(\frac{d_p}{2} \right)^3 \right] \quad (16)$$

The average Grashof number (Gr_{av}) is **Vafai, 2005** and **Nield, and Bejan, 2013**:

$$Gr_{av} = \frac{g\beta(T_{iav} - T_{oav})\delta^3}{\nu^2} \quad (17)$$

Define average Rayleigh number (Ra_{av}) as the product of the average Grashof number and Prandtl number, **Lienhard, 2008**:

$$Ra_{av} = Gr_{av} Pr \quad (18)$$

where,

$$Pr = \frac{\nu}{\alpha} = \frac{C_p \mu}{k_e} \quad (19)$$

and,

$$\nu = \frac{\mu}{\rho} \quad (20)$$

By substituting Eqs. (17), (19) and (20) in Eq. (18), the average Rayleigh number based on the annulus gap (δ) can be written as follows:

$$Ra_{av} = \frac{g\beta C_p \rho_f \rho_s (T_{iav} - T_{oav}) \delta^3}{\mu k_e} \quad (21)$$

$$\beta = \frac{1}{T_m} \quad (22)$$

All properties of fluid (air) inside a gap spacing of the annular tube are taken at mean temperature (T_m). It is calculated as the arithmetic mean between average surface temperature of the inner and outer tube along the annulus gap as follows:

$$T_m = \left(\frac{T_{iav} + T_{oav}}{2} \right) + 273.18 \quad (23)$$

3. RESULTS AND DISCUSSION

The present work investigates experimentally the effect of porous media material, particle diameter (d_p), radius ratio of the annular tube (R) and heat flux (q) on the performance and characteristics of natural-convective heat transfer through a horizontal concentric annular tube filled with porous medium.

Figs. 4 and **5** illustrate the behavior of average Nusselt number with variation of annulus radius ratio for two tested materials namely glass and PVC balls at two different heat fluxes. Two different particle diameters are used for PVC porous medium to study the influence of particle size on performance of natural-convection while it's constant for glass. The figures illustrate that average Nusselt number always increases by increasing the annulus radius ratio and heat flux. This increases because average Nusselt number depends directly on annulus gap and natural-convection heat transfer coefficient as function of heat input. **Fig. 4** clears that the highest values of average Nusselt number is linked with the use of glass porous media compared with plastic PVC for same particles size because the thermal conductivity of glass balls are

higher seven times approximately than PVC particles and the thermal conductivity of balls effects directly on heat transfer rate. An increase in annulus radius ratio or a decrease in the annulus gap yields faster flow and giving higher and thinner of boundary layers and thus, higher rate of heat transfer is based on average Nusselt number. Also **Fig. 5** illustrates that the average Nusselt number increases with the increase of particle diameter for same material because increasing of the convection currents through annulus gap and consequently increasing in the heat transfer rate.

Figs. 6 and 7 show the variation of average Nusselt number with average Rayleigh number based on the annulus gap, heat flux and particle diameter for two different porous media materials. The average Rayleigh number increases always as the average Nusselt number, heat flux and particle diameter increases. Highest values of the average Rayleigh number with higher thermal conductivity of glass particles respect to the PVC packing medium is shown in **Fig. 6**. The high thermal conductivity of glass particles causes high contact conduction for particles dabbing the heated surface inside of the annulus. Hence, an increase in thermal conductivity of particle leads an increase in rate of heat transfer in terms of average Nusselt and Rayleigh numbers at same particle diameter.

Fig. 8 shows a comparison of average Nusselt number of present work with experimental results of Al-Joboury et al. work for glass particles. It shows a good similarity in the behavior, but the present work gives an average Nusselt number higher than that done in Al-Joboury et al. work because higher heat flux levels are used in the present work. Based on the experimental results showed in **Figs. 8 and 9**, two empirical correlations of average Nusselt number as a function of average Rayleigh number are developed for glass and PVC packing materials as follows:

$$Nu_{av} = 0.000002Ra_{av}^3 - 0.0005Ra_{av}^2 + 0.0546Ra_{av} + 0.7269 \quad (24)$$

which is valid for glass particle at: $d_p = 12.5 \text{ mm}$, $20 \leq Ra_{av} \leq 175$ and $0.16 \leq R \leq 0.33$.

$$Nu_{av} = 0.000004Ra_{av}^3 - 0.0006Ra_{av}^2 + 0.044Ra_{av} + 1.0468 \quad (25)$$

which is valid for PVC particle at: $6.25 \text{ mm} \leq d_p \leq 12.5 \text{ mm}$, $15 \leq Ra_{av} \leq 135$ and $0.16 \leq R \leq 0.33$.

Figs. 10 and 11 illustrate a comparison of the correlated average Nusselt numbers using the correlation Eqs. (24) and (25) with the experiments of present work for glass and PVC packing materials. They are clear that most of experimental results are located within 10% and 6% of the mentioned correlation equations for glass and PVC particles respectively.

4. CONCLUSIONS

Steady state natural-convective heat transfer through a porous structure inside gap spacing of concentric annular tube in horizontal position is investigated experimentally. The inner tube is electrically heated under constant heat flux while the outer tube is isothermally cooled. Two types of porous media materials, two different wall heat fluxes and particle diameters with four radii ratios are used. The conclusions can be summarized as follows:

- The average Nusselt number increases as the particle diameter increases for same material of porous media.
- Average Nusselt number always increases with increasing radius ratio of annular tube and wall heat flux.



- The average Rayleigh number based on the annulus gap increases as the average Nusselt number increases.
- The glass porous media gave better natural-convective heat transfer performance in terms of average Nusselt number reaching to 26% higher compared with plastic (PVC) particles for same size (diameter).
- Two experimental correlations are developed to predict the average Nusselt number for annulus tube filled with glass and PVC porous medium.

REFERENCES

- Ahamad, N. A., El-Arabawy, H. A. and Ahmed, S. I., 2014, *Visualization of Natural Convection in a Vertical Annular Cylinder with a Partially Heat Source and Varying Wall Temperature*, International Journal of Engineering Research and Applications, Vol. 4, Issue 9, version 1 , pp. 185-197.
- Al-Joboury, O. K., Ali, O. M., and Yaseen, K. F., 2009, *Experimental and Theoretical Study of Natural Convection Heat Transfer between Two Concentric Cylinder Filled with Porous Medium*, Journal of Al-Rafidain Engineering, Vol. 17, No. 6, pp. 65-75.
- Atwan, E. F. , El-Shamy, A. R. and El-Shazly, K. M., 2000, *An Experimental Study of Forced Convection in Horizontal Porous Annuli*, Al-Azhar Engineering Sixth International Conference.
- Favre-Marient , M. and Tardu, S., 2009, *Convective Heat Transfer*, John-Wiley & Sons, Inc., 1st Edition, USA.
- Hussein, A. M., Tahseen, T. A. and Jasim, A. H., 2009, *Convection Concentric Annulus Vertical Cylinders Filling Porous Media*, Journal of Kirkuk University-Scientific Studies, Vol. 4, No. 2 , pp. 55-71.
- Khanafer, K. and Chamkha, A. J., 2003, *Mixed Convection within a Porous Heat Generating Horizontal Annulus*, International Journal of Heat and Mass Transfer (46), p.p. 1725-1735
- Lienhard, J.H., 2008, *A Heat Transfer Textbook*, Phlogiston Press, 3rd Edition, U.S.A.
- Long, C. and Sayma, N., 2009, *Heat Transfer*, Ventus Publishing, 1st Ed., London.
- Mahdi, R. A., Mohammed, H. A. and Munisamy, K.M., 2013, *Improvement of Convection Heat Transfer by Using Porous Media and Nanofluid: Review*, International Journal of Science and Research, Vol. 2, Issue 8.
- Nield, D. A. and Bejan, A., 2013, *Convection in Porous Media*, Springer Science & Business Media, New York.
- Prasad, V. and Kulacki, F. A., 1985, *Natural Convection in Porous Media Bounded by Short Concentric Vertical Cylinders*, Journal of Heat Transfer 107(1), pp. 147-154.



- Shi, Y., Zhao, T. S. and Guo, Z. L., 2006, *Finite Difference-Based Lattice Boltzmann Simulation of Natural Convection Heat Transfer in a Horizontal Concentric Annulus*, Journal of Computers & Fluids (35) , pp.1-15.
- Vafai, K., 2005, *Handbook of Porous Media*, Taylor & Francis Group, 2nd Edition, USA.

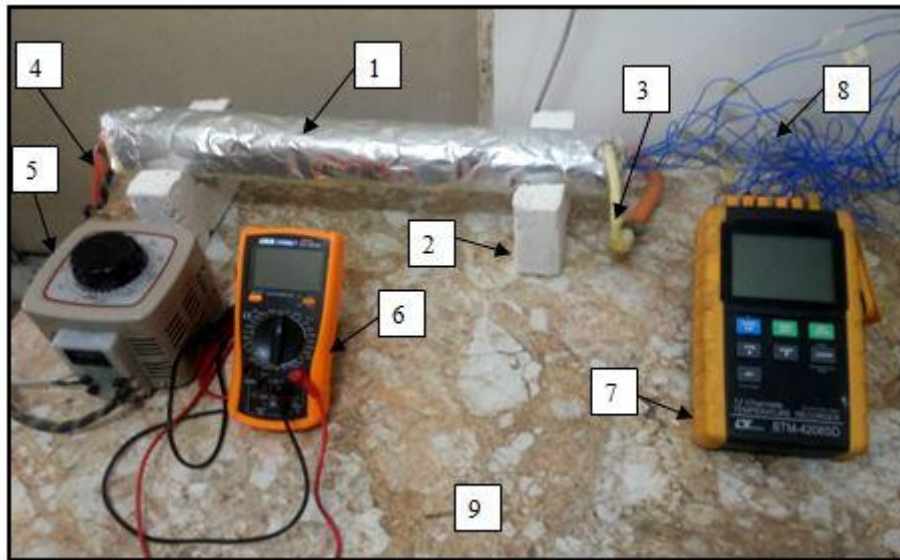
NOMENCLATURE

A= surface area of heat transfer, m².
C_p= specific heat at constant pressure, kJ/kg.K .
d_p= diameter of particle (ball), m.
g= gravitational acceleration, m/s².
Gr= Grashof number, dimensionless.
h= convection heat-transfer coefficient, W/m².K .
I= input current intensity, A.
k= thermal conductivity, W/m.K .
L= length of the annular tube, m.
N= number of particles (balls), dimensionless.
Nu= Nusselt number, dimensionless.
Pr= Prandtl number, dimensionless.
q= heat flux, W/m².
Q_c= convection heat transfer, W.
Q_{cd}= conduction heat lost, W.
Q_{in}= electrical power input, W.
Q_r= radiation heat transfer, W.
r= radius tube, m.
R= radius ratio (R= r_i /r_o), dimensionless.
Ra= Rayleigh number, dimensionless.
T= surface temperature, °C.
T_m= arithmetic mean of the surface temperatures, °C.
V= voltage supplied, V.
β= volumetric coefficient of thermal expansion, 1/K.
δ= annulus gap, m.
ε= emissivity of the surface, dimensionless.
ϑ_b= bulk volume, m³.
ϑ_p= volume of particles (balls), m³.
ϑ_v= volume of a void space, m³.
μ= dynamic viscosity, kg/m.s.
ρ= density, kg/m³.
σ= Stefan-Boltzmann constant, σ = 5.67 × 10⁻⁸ W/ m².K⁴.
φ= porosity of media porous, dimensionless.
ν= kinematic viscosity, m²/s.

Subscript symbols:

av= average.
e= effective.
f = fluid (air).
i= outer surface of inner tube for annulus.

o= inner surface of outer tube for annulus.
s= solid (balls).



1. Test-section 2. V-wooden block 3. Water flow inlet 4. Water flow outlet 5. Voltage regulator with digital display 6. Digital multi-meter 7. Data logger thermometer 8. Thermocouple wires 9. Planar table.

Figure 1. Photograph of the experimental test rig.

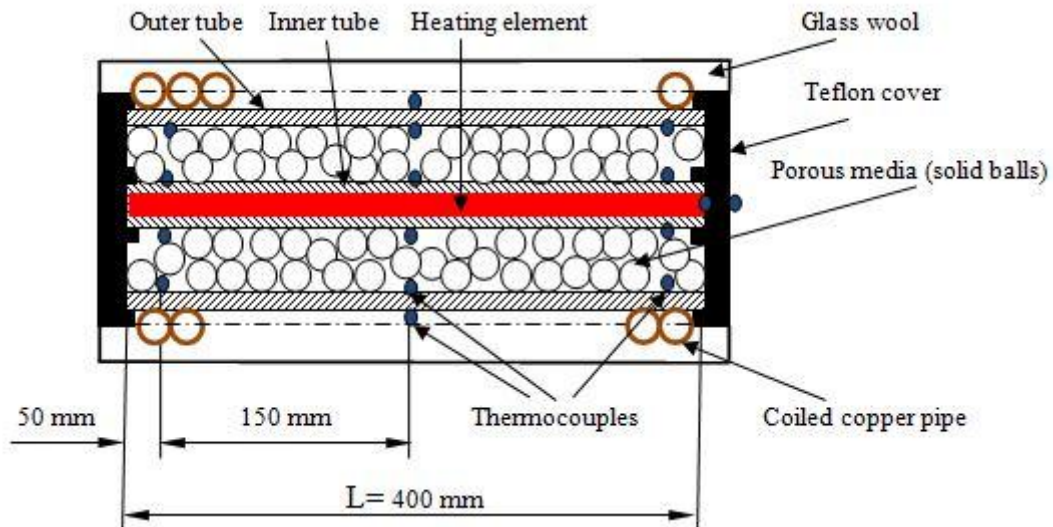


Figure 2. Longitudinal section of the test-section with locations of the thermocouples.

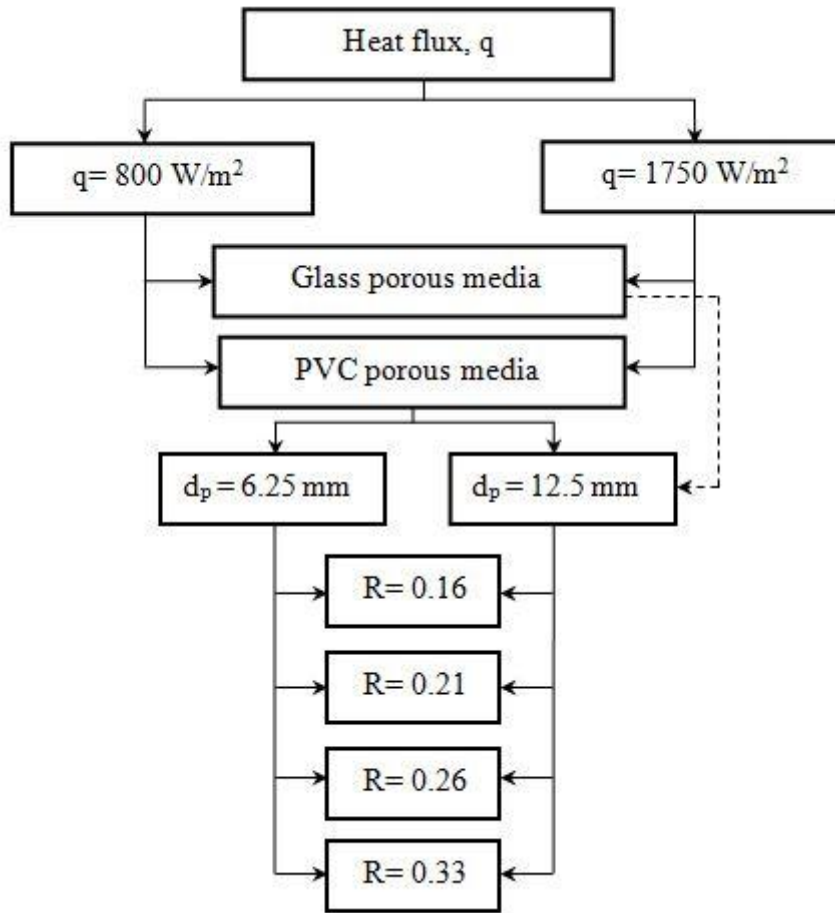


Figure 3. Flow chart of the tested cases.

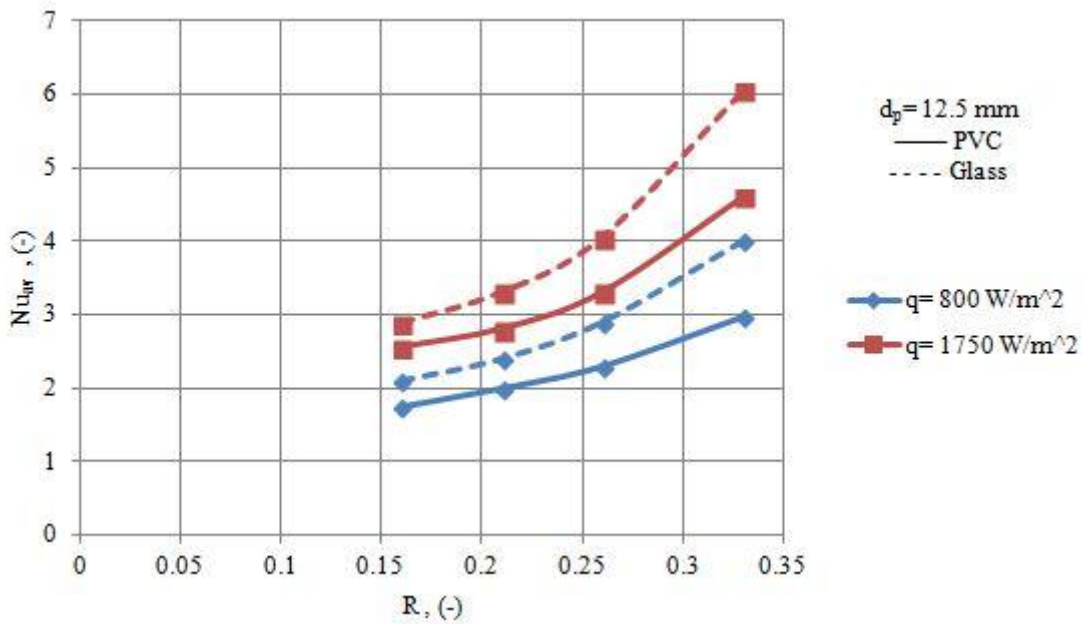


Figure 4. Average Nusselt number against radius ratio for PVC and glass porous medium with same particle diameters.

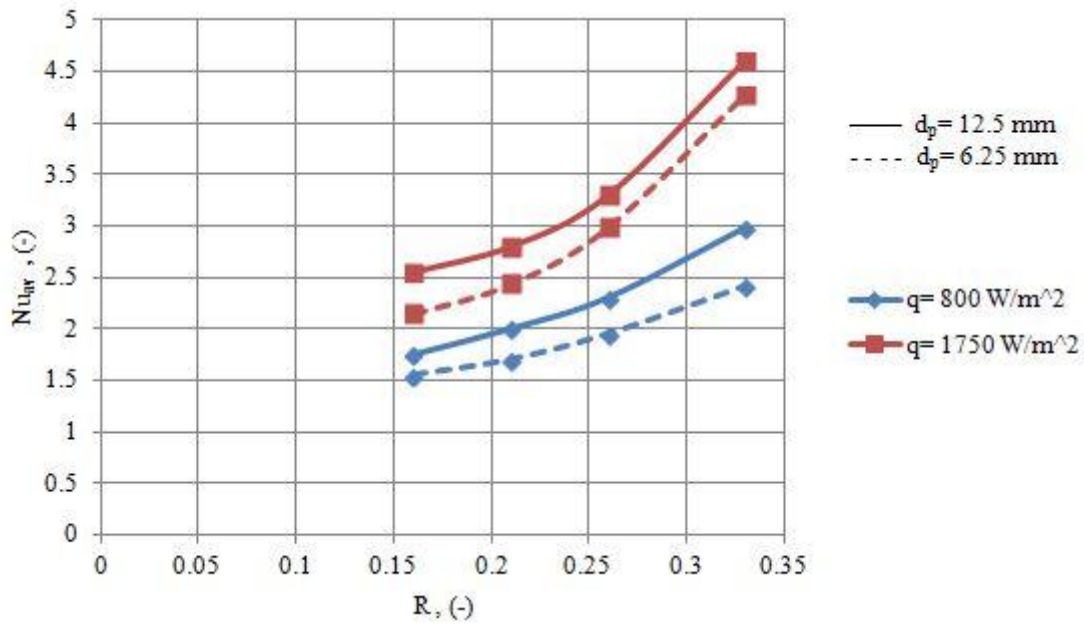


Figure 5. Average Nusselt number against radius ratio for PVC porous medium with different particle diameters.

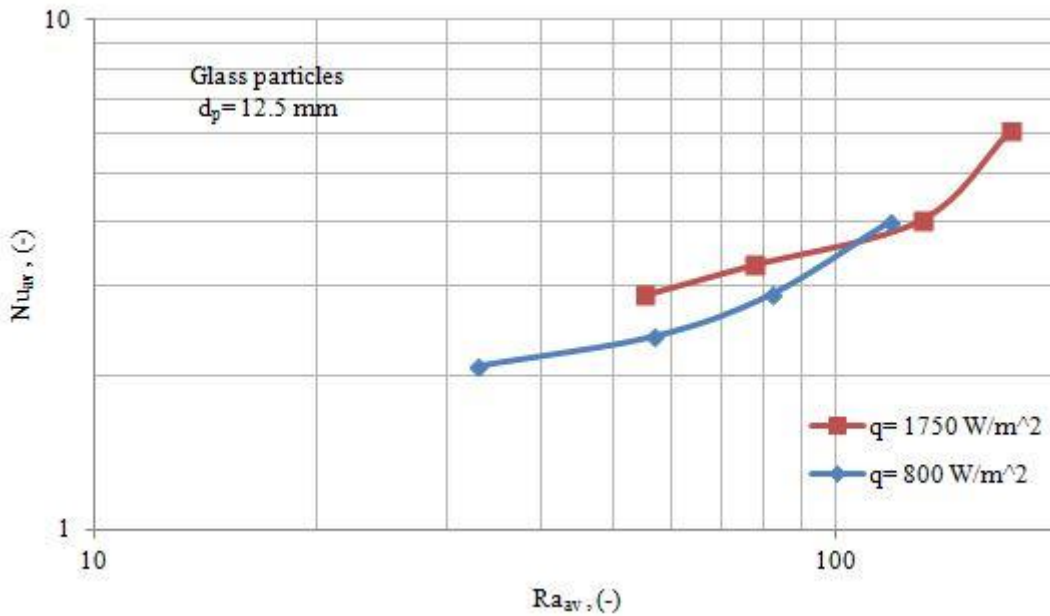


Figure 6. Average Nusselt number against average Rayleigh number for glass porous medium and different heat fluxes.

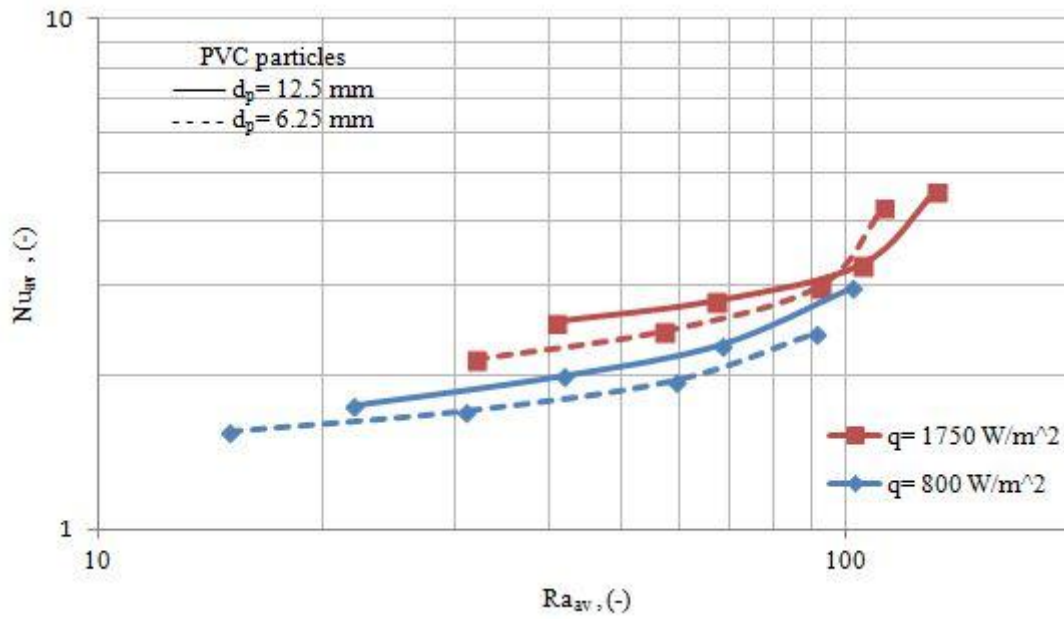


Figure 7. Average Nusselt number against average Rayleigh number for PVC porous medium with different particle diameters and wall heat fluxes.

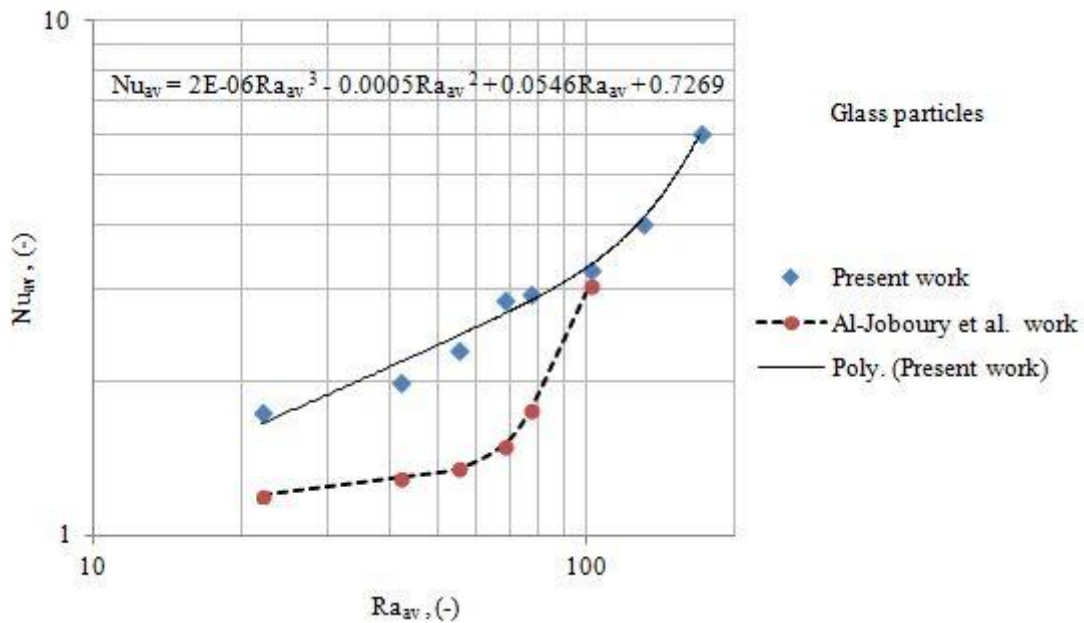


Figure 8. Analysis of the present work to the polynomial function fits with comparison of average Nusselt number than experimental results of Al-Joboury et al. work for glass particles.

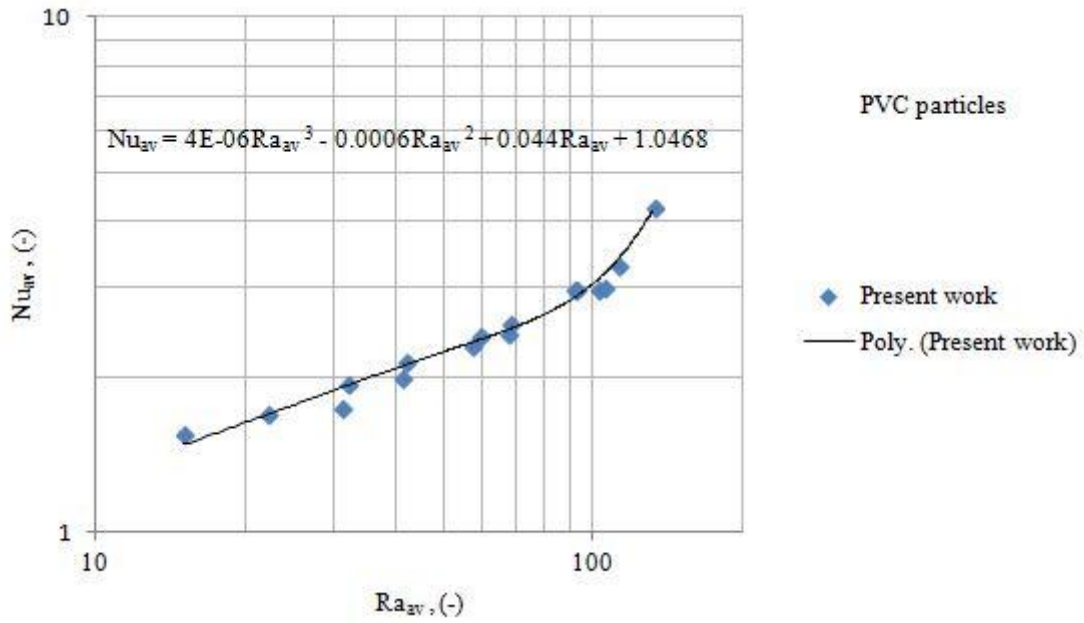


Figure 9. Analysis of the present work to the polynomial function fits for PVC particles.

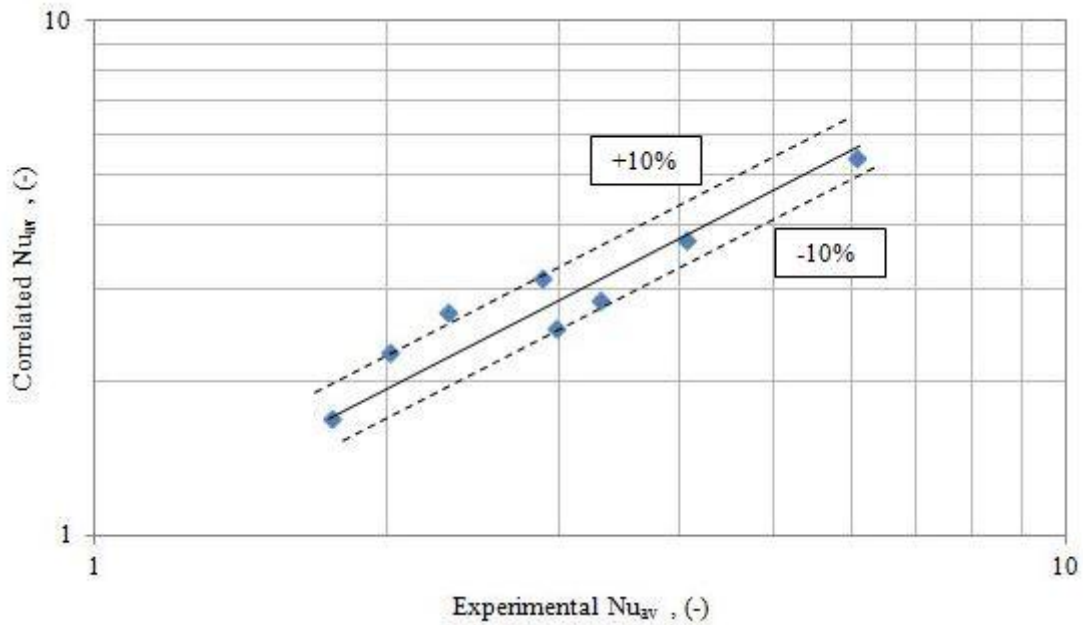


Figure 10. Comparison of correlated average Nusselt numbers (Nu_{av}) than those experimental of present work for glass particles.

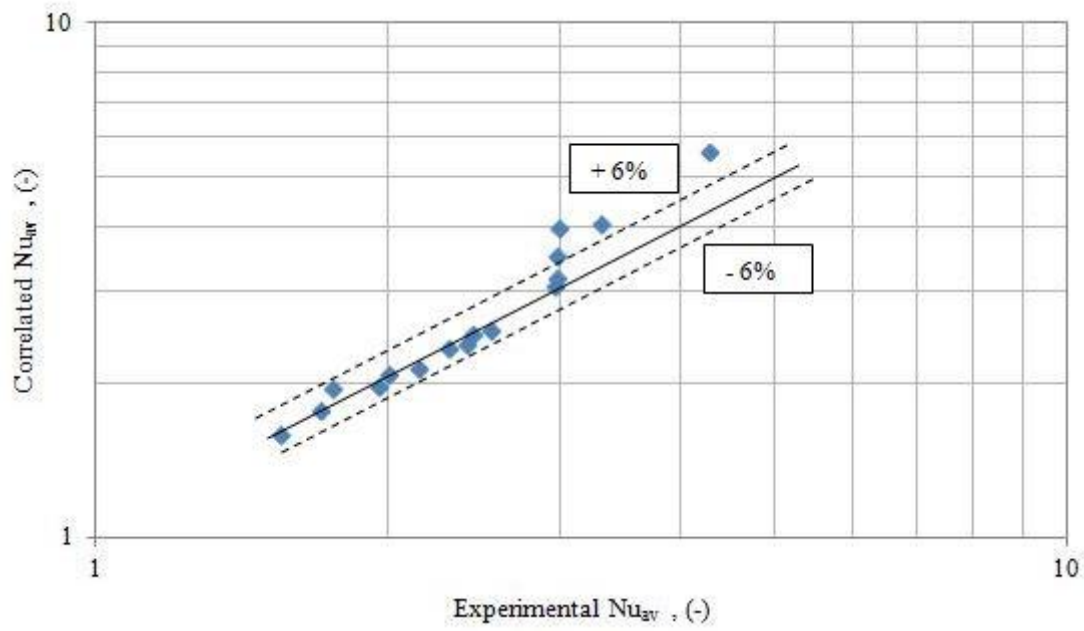


Figure 11. Comparison of correlated average Nusselt numbers (Nu_{av}) than those experimental of present work for PVC particles.

Analytical and Experimental Investigation for the Effect of Air Injection Angle on the Performance of Airlift Pump

Ali Abdul Mohsin Hasan Alasadi

Assistant Professor

College of Engineering-University of Baghdad

dralicit@yahoo.com

Ahmed Khalid Habeeb

M.Sc.

College of Engineering-University of Baghdad

eng_ahmedkhalid@yahoo.com

ABSTRACT

The effect of air injection angle on the performance of airlift pump used for water pumping has been studied analytically and experimentally. An airlift pump of dimensions 42mm diameter and 2200 mm length with conventional and modified air injection device was considered. A modification on conventional injection device (normal air-jacket type) was carried out by changing injection angle from 90° (for conventional) to 45° and 22.5° (for modified). Continuity and one-dimensional momentum balance for the flow field with basic principle of two-phase flow and expressions of slip ratio and friction factor as function of flow rates were formulated. The analytical and experimental investigations were carried out for both conventional and unconventional air-jackets at submergence ratios 0.75, 0.6 and 0.5 and air mass flow rate from 0.5 to 97kg/hr. The comparison between the analytical and experimental results shows agreement and the main results showed that the performance and maximum efficiency of airlift pump is increased for higher mass flow rate of injected air for all tested submergence ratio using unconventional air-jacket and the higher performance was associated with injection angle 22.5° , with average enhancement were 9% and 10% for performance and maximum efficiency respectively.

Key words: airlift pump, air injection angle, submergence ratio, two-phase flow

دراسة تحليلية وعملية حول تأثير زاوية حقن الهواء على أداء مضخات الرفع الهوائية

احمد خالد حبيب

ماجستير

كلية الهندسة-جامعة بغداد

علي عبد المحسن حسن الاسدي

أستاذ مساعد

كلية الهندسة-جامعة بغداد

الخلاصة

تم إجراء دراسة تحليلية وعملية حول تأثير زاوية حقن الهواء على أداء مضخات الرفع الهوائية التي تستخدم في رفع الماء. تم الأخذ بنظر الاعتبار مضخة رفع هوائية بقطر 42 ملم لأنبوب الرفع وبطول 2200 ملم باستخدام منظومة حقن هواء تقليدية ومنظومة أخرى معدلة. تم تعديل منظومة حقن الهواء التقليدية نوع (Air-Jacket) من خلال تغيير زاوية الحقن من 90° درجة (للمنظومة التقليدية) إلى زاوية 45° و 22.5° درجة (للمنظومة المعدلة). تم في الدراسة التحليلية بناء موديل رياضي اعتماداً على قانون حفظ الكتلة وقانون الزخم أحادي البعد لمنطقة الجريان واستخدام المبادئ الأساسية لجريان ثنائي الأطوار بالإضافة إلى المعادلات الخاصة بنسبة الانزلاق ومعامل الاحتكاك وتم إجراء الحل الرياضي والفحص العملي للمضخة مع منظومة حقن تقليدية ومعدلة عند نسبة غمر مقدارها 0.75، 0.6، 0.5 مع معدل تدفق كتلة الهواء المحقون من 0.5 إلى 97 كغم/ساعة. بينت المقارنة

بين النتائج التحليلية والنتائج العملية مقبولة جيدة قد أظهرت النتائج زيادة في أداء وكفاءة المضخة عند معدلات الحقن العالية عند استخدام منظومة الحقن المعدلة لكل ظروف الفحص، وان أفضل زاوية حقن هي 22.5 درجة مع تحسن 9% في الأداء و 10% لأعلى كفاءة.

الكلمات الرئيسية: مضخات الرفع الهوائية، زاوية حقن للهواء، نسبة الغمر، جريان ثنائي الطور.

1. INTRODUCTION

Airlift pump is generally regarded to be part of a unique kind of alternative pumping technology. The importance of this technology is arising when rotodynamic pumps are inappropriate for a given application. Most of these application that uses the technologies involve mixture of fluid-solid, very viscous fluid, hazardous fluids, fluid containing live organisms suspend in fluid, situation of low head or low submergences, applications with variable inlet water surface level and irregular shape wells. This class of pumps has simplicity in design and absence of moving and rotating parts which made the maintenance easy with low cost and high reliability. From the very beginning of the 20th century and in order to predict the airlift pump performance many analytical studies have been developed. **Stenning and Martin, 1968**, developed analytical model using one-dimensional continuity and momentum equations together with the basic relation of two-phase flow. A comparison with experimental work is carried out, and they predicted that the theory of one-dimensional flow gives a good knowledge for the analysis of airlift pump performance and they recommended using the model for pumps working in larger depths by dividing the pipe length into segments for which the density of air can be considered constant. This model is extended by, **Parker, 1980**, in order to take into consideration the momentum of injected air when nozzle injection device is used. He found that size and number of injection holes of air-jacket does not affect the discharge characteristic of the pump, and the nozzle design gives higher pumping rate at high air mass flow rates for small orifice area, but with very low efficiency. **Chisholm, 1982**, developed simple expressions based on homogenous theory to predict rapidly the performance, fraction of mass dryness and total mass flow rate of airlift pumps at "Maximum Flow Condition". The predicted mass flow rate is compared with theoretical and experimental of, **Stenning and Martin, 1968**, and found to be within 15%. **Clark and Dabolt, 1986**, developed a general design equation for airlift pumps working in slug flow pattern by extending the theory of, **Nicklin, 1963**, to long pumps. An explicit formula of design equation is obtained by integrating the combination of momentum, friction loss and void fraction expression over the complete length of the pump. The new design equation is supported experimentally using variety of liquids and submergence ratios. They stated that design of airlift pump using this method is more rapid with less energy required than the incremental procedure, as well as the method is more accurate than the results of existing empirical equation. **Reinemann et al., 1990**, extended the theory proposed previously by, **Nicklin, 1963**, into small diameter airlift pump from 3 mm to 25 mm by taking into consideration the effect of surface tension on the gas void rising velocity. They noted a difference between the rise velocity of single gas slug and train of gas slugs in small vertical tube. They noted that the efficiency increased for this range of tube diameter. **De Cachard and Delhaye, 1996**, proposed a new steady state model to predict the performance of small airlift pump (less than 40 mm) by combination of specific model describing slug and churn flow and supported his work by experimental investigation. They reported that the new proposed model is more accurate tool than the existing model in design small airlift pump with diameter up to 40 mm and length to diameter ratio greater than 250. **Kassab et al., 2009**, developed a modified version of the model proposed by, **Stenning and Martin, 1968**, by introducing slip ratio as expressed by, **Griffith and Wallis, 1961**, for slug flow and the friction factor which is obtained from Colebrook equation, **Haaland, 1983**. The

proposed modified model is compared with the experimental results that predicted by, **Kassab et al., 2001**, as well as, the theoretical prediction using the proposed model of, **Stenning and Martin, 1968**, and, **Clark and Dabolt, 1986**. They reported that the model of **Clark and Dablot** is appropriate only for the first zone of pump performance curve where the flow pattern is slug and the modified one-dimensional model gives more agreement with the experimental results for airlift pump working in different flow pattern (bubbly, slug and churn) except the annular flow.

The present work investigates analytically and experimentally the effects of changing the injection angle of injection device (air-jacket) at various submergence ratios and mass flow rate of injected air on the performance of airlift pump. A regular airlift pump with conventional and modified air-jacket is considered in this work.

2. EXPERIMENTAL WORK

The experimental work has been carried out in the Fluid Mechanics Laboratory in the Department of Mechanical Engineering - Collage of engineering/University of Baghdad in order to obtain water discharge rate and analyze the structure of flow filed within riser pipe. The experimental setup is shown in **Fig.1 and Fig.2** and the equipment used in the experimental work consists of:

2.1 Test Rig

The test rig consists of the riser pipe which is a transparence smooth pipe made of acrylic resin with 2000 mm length and 42mm inner diameter. The discharge side (upper end) of the riser pipe is connected to a collecting header of 4" diameter made of PVC. The highest point of the header is opened to ambient which allows air to escape from the pumped mixture. The lower end of the collecting header is divided into two branches with 2" PVC quick closing ball valve at its end to direct water from riser either, to intermediate tank or to metering tank. A 0.5 hp electric centrifugal water pump has maximum head of 35 m and maximum discharge of 36 liters/minute is used to pump water from the intermediate tank to the movable tank. The movable tank is a cylindrical tank holed by steel cable connected to a manual hoist can be moved upward and downward in order to change the submergence ratio and feed the riser pipe with water at constant head through the transient tank. A 1" quick closing ball valve made of brass is fitted at the bottom side of the transient tank as inlet to the tank. The riser pipe is fitted to the transient tank through the injection device, in which the compressed air is distributed uniformly and injected into the riser pipe to perform the pumping action. The injection device is designed as three independent injection stages, each stage delivered air through two ports and have 52 holes per stage drilled of diameter 3mm distributed in two rows and holes center line are inclined from injector wall by 90° , 45° , 22.5° for the first, second and third stages respectively. Injection device with holes center line vertical to the injector wall (90°) is considered as normal or standard air jacket. All the elements above of the test rig are assembled to gather in a main steel frame. The frame is made of standard 2" galvanized angle iron rack, fabricated into proper length and connected to gather.

2.2 Air Supply System

The experimental work is performed using a high pressure air compressor which delivered 1.05 m^3/min with a storage vessel of 1200 lit capacity and cutoff pressure of 14 bar, this compressor supply compressed air to a pressure reducing valve (0.5 – 5) bar to ensure a constant air pressure supply from the compressor. A constant area air flow meter of range (2 – 27) m^3/hr is used to

measure the volume flow rate of injected air and the temperature of supplied air was measured by a calibrated thermocouple. A needle valve 3/4" made of stainless steel is used to control the volume flow rate of injected air to the rig, as well as a 3/4" quick closing ball valve made of brass is used to simultaneously cutoff air supplying to the rig.

2.3 Experimental Procedure

The main part of the experiment was the measuring of the water discharged from the airlift pump for different angles of injection. The experimental procedures are as follows:

1. The air compressor is started and the pressure reducing valve is adjusted to the desired pressure.
2. The connection hose of the air system is linked to the desired stage of injection.
3. The centrifugal pump is started.
4. The level of movable tank is adjusted to the desired submergence ratio.
5. Injection of compressed air into the pipe is started; the needle valve is adjusted to the desired volume flow rate (Q_{air}), then the pressures (P_{air}) and temperature (T_{air}) are recorded.
6. The air mass flow rate is computed from the following equation:

$$\dot{m}_{air} = \rho_{air} \times Q_{air} \quad (1)$$

Where the density of air is calculated using ideal gas equation:

$$\rho_{air} = \frac{P_{air}}{R \times T_{air}} \quad (2)$$

7. The system is left to reach quasi- steady state.
8. The discharged water from intermediate tank is directed to the metering tank for a certain time (usually is taken 20 s) by closing the valve at the end of the collecting header which routed the water to the intermediate tank and open the other to the metering tank:
9. The volume of water accumulated in the metering tank ($V_{accumulate}$) is recorded.
10. The water mass flow rate is computed from the following equation:

$$\dot{m}_{water} = \rho_{water} \times \frac{V_{accumulate}}{t} \quad (3)$$

11. An estimation of flow regime type is reported.
12. The ball valves 14 and 15 are simultaneously closed, **Hamid et al., 2013**:
13. The retained volume of the riser (V_L) is recorded and the volumetric void fraction is computed from the equation:

$$\alpha = 1 - \frac{V_L}{\text{total volume of riser}} \quad (4)$$

(7) and (8) are repeated three times for each mass flow rate of air and take the average results.

The procedure above is repeated for different submergence ratio and injection angle for the same range of air mass flow rate.

A high speed camera made by SAMSUNG (model WB2000, 10 megapixels and 1000 f/s) is used to capture photos of flow regime detected in the riser tube, and water is colored by adding a light color in order to make the reorganization of flow pattern easier.

2.4 Error Analysis

Deviation was calculated for the experimental data using the formula for calculating percentage error as:

$$\text{Percentage error} = \left(\frac{\text{measured value} - \text{estimated value}}{\text{measured value}} \right) * 100 \quad (5)$$



Where measured values are result from the experimental work and the estimated value from the theoretical.

3. MATHEMATICAL FORMULATION

The basic model that was proposed by, **Stenning and Martain, 1968**, based on assumption of steady state one-dimensional flow in the pump riser, continuity and momentum equations together with the basics principles of two phase flow is used to solve the governing equations analytically. The modification is carried out to take account of the effect of momentum due to the velocity component of air injected in flow direction as well as, the characteristic of flow pattern that occurred at best operation of air lift pump was considered, **Kassab et al., 2009**. However, because of the steady state one-dimensional nature of these analytical models, they are inadequate of providing vision and information about the characteristic of different flow patterns developed in the riser pipe of the pump and the transient nature of the pumping process, **Wahba et al., 2014**.

3.1 Governing Equations

In the present work, the working fluids are water and air and the following assumptions are made:

1. Planes of equal velocity and equal pressure are normal to the pipe axis which is makes the case one-dimensional).
2. No exchange of mass between phases.
3. Isothermal flow for all phases.
4. Incompressible for the air phase.
5. Newtonian fluids.
6. Constant properties of air and water.
7. Neglect the pressure of compressed air at inlet.

Consider the airlift pump basically is a vertical pipe with a diameter D and total length L , partially full of water with reference height (zero) at the base of the pipe, the pump is divided into two parts, injection zone and the remained of the riser as shown in **Fig.3** Governing equations are applied to each part and the results combined together to obtain a non-linear equation governing the complete pump, **Stenning and Martain, 1968**. The governing equations basically are:

Continuity equation:

$$\sum \rho \vec{u} A = 0 \quad (6)$$

Momentum equation:

$$\sum \rho u A \vec{u} = \sum F \quad (7)$$

3.1.1 Injection Zone

The pump is partially immersed in water (surrounding field) into a height of H_s , Bernoulli's equation is applied between free surface of water and the pump inlet (1) in order to take in account the effect of the static head of immersed length as follow:

$$P_1 = P_a + \rho_L g H_s - \frac{1}{2} \rho_L u_1^2 \quad (8)$$

where: u_1 is the velocity of water at the inlet to the pump.

To find a relation for the velocity and density leaving the injection zone with the velocities and densities entered to the zone, the continuity equation is applied for the control volume between (1) and (2) as shown in **Fig.3**, neglecting the changes of air density, **Kassab et al. 2009**, is written as:

$$A u_2 = Q_g + Q_L \quad (9)$$

where u_2 is the velocity of mixture (water and air) leaving the injection zone, and $Q_L = A u_1$ is the water flow rate inlet to the pump.

Divided Eq. (9) by Q_L which is yield:

$$u_2 = u_1 \left(1 + \frac{Q_g}{Q_L} \right) \quad (10)$$

The air mass flow rate entered to the injection zone is too small if compared with the water mass flow rate, therefore the air mass flow rate can be neglected and the continuity equation can be written again as:

$$\rho_2 A u_2 = \rho_L A u_1 \quad (11)$$

and rearranging

$$\rho_2 = \rho_L \frac{u_1}{u_2} \quad (12)$$

By substituting Eq. (10) in to Eq. (12) yields mixture density as function of inlet air flow rate, inlet water flow rate and water density as shown:

$$\rho_2 = \frac{\rho_L}{\left(1 + \frac{Q_g}{Q_L} \right)} \quad (13)$$

The momentum equation is applied for the control volume between (1) and (2), neglecting the friction losses of wall, **Parker, 1980**, and is written as:

$$A P_1 - A P_2 = (\rho_L Q_L + \rho_g Q_g) u_2 - \rho_L Q_L u_1 - \rho_g Q_g u_g \cos \theta \quad (14)$$

where $u_g \cos \theta$ is the vertical component of injected air velocity in the direction of main flow.

Since $\rho_g Q_g \ll \rho_L Q_L$ therefore the term $(\rho_L Q_L + \rho_g Q_g)$ on the right hand side of Eq. (14) is approximately $\approx \rho_L Q_L$ and Eq. (14) reduces to:

$$A P_1 - A P_2 = \rho_L Q_L u_2 - \rho_L Q_L u_1 - \rho_g Q_g u_g \cos \theta \quad (15)$$

Substituting Eq. (10) into Eq. (15) and rearrange, the result equation becomes:

$$P_2 = P_1 - \rho_L \frac{Q_g}{A} u_1 + \rho_g \frac{Q_g}{A} u_g \cos \theta \quad (16)$$

The total air flow rate injected in the pump Q_g is equal to the summation of air flow rate of each injection hole of injection device, as:

$$Q_g = \sum Q_{hole} \quad (17)$$

The design of injection device is ensured evenly distribution of injection air on the all holes, therefore, Eq. (17) becomes:

$$Q_g = u_g N A_{hole} \quad (18)$$

and

$$A_j = N A_{hole} \quad (19)$$

where A_j is the total area of injection holes, N is number of holes and A_{hole} is the area of a hole. Combining Eqs. (8), (18), (19) and (16) gives the pressure at the outlet of injection zone depending on the parameters of the zone, as follows:

$$P_2 = P_a + \rho_L g H_s - \frac{1}{2} \rho_L u_1^2 - \rho_L \frac{Q_g}{Q_L} u_1^2 + \rho_L u_1^2 \frac{\rho_g}{\rho_L} \frac{A}{A_j} \left(\frac{Q_g}{Q_L} \right)^2 \cos \theta \quad (20)$$

3.1.2 The Riser Pipe

The momentum equation is applied for the control volume between (2) and discharges of the pipe, **Fig.3**, and taking into consideration the friction losses of wall and the weight of the mixture in the pipe as follows:

$$P_2 = P_a + \frac{\tau_w \pi D L}{A} + \frac{W}{A} \quad (21)$$

where τ_w is the average shear stress for slug flow of riser wall and is suggested by, **Griffth and Wallis, 1961**, and, **Kassab et al., 2009**, and W is the weight of mixture in the riser pipe, **Parker, 1980**, as follows:

$$\tau_w = f \frac{\rho_L}{2} \left(1 + \frac{Q_g}{Q_L} \right) \left(\frac{Q_L}{A} \right)^2 \quad (22)$$

$$W = \frac{\rho_L g L A}{\left(1 + \frac{Q_g}{S Q_L} \right)} \quad (23)$$

where f is the friction factor of the wall assuming water alone flows through the riser with flow rate equal to $(Q_L + Q_g)$ and is obtained using Colebrook formula, **Haaland, 1983**, as:

$$\frac{1}{\sqrt{f}} = -2.0 \log \left(\frac{\epsilon/D}{3.7} + \frac{2.51}{Re \sqrt{f}} \right) \quad (24)$$

and S is slip ratio and equals to:

$$S = \frac{u_{ga}}{u_{La}} \quad (25)$$

where u_{ga} and u_{La} are phase actual velocities of air and water respectively in the riser pipe, **Kreith et al., 1999**.

Substituting Eq. (22) and (23) into Eq. (21) gives a correlation of P_2 (pressure at the outlet of injection zone) in terms of the parameters of the riser pipe, as follows:

$$P_2 = P_a + K \left(\frac{\rho_L u_1^2}{2} \right) \left(1 + \frac{Q_g}{Q_L} \right) + \frac{\rho_L g L}{\left(1 + \frac{Q_g}{S Q_L} \right)} \quad (26)$$

3.1.3 The Complete Pump

The performance equation for the whole pump is determined by equating Eq. (20) and Eq. (26) and rearranging gives:

$$\frac{H}{L} - \frac{1}{\left(1 + \frac{Q_g}{S Q_L} \right)} = \frac{Q_L^2}{2 g L A^2} \left[(K + 1) + (K + 2) \frac{Q_g}{Q_L} - 2 \frac{\rho_g}{\rho_L} \frac{A}{A_j} \left(\frac{Q_g}{Q_L} \right)^2 \cos \theta \right] \quad (27)$$

where S is described as a function of water and air flow rate by, **Griffth and Wallis, 1961**, and, **Kassab et al., 2009**, for slug flow as:

$$S = 1.2 + 0.2 \frac{Q_g}{Q_L} + \frac{0.35\sqrt{gD}}{V_1} \quad (28)$$

and

$$K = \frac{4fL}{D} \quad (29)$$

All other losses due to water entrance losses, sudden expansion, elbow, tee and valves are accounted by increasing the effective value of K .

The term $\left[2 \frac{\rho_g A}{\rho_L A_j} \left(\frac{Q_g}{Q_L} \right)^2 \cos\theta \right]$ in the right hand side of the non-linear Eq. (27), is considered a gain of air momentum that affected the performance in the direction of main flow and the angle θ governed this effect, therefore, for $\theta = 90$ the term is disappeared from the equation and reduced to the same equation derived by, **Stenning and Martin, 1968**, for standard air-jacket injection device, and vice versa, for $\theta = 0$, yield the same performance equation for air-nozzle injection device derived by, **Parker, 1980**, therefore Eq. (27) is theoretically applicable to find the performance of airlift pumps range from standard air-jacket to air-nozzle device and between them for various injection angle.

3.2 Method of Solution

The theoretical performance of airlift pump was evaluated by solving the governing equation (Eq. (27)) by iteration and a corresponding computer program is developed for this purpose. Solution procedure is described in steps as follows:

1. The geometrical parameters D, L, ϵ, d_j, N , and θ is introduced and sub calculations to find A and A_j are performed.
2. H_s is introduced corresponding with selected submergence ratio as follows:
$$Sr = \frac{H}{L} \quad (30)$$
3. Properties for water and air for certain condition are assigned.
4. Inlet air flow rate is assigned.
5. A trial value for water flow rate is assumed.
6. Reynolds number is calculated assuming water alone flows through the riser with flow rate equal to $(Q_L + Q_g)$
7. Friction coefficient f is calculated from Colebrook Eq. (24) by trial and error, and then K is calculated from Eq. (29).
8. Slip ratio from Eq. (28) is calculated.
9. New value (better approximation) of water flow rate ($newQ_L$) is calculated by solving equation (27) using proper iterative method.
10. The procedure from step 5 is repeated with new trial value of water flow rate until the total absolute difference between $newQ_L$ and assumed Q_L becomes less than 10^{-6} .

Newton-Raphson method is used to solving the set of the equations, **Alan, 2002**, and a computer program is built for implementing the solution procedure by employing MATLAB R2013b software.

3.3 Airlift Pump Characteristics

The most important airlift pump characteristics in this work are the water pumping rate, and efficiency coefficients. Application of continuity and momentum conservation laws give amount of pumped water for specified operational and geometrical parameters. Once water flow rate is predicted, other pump characteristics can be found directly. Efficiency (η) of airlift pump is defined by, **Nicklin, 1963**, as a ratio of beneficial work done in water to the energy released from the isothermal expansion of injected air from injection pressure to the ambient pressure as follows:

$$\eta = \frac{g\rho_L Q_L(L - H_s)}{P_a Q_g \ln(P_{in}/P_a)} \quad (31)$$

4. RESULTS

In general, performance curve of any airlift pump shows the behavior of the pump output over the input range of air; it is obtained by plotting the values of induced water mass flow rate against input air mass flow rate at a specified value of submergence ratio and injection angle. **Fig.4** shows performance curve predicted using the proposed analytical model as well as the results of experimental work. As expected, injection device with angles (45° and 22.5°) gives higher water mass flow rate at higher mass flow rates of injected air than the conventional air-jacket with injection angle (90°) for all tested submergence ratios, this increasing of water flow rate can be related to the initial momentum result from the velocity component of injected air in the flow direction in the riser pipe. A comparison of performance curve between the experimental and analytical prediction for the same investigation conditions are in agreement with average deviation about 9%, 17% and 23% for submergence ratios of 0.5, 0.6 and 0.75 respectively.

Fig.5 shows the variation of analytical and experimental performance curves with submergence ratio, these curves for each injection angle at different submergence ratios have similar trend and shows that decreasing in pumped water mass flow rate is associated with decreasing in submergence ratio, this is true, because when submergence ratio decreases, the length that the water should traverse is increased through the riser pipe and this length is proportional to the lifting head ($L - H_s$). The average enhancement results from modifying conventional air-jacket by changing the injection angle from (90°) to (45° and 22.5°) based on experimental results are, increasing the pumping rate about 8% for injection angle (45°) and 11% for injection angle (22.5°), while the average enhancement based on the analytical results are 10% for injection angle (45°) and 14% for injection angle (22.5°).

The variation of efficiency of the airlift pump, which is obtained from proposed model and experimental work, with injection angle at a specified submergence ratio are shown in **Fig.6**. Both, analytical and experimental efficiency results has similar trend that the efficiency increased rapidly from its minimum value (0) until a maximum value is achieved then decreases gradually. It was noticed that the maximum efficiency increased for injection angle 45° and 22.5° , and this increase is related to the increasing of work done by the pump which is associated with increasing of water output from the pump for the same mass flow rate of injected air and submergence ratio. The comparison between predicted efficiencies from the proposed model and experimental efficiency for the same investigation conditions shows good agreement with average deviation of 8%, 12% and 9% for submergence ratio 0.5, 0.6 and 0.75 respectively. The increase in maximum efficiency based on the experimental results is about 9% for injection angle 45° and 11% injection angle 22.5° .

To discuss the behavior of air lift pump efficiency with the water flow rate at a specified injection angle and submergence ratio, efficiency curve and performance curve are plotted together in one figure as shown in **Fig.7**, it is observed for all investigated cases that the maximum efficiency achieved by airlift pump does not correspond to the maximum output water mass flow rate due to the transition of flow pattern from stable slug flow to churn flow which is characterized as chaotic and unstable. Another observation that the best efficiency points achieved when the flow is slug and slug-churn flow, this is approved by comparing the distribution of best experimental efficiencies on the flow map proposed by, **Taitel et al., 1980**, and **Fig.8, Fig.9 and Fig.10** shows that the best efficiency points located at slug and slug-churn zones.

5. CONCLUSIONS

- The optimum angle of air injection was found to be at 22.5° for the selected operational and geometrical parameters.
- Average enhancement of airlift pump performance is about 8% for air injection angle 45° and 11% for 22.5° .
- Increasing of water mass flow rate as the submergence ratio increased for all tested injection angle and the maximum mass flow rate of water achieved is 2794, 2371 and 1720 kg/hr for submergence ratio 0.75, 0.6 and 0.5 respectively.
- Maximum efficiency is increased as the submergence ratio increased and maximum efficiency achieved is 36%, 32% and 30% for submergence ratio 0.75, 0.6 and 0.5 respectively.
- Maximum efficiency of airlift pump does not occur with the maximum mass flow rate of water.
- Best efficiency points corresponds to the slug and slug-churn flow pattern, therefore, it's recommended to operate any airlift pump with these patterns of flow.
- The proposed one-dimensional analytical model is incapable of providing any information about the flow patterns and transient nature of the flow.
- The proposed one-dimensional analytical model gave better results and good agreement with experimental results and the proposed analytical model can be used as efficient tool in predicting the overall performance and design of airlift pump.

NOMENCLATURE

A = cross section area of the riser pipe, m^2

A_{hole} = area of injection hole, m^2

A_j = total areas of injection, m^2

D = diameter of riser pipe, m

D_h = hydraulic diameter, m

D = diameter of injection hole, m

F = force, N

f = friction factor

g = gravity acceleration, m/s^2

H_s = static Head or Submerged length, m

K = friction parameter

L = length of riser pipe, m

\dot{m} = mass flow rate, kg/s



N = number of holes

P = pressure, N/m^2

Q = volume flow rate, m^3/s

Q_{hole} = air volume flow rate per hole, m^3/s

Re = Reynolds number

S = slip ratio

u = velocity, m/s

\bar{u} = velocity vector, m/s

V = volume, m^3

W = weight of mixture in the riser pipe, N

θ = angle of air injection, Degree

ϵ = pipe roughness, m

μ = molecular or dynamic viscosity, $kg/m.s$

ρ = density, kg/m^3

τ_w = wall shear stress, N/m^2

η = efficiency

SUBSCRIPTS

g = gas

L = liquid

ga = gas average

La =liquid average

gs = gas superficial

ls = liquid superficial

a = ambient

REFERENCES

- Alan Jeffery, 2002, *Advance Engineering Mathematics*, Harcourt/Academic press.
- Chisholm D., 1982, *Prediction of the performance of air-lift pumps*, International Journals of Heat and Fluid Flow, Vol. 3, pp. 149-152.
- Clark, N.N., Dabolt, R.J., 1986, *A general design equation for air-lift pumps operating in slug flow*, AICHE J., Vol. 32, pp. 56-64.
- De Cachard F., Delhay J.M., 1996, *A slug-churn model for small- diameter airlift pumps*, Int. J. Multiphase Flow, Vol. 22, pp. 627-649.
- Griffith, P., Wallis, G.B., 1961, *Two-phase slug flow*, J. Heat Transfer, Trans. ASME, Vol. 83, pp. 307-320.
- Haaland S. E., 1983, *Simple and Explicit Formulas for the Friction Factor in Turbulent Pipe Flow*, Journal of Fluids Engineering, , Vol. 105, pp. 89-90.
- Kassab, S.Z., Kandil, H.A., Warda, H.A., Ahmed, W.H., 2001, *Performance of an air lift pump operating in two-phase flow*, in Proceedings of ICFDP7: The Seventh International Congress on Fluid Dynamics & Propulsion, Cairo, Egypt, Paper No. ICFDP7-2001004.
- Kassab Sadek Z., Hamdy A. Kandil, Hassan A. Warda, Wael H. Ahmed, 2009, *Air-lift pumps characteristics under two-phase flow conditions*, International Journal of Heat and Fluid Flow, Vol.30, pp. 88-98.



- Kreith Frank, Berger A., Churchill W., Tullis P., White M., 1999, *Fluid Mechanics*, Mechanical Engineering Handbook, CRC press LLC.
- Nicklin D. J., 1963, *The airlift pump theory and optimization*, International chemical Eng., Vol. 41, pp. 29-39.
- Parker G. J., 1980, *The Effect of Footpiece Design on the Performance of a Small Air Lift Pump*, INT. J. HEAT & FLUID FLOW, Vol. 2, No. 4, pp. 245-252.
- Reinemann D. J., J. Y. Parlange, M. B. Timmons, 1990, *Theory of Small-Diameter Airlift Pump*, I. J. Multiphase flow, Vol. 16, pp. 113-122.
- Stenning, A.H., Martin, C.B., 1968, *An analytical and experimental study of air lift pump performance*, J. Eng. Power, Trans. ASME' Vol. 90, pp.106–110.
- Taitel Yehuda, Dvora Bornea, A. E. Dukler, 1980, *Modeling Flow Pattern Transitions for Steady Upward Gas-Liquid Flow in Vertical tubes*, AICh journal, Vol. 26, No. 3, pp. 345-354.
- Wahba E. M., M. A. Gadalla, D. Abueidda, A. Dalaq, H. Hafiz, K. Elawadi and R. Issa, 2014, *On the Performance of Air-Lift Pumps: From Analytical Models to Large Eddy Simulation*, Journal of Fluids Engineering, Vol. 136, pp.1-7.

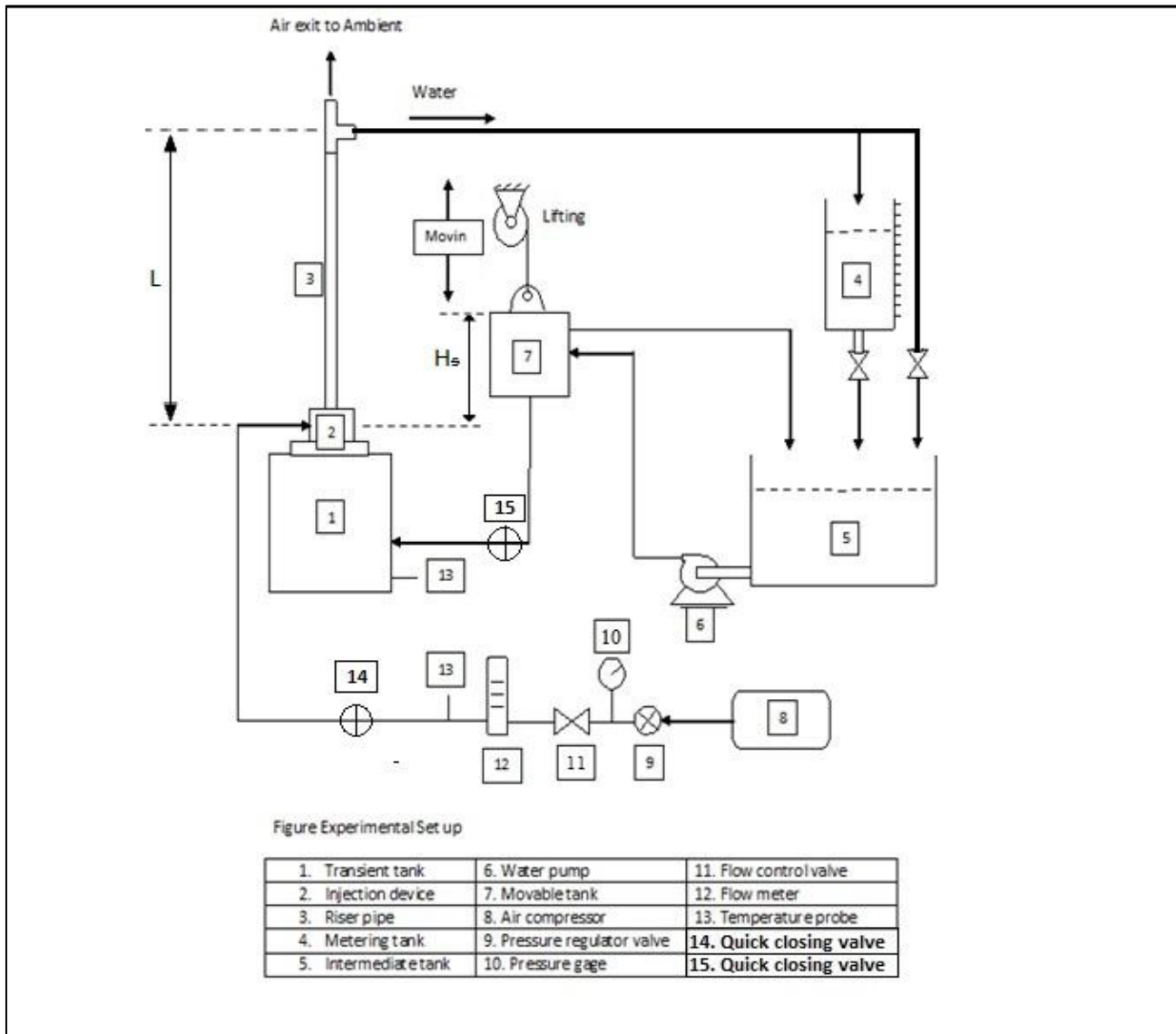


Figure 1. Testing schematics drawing.

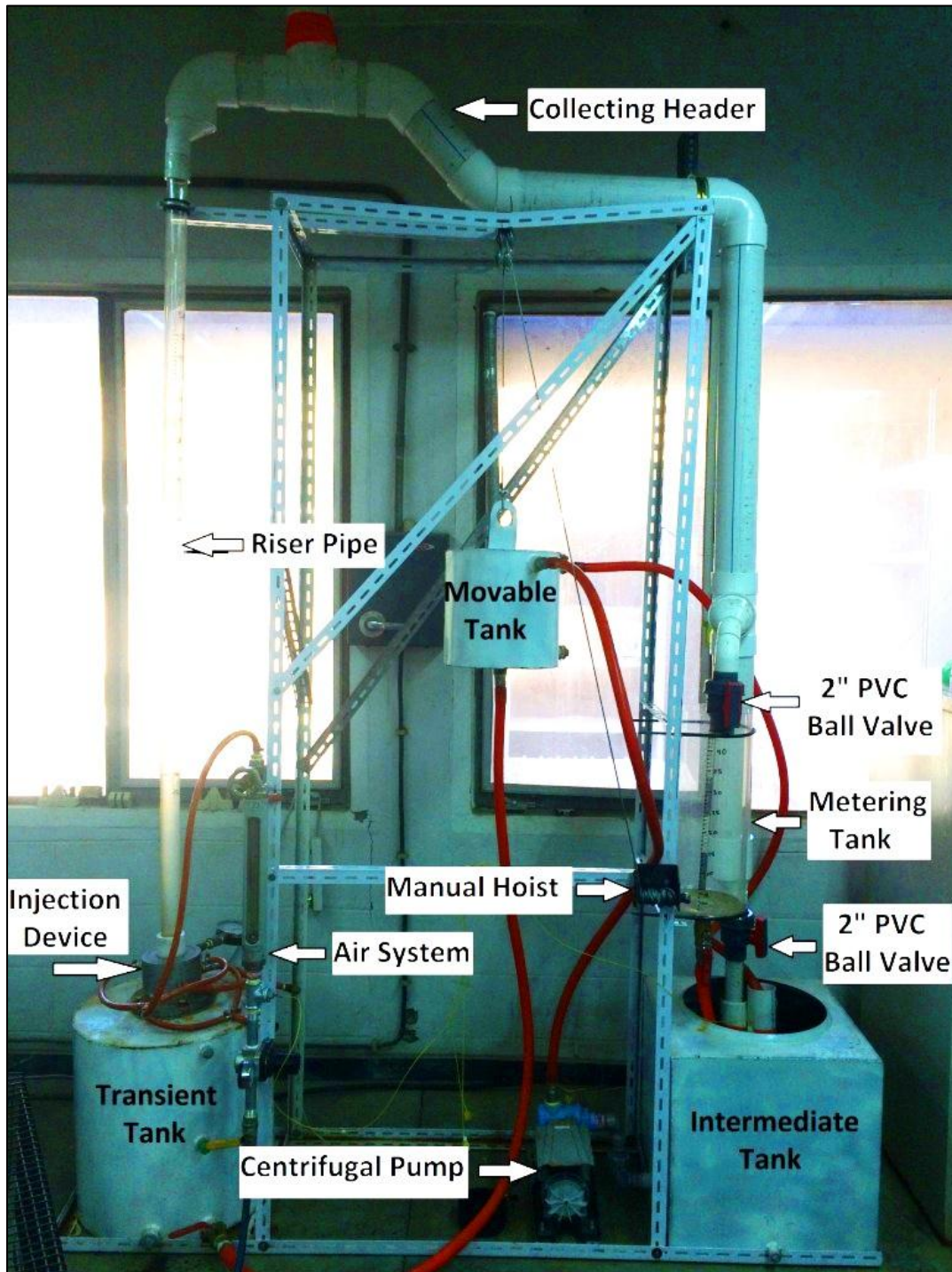


Figure 2. Experimental setup.

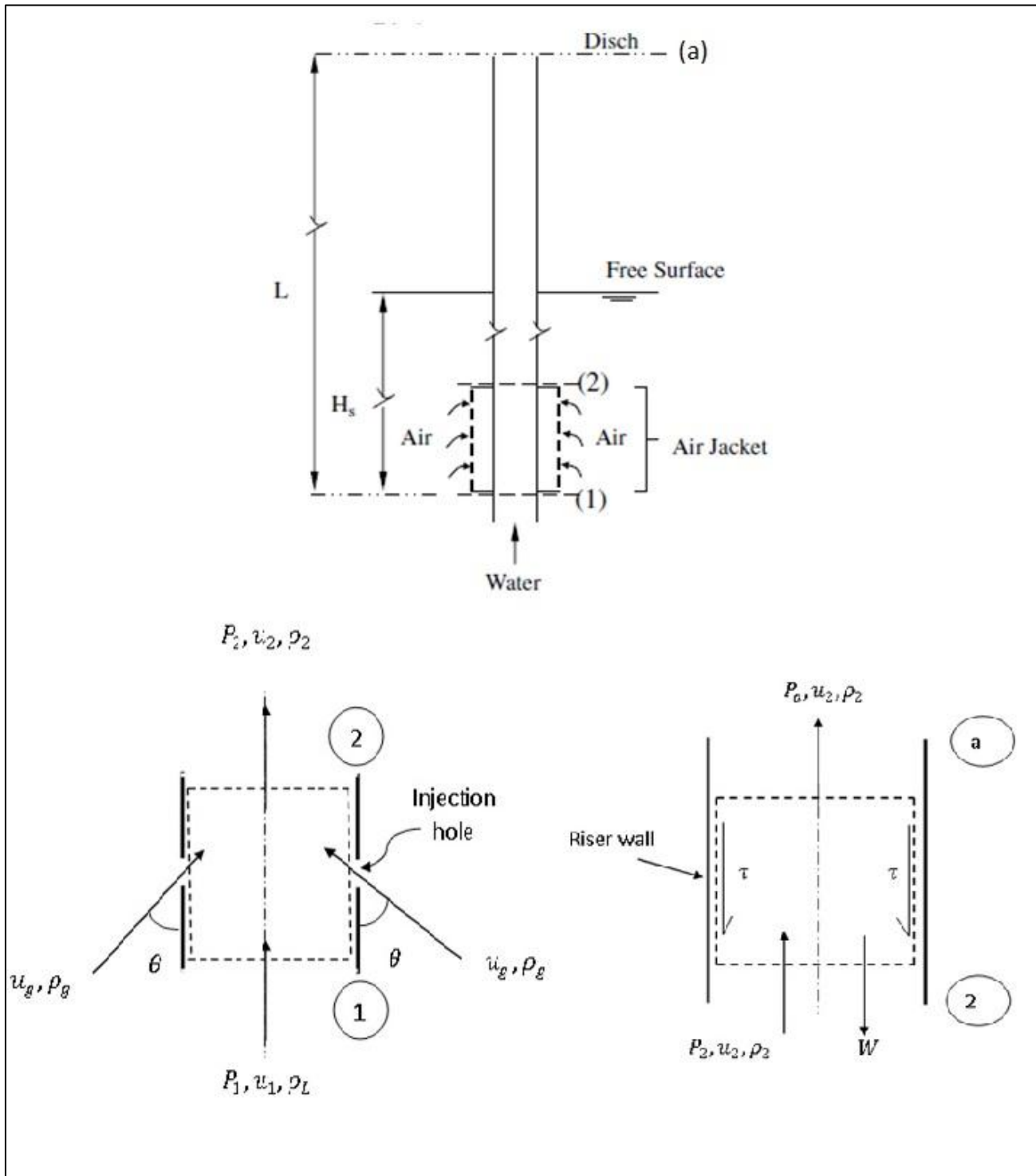


Figure 3. Schematic of airlift pump for analysis.

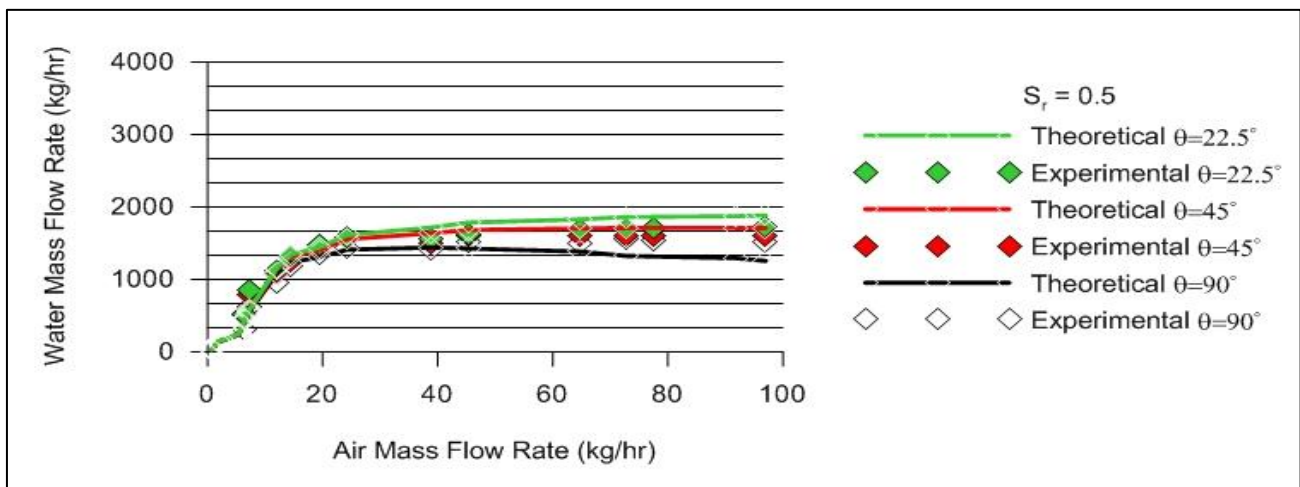
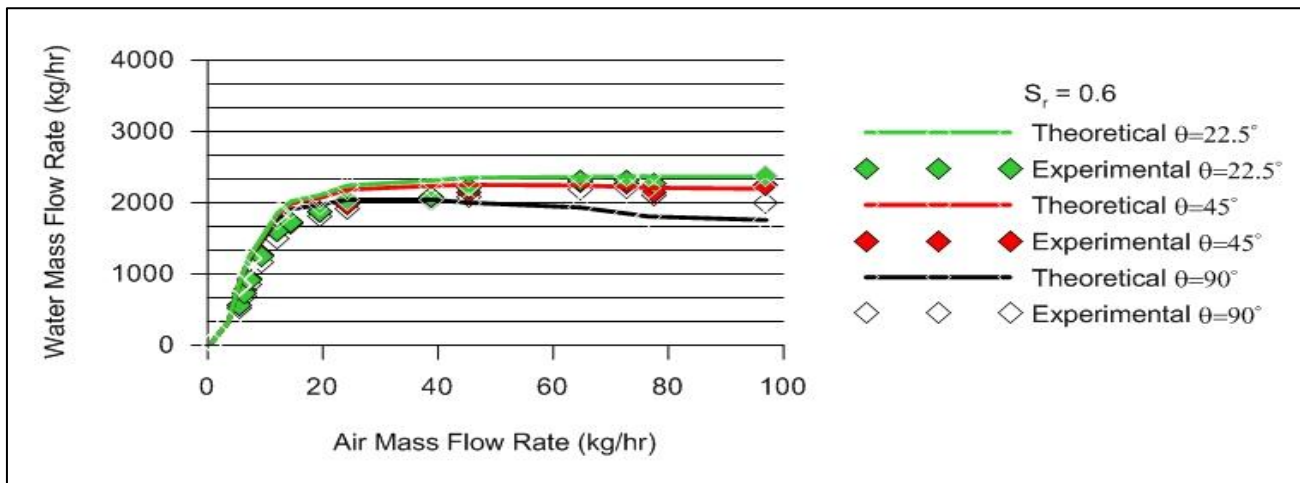
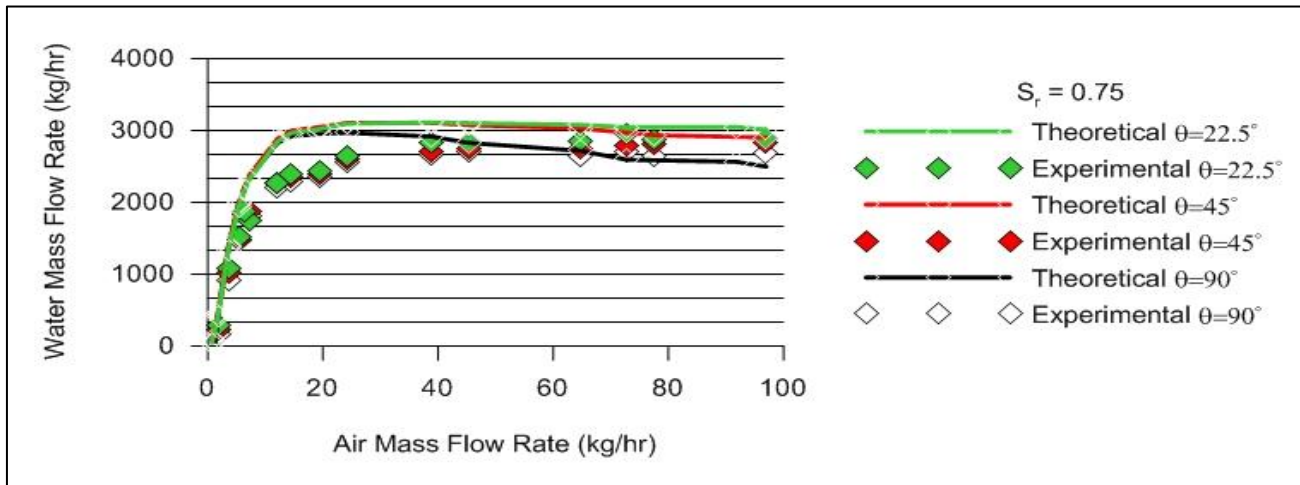


Figure 4. Variation of airlift pump performance curve with various injection angles at submergence ratio (a): 0.75, (b): 0.6 and (c): 0.5.

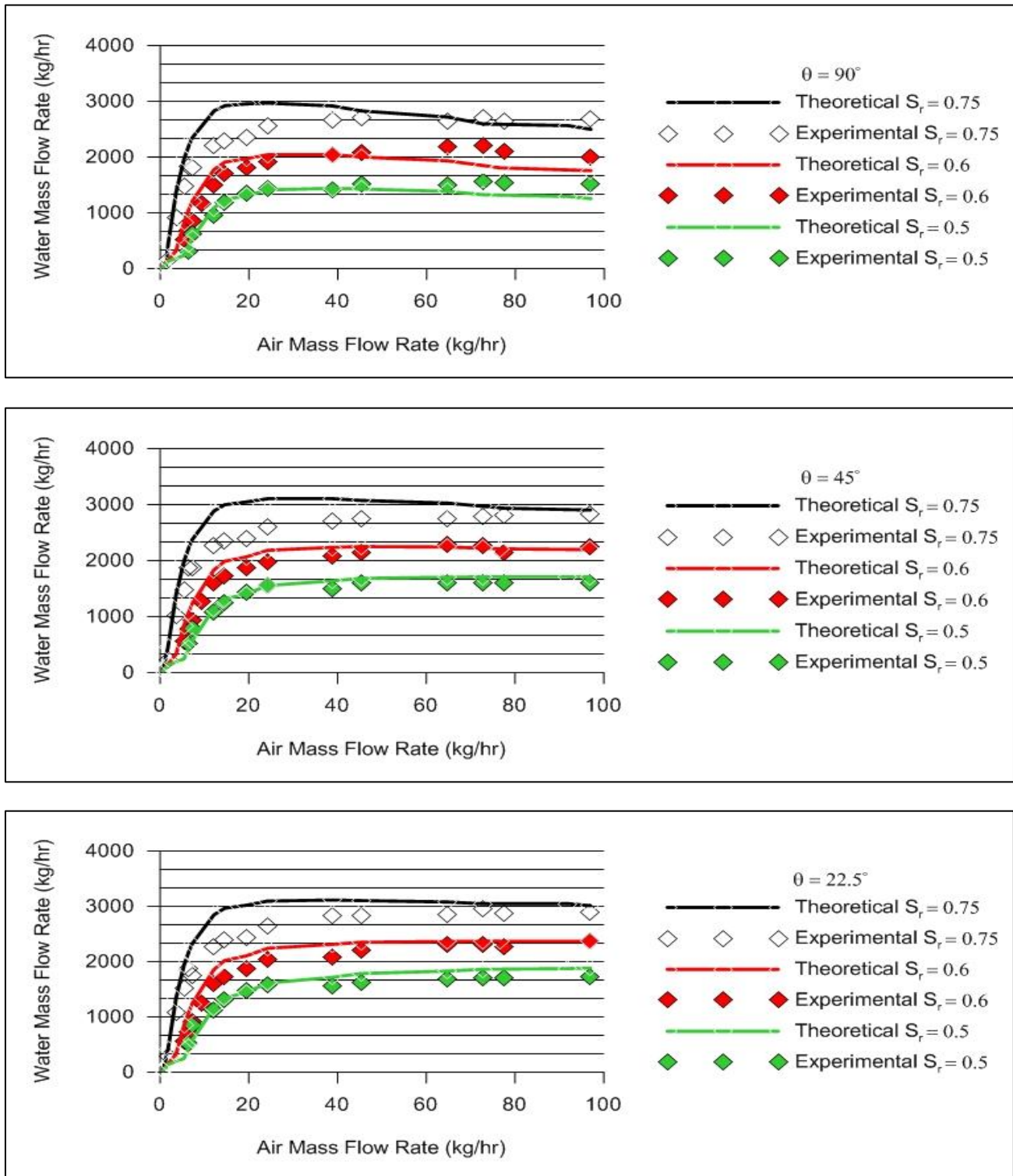


Figure 5. Variation of airlift pump performance curve with various submergence ratio at injection angles (a): 90°, (b): 45° and (c): 22.5°.

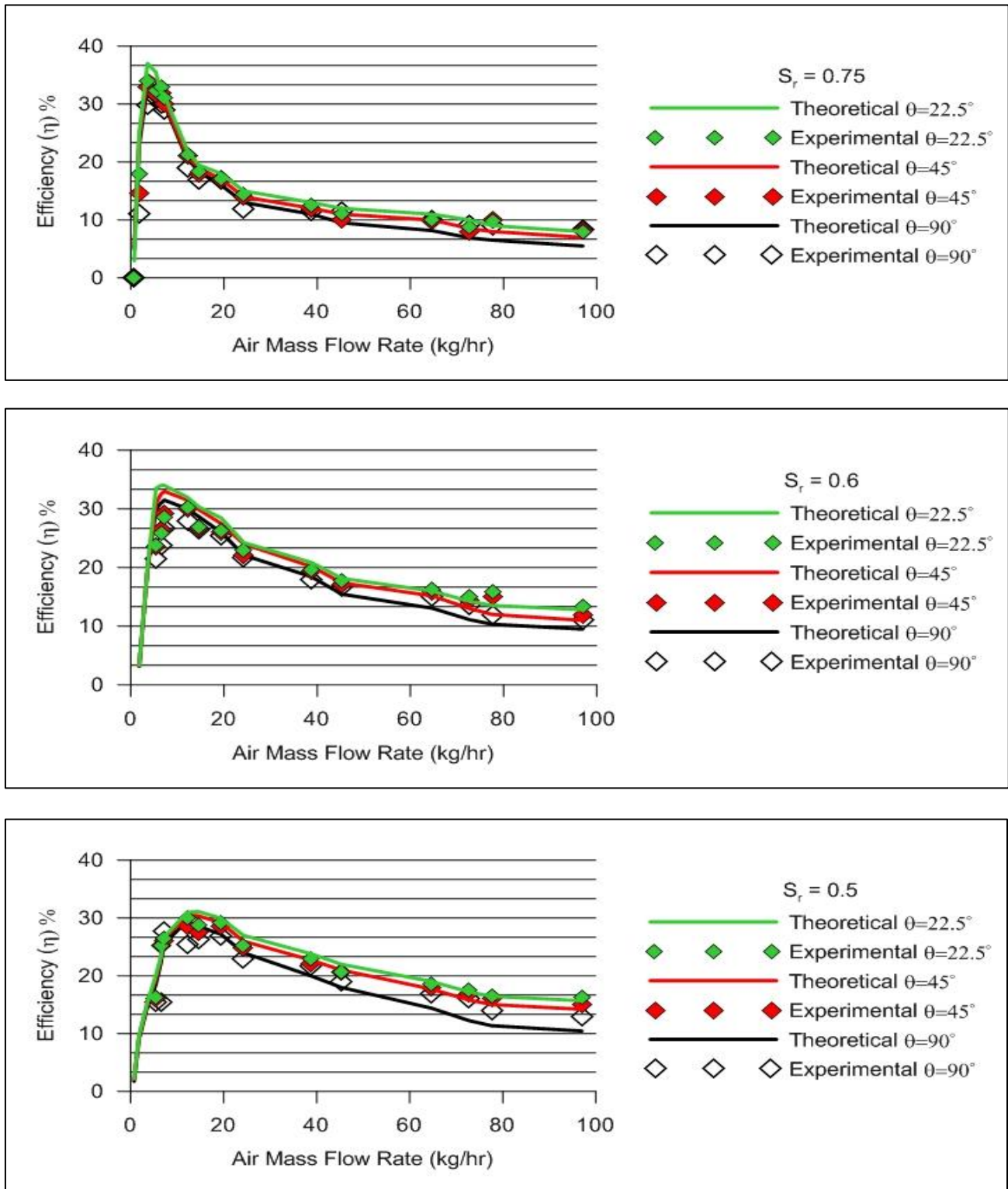


Figure 6. Variation of airlift pump efficiency various submergence ratio at injection angles (a): 90° , (b): 45° and (c): 22.5° .

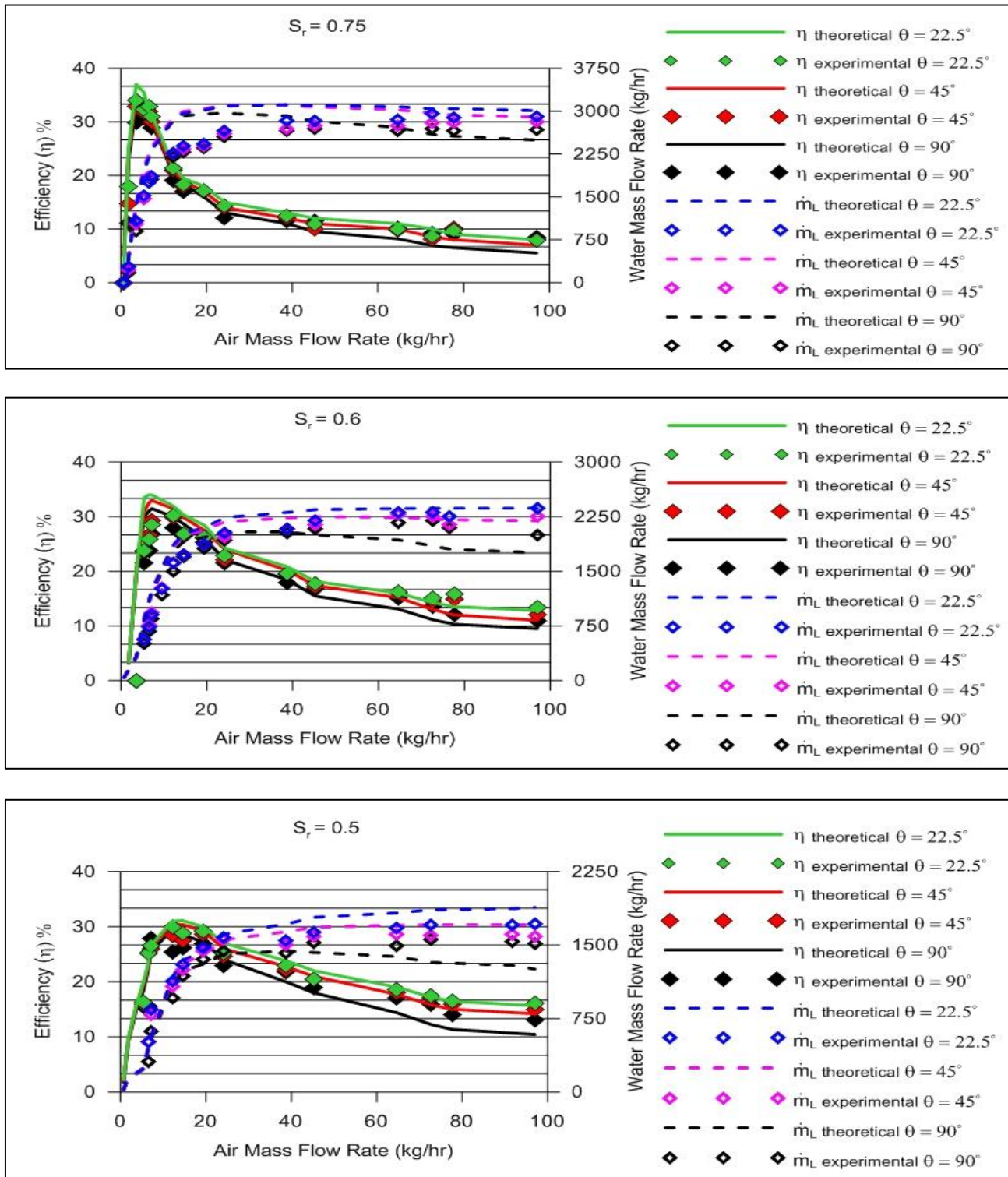


Figure 7. Variation of airlift pump efficiency and performance curve with various submergence ratio at injection angles (a): 90° , (b): 45° and (c): 22.5° .

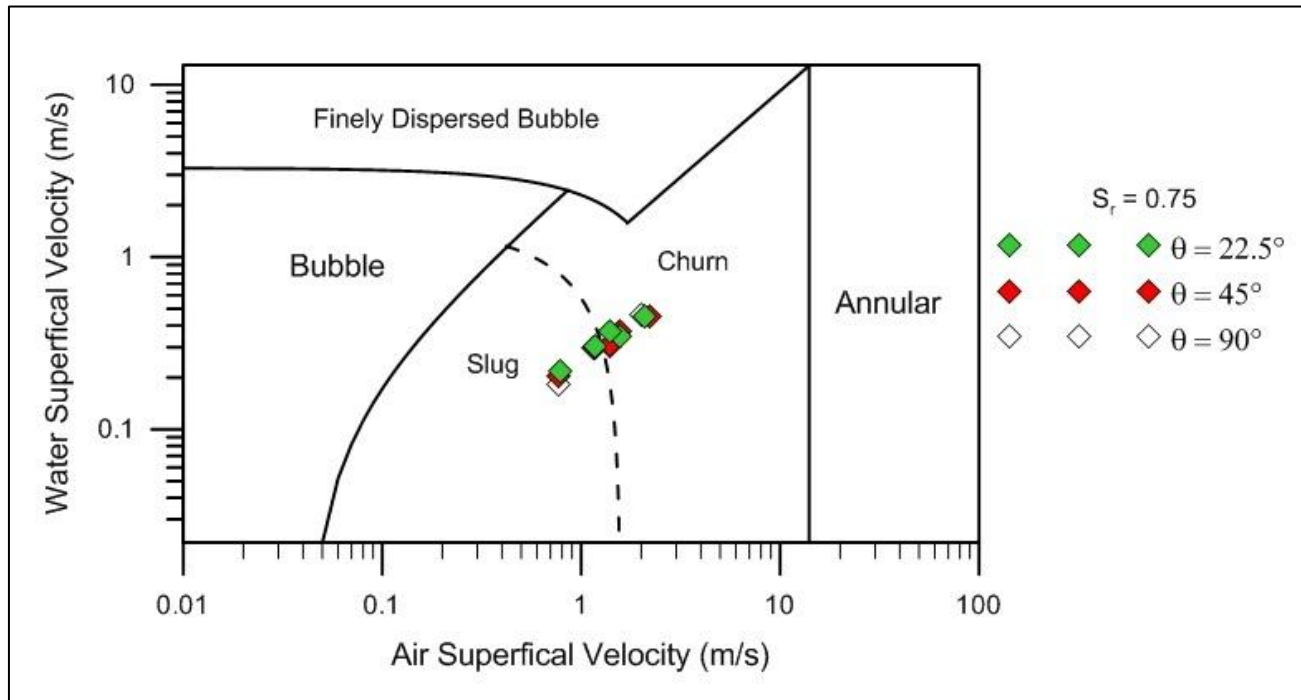


Figure 8. Distribution of experimental best efficiency point for various injection angles on the flow map proposed by, **Taitel et al., 1980**, at submergence ratio (0.75).

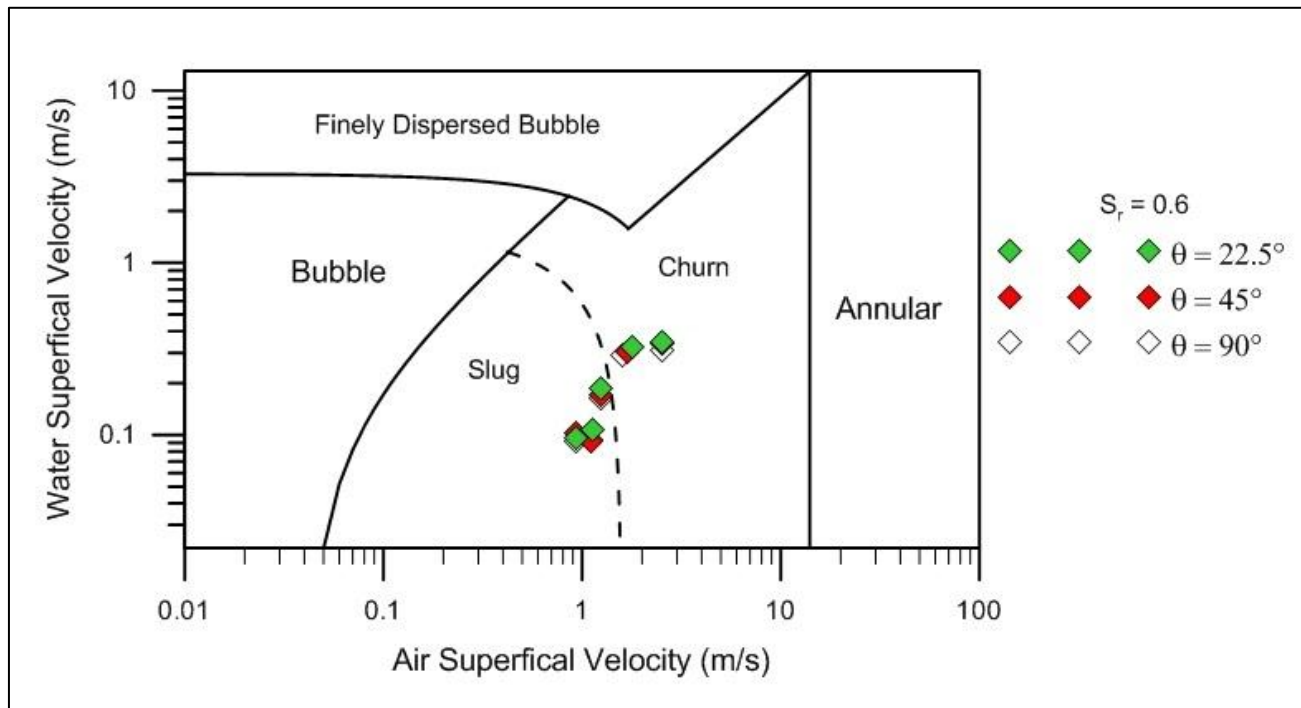


Figure 9. Distribution of experimental best efficiency point for various injection angles on the flow map proposed by, **Taitel et al., 1980**, at submergence ratio (0.6).

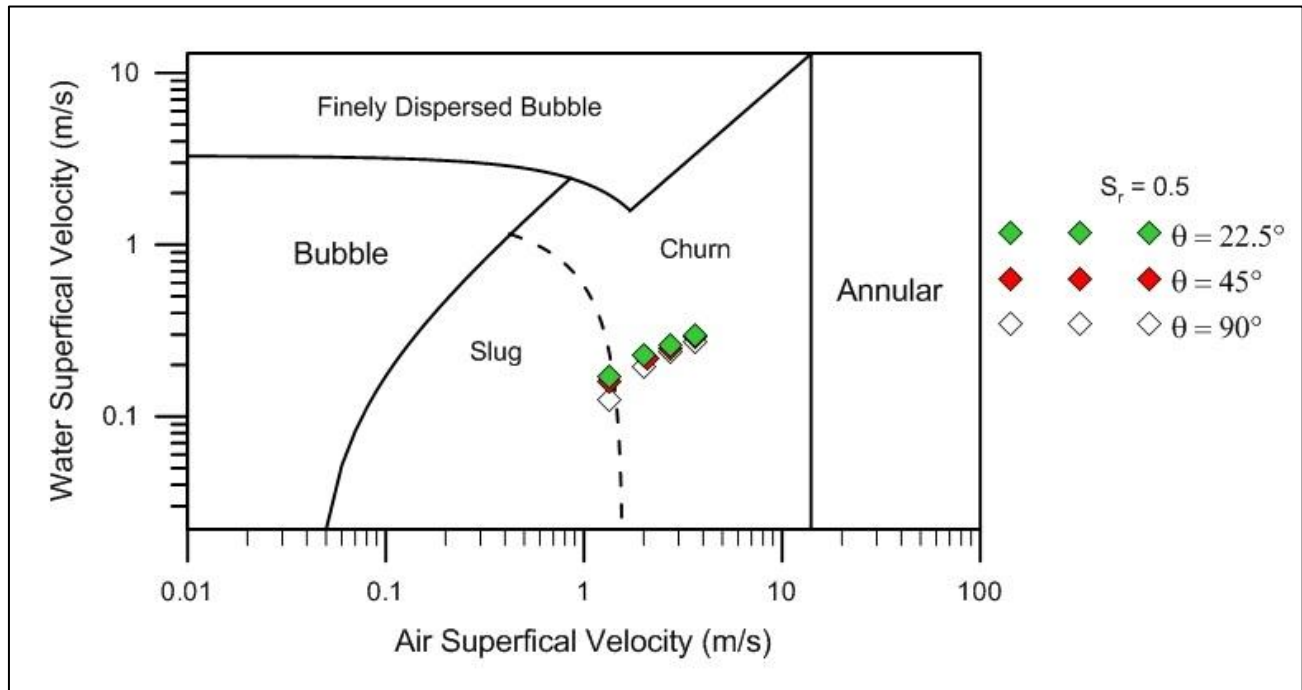


Figure 10. Distribution of experimental best efficiency point for various injection angles on the flow map proposed by, **Taitel et al., 1980**, at submergence ratio (0.5).

Robustness Assessment of Regional GNSS Geodetic Networks for Precise Applications

Dr. Oday Y. M. Zeki Alhamadani
Lecturer in Engineering Surveying and Space Geodesy
College of Engineering- University of Baghdad
oday_alhamadani@hotmail.com

Ahmed Zaidan Khalaf
Survey Engineer
ahmed_GIS10@yahoo.com

ABSTRACT

Over the past few decades, the surveying fieldworks were usually carried out based on classical positioning methods for establishing horizontal and vertical geodetic networks. However, these conventional positioning techniques have many drawbacks such as time-consuming, too costly, and require massive effort. Thus, the Global Navigation Satellite System (GNSS) has been invented to fulfill the quickness, increase the accuracy, and overcome all the difficulties inherent in almost every surveying fieldwork. This research assesses the accuracy of local geodetic networks using different Global Navigation Satellite System (GNSS) techniques, such as Static, Precise Point Positioning, Post Processing Kinematic, Session method, and finally Real Time Kinematic for different surveying applications. To achieve this assessment, GNSS observations were executed to highlight the characteristics for each GNSS observation technique. Furthermore, the level of accuracy which is gained from each positioning technique is enormously investigated to figure out the amount of allowable error and the suitability for different geodetic applications. In relative positioning, at least two receivers (or more) are required for timing and positioning while the Precise Point Positioning necessitates single receiver. Some of geodetic applications require about positions with centimeter level of accuracy or less. The robust geodetic networks provide accurate positions which in turn serve different earth science applications.

Key words: GNSS, Precise Point Positioning, Geodetic Network, DGPS, ITRF, IGS, CORS

تقييم متانة الشبكات الجيوديسية (GNSS) للتطبيقات الدقيقة

احمد زيدان خلف
مهندس
كلية الهندسة- جامعة بغداد

د. عدي ياسين محمد زكي
مدرس
كلية الهندسة- جامعة بغداد

الخلاصة

خلال العقود الاخيرة، كانت اعمال المسح الحقلية تنجز بالطرق التقليدية لانشاء الشبكات الجيوديسية الافقية والراسية. إلا أن اساليب مسح المواقع التقليدية هذا تتسم بالكثير من السلبيات كأستهلاكها للوقت وحاجتها الى جهد كبير لانجاز العمل الحقلية والحسابي بالإضافة الى الكلفة العالية. ولهذا السبب تم التوجه الى استخدام انظمة التوابع الملاحية العالمية لتعيين المواقع الافقية والرئيسية والتي تتسم بزيادة الدقة والتغلب على اغلب الصعوبات المرافقة لاعمال المسح الحقلية. يهدف هذا البحث الى تقييم دقة الشبكات الجيوديسية الصغيرة (المحلية) والنتيجة من استخدام تقنيات رصد ملاحية مختلفة كالرصد المستمر والرصد النقطي الدقيق والرصد المتحرك والرصد باستخدام عدد من المستلمات المتزامنة. لانجاز هذا التقييم تمت عملية رصد عدد من المواقع حيث تمت عملية تحليل ارسادات GNSS احصائيا لتسليط الضوء على الخصائص لكل من طرق الرصد المستخدمة. بالإضافة الى ذلك فان هذا البحث قيم مستوى الدقة المتوقع لكل اسلوب رصد لتعيين مقدار الخطأ المتوقع والمسموح به في الاحداثيات الافقية والرئيسية. فيما يخص اسلوب الرصد التناسبي، فان هذا الاسلوب يتطلب على الاقل استخدام مستلمات ملاحية عدد 2 لتعيين كلا من الموقع والوقت



بشكل دقيق، في حين ان اسلوب الرصد النقطي الدقيق يعمل بمستلم ملاحى واحد ولكن يحتاج الى فترة رصد طويلة. من هذا نجد ان التطبيقات الجيودسية تحتاج الى مستويات مختلفة من الدقة قد تصل الى حدود السنتيمترات او اقل من ذلك ولهذا السبب يجب التركيز على دراسة متانة الشبكات الجيودسية لتأسيس مواقع دقيقة لمحطات السيطرة والتي بدورها تخدم التطبيقات العلمية الدقيقة.

الكلمات الرئيسية: متانة الشبكات الجيودسية، المواقع الجيودسية، الرصد الملاحى

1. INTRODUCTION

In the field of surveying engineering, various definitions of Land Surveying are found. However, the term of Land of Surveying, generally, is defined as a science and technique of precisely observing the distances and angles between stations on the surface of the Earth. Recently, the Global Navigation Satellite System (GNSS) has been widely used by land surveyors since three decades. Consequently, the GNSS is vastly employed for the purpose of determining the positions, velocities, and time. Consequently, the GNSS, in general, has been considered as the main source for the different applications such as agriculture, mapping, public safety, military, monitoring, surveying and geographical information system (GIS), **Bakula, 2013; Wielgosz et al., 2013; Baryla et al., 2014; Krzan and Przestrzelski, 2016.**

In various field survey actions, there is always desperate need to involve different measurement techniques e.g. GNSS and Total Station. As a result it is important to evaluate the level of accuracy that can be accessible using each positioning technique and gain full understanding the methodology behind each technique. In GNSS relative positioning technique, at least one or more reference (base) stations are needed to determine the unknown positioning, whereas the Precise Point Positioning (PPP) just needs one receiver without base station **Ebner and Featherstone, 2008, Abdallah and Schwieger, 2014.** Some of applications required meter level or centimeter level positioning and this depends on the required accuracy, **Hofmann-Wellenhof et al., 2008.** This research focuses on achieving many goals using GPS and GLONASS. These goals include studying the accuracies of Iraqi CORS stations and assessment different GNSS positioning methods in comparison with Total Station solution.

In the literature on GNSS observations, the relative importance of the accuracy that can be gained from different GNSS positioning techniques has been subjected to considerable discussion. Furthermore, studying the mechanism of GNSS observation methods (field work) together with the procedures of GNSS raw data processing are important for evaluation the level of accuracy and how to mitigate all possible errors involved in the satellites-related errors, receiver-related errors, and signal-related errors.

When using Differential GPS (DGPS) positioning technique, millimeter level accuracy can significantly be obtained due to the reason that some errors can relatively vanished by both of between receiver's difference and between satellites difference. The accuracy of the height component is relatively lower than the accuracy of the horizontal components due to the reason that there is no observations of satellites appear below the horizon. Furthermore, the accuracy of the northern component is slightly better than the eastern component because of the designing of motion of satellites and satellite orbits, **GPS, 2016.**

Generally, double-differences corresponding to between receives difference and between satellites difference are noticeably reduce satellite clock and orbit errors, localized atmospheric errors, and receiver

clock errors. Furthermore, triple-differences correspond to between receives difference, between satellites difference, and between time difference is considerably eliminates the effect of integer ambiguities, **Hofmann-Wellenhof et al., 2008**.

The GNSS receivers have their point position referenced for the geodetic world system 1984 (WGS84). The reference system of WGS84 is used for Continuously Operating Reference Station (CORS) stations network. A link for the another reference such as International Terrestrial Reference Frame (ITRF) is created for the CORS network besides that the difference between the WGS84 reference frame system and the ITRF is a few centimetres only. The ITRF reference frame is a realization of an International Terrestrial Reference System (ITRS), which are Cartesian coordinates of Earth centred earth fixed and they are computed at different epochs, **ESA, 2016**. The potential of error sources include the sources of conventional error that frequently required to be handled with PPP, for example the satellite orbit and clock errors, troposphere delays error and ionospheric delay error, **Bidikar et al., 2014**. It is important to mention here that most of these error sources can considerably be mitigated to some extent through modeling processes. The ionospheric delay effect can be reduced throughout constructing the ionosphere-free observation combinations while the receiver clock offset and tropospheric delay effect could estimate as unknown parameters, **Gérard and Luzum, 2010**.

Table .1 highlights the small changes in the coordinates per year for six Continuously Operating Reference Stations (CORS) in Iraq which were established by National Geodetic Survey “<http://www.ngs.noaa.gov/>”. These six CORS stations are ISBA in Baghdad, ISBS in Basra, ISER in Erbil, ISNA in Najaf, ISSD in Tikrit, and finally ISKU in Kut. The changing estimates in both of Cartesian and East, North, and Up coordinates were estimated using the velocity estimates of International Terrestrial Reference Frame 2000 (ITRF00) and IGS08. These velocity estimates are referred in the **Table .1** as VX, VY, VZ for the Cartesian coordinates (X, Y, Z) and VN, VE and UP for the North, East, Up coordinate system, **NGS, 2016**.

2. CASE STUDY AND DATASET

This research was carried out based on two case studies. The first case study was the University of Baghdad, Al-Jadiryia Campus, where eleven control stations were established as shown in **Fig .1**. The selection of locations of these ten control stations was accomplished under two conditions, the first condition is avoiding any obstructions and reflective surfaces, and the second condition is to keep the visibility between adjacent control stations which is one of the most important conditions for performing the field survey works by TS.

The second case study was local GNSS observation data which were taken from six sites, these are Al-Basra city, Al-Mosul city, Wasit city, Al-Najaf city, Babylon city, and Baghdad city. The raw GNSS data from these six sites were processed based on Iraqi CORS stations and some selected IGS (International GNSS Services) stations which are located outside Iraq. The positions of these six selected sites were computed based on DGPS processing solution using two schemes. The first scheme is to correct the raw GNSS data based on Iraq CORS stations and the second scheme is to correct the raw GNSS data based on

the IGS stations which are located outside of Iraq. The comparison between two solutions (schemes) was employed for evaluation the characteristics of Iraqi CORS stations in comparison with the IGS stations.

3. METHODOLOGY

Although extensive studies have been carried out to address the accuracy of GNSS solutions, no single study exists which gives clear evidence about the level of accuracy that can be reached out from GNSS solutions, particularly the differential GNSS solutions. However, most of research and studies which have been performed in the subjects of using GNSS for geodetic applications, discussed intensively the precision of GNSS solutions based on number of factors, e.g. error sources, data processing, length of observation, baseline length, etc...

The assessment of accuracy for different GNSS techniques is explained in this research such as studying of characteristics of Iraqi CORS stations and explaining different observation techniques of GNSS based on (DGPS) and Total Station measurements.

First Case Study:

Regarding field works, a network of twelve stations were established in the University of Baghdad, Al-Jadiryia campus and observed using different GNSS positioning techniques and Total Station, see **Fig. 1**. The Topcon GPS GR5 and Total Station (GTS751) were employed in this research. In this research, the term TS will be used in its broadest sense to refer to Total station solution. Topcon tools software was also used for processing the GNSS raw data from DGPS. Additionally, AutoCAD civil 3D (2016) was used to adjust the traverse observation data taken by GTS751. In this research, the robustness of the geodetic networks which are established by GNSS observations was carried out based on five GNSS positioning techniques, these are Static GNSS survey, Post-Processing Kinematic Survey (PPK), Real-Time Kinematic Survey (RTK), Precise Point Positioning Survey (PPP), and finally Session Survey. The precise positions from the land surveying by TS were considered as a reference solution to evaluate the GNSS positioning accuracy in term of geometry of Travers shape (baseline lengths, baseline bearings, and areas).

Fig. 2 addresses the baseline length differences in millimeters between TS solution and five GNSS solutions. **Fig. 3** illustrated the different in baseline bearing in seconds between TS solution and five GNSS solutions. In both of **Fig. 2** and **Fig. 3**, the dark blue color stands for the difference between TS solution and PPK solution, the red color is the difference between TS solution and PPP solution, the green color corresponds to the difference between TS solution and RTK solution, the magenta color represents the difference between TS solution and Session solution, and finally, the light blue color stands for the difference between TS solution and Static solution. **Fig. 4** shows the differences between Travers areas in meter square between TS solution and five GNSS solutions. Finally, the differences in the point positions for each station between the TS solution and each of the five GNSS solutions are presented as vectors as shown in **Fig. 5**.

Second Case Study:

Regarding the assessment of Iraqi CORS stations, the raw data from six CORS stations were downloaded in RINEX format by the IGS website and processed using online services such as Online Positioning User Service (OPUS). The computed positions of these six stations were compared with the results from International GNSS Service (IGS08) solution and International Terrestrial Reference Frame (ITRF00) solution over the period from 2008 to 2015. **Fig. 6** shows the differences in Easting, Northing, and Up components for these six CORS stations between OPUS solution (as own solution) and IGS08 solution and ITRF00 solution. What is more, **Fig. 7** demonstrates the differences in X-, Y-, and Z-coordinates for six CORS stations between OPUS solution (as own solution) and IGS08 solution and ITRF00 solution.

4. RESULTS , DISCUSSION AND CONCLUSIONS

The Iraqi Geospatial Reference System (IGRS) could be considered as a combines of network for Global Positioning System (GPS), CORS and a High Accuracy Reference Network (HARN) for application of surveying control points.

There are clear differences among the results when using the NGS Online Positioning User Service (OPUS) and the other results depending on the velocity of CORS stations in Iraq.

The results of coordinates that acquired from the different sources such as online services (OPUS) or the velocities of IGS08 solution and ITRF00 solution are listed **table.1**.

In this research, the precise applications for accurate positioning were introduced. In general, two main themes were applied. The first part includes the analysis of Iraqi CORS stations and study the changing depending on characteristics such as velocities based on IGS information in addition to the accuracy of positioning using Iraqi CORS stations and that located outside. The second part includes the comparison between the results of observations from DGPS solutions and these which were obtained from using total station. These different techniques such as STATIC, PPK, PPP, SESSION, RTK and total station were applied in this research. Online services were used for processing the data for all DGPS raw data. In this research, two stations were taken with DGPS as static techniques which were observed more than eight hours for two control points which related with the baseline and other deferent technique had different times depending on the method of techniques. From the experimental results obtained data in this research the following conclusions had been made:

1. Under the conditions of visible satellites, when the number of visible satellites was greater than 6, PDOP value did not exceed 2.66.
2. There is a clear difference in the accuracy when using Iraqi CORS stations as compared with another CORS stations located outside Iraq, such as Bahrain, Iran, Israel and others. These irregular differences may reach to 4.5 cm.



3. Over the period of 2009-2015 in Iraq, there is an increasing in easting and northing components around (3.5cm), while ellipsoid height has irregular differences.
4. This study showed that the differences in positions between those based on OPUS processing software and those based either IGS08 or ITRF00 are small.
5. When Point Positioning technique could achieve centimeter positioning accuracy level and it has the ability to solve the satellite Orbit and clock error.
6. The reference datum of GNSS is WGS84, where heights are referred to a theoretical "mathematical" ellipsoid, not to real-life terrain or geopotential surface. Hence, in order to reference GNSS derived heights to terrain, the geoid–ellipsoid separation must be known to be used in the equation of $h = H + N$.
7. The difference in X-coordinates when using OPUS and both of IGS08&ITRF00 reach to 2.30 cm and 2.50 cm, correspondingly.
8. The difference in Y-coordinates when using OPUS and both of IGS08&ITRF00 reach to 0.76 cm and 2.96 cm, correspondingly.
9. The difference in Z-coordinates when using OPUS and both of IGS08&ITRF00 reach to 17.20 cm and 17.99 cm, correspondingly.
10. The difference of Easting coordinates when using OPUS and both of (IGS08&ITRF00) reach to 17.40 cm and difference of northing coordinates reach to 20.40 cm for each of them and for EL.H coordinates reach to 0.90 cm.
11. The difference of PPK and RTK techniques comparing with classical surveying (Total Station) is in millimeter level, but for Stand-alone is in centimeter level.
12. Regarding the length of baseline, the difference between PPK technique and Total Station technique reaches to (1.90 mm) and RMSE of (1.20 mm) for all baselines.
13. Regarding the length of baseline, the difference between RTK technique and Total Station technique reaches to (3.20 mm) and RMSE of (1.50 mm) for all baselines.
14. Regarding the length of baseline, the difference between session technique and Total Station technique reaches to (2.10 mm) and RMSE of (1.30 mm) for all baselines.
15. Regarding the length of baseline, the difference between Static technique and Total Station technique reaches to (4.34 mm) and RMSE of (3.20 mm) for all baselines.
16. Regarding the length of baseline, the difference between PPP technique and Total Station technique reaches to (11.2mm) and RMSE of (4.2 mm) for all baselines.



5. RECOMMENDATION

Future work will be focused on improving the GPS orthometric heights using another local Geoid Model (if it possible) and more developer than the last version of Global Geoid Model which had used in this research (EGM 2008) and Study the accuracy when using another collection of Satellite System such as European satellites and china satellites in the surveying applications in Iraq.

REFERENCES

- Abdallah, A., and Schwieger, V., 2014, *Accuracy Assessment Study of GNSS Precise Point Positioning for Kinematic Positioning*, MSc. Thesis, University of Stuttgart, Institute of Engineering Geodesy, PP.115-116.
- Baryła, R., Paziewski, J., Wielgosz, P., Stępnik, K., and Krukowska, M., 2014, *Accuracy assessment of the ground deformation monitoring with the use of GPS local network: Open*
- *Pit mine Koźmin Case Study*. Acta Geodyn. Geomater., Vol.11, No. 4(176),PP.317-324,DOI: 10.13168/AGG.2014.0013.
- Bidikar, B., Rao, G.S., Ganesh, L., Kumar, M.S., 2014, *Satellite Clock Error and Orbital Solution Error Estimation for Precise Navigation Applications*. Department of ECE, Andhra University.
- Bakula, M., 2013, *Study of reliable rapid and ultra-rapid static GNSS surveying for determination of the coordinates of control points in obstructed conditions*. Journal of Surveying Engineering, vol. 139, No. 4, PP. 188 –193, DOI: 10.1061/ (ASCE) SU.1943-5428.0000109.
- Ebner, R. and Featherstone, W. E., 2008, *How well can online GPS PPP post-processing services be used to establish geodetic survey control networks?* , Journal of Applied Geodesy, PP. 149–157, DOI 10.1515/JAG.2008.017.
- ESA, 2016, *Reference Frames in GNSS*. http://www.navipedia.net/index.php/Reference_Frames_in_GNSS#cite_note-1 (accessed 25 January. 2016).
- GPS.gov, 2016, *Surveying & Mapping*. , GPS.GOV, Official U.S. Government information about the Global Positioning System (GPS) and related topics. <http://www.gps.gov/applications/survey/> (accessed 25 January. 2016).
- Gérard P., and Luzum, B., 2010, *International Earth Rotation and Reference Systems Service (IERS)*, IERS Technical Note No. 36.PP.137-142.
- Hofmann-Wellenhof, B., Lichtenegger, H., and Wasle, E., 2008, *GNSS – Global Navigation Satellite Systems*. ISBN 978-3-211-73012-6 SpringerWienNewYork, PP.175-178.
- Krzan, G., and Przestrzelski, P., 2016, *GPS/GLONASS Precise Point Positioning With IGS Real-Time Service Products*, Acta Geodyn. Geomater., Vol.13, No. 1 (181), xx1–x13, DOI: 10.13168/AGG.2015.0047.



- NGS, 2016, *Continuously Operating Reference Station (CORS)*.<http://www.ngs.noaa.gov/CORS/> (accessed 25 January. 2016).
- Wielgosz, P., Krukowska, M., Paziewski, J., Krypiak-Gregorczyk, A., Stępniaak, K., Kapłon, J., Sierny, J., Hadaś, T., and Bosy, J., 2013, *Performance of ZTD models derived in near real-time from GBAS and meteorological data in GPS fast-static positioning*, *Measurement Science and Technology*, Vol.24, No. 12,DOI:10.1088/0957-0233/24/12/125802.

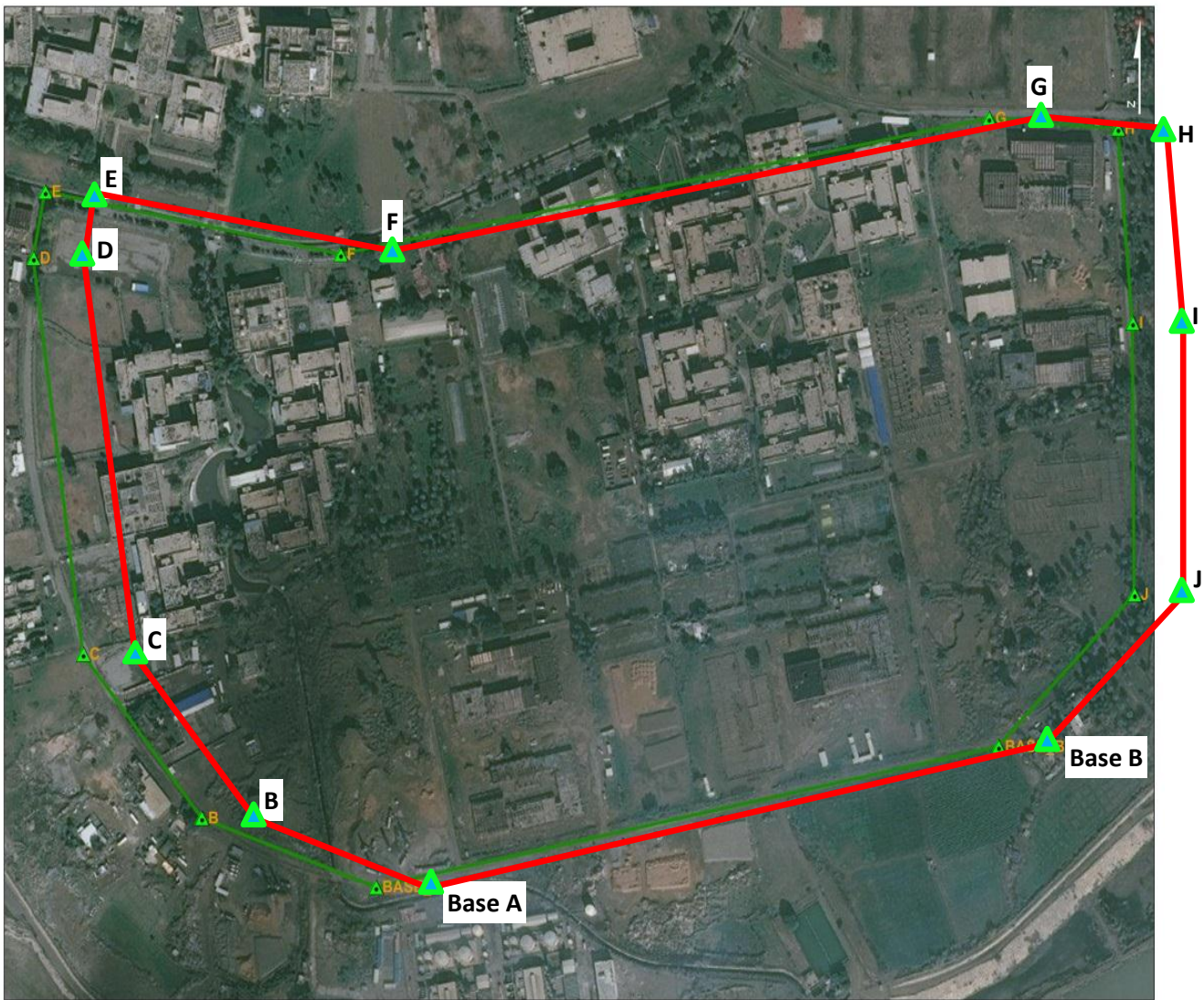


Figure 1. Area of Study, University of Baghdad, Aljadiriya Campus.

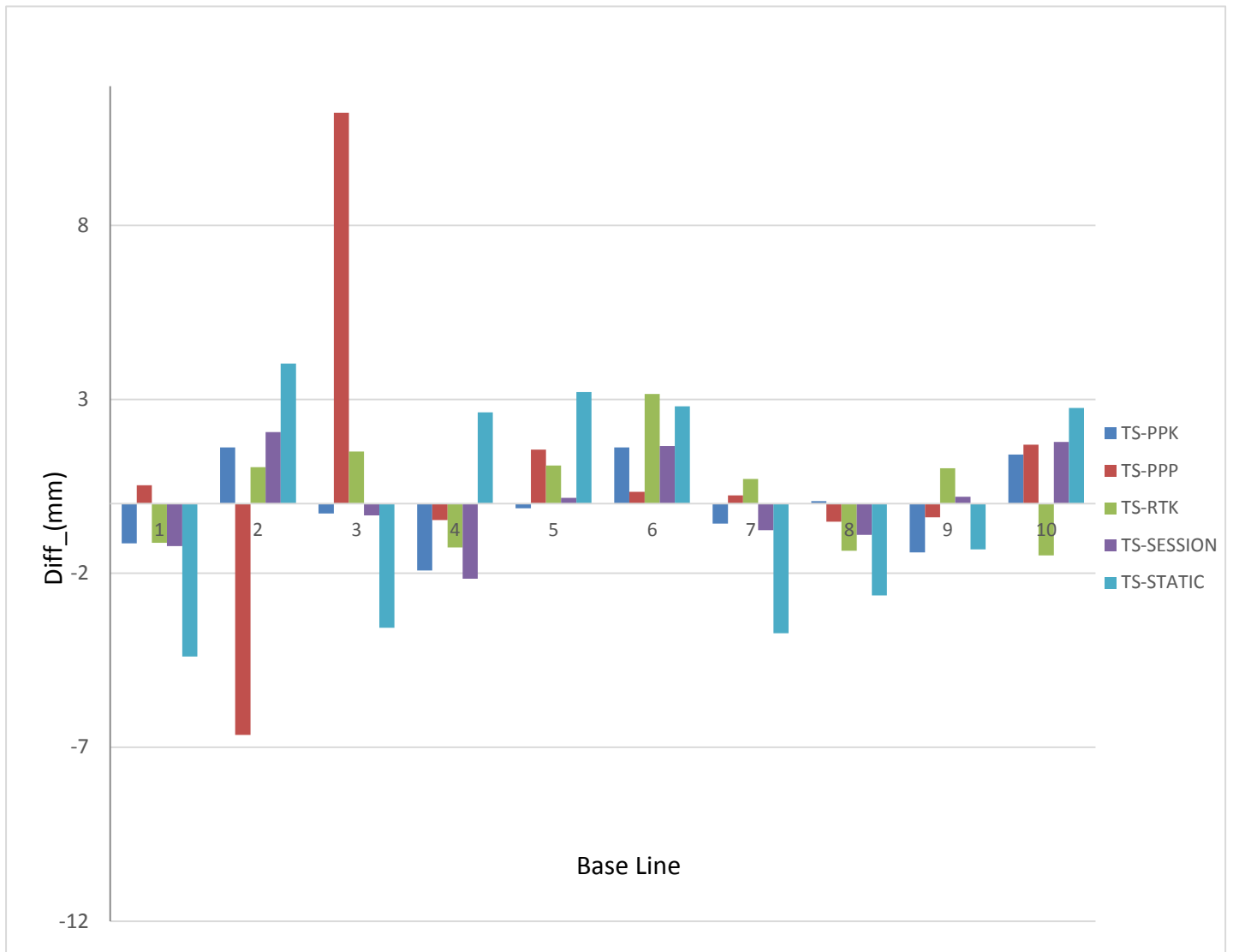


Figure 2. The difference in Baseline length in millimeter between different GNSS observation techniques and total station technique.

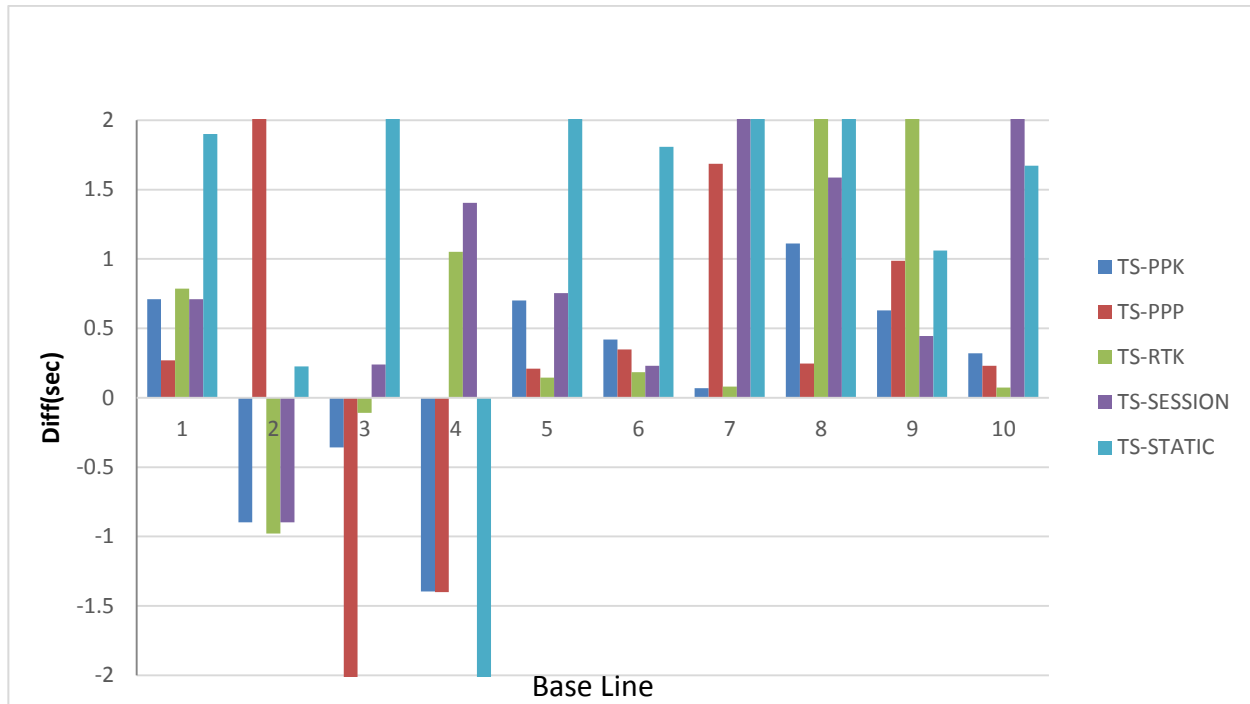


Figure 3. The difference in Baseline bearing in second between different GNSS observation techniques and total station technique.

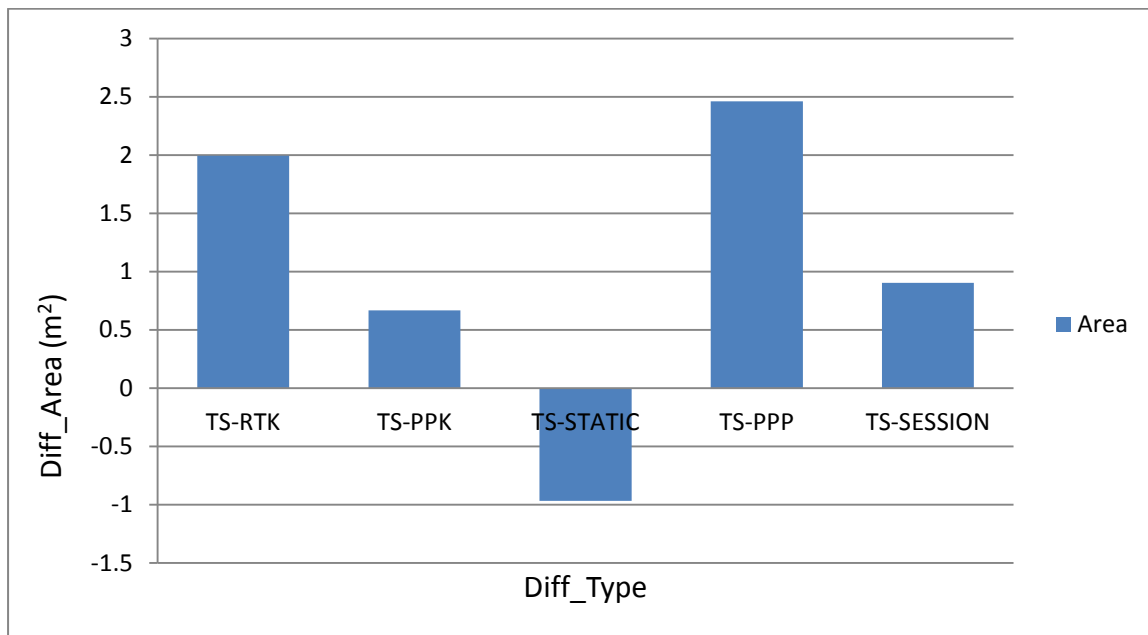


Figure 4. The difference in areas in square meter between different GNSS observation techniques and total station technique.

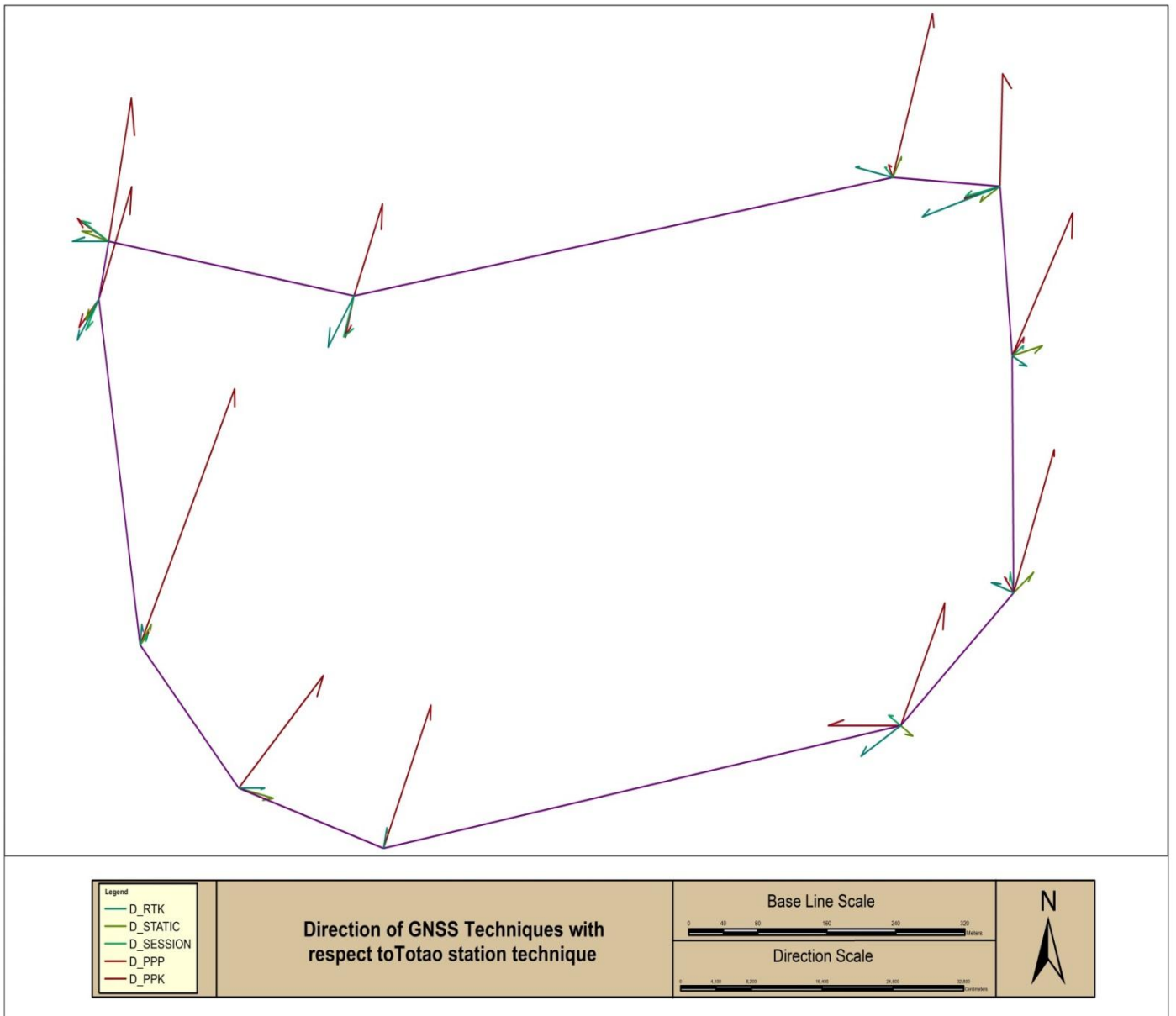


Figure 5. The Differences in Directions between TS Solution and Each of GNSS Solution.



Table 1. Characteristics of changing for coordinates per year depending on IGS information.

ISBA			ISBS			ISER		
Velocity(m/year)	IGS08	ITRF00	Velocity(m/year)	IGS08	ITRF00	Velocity(m/year)	IGS08	ITRF00
VX	-0.0298	-0.0271	VX	-0.0330	-0.0293	VX	-0.0299	-0.0262
VY	0.0058	0.0024	VY	0.0067	0.0034	VY	0.0035	0.0000
VZ	0.0224	0.0269	VZ	0.0294	0.0291	VZ	0.0262	0.0258
VN	0.0282	0.0322	VN	0.0341	0.0338	VN	0.0324	0.0319
VE	0.0250	0.0207	VE	0.0289	0.0240	VE	0.0233	0.0182
UP	-0.0021	0.0000	UP	0.0001	0.0000	UP	0.0001	0.0000
ISNA			ISSD			ISKU		
Velocity(m/year)	IGS08	ITRF00	Velocity(m/year)	IGS08	ITRF00	Velocity(m/year)	IGS08	ITRF00
VX	-0.0310	-0.0274	VX	-0.0301	-0.0265	VX	-0.0316	-0.0279
VY	0.0071	0.0036	VY	0.0051	0.0016	VY	0.0060	0.0025
VZ	0.0277	0.0273	VZ	0.0266	0.0262	VZ	0.0280	0.0277
VN	0.0326	0.0322	VN	0.0323	0.0318	VN	0.0331	0.0328
VE	0.0267	0.0217	VE	0.0245	0.0195	VE	0.0268	0.0217
UP	0.0001	0.0000	UP	0.0001	0.0000	UP	0.0001	0.0000

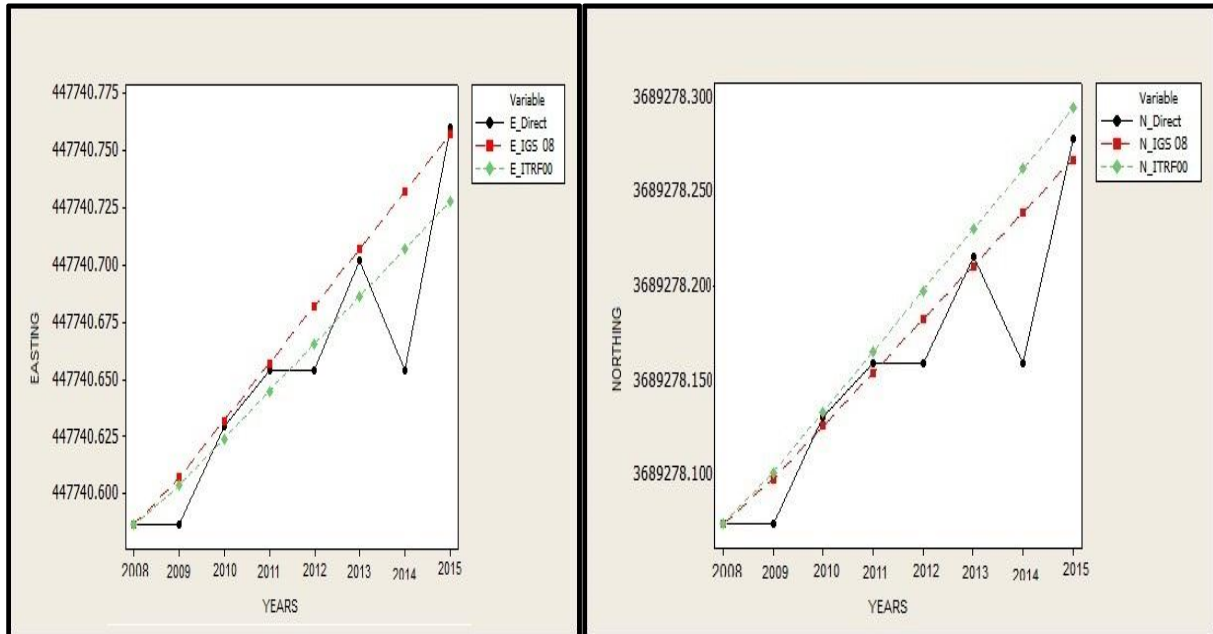


Figure 6a. The difference of easting coordinates.

Figure 6b. The difference of northing coordinates.

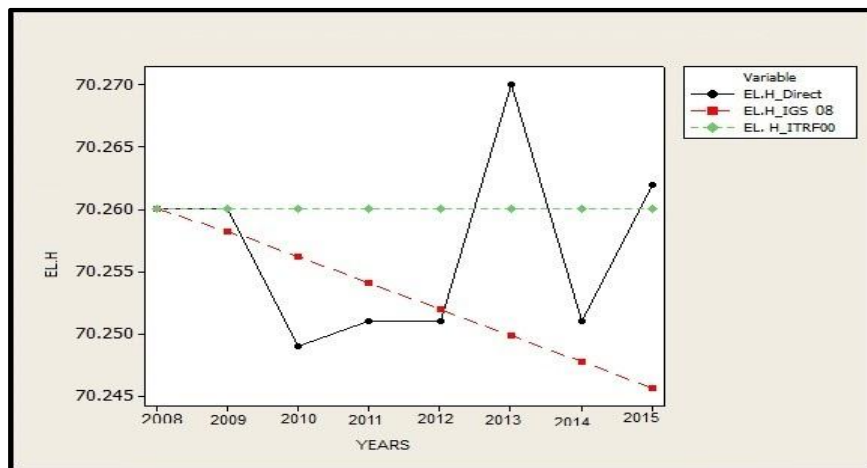


Figure 6c. The difference of ellipsoid height coordinates.

Figure 6. The difference of easting, northing and ellipsoid height.

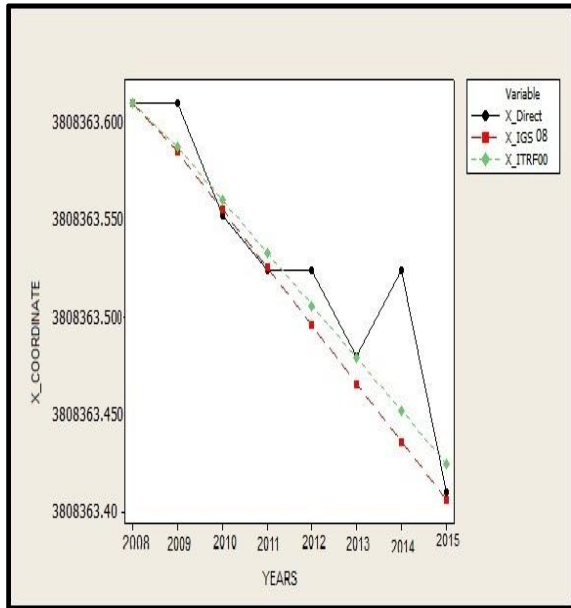


Figure7a. The difference of Cartesian coordinates for X.

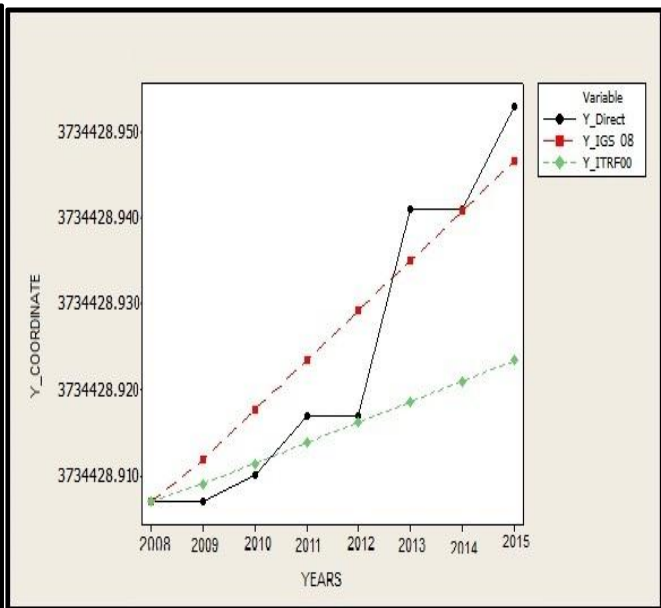


Figure7b. The difference of Cartesian coordinates for Y.

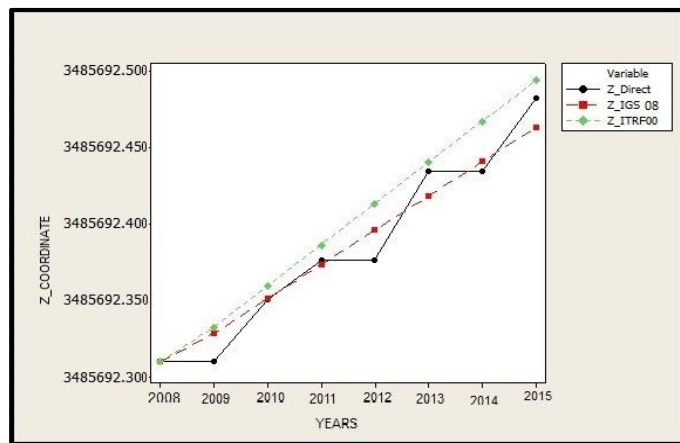


Figure7c. The difference of the difference of Cartesian coordinates for Z coordinates.

Figure 7. The difference of X, Y and Z.